# The Turn of the

# Screw & the Slide of the Skyrmion

N. del Ser

# The Turn of the Screw and the Slide of the Skyrmion

Inaugural-Dissertation

zur

Erlangung des Doktorgrades

der Mathematisch-Naturwissenschaftlichen Fakultät

der Universität zu Köln

*vorgelegt von*

## Nina del Ser

*geboren in*

Colombo, Sri Lanka

*aufgewachsen in*

Almaty, Kasachstan und London, Großbritannien

*aus*

Frankreich und Spanien

Köln 2022

Berichterstatter:                                  Prof. Dr. Achim Rosch
                                                   Prof. Dr. Sebastian Diehl
                                                   Prof. Dr. Jairo Sinova (externer)

Vorsitzender der Prüfungskommission:   Prof. Dr. Joachim Hemberger

Tag der mündlichen Prüfung: 3 Juni 2022

All (wo)men by nature desire to know.
— Aristotle, tweaked NdS ;)

# Abstract

For hundreds of years, human beings have developed technologies based on magnetism. From the humble compasses of our ancestors to the smartphones, hard drives and maglev trains that have come to symbolise the modern age, magnets have shaped civilisations and will continue to do so for generations to come.

Recently, physicists have discovered a new class of magnets known as chiral magnets, which are characterised by a lack of inversion symmetry. This property encourages the formation of twisted magnetic structures such as helices and exotic topological particles called skyrmions. Touted as promising candidates for use in future memory storage devices, skyrmions in particular have enjoyed a boom in scientific interest since their experimental discovery over ten years ago.

To use a chiral magnet in a technological setting, we have to interact with it via external forces, for example electric and magnetic fields, heat gradients or currents. In this thesis, we will investigate how chiral magnets can be manipulated by driving them with oscillating magnetic fields. We will do this for both the helical phase and for the single skyrmion, in both cases showing that such driving activates the translational Goldstone modes of the system at second order in the amplitude of the field. Translated into plain English, this means that the magnetic helices start to rotate on their axes at constant speed $\omega_{\text{screw}}$, a type of rotational motion which exactly mimics that of Archimedean screws, while the skyrmion starts to slide like an air hockey puck at constant velocity $\mathbf{v}_{\text{slide}}$. We will show how the magnetic Archimedean screw, in particular, can be used as a tool to transport electrons, with the potential of generating large DC electric currents in very clean metallic chiral magnets such as MnSi. We will also see how stronger driving leads to the formation of an interesting "time quasicrystal" instability, where the magnetisation oscillates at temporal and spatial frequencies which are incommensurate with the driving frequency and lattice momentum.

We will also explore the theme of topology, in particular the concept of fractional topological charges in magnets. We will show that such objects exist in both quantised and non-quantised form, including at the intersections of three or more domain walls or in the remnants of exploding skyrmions. There will be a discussion of their exceptional

scattering properties, a feature which distinguishes them from ordinary integer charges which are not able to scatter electrons and magnons. Using these scattering properties we will suggest how to build a magnon-powered fractional charge engine.

The thesis is organised as follows: in chapter 1 we provide an introduction to the chiral magnet model and its different phases, as well as the equation of motion governing magnetisation dynamics. Chapters 2 ("Archimedean screw"), 3 ("Driven skyrmions") and 4 ("Fractional charges") then contain the actual research work. We recommend reading chapters 2 and 3 consecutively, as a lot of the ideas for the driven skyrmions project build on the first third or so of the Archimedean screw work. Chapter 4 is a stand-alone chapter which can be understood separately. Finally in the Conclusion and Outlook we provide a summary of our achievements and suggest some natural follow-up questions to think about.

# Contents

# List of Figures

# Nomenclature

## Dimensionless Numbers

| Symbol | Description | Definition |
|---|---|---|
| $\alpha$ | damping coefficient | $-$ |
| $\delta$ | strength of dipolar interactions | $\dfrac{\gamma^2 \mu_0}{d^2 a^3 J}, \dfrac{\mu_0 \tilde{J} M_0^2}{\tilde{D}^2}$ |
| $\omega$ | reduced driving frequency | $\dfrac{J\Omega}{SD^2}, \dfrac{\tilde{J} M_0 \Omega}{\gamma \tilde{D}^2}$ |
| $b_i$ | reduced magnetic field | $\dfrac{\gamma B_i}{JSd^2}, \dfrac{M_0 \tilde{J} B_i}{\tilde{D}^2}$ |
| $d$ | ratio of DMI to Heisenberg energy scales | $\dfrac{D}{J}, \dfrac{a\tilde{D}}{\tilde{J}}$ |

## Greek Symbols

| Symbol | Description | Units |
|---|---|---|
| $\gamma$ | gyromagnetic ratio | $\mathrm{T}^{-1}\mathrm{s}^{-1}$ |
| $\Omega$ | driving frequency | $\mathrm{s}^{-1}$ |

## Roman Symbols

| Symbol | Description | Units |
|---|---|---|
| $\tilde{D}$ | Dzyaloshinskii-Moriya coupling constant, continuous model | $\mathrm{Jm}^{-2}$ |
| $\tilde{J}$ | Heisenberg coupling constant, continuous model | $\mathrm{Jm}^{-1}$ |
| $B$ | magnetic field | $\mathrm{T}$ |

| | | |
|---|---|---|
| $D$ | Dzyaloshinskii-Moriya coupling constant, discrete model | $J^{-1}s^{-2}$ |
| $J$ | Heisenberg coupling constant, discrete model | $J^{-1}s^{-2}$ |
| $K_u$ | easy axis anisotropy coupling | $Jm^{-3}$ |
| $K_{c,d}$ | cubic anisotropy coupling | $Jm^{-3}$ |
| $K_p$ | cubic plane coupling | $Jm^{-3}$ |
| $M_0$ | Magnetisation | $Am^{-1}$ |
| $S$ | Spin | $Js$ |

# 1

# Model and Fundamentals

## 1.1   Introduction

The average person probably doesn't realise how much of their life they owe to magnets. Every second of every day the Earth's magnetic core shields our planet and its inhabitants from lethal cosmic radiation which would otherwise penetrate our cells, causing unwanted mutations and ultimately fatal damage. Without magnetic compasses, our ancestors could never have navigated the world, explored continents or established important trading links. And neither would any of the comforts of the modern day, such as cars, dishwashers, coffee machines, computers, phones (indeed anything at all that runs on an electric motor) have ever been invented. Not to mention the fact that the absence of cheap souvenir magnets would force us to think twice as hard during our holidays about what gifts to get our friends back home. So magnets certainly are omnipresent and all-important.

In reality the particular type of magnetic behaviour discussed in the previous paragraph, called ferromagnetism[1], forms only a tiny subset of a vast wealth of magnetic phenomena which have been — and are still being — observed in nature. Some of these phenomena, for instance paramagnetism and diamagnetism, have been known about for a long time, but a lot of new and exciting types of magnets have only been discovered in recent years. In their laboratories, physicists have identified helical and conical magnets, and even exotic topological textures known as magnetic skyrmions. In addition to being a fun playground for physicists, a proper understanding and harnessing of these new magnetic phenomena could pave the way to various technological applications in the future, for instance in the form of new more efficient data storage devices [1, 2]. The

---

[1]the name comes from the Latin word *ferrum* — iron — a metal where this magnetic behaviour occurs naturally.

potential positive consequences for humanity as a whole could be as far-reaching as when our ancestors learned to use ferromagnetism to help them navigate the globe.

Although, as already mentioned, experimentalists have observed a huge range of magnetic textures in their labs, many of these can in fact be understood theoretically as originating beautifully from the same basic physics. The philosophy consists of considering magnets as collections of thousands and thousands of microscopic spins, each of which interacts with its neighbours as well as any externally applied magnetic fields. In this thesis we will consider a microscopic model for a broad subset of magnetic textures in nature which are known as *chiral magnets*. Their behaviour can be well-modelled by the following microscopic Hamiltonian

$$H = \sum_{\langle i,j \rangle} -J\mathbf{S}_i \cdot \mathbf{S}_j - \mathbf{D} \cdot (\mathbf{S}_i \times \mathbf{S}_j) - \gamma \mathbf{B}_{\text{ext}} \cdot \mathbf{S}_i + H_{\text{dip}}, \qquad (1.1)$$

where the indices $i, j$ label the lattice positions of the individual spins $\mathbf{S}_{i,j}$ and $\langle i, j \rangle$ indicates nearest neighbour summation. Different types of lattices (e.g. hexagonal, triangular, etc) are of course possible, but we will stay with the simplest cubic lattice, where all lattice positions can be reached by a combination of the three orthogonal cartesian basis vectors $\mathbf{e}_x, \mathbf{e}_y, \mathbf{e}_z$. Let us unpack this Hamiltonian and understand the physical origin of each term. The term $-J\mathbf{S}_i \cdot \mathbf{S}_j$ is known as the Heisenberg or exchange energy, and favours parallel alignment of neighbouring spins for positive $J$ — ferromagnetism — or antiparallel for negative $J$ — antiferromagnetism. $\mathbf{D} \cdot (\mathbf{S}_i \times \mathbf{S}_j)$ is the Dzyaloshinskii-Moriya[2] term, often shortened to DMI for **D**zyaloshinskii-**M**oriya **I**nteraction. DMI finds its physical origin in weak spin orbit interactions [3–5]. It is responsible for the "chiral" part of the name "chiral magnet" because it is the only energy term to breaks spatial inversion symmetry in Eq. (1.1). The $\mathbf{D}$ vectors point in the same directions as the displacement vectors between the spins $\mathbf{S}_i$ and $\mathbf{S}_j$, i.e. parallel to the three orthogonal cartesian basis vectors $\mathbf{e}_x, \mathbf{e}_y, \mathbf{e}_z$, and have magnitude $D$. DMI favours neighbouring spins being at right angles to each other, which encourages twisting in the magnetic texture. The third term in our Hamiltonian accounts for the Zeeman energy that the spins will acquire in the presence of any externally applied magnetic field $\mathbf{B}_{\text{ext}}$. Depending on the sign of the gyromagnetic ratio $\gamma$ — positive if the atoms are "hole-like" and negative if they are "electron-like" — it favours spin alignment or anti-alignment with $\mathbf{B}_{\text{ext}}$. Finally $H_{\text{dip}}$, whose precise mathematical form we will elaborate on later, contains all the long-range demagnetisation field and dipolar interaction energy contributions.

---

[2]The name is an homage to Russian and Japanese physicists Igor Dzyaloshinskii and Toro Moriya, who both made seminal contributions to the field in the 1950s

So far we have discussed the discrete lattice Hamiltonian, but a continuous version of Eq. (1.1) is also possible. To achieve this, we must switch from the discrete $\mathbf{S}_i$ to a continuous vector field $\boldsymbol{M}(\boldsymbol{r})$ known as the *magnetisation* field. Mathematically, the magnetisation corresponds to the local magnetic moment per unit volume. By defining the cubic lattice spacing $a$ in our discrete model Eq. (1.1) we arrive at the following mathematical relations between $\mathbf{S}_i, \mathbf{m}_i$ and $\mathbf{M}(\mathbf{r})$

$$\mathbf{m}_i = \gamma \mathbf{S}_i, \quad \mathbf{M}(\mathbf{r}) = \frac{\mathbf{m}_i}{a^3}. \tag{1.2}$$

The continuous version of the Hamiltonian, more often referred to as the free energy $F$ in the literature, takes the form

$$F = \int \mathrm{d}^3 r \left( -\frac{\tilde{J}}{2} \hat{\mathbf{M}} \cdot \nabla^2 \hat{\mathbf{M}} + \tilde{D} \hat{\mathbf{M}} \cdot (\boldsymbol{\nabla} \times \hat{\mathbf{M}}) - \mathbf{B}_{\mathrm{ext}} \cdot \mathbf{M} \right) + F_{\mathrm{dip}}, \tag{1.3}$$

where $\hat{\mathbf{M}} = \mathbf{M}/M_0$, with $M_0 = |\mathbf{M}|$, is the reduced magnetisation and we introduced rescaled exchange and DMI couplings $\tilde{J} = J a^5 M_0^2 / \gamma^2$ and $\tilde{D} = D a^4 M_0^2 / \gamma^2$ to make the formula neater. Eq. (1.3) is generally a valid approximation to the discrete model Eq. (1.1) if $\mathbf{M}(\boldsymbol{r})$ varies on a scale much larger than the lattice spacing $a$.

In the next section we will take a short look at the phase diagram which is generated for this model by varying the external magnetic field $\mathbf{B}_{\mathrm{ext}}$ and temperature $T$.

## 1.2 Phase Diagram and Experimental Realisation

By varying the temperature $T$ and the applied magnetic field $\mathbf{H} = \mathbf{B}_{\mathrm{ext}}/\mu_0$, we obtain the phase diagram shown in Fig. 1.1a. At high temperatures $T > T_c$ one finds a ferromagnetic (FM) or paramagnetic ("para") phase, depending on the strength of the applied magnetic field, $H$. To distinguish between these two phases we look at the order parameter $\langle \mathbf{M} \rangle$, which is non-zero for a ferromagnet but vanishes in a paramagnet. For a representation of the ferromagnet and paramagnet on a two-dimensional lattice, see panels i),ii) in Fig. 1.1c. The phase transition between the ferromagnet and paramagnet is usually second order, but turns into a first order phase transition if we enter the fluctuation driven regime (FD). If the applied field $H$ is not too large, $H < H_{c2}$, the behaviour of the $\langle \mathbf{M} \rangle$ will be determined by a competition between the DMI term and crystalline anisotropies (more on those in Chapter 4). If the DMI term dominates, the magnetic texture will start to twist. In this case, for $T < T_c$ we generally enter either a helical or conical phase, panels iii) and iv), respectively, in Fig. 1.1c). Both are characterized by a winding local
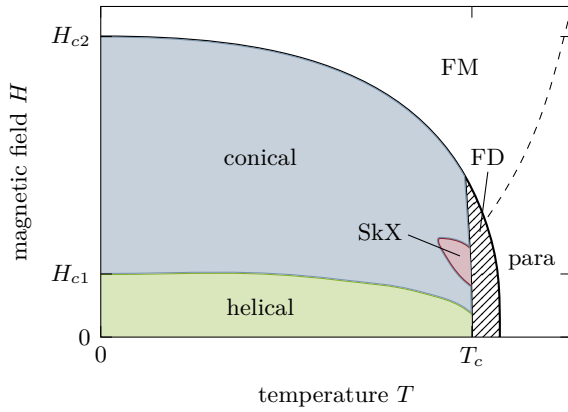
(a) Phase diagram (from [6]).
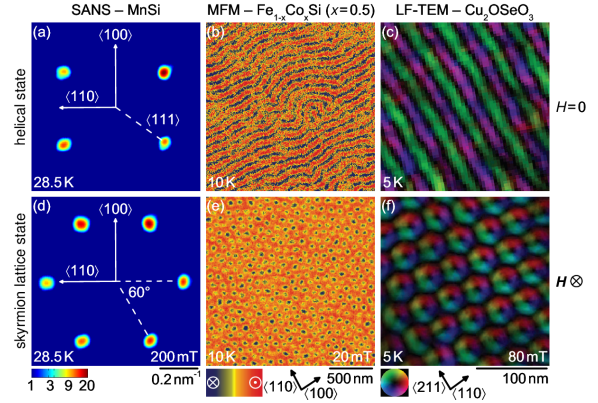
(b) Experimental evidence of helical/conical and skyrmion phases (from [7]).
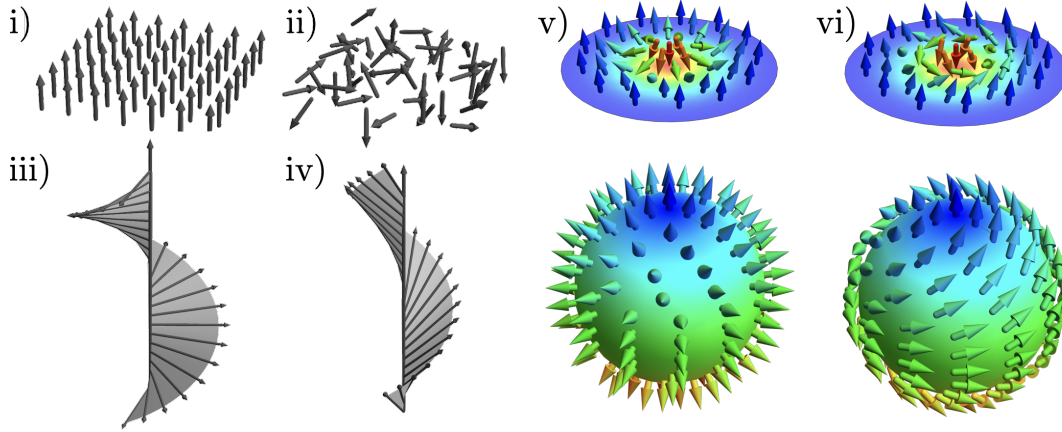


(c) Spin textures in a chiral magnet. i) Ferromagnet. ii) Paramagnet. iii) Helical state. iv) Conical state. v) Néel skyrmion. vi) Bloch skyrmion.

Figure 1.1 Phases in a Chiral Magnet and their Experimental Signatures

magnetisation which rotates in space around a fixed vector $\mathbf{q}$, called the pitch vector. At zero or very small values of the applied field $\mathbf{H}$ the direction of $\mathbf{q}$ is usually determined by the anisotropies in the system, but as $\mathbf{H}$ increases $\mathbf{q}$ becomes parallel to $\mathbf{H}$. In the helical phase, the local magnetisation is always perpendicular to $\mathbf{q}$, resulting in net zero total magnetisation, $\langle \mathbf{M} \rangle = 0$. By contrast, in the conical phase the spins form some angle $\theta < 90°$ with $\mathbf{q}$, resulting in a net total magnetisation $\langle \mathbf{M} \rangle = \hat{\mathbf{q}} M_0 \cos(\theta)$. This occurs because for larger applied fields $H > H_{c1}$ it becomes energetically beneficial for the magnetisation to tilt in the direction of the field. As $\mathbf{H}$ is further increased to a critical value $H > H_{c2}$ the cone angle $\theta$ decreases to zero and $\mathbf{M} \parallel \mathbf{q}$, i.e. we reenter the ferromagnetic phase via a second order phase transition. A more exotic type of magnetic ordering forms in a small region of the phase diagram just below $T_c$. Historically called the "A"-phase, but nowadays more commonly referred to as the *skyrmion lattice phase*

(SkX), this phase has the peculiarity of being topologically non-trivial (more on this later). It was first experimentally observed in small angle neutron scattering (SANS) experiments by Mühlbauer et al. in 2009 [8]. This discovery proved to be a turning point, and in the following decade and beyond the field of skyrmionics has enjoyed a boom in scientific interest and publications. Experimentally, the defining signature of the skyrmion phase is a six-peak pattern in the momentum-space intensity spectrum, which arises because of the hexagonal nature of the underlying skyrmion lattice, see the bottom left-most panel of Fig. 1.1b). Techniques such as Magnetic Force Microscopy (MFM) and Transmission Electron Microscopy (TEM) additionally provide the opportunity to compare and contrast the different magnetic phases in real space, see also the second and third columns in Fig. 1.1b. Looking at these images, one can clearly distinguish the wave front-like pattern generated by the winding magnetisation in the helical and conical phases from the six-fold pattern which characterises the skyrmion lattice. By now experimentalists have discovered a great deal of alloys which are well described by the chiral magnet model. The best investigated one is arguably manganese silicide (MnSi), a metal which can be grown with remarkable purity — with electrons enjoying mean free paths of up to $1000\,\text{Å}$ at low temperatures [9] — making it a very good candidate for experiments involving conductivity measurements. Also commonly used are the insulator copper oxide selenite ($Cu_2OSeO_3$) and metal iron germanium (FeGe).

Note that we have deliberately kept this overview of chiral magnets and their experimental realizations brief, as excellent overviews already exist elsewhere in the literature, e.g. see [10] for more details. In this thesis we will work in particular with the helical, conical and skyrmion phases of chiral magnets, which we explore in the next two subsections in more mathematical detail.

## 1.3   Helical & Conical State

In this section we concentrate on the helical and conical phases which occupy the lower left side of the phase diagram in Fig. 1.1a. We set up our coordinate axes such that the constant magnetic background field $\mathbf{B}_{\text{ext}} = \mathbf{B}_0$ points parallel to $\mathbf{e}_z$. With this choice of coordinates, $\mathbf{q} \parallel \mathbf{B}_0 \parallel \mathbf{e}_z$ if we are in the conical phase. For the helical phase we are free to choose the direction of spontaneous symmetry breaking for the pitch vector $\mathbf{q}$, and for simplicity we also set it to be $\mathbf{e}_z$. The unit magnetisation vector $\hat{\mathbf{M}}$ can then be

parametrised as

$$\hat{\mathbf{M}} = \begin{pmatrix} \sin(\theta_0)\cos(qz) \\ \sin(\theta_0)\sin(qz) \\ \cos(\theta_0) \end{pmatrix}. \tag{1.4}$$

The variables $q$ and $\theta_0$ are usually referred to as the pitch and conical angle of the helix, respectively. They can be determined by substituting Eq. (1.4) into the Hamiltonian Eq. (1.1) and (1.3) and minimising the energy with respect to $q, \theta_0$, see App. A for a detailed derivation. Neglecting the demagnetisation fields and dipolar interactions for now, we obtain the following discrete lattice expressions for $q, \theta_0$

$$\tan(qa) = d, \quad \cos(\theta_0) = b_0 \frac{1}{\frac{2}{d^2}(\sqrt{1+d^2}-1)}, \tag{1.5}$$

for the discrete model. For simplicity of notation we have switched to the dimensionless reduced quantities $d = D/J = a\tilde{D}/\tilde{J}, b_0 = \gamma B_0 J S/D^2 = B_0 M_0 \tilde{J}/\tilde{D}^2$, defined here in terms of the dimensional couplings of both the discrete and continuous models, Eq. (1.1) and (1.3). The expressions for $q, \theta_0$ in the continuous limit may be easily accessed by going to the limit $qa \ll 1$, where the helix wavelength is much greater than the lattice spacing. Then $q \simeq \tilde{D}/\tilde{J}$ and $\cos(\theta_0) \simeq b_0$. The helical phase ($\theta_0 = \frac{\pi}{2}$) occurs when $b_0 = 0$ exactly, and the conical phase occurs when $0 < b_0 < 1$. When $b_0 = 1$ exactly, the cone angle $\theta_0 = 0$ and we are in the ferromagnetic (FM) phase.

We will now take a short excursion into dipolar interactions, explaining their physical origin and how they affect the helical pitch $q$ and conical angle $\theta_0$ of our helices.

### 1.3.1 Dipolar Interactions

The following model for including dipolar interactions closely follows section 3.3 of J. Waizner's thesis [10]. $H_{\text{dip}}$ arises because in addition to the short range Heisenberg and DMI interactions, the spins also experience long range interactions. Each spin can be thought of as a tiny magnet whose magnetic moment $\mathbf{m}_1$ produces a magnetic field

$$\mathbf{B}_{\text{dip}}(\mathbf{r}) = \frac{\mu_0}{4\pi} \frac{3\hat{\mathbf{r}}(\mathbf{m}_1 \cdot \hat{\mathbf{r}}) - \mathbf{m}_1}{r^3} \tag{1.6}$$

at position $\mathbf{r}$ relative to itself. Another spin with magnetic moment $\mathbf{m}_2$ located at $\mathbf{r}$ would therefore experience a Zeeman-like energy $E_{\text{dip}} = -\mathbf{m}_2 \cdot \mathbf{B}(\mathbf{r})$ . Typically, the exchange constant is approximately a thousand times larger than the dipolar interaction on the atomic scale, but the dipolar interaction is long-ranged and therefore becomes increasingly important for large sample sizes.

As we are dealing with macroscopic solids rather than a few individual spins, it is usually too difficult to calculate the dipolar energy contribution by summing up all the individual dipole energies between each pair of spins. However, for spin textures with regular modulations in space, a calculation in the Fourier domain can be much cost-effective and easy to implement. In our particular case we are investigating helical and conical magnetic textures, which have only three non-zero Fourier components: $k = 0$ and $k = \pm q$, making them ideal for a momentum space approach. We will therefore switch to momentum space from now on. The limit of $k = 0$ actually needs to be treated separately, thus we will split

$$F_{\mathrm{dip}} = F_{\mathrm{dip},k=0} + F_{\mathrm{dip},k\neq0}, \tag{1.7}$$

and explain the physical origin and mathematical treatment of the these two sub-contributions in the following two short subsections.

## Demagnetisation Fields

When $k = 0$ we are dealing with a uniform component of magnetisation, which will lead to the formation of *demagnetisation* fields. Historically, Kittel was the first to take into account the effect of these fields on ferromagnetic resonances [11]. The calculation of demagnetisation fields is particularly simple for samples which have an ellipsoidal shape. When a constant background field $\mathbf{B}_0$ is applied along one of the principal axes of an ellipsoidal magnetisable body, the microscopic magnetic moments inside the sample will try to line up with the direction of that field. This means that inside the sample, neighbouring "north" and "south" poles cancel, whereas at the boundaries there will be an accumulation of "north" poles on one side and "south" poles on the opposite side of the sample. The net result is that these surface "magnetic charges" set up a *demagnetisation* field $\mathbf{B}_{\mathrm{demag}}$, which points opposite to the applied field. The physical idea here is very similar to the polarization field created by surface electric charges that arises inside a dielectric material when it is subjected to an external electric field, $\mathbf{B}_0$. The strength and direction of $\mathbf{B}_{\mathrm{demag}}$ is determined not only by $\mathbf{B}_0$ but also by demagnetisation factors, which depend purely on the shape of the ellipsoidal sample and always obey the identity

$$N_x + N_y + N_z = 1.$$

The demagnetisation factors reflect the symmetry of the sample. In highest symmetry case, where the sample is spherical, they would all be equal to each other, $N_x = N_y = N_z = \frac{1}{3}$.

The next highest symmetry case would be cylindrical symmetry, where only two of the demagnetisation factors are equal. In general, each demagnetisation factor is inversely proportional to the length of the sample in that direction, because the larger the distance between the surface "north" and "south" poles, the smaller the corresponding demagnetisation field. So for example if we had a thin film which extends infinitely in the $xy$-plane we would expect $N_x = N_y = 0, N_z = 1$. Once we know the demagnetisation factors we can write down the expression for the demagnetisation field $\mathbf{B}_{\text{demag}}$ which gets induced inside the sample,

$$\mathbf{B}_{\text{demag}} = -\mu_0 \underline{\underline{N}} \cdot \overline{\mathbf{M}} = -\mu_0 \begin{pmatrix} N_x & 0 & 0 \\ 0 & N_y & 0 \\ 0 & 0 & N_z \end{pmatrix} \cdot \begin{pmatrix} \overline{M}_x \\ \overline{M}_y \\ \overline{M}_z \end{pmatrix}, \tag{1.8}$$

where the components $\overline{M}_i$ are measured relative to the three principal axes of the sample. The bar over $\overline{\mathbf{M}}$ denotes the spatially uniform component of the magnetisation $\mathbf{M}$. It is mathematically defined via a spatial average over all space, $\overline{\mathbf{M}} = \int \mathrm{d}^3 r \mathbf{M}(\mathbf{r})$. From the relation between free energy density and magnetisation $\frac{\delta F}{\delta \mathbf{M}} = -\mathbf{B}_{\text{demag}}$, we can deduce that the total energy contribution due to demagnetisation fields is

$$F_{\text{dip},k=0} = \frac{1}{2}\mu_0 (\overline{\mathbf{M}} \cdot \underline{\underline{N}} \cdot \overline{\mathbf{M}})V, \tag{1.9}$$

where $V$ is the total volume of the sample.

## Dipolar Interactions at Finite $k$

For all the finite momentum modulations in the spin texture, the dipole-dipole interaction energy can be calculated using the following formula in Fourier space,

$$F_{\text{dip}} = \frac{\mu_0 V}{2} \sum_{\mathbf{k} \neq 0} \frac{(\mathbf{M}_{\mathbf{k}} \cdot \mathbf{k})(\mathbf{M}_{-\mathbf{k}} \cdot \mathbf{k})}{k^2}, \tag{1.10}$$

where $\mathbf{M}_{\mathbf{k}}$ are Fourier components with spatial frequency $\mathbf{k}$, defined according to the Fourier convention given in Eq. (B.2). A detailed derivation of Eq. (1.10) is given in App. B.1. Note that Eq. (1.10) is valid for 3D samples, in 2D the term looks somewhat different, see [10, 6] for details. However this doesn't concern us in this thesis, as we will be dealing exclusively with dipolar interactions in 3D textures.

Summarising the results of these two short subsections in a single expression, we can write

$$F_{\text{dip}} = \begin{cases} \frac{\mu_0 V}{2}(\overline{\mathbf{M}} \cdot \underline{\underline{N}} \cdot \overline{\mathbf{M}}), & \mathbf{k} = 0, \\ \frac{\mu_0 V}{2}\sum_{\mathbf{k}\neq 0}\frac{(\mathbf{M_k}\cdot\mathbf{k})(\mathbf{M_{-k}}\cdot\mathbf{k})}{k^2}, & \mathbf{k} \neq 0. \end{cases} \tag{1.11}$$

## 1.3.2 Effect of Dipolar Interactions on Helical & Conical state

Let us now see what effect dipolar interactions have on our helical and conical textures. We know that the magnetisation in these phases only has one non-zero spatially uniform component, $\overline{\mathbf{M}} = M_0\cos(\theta_0)\mathbf{e}_z$ using the parametrisation in Eq. (1.4). Thus the additional term in the Hamiltonian due to demagnetisation fields is

$$F_{\text{dip},k=0} = \frac{1}{2}\mu_0 M^2 N_z\cos^2(\theta_0)V = \frac{1}{2}NJS^2d^2(\delta N_z\cos^2(\theta_0)). \tag{1.12}$$

For the second equals sign we substituted $\mathbf{m} = \gamma\mathbf{S}/a^3$. We then used $V = Na^3$, where $N$ is the total number of spins in the system and additionally defined a dimensionless number $\delta = \frac{\gamma^2\mu_0}{d^2a^3J} = \frac{\mu_0 M_0^2\tilde{J}}{\tilde{D}^2}$, a measure of the "strength" of dipolar interactions. The addition of $H_{\text{dip},k=0}$ to the Hamiltonian does not change the equilibrium value of $q$, but it does modify $\theta_0$ to

$$\cos(\theta_0) = b_0\frac{1}{\frac{2}{d^2}(\sqrt{1+d^2}-1)+\delta N_z}, \tag{1.13}$$

see App. A for a derivation of this result. As $\delta$ is a positive number, the demagnetisation field increases the opening angle $\theta_0$ of the conical state. We expect this to happen because the demagnetisation fields always try to oppose the applied background field, in this particular case reducing it from $b_0\mathbf{e}_z$ to $(b_0 - \delta N_z\cos(\theta_0))\mathbf{e}_z$.

For the finite $k$ dipolar energy contribution we first need to calculate $\mathbf{M_k}$. Applying the Fourier tranform defined in Eq. (B.2) to the parametrisation Eq. (1.4), we obtain

$$\mathbf{M_k} = M_0 V\begin{pmatrix} \frac{1}{2}\sin(\theta_0)[\delta(\mathbf{k}-q\mathbf{e}_z)+\delta(\mathbf{k}+q\mathbf{e}_z)] \\ \frac{1}{2}\sin(\theta_0)[\delta(\mathbf{k}-q\mathbf{e}_z)-\delta(\mathbf{k}+q\mathbf{e}_z)] \\ \cos(\theta_0)\delta(\mathbf{k}) \end{pmatrix}. \tag{1.14}$$

As we have $\mathbf{M_k}\cdot\mathbf{k} = 0$ for all $\mathbf{k}$ there can be no energy contribution to the Hamiltonian from dipolar interactions. This term will however contribute when we start driving the system in Chapter 2.

## 1.4 Skyrmions

The building blocks of the skyrmion lattice phase are unsurprisingly called skyrmions. They owe their name to Tony Skyrme, a British physicist who pioneered the mathematical formulation of topological solitons in particle physics [12]. Topological solitons in condensed matter settings, first predicted as metastable excitations of ferromagnets in 1989 by Bogdanov and Yablonskii [13], later earned the shorter and catchier name "skyrmions". In this thesis we will concentrate in particular on two-dimensional magnetic skyrmions, the two most common examples of which are the Bloch and Néel skyrmion. In Fig. 1.1cv),vi) we show two differemt representations of these two skyrmions. The top row shows them in their actual physical manifestation as magnetic textures on a 2D plane, while the bottom row is a mathematical representation of the skyrmions' magnetisation on a 2-sphere. Mathematically we can describe the skyrmion magnetisation on the 2D plane in the following way,

$$\hat{\mathbf{M}} = \begin{pmatrix} \sin(\theta)\cos(\phi) \\ \sin(\theta)\sin(\phi) \\ \cos(\theta) \end{pmatrix} \quad \theta = \theta(r), \; \phi = \chi + h. \tag{1.15}$$

Here $r, \chi$ are the usual polar coordinates parametrising the 2D plane, related to the cartesian coordinates via $x = r\cos(\chi), \; y = r\sin(\chi)$. $h$, short for *helicity*, is the quantity which determines whether we have a Néel ($h = 0$) or Bloch ($h = \frac{\pi}{2}$) skyrmion. These two skyrmions are therefore mathematically related to each other via a local rotation of each spin by $\pm\frac{\pi}{2}$ around the $z$-axis. The 2D plane and 2-sphere representations shown in Fig. 1.1c are related to each other via stereographic projection. Stereographic projection is a very useful practical tool, commonly used for example by cartographers to make 2D maps of our 3D Earth. Mathematically, it consists of the following mapping [14],

$$x = \frac{X}{1 - Z}, \, y = \frac{Y}{1 - Z},$$

where we start with a point $(X, Y, Z)$ on the unit sphere centred at the origin, and end up with a point $(x, y)$ on the 2D plane. With this mapping every point on the sphere is mapped to a single other point on the plane, with the exception of the North pole, which gets mapped to infinitely many points at $x, y = \infty$. Representing skyrmions on a sphere in this manner is useful because it allows us to intuitively understand why they are topological objects. To determine whether a magnetic texture is topologically trivial or non-trivial, we compare it to a texture we know to be topologically trivial, the easiest

one to consider being a ferromagnet. In a ferromagnet, the spins are all parallel to each other, and in Fig. 1.2 we show their representation on a sphere. Note that you can't see the spins on the lower half of the sphere because they are pointing up *inside* the surface of the sphere. If another magnetic texture can be transformed by *continuous deformation* to this arrangement, it too must be topologically trivial. Let us play the following game: imagine that the spins are all tiny hairs[3], with their bottom part (the non-arrowhead end) firmly attached to the surface of the sphere and the top end (with the arrowhead) free to move. Continuous deformations are those achievable by combing these tiny hairs with a hair comb. There is a further important rule to the game: we may not force the hairs through the surface of the sphere. If we try this with either of the skyrmions shown in Fig. 1.1c v),vi), we quickly realise that combing them into the ferromagnetic arrangement is an impossible task, as we would need to force the spins on the bottom hemisphere out through the surface of the sphere. Thus skyrmions are topologically *non-trivial* objects. Further experimentation with the comb shows that the Néel skyrmion can quite comfortably be combed into the Bloch skyrmion and vice versa, suggesting that these two objects have the same topology. While this qualitative
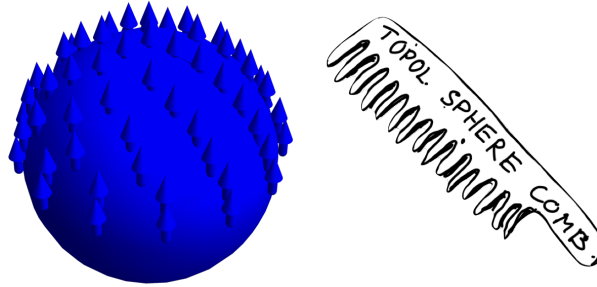


Figure 1.2 Ferromagnet projected on a sphere and topological hair comb

picture is pleasing, it is also helpful to have a concrete mathematical framework for the topological properties of magnetic systems. A useful quantity to consider is the topological charge $Q$, defined as

$$Q = \frac{1}{4\pi} \int \mathrm{d}^2 r \hat{\mathbf{M}} \cdot (\partial_x \hat{\mathbf{M}} \times \partial_y \hat{\mathbf{M}}), \tag{1.16}$$

where $\hat{\mathbf{M}}$ is again the unit local magnetisation and the integral is taken over the entire 2D domain of the magnetic texture. For $Q$ to be non zero we require a magnetic texture that twists and turns in space — a collinear texture (e.g. a ferromagnet) will have

---

[3]see also the *Hairy Ball Theorem* [15] (I mostly included this remark because I find the name of the theorem hilarious).

$\partial_x \hat{\mathbf{M}} = \partial_y \hat{\mathbf{M}} = 0$ everywhere, resulting in zero topological charge, $Q = 0$. In a twisting texture such as a skyrmion, $Q$ measures the total solid angle spanned by the magnetisation field $\hat{\mathbf{M}}$ divided $4\pi$, the solid angle of a sphere. Inserting the skyrmion parametrisation Eq. (1.15) into Eq. (1.16), and performing the calculation with the boundary conditions $\theta(r = 0) = \pi, \theta(r = \infty) = 0$, we find that both Néel and Bloch skyrmions have a topological charge of exactly $Q = -1$, which confirms the topological equivalence we expected intuitively from the comb thought experiment. The topological charge $Q$ can also be a non-integer number. Non-integer, or *fractional* topological charges can form for example at the meeting point of three or more domains, or when a skyrmion splits into several smaller fragments. Fractional topological charges have the distinguishing property that they scatter low energy electrons or magnons very strongly, which is not the case for charges of integer $Q$. All of this and more will be discussed in Chapter 4.

### 1.4.1 Physical Consequences of Non-Trivial Topology

Non-trivial topology in magnetic textures is not just a pretty mathematical phenomenon — it also has important physical consequences. One such consequence is that charged particles, in particular electrons, moving in the vicinity of topological magnetic textures experience forces which modify their trajectories. An electron traversing a magnetic texture does so *adiabatically*, meaning that the spin of the electron $\boldsymbol{\sigma}$ always points parallel to the local magnetisation $\mathbf{M}$. This means that if the local magnetisation twists in real space, the spin of the electron will move around in spin space over the course of its trajectory, picking up a Berry phase in the process. This Berry phase can be used to calculate the emergent electric and magnetic fields which act on the electron. They are given by

$$
\begin{aligned}
E_i^e &= \frac{\hbar}{2|e|} \hat{\mathbf{M}} \cdot (\partial_i \hat{\mathbf{M}} \times \partial_t \hat{\mathbf{M}}), \\
B_i^e &= \frac{\hbar}{2|e|} \frac{1}{2} \epsilon_{ijk} \hat{\mathbf{M}} \cdot (\partial_j \hat{\mathbf{M}} \times \partial_k \hat{\mathbf{M}}).
\end{aligned}
\tag{1.17}
$$

We will derive Eq. (1.17) properly in Sec. 4.2.

Note the resemblance of the emergent $\mathbf{B}_i^e$ field experienced by the electron in Eq. (1.17) to the topological charge density from Eq. (1.16). As these two quantities are proportional to each other a physical measurement of the $\mathbf{B}^e$ field experienced by an electron traveling through the magnetic texture gives us information on the latter's topological charge $Q$. In experiments, this has been widely studied in measurements of the so-called *topological* Hall effect, which gets its name from the emergent $B^e$-field's dependence on the topological charge. As a reminder, a Hall effect experiment usually involves measuring the resistivity

of a sample as a function of applied current, in a direction perpendicular to both the applied current and the total $B$-field experienced by the electrons. From this resistivity measurement one can deduce the magnitude of the $B$-field felt by the electrons. In the presence of a topological magnetic texture we would expect an additional contribution from the topological Hall effect, alongside the usual normal and anomalous Hall effects [16–18]. In fact, it was a topological Hall effect measurement that first confirmed the experimental existence of the skyrmion lattice phase in 2009 [19], by allowing it to be distinguished from the topologically trivial helical, conical and ferromagnetic phases.

From Eq. (1.17) we can immediately conclude that an emergent $E^e$-field is only possible in the presence of a *moving* magnetic texture, where $\partial_t \hat{\mathbf{M}} \neq 0$. Experimentally this can be achieved for example by applying an electric current to the skyrmion lattice phase. Above an ultrasmall threshold current density of $10^6 \text{A/m}^2$ the skyrmion lattice starts to move, generating an emergent $E$-field which can again be measured in Hall effect experiments [20].

So far we have discussed how a topological magnetic texture influences the trajectories of conduction electrons through emergent electric and magnetic fields. The reverse effect also occurs, i.e. moving electrons produce forces on the skyrmions — in fact this is what caused the skyrmion lattice to move under application of an electric current in the first place! In addition to electric currents one can also manipulate skyrmions (and magnetic textures more generally) by applying temperature gradients, electromagnetic fields and pinning forces [21–25].

In the following section we will introduce a model for describing how magnetic textures evolve in time and their dynamic response to externally applied forces.

## 1.5   Landau-Lifshitz-Gilbert Equation

Spins evolve in time according to the Landau-Lifshitz-Gilbert (LLG) equation of motion,

$$\dot{\mathbf{M}} = \gamma \mathbf{M} \times \mathbf{B}_{\text{eff}} - \frac{\gamma}{|\gamma|} \alpha \hat{\mathbf{M}} \times \dot{\mathbf{M}}, \tag{1.18}$$

where $\mathbf{B}_{\text{eff}} = -\frac{\delta F[\mathbf{M}]}{\delta \mathbf{M}}$ is the local effective magnetic field felt by the spin, $\gamma$ is the gyromagnetic ratio and $\alpha$ is a dimensionless positive damping constant. Note that in our convention, $\gamma_e = -\frac{|e|g}{2m_e}$ is negative for an electron with charge $-|e|$, mass $m_e$ and $g$-factor $g$. The slightly awkward-looking prefactor $\gamma/|\gamma|$ ensures that the formula remains valid independently of the sign of $\gamma$. The LLG was first proposed by Landau and Lifshitz in 1935 [26]. In 1955 it was modified by Gilbert, who introduced a time derivative to the
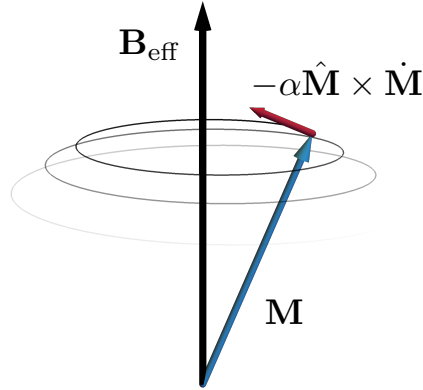
Figure 1.3 Path of a damped, non-driven single spin over time for positive $\gamma$ or "hole-like" spin (for negative $\gamma$ it would precess in the opposite direction, i.e. anticlockwise). The spin (blue arrow) experiences a torque perpendicular to itself and $\mathbf{B}_{\text{eff}}$ (black vertical arrow), which makes it precess around $\mathbf{B}_{\text{eff}}$. The phenomenological damping force $-\alpha\text{sgn}(\gamma)\hat{\mathbf{M}} \times \dot{\mathbf{M}}$ (red arrow) always points in towards the axis of precession and forces the spin to spiral inwards over time, losing speed and angular momentum until it eventually comes to rest parallel to $\mathbf{B}_{\text{eff}}$. We used Eq. (D.3) to plot the path of the spin over time, with $\omega_L = -1, \alpha = 0.04, \theta_0 = 0.81$ for $0 < t < 2.9 \times 2\pi$.

damping term [27]. Physically, the LLG says that the rate of change of $\hat{\mathbf{M}}$ is given by the sum of two different forces on the RHS of the equation. The first force term causes the spin to precess around the local effective magnetic field at the Larmor frequency $\omega_L = \gamma|\mathbf{B}_{\text{eff}}|$, and can be derived both using classical and quantum physics. We know from classical physics that a magnetic moment $\mathbf{m}$ placed inside an external magnetic field will experience a torque

$$\tau = \mathbf{m} \times \mathbf{B}.$$

In addition, the rotational mechanics version of Newton's II law relates the rate of change of angular momentum $\mathbf{J}$ to the applied torque $\tau$

$$\dot{\mathbf{J}} = \tau.$$

Putting these two equations together, and using $\mathbf{m} = \gamma\mathbf{J}$, we derive the following equation of motion of a magnetic moment in an external magnetic field,

$$\dot{\mathbf{m}} = \gamma\mathbf{m} \times \mathbf{B}. \tag{1.19}$$

For the quantum version, one can write down the Heisenberg equation of motion for the spin operator

$$\dot{\mathbf{S}} = \frac{i}{\hbar}[\hat{H}, \hat{\mathbf{S}}],$$

with Hamiltonian $\hat{H} = -\gamma\hat{\mathbf{S}}\cdot\mathbf{B}_{\text{eff}}$. Using the spin commutation relation $[\hat{S}_i, \hat{S}_j] = i\hbar\epsilon_{ijk}\hat{S}_k$[4] we once again obtain Eq. (1.19).

The second term on the RHS of Eq. (1.18) is a phenomenological damping term. There is no proper microscopic derivation of it, except to notice that it leads to sensible physical behaviour. The damping term is perpendicular to both the spin's direction and its velocity and always points inwards, towards the effective magnetic field. In the absence of external driving the spin spirals inwards over time and eventually reaches the lowest energy configuration, where is parallel to $\mathbf{B}_{\text{eff}}$. See Fig. 1.3 for a graphical representation and App. D for a precise analytical derivation of the dynamics of the damped, non-driven spin.

## Other Versions of the LLG

In the literature Eq. (1.18) has been reworked into other forms to make it more useful for specific applications. Perhaps most notably, in 1972 A. A. Thiele remoulded the LLG into the Thiele equation [28], a clever formalism to describe purely translational modes of motion in magnetic textures. The idea is to assume that all the time-dependence of the magnetisation can be transferred to a generalised coordinate $\mathbf{R}(t)$, so that $\mathbf{M}(\mathbf{r}, t) = \mathbf{M}(\mathbf{r} - \mathbf{R}(t))$. By a series of projections and spatial integration it is then possible to rewrite Eq. (1.18) as an equation of motion for $\mathbf{R}$,

$$\text{sgn}(\gamma)\mathbf{G} \times \dot{\mathbf{R}} - \alpha\mathcal{D}\dot{\mathbf{R}} = -\frac{\partial F}{\partial \mathbf{R}}, \tag{1.20}$$

where $G_\alpha = \frac{1}{2}\frac{M_0}{|\gamma|}\epsilon_{\alpha\beta\gamma}\int \mathrm{d}^3r\hat{\mathbf{M}}\cdot(\partial_\beta\hat{\mathbf{M}}\times\partial_\gamma\hat{\mathbf{M}})$[5] and $\mathcal{D}_{\alpha\beta} = \frac{M_0}{|\gamma|}\int \mathrm{d}^3r\partial_\alpha\hat{\mathbf{M}}\cdot\partial_\beta\hat{\mathbf{M}}$ are known as the gyrocoupling vector and dissipation matrix, respectively, see App. C for a derivation. On the RHS of Eq. (1.20) we have $-\frac{\partial F}{\partial \mathbf{R}} = \mathbf{F}_{\text{ext}}$. These are all the external forces that might be acting on the magnetic texture, such as pinning by disorder or temperature gradients [29–32]. In Chapter 3 we will show how an effective force arising from oscillating magnetic fields can also be included within the Thiele framework. The Thiele equation

---

[4]Note that here, the hat symbol in $\hat{S}_i$ is used to specify that $\hat{S}_i$ is a quantum operator, and not that it is normalized, in contrast to the usage we made of it for $\hat{\mathbf{M}}$.

[5]Note again the resemblance of $\mathbf{G}$ to the topological charge $Q$ and emergent magnetic field $\mathbf{B}^e$, Eq. (1.16) and (1.17)! When the same quantity appears three times in different contexts you know it must be important :).

is particularly useful for investigating the dynamics of skyrmions or other topologically charged magnetic objects. Solving Eq. (1.20) for the coordinate **R**, which could for example designate the centre of a skyrmion, gives an idea of the main dynamical features of the problem without having to solve the full space- and time-dependent LLG.

Another useful way to rewrite Eq. (1.18) involves getting a little inspiration from quantum mechanics. We already showed that the precessional force has a direct analog in the quantum language via the Heisenberg equation of motion and spin commutation relations. What about the damping force? From a classical perspective, we are free to add damping forces to our equation of motion, but in quantum mechanics this is more tricky to do conceptually with the Heisenberg equation approach adopted so far, as Hamiltonian physics becomes ill-defined in the presence of damping. To do it properly, one could for example write down the Lindblad master equation for open quantum systems, which incorporates damping through dissipation of energy to the surroundings while preserving the important properties that the density operator is positive, $\rho > 0$, and its trace remains unity, $\mathrm{tr}(\rho) = 1$ [33]. In this thesis we will not take this Lindbladian approach, instead choosing to remain completely classical and use the Gilbert damping provided by the LLG. Nevertheless, the mathematical formalism of commutators in the quantum mechanics inspired approach is very useful for calculations. In classical physics commutators are replaced by Poisson brackets, so that the correspondence between the quantum mechanical commutator of the spin operators $\hat{S}_i, \hat{S}_j$ and the Poisson bracket classical magnetisation fields $M_i(\mathbf{r}), M_j(\mathbf{r}')$ is given by

$$[\hat{S}_i(\mathbf{r}), \hat{S}_j(\mathbf{r}')] = i\hbar\epsilon_{ijk}\hat{S}_k\delta(\mathbf{r} - \mathbf{r}') \Leftrightarrow \{\hat{M}_i(\mathbf{r}), \hat{M}_j(\mathbf{r}')\} = i\epsilon_{ijk}\hat{M}_k(\mathbf{r})\delta(\mathbf{r} - \mathbf{r}'). \quad (1.21)$$

This allows us to rewrite Eq. (1.18) as

$$\dot{\mathbf{M}} = i\gamma\{F, \hat{\mathbf{M}}\} - \frac{\gamma}{|\gamma|}\alpha\hat{\mathbf{M}} \times \dot{\mathbf{M}}. \quad (1.22)$$

Eq. (1.22) will be very useful once we introduce the Holstein-Primakoff spin expansion in Chapters 2 and 3.

# 2

# Archimedean Screw



– "Screw" theme from B. Britten's 1954 opera *"The Turn of the Screw"*

The Archimedean screw is one of the simplest and oldest machines known to mankind. This chapter will reveal to you how to build a nano-size Archimedean screw of approximately $20\,\mathrm{nm}$, or about $\frac{1}{80,000}$ of the thickness of a single strand of human hair (!) using a chiral magnet. By driving the conical state of the chiral magnet with an oscillating magnetic field $\mathbf{B}_1(t)$ we can activate the rotational Goldstone mode of the system, setting the "screw" into motion with angular frequency $\omega_{\mathrm{screw}} \propto |\mathbf{B}_1|^2$. This kind of motion is directly analogous to the rotational motion of a mechanical Archimedean screw. Just like regular Archimedean screws, which we use daily for transport in a variety of settings, the nano-size magnetic Archimedean screw can also be used to transport nano-scale materials such as spin or charge. At the end of the chapter we give an example of this transport application by estimating the electric current generated by the nano-Archimedean screw as it pumps electrons in metallic chiral magnets (experiments are already underway to check this effect...). In addition, some cool physics occurs upon increasing the amplitude of $\mathbf{B}_1(t)$ with the formation of a new "time quasicrystal" phase, where the magnetisation oscillates in space and time at frequencies that are incommensurate with the lattice pitch vector and the driving frequency of the oscillating magnetic field. We will show that this effect can be predicted and explained theoretically using Floquet spin wave theory.

Many of the results presented in this chapter were published in [34], written in collaboration with Lukas Heinen and Achim Rosch.

– smurfs trying to use an Archimedean screw
to deliver gifts to an uninterested smurfette.
(made by NdS with help from [35–39])

## 2.1   Origin and Principles of the Archimedean Screw

The Archimedean screw owes its name to Archimedes of Syracuse, the famous Greek scientist and polymath, who first mentioned it in one of his texts in 234 BC. There is some evidence that even before his time the device already existed in Egypt and was used to transport water from the Nile for irrigation purposes [40]. However Archimedes' story with the screw, even if it might be slightly apocryphal, is too good not to be mentioned here. According to legend, Archimedes had been hired by the king of Syracuse (modern day Sicily) to build him a ship, larger and more luxurious than that of any of the neighbouring rulers. Back then, Syracuse was the capital of a prosperous empire which excelled in trading and was especially proud of its naval fleet. So when Syracusia – the ship built by Archimedes – started to show signs of leakage, it was the ultimate form of embarrassment for everyone involved in the enterprise, and most of all for its architect. Necessity being the mother of invention, this urgent situation spurred Archimedes to design a manually activated screw-shaped pump to drain the water from the ship, helping to keep it — and the reputation of Syracuse — intact. The screw-shaped pump, subsequently referred to simply as the *Archimedean screw*, is still used widely to this day. Its most obvious and widespread applications are in irrigation and for transport of powders and grains in industrial and agricultural settings. Perhaps more surprisingly, Archimedean screws are also used on fish farms as "pescalators" to transfer fish delicately and safely between reservoirs. Long before Archimedes, Darwinian evolution had already harnessed Archimedean screws, and plenty of examples of their occurrence can be found in the natural world. For example many bacteria grow corkscrew shaped tails (flagella) to propel themselves through liquids using a mechanism analogous to that of the Archimedean screw.

   With all that said, how does an Archimedean screw actually work? As with many good things in physics, symmetry is the driving principle. Specifically, one kind of symmetry known as helical, or more colloquially "screw", symmetry. Helical symmetry occurs in objects where rotation and translation along the axis of rotation are equivalent operations. This is precisely the case for a screw — if you imagine rotating or translating an infinitely long screw, the two actions look identical. Therefore, a precise mathematical formulation of screw symmetry is that translation of the texture by $\Delta z$ in the $+z$ direction combined with rotation clockwise by $\Delta\phi = q\Delta z$ around the $z$ axis leaves screw unchanged. Another important aspect to consider is the *chirality*, or equivalently the handedness, of the screw. To determine whether a screw is left- or right-handed just align the thumbs on both of your hands parallel to the axis of the screw and check in which sense the screw rotates as you move your eyes up, along your thumb. If the screw rotates clockwise,
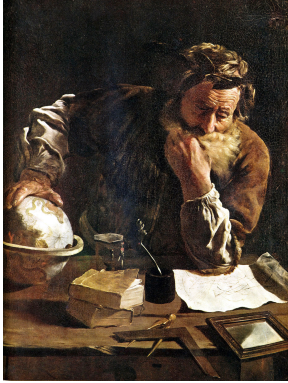
(a) *Archimedes thoughtful,* painted by Domenico Fetti in 1620.
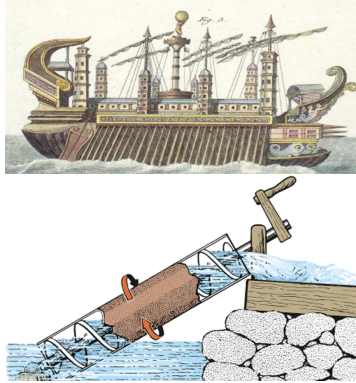
(b) Archimedes' ship *Syracusia* and the screw pump to drain it (from [41, 42]).

(c) A modern Archimedean screw, photographed by Anne Matthies in 2021.

Figure 2.1 History and Applications of the Archimedean Screw

like the fingers on your right hand, it is right-handed[1], if it rotates anti-clockwise, it is left-handed. Using these definitions, we conclude that the conical phase magnetisation defined in Eq. (1.4) is right-handed[2].

So the scene is set: we have a perfect candidate for realising an Archimedean screw in the conical phase of a chiral magnet, because of the shared helical and chiral symmetry properties. Now we need to figure out a way to "activate" our magnetic screw, i.e. make it rotate on its axis in time just like an Archimedean screw!

## 2.2    Driven Conical Phase: Steady State

Mechanical Archimedean screws only start to turn when we provide energy for them to do so. In the old days this power was supplied by men or horses, nowadays the job is often done by electric motors. Naturally to "activate" our magnetic Archimedean screw, we also need to inject some power into the chiral magnet. We choose to do this by driving the system with an oscillating magnetic field, $\mathbf{B}_1(t)$.

The problem of driving magnetic textures with oscillating magnetic fields was first studied in experiments by Onose et al. [43], using the insulating chiral magnet $Cu_2OSeO_3$. For weak driving fields $\mathbf{B}_1(t)$, spin waves — modes of collective excitation — are excited at linear order in $B_1$ in the magnetic texture. Theoretical calculations of the spin waves

---

[1]in most cases screws are right-handed as there are overwhelmingly (over 90%!) more right-handed than left-handed people in the world. Using a screwdriver of the same handedness as your dominant hand means you can apply more force to it.

[2]For the chiral magnet, the handedness is determined by the sign of $D$, the DMI constant. Making it negative would make our conical phase left-handed.

and their resonances in the different phases of the chiral magnet (skyrmion, conical, etc) and in different materials have also been performed in the past [44–47]. However, up until now analytical treatment of damping as well as higher than linear order dynamics constituted a mostly unexplored territory. In this thesis we address these aspects in detail for the first time.

Let us now set up our problem more concretely. We take a chiral magnet in the conical phase and apply to it an external magnetic field $\mathbf{B}_{\text{ext}}$, which consists of a static component $\mathbf{B}_0$ and a sinusoidally time-varying "driving" component $\mathbf{B}_1(t)$,

$$\mathbf{B}_{\text{ext}} = \mathbf{B}_0 + \epsilon \mathbf{B}_1(t), \quad \mathbf{B}_0 = \begin{pmatrix} 0 \\ 0 \\ B_0 \end{pmatrix}, \quad \mathbf{B}_1(t) = \begin{pmatrix} B_\perp^x \cos(\Omega t) \\ B_\perp^y \sin(\Omega t) \\ B_\parallel \cos(\Omega t + \Delta) \end{pmatrix}. \tag{2.1}$$

We assume that the driving frequency $\Omega$ is in the GHz range, which is the "fast"-driving regime. The problem of "slow" driving, when $\Omega$ is in the Hz range, is currently also being investigated in the group of Prof. Rosch. The physics there is very different and results for example in "bending" or even "breaking" of skyrmion lines in the SkX phase — something we need not concern ourselves with here. We assume that the driving field is very weak compared to the static field, with $\frac{B_1}{B_0} \sim \frac{1}{100}$. This allows us to take a perturbative approach in solving for the dynamics of the system; the parameter $\epsilon$ is a book-keeping device which will help us with that. Note also that both the static and driving components are chosen to be homogeneous in space, i.e. independent of the location $\mathbf{r}$. This simplifies the analysis significantly and further theoretical work will be needed to address the problem of non-homogeneous magnetic fields in realistic experimental setups, a complication which we do not consider in the present thesis. The notation $B_\parallel, B_\perp$ designates components of the driving field parallel and perpendicular to the constant $\mathbf{B}_0$ field, respectively. With the inclusion of a phase $\Delta$ in the parallel component, this form of driving field is the most general one possible if one assumes a sample of cylindrical symmetry where the demagnetisation factors in the $xy$-plane are identical, $N_x = N_y$[3]. In the following analysis we will show that driving with a purely parallel ($B_\perp^{x,y} = 0$) or purely perpendicular ($B_\parallel = 0$) magnetic field results in qualitatively different dynamics, with the Archimedean screw-type motion only activated by perpendicular driving. We will cover both types of response, as the comparatively more simple parallel driving analysis serves as a good pedagogical stepping stone for the more complicated of perpendicular driving.

---

[3]for the asymmetrical case $N_x = N_y$ one would have to add a further phase to either of the $B_\perp^{x,y}$ components.

One final thing we need to write down before starting to calculate is a dynamic ansatz for the magnetisation. As already mentioned, the driving field is very weak, which motivates us to use a perturbative analysis to obtain the dynamical response. Practically, this means solving the LLG Eq. (1.18) in powers of $B_1$. To do this, we also need to expand our magnetisation ansatz in powers of $B_1$. The following ansatz achieves this, while also keeping the magnetisation unit vector normalized to unity,

$$\hat{\mathbf{M}} = \begin{pmatrix} \sin\left(\theta_0 + \epsilon\theta_1 + \epsilon^2\theta_2 + O(\epsilon^3)\right)\cos\left(qz + \epsilon\phi_1 + \epsilon^2\phi_2 + O(\epsilon^3)\right) \\ \sin\left(\theta_0 + \epsilon\theta_1 + \epsilon^2\theta_2 + O(\epsilon^3)\right)\sin\left(qz + \epsilon\phi_1 + \epsilon^2\phi_2 + O(\epsilon^3)\right) \\ \cos\left(\theta_0 + \epsilon\theta_1 + \epsilon^2\theta_2 + O(\epsilon^3)\right) \end{pmatrix}, \qquad (2.2)$$

where $\epsilon$ is the same book-keeping device we introduced in Eq. (2.1). Note that for the moment the fields $\theta_n, \phi_n$ are completely general functions of both space $\mathbf{r}$ and time $t$. Later we will see that the direction of the drive (parallel vs. perpendicular) and the order $n$ very helpfully restrict the kind of functions we can use to very few candidates. The game now consists of inserting Eq. (2.2) and Eq. (2.13) into the LLG and expanding the equation order by order in $\epsilon$. At each consecutive order $n$ we solve for $\theta_n, \phi_n \propto B_1^n$. Throughout this thesis we will be doing this up to order $n = 2$ — this is enough to capture the most salient physics for reasons that will soon be revealed.

We are now all set to get our hands dirty with calculating the dynamic response of the conical state to parallel and perpendicular drive. We investigate each of these respectively in the next two subsections.

## 2.2.1   Parallel Driving

As a gentle introduction, let us calculate the response of the conical state to purely parallel driving. We set $B_\perp^{x,y} = 0$ in Eq. (2.1). The phase $\Delta$ can also be set to zero without loss of generality, as in the absence of perpendicular driving field components it would just change the phase of the spin response without introducing any new dynamical features. Thus we want to solve for the dynamical response of the conical texture to

$$\mathbf{b}_\parallel(t) = \epsilon b_\parallel \cos(\omega t)\mathbf{e}_z, \qquad (2.3)$$

where we use the same definition of reduced magnetic field $b_\parallel = \frac{|\gamma|}{JSd^2}B_\parallel = \frac{M_0\tilde{J}}{\tilde{D}^2}B_\parallel$ as previously. We also introduced the reduced frequency $\omega = \frac{J}{SD^2}\Omega = \frac{\tilde{J}M_0}{|\gamma|\tilde{D}^2}\Omega$ and corresponding reduced time $\tilde{t} = \frac{SD^2}{J}t = \frac{|\gamma|\tilde{D}^2}{\tilde{J}M_0}t$, immediately dropping the tilde on $\tilde{t}$

to avoid cluttering the notation unnecessarily. All these reduced quantities have the advantage of being dimensionless and being in the more user friendly $10^{-3} - 1$ range.

Now we begin the perturbative calculation. As a sanity check, we first consider order $n = 0$. At zeroth order there is no driving term in the LLG, which only enters for orders $n \geq 1$. Consequently, expanding Eq. (2.2) to zeroth order in $\epsilon$ just returns us the static spin ansatz Eq. (1.4), as expected.

For the non trivial higher orders $n > 0$ we can make the LLG equation, which is a vector equation, more tractable by projecting it onto the two vectors $\frac{\partial \hat{\mathbf{M}}}{\partial \theta}$ and $\frac{\partial \hat{\mathbf{M}}}{\partial \phi}$, both of which are instantaneously orthogonal to $\hat{\mathbf{M}}(\mathbf{r}, t)$ and to each other. This gives us two sets of coupled differential equations in $\theta_n$ and $\phi_n$ at each order of $b_\parallel^n$. At first order in $\epsilon$ the coupled differential equations are

$$
\begin{aligned}
\mathrm{sgn}(\gamma)\dot{\theta}_1 - \alpha s \dot{\phi}_1 &= -s\phi_1'', \\
\mathrm{sgn}(\gamma) s \dot{\phi}_1 + \alpha \dot{\theta}_1 &= \theta_1'' - s^2(1 + \delta N_z)\theta_1 - s b_z \cos(\omega t),
\end{aligned}
\tag{2.4}
$$

where we have used the shortened notation $s = \sin(\theta_0), c = \cos(\theta_0)$. The dashes denote spatial derivatives in the $z$ direction, eg $\theta_1' = \frac{\partial \theta_1}{\partial \tilde{z}}$, with respect to a rescaled dimensionless coordinate $\tilde{z} = qz$. For notational simplicity we dropped the tilde on $\tilde{z}$, just like we did for $\tilde{t}$. Notice that there are no spatial derivatives in the $x, y$ directions — this is because we have simplified the problem by tacitly assuming that the magnetisation remains translationally invariant in the $xy$-plane. This simplifying assumption is justified by the fact that we are considering an infinite system and only homogeneous magnetic fields. Looking at the driving term on the RHS of the second equation in Eq. (2.4), $s b_z \cos(\omega t)$, we see that it actually doesn't contain any spatial dependence at all, so that $\theta_1, \phi_1$ must have the form

$$
\begin{aligned}
\theta_1(t) &= \theta_1^{(1)} e^{i\omega t} + \theta_1^{(-1)} e^{-i\omega t}, \\
\phi_1(t) &= \phi_1^{(1)} e^{i\omega t} + \phi_1^{(-1)} e^{-i\omega t}.
\end{aligned}
\tag{2.5}
$$

$\theta_1^{(\pm 1)}, \phi^{(\pm 1)}$ are constant coefficients which we can solve for by substituting Eq. (2.5) into Eq. (2.4) and comparing terms oscillating at the same frequency. We obtain

$$
\begin{aligned}
\theta_1^{(1)} &= \frac{b_\parallel \alpha \sqrt{1 - c^2}}{2\left(\alpha\left(c^2 - 1\right)\left(\delta N_z + 1\right) - i(1 + \alpha^2)\omega\right)}, \\
\phi_1^{(1)} &= \frac{b_\parallel \mathrm{sgn}(\gamma)}{2\left(\alpha\left(c^2 - 1\right)\left(\delta N_z + 1\right) - i(1 + \alpha^2)\omega\right)}.
\end{aligned}
\tag{2.6}
$$

We have not taken the trouble to write out $\theta_1^{(-1)}, \phi_1^{(-1)}$ because they are just the complex conjugates of $\theta_1^{(1)}, \phi_1^{(1)}$ in Eq. (2.5), respectively — this guarantees that the overall first

order solutions $\theta_1(t), \phi_1(t)$ are real. Note that incorporating dipolar interactions as we have done above can be a bit tricky; if you are trying to reproduce this calculation see Sec. B.2 for technical tips on how to do it. We can check the physical validity of our solution at the special point $\omega = 0$. At $\omega = 0$, we are not really driving with a time-dependent field — rather we are adding a static component $b_\parallel$ to the background static field $b_0$. This additional background field changes $c$, the cosine of the equilibrium angle $\theta_0$, to $c + s\theta_1$, in exactly the same way as if we had just replaced $b_0 \to b_0 + b_\parallel$ in Eq. (1.5) — as expected. Physically, the main features that we extract from the first order dynamical response are that $\theta_1(t)$ and $\phi_1(t)$ oscillate in phase with each other, and that the amplitude of oscillation in the $\frac{\partial \mathbf{M}}{\partial \theta}$ direction is reduced by a factor $\alpha\sqrt{1 - c^2}$. An important physical feature of the dynamical first order solution Eq. (2.5) is that the magnetisation retains its screw symmetry to first order in $b_\parallel$, see also Fig. 2.2b. This might be because parallel driving preserves the rotational symmetry of the free energy of the system. One useful quantity to plot using our first order solution is the deviation of the magnetisation from its equilibrium (non-driven) value, $\delta \hat{\mathbf{M}} = \hat{\mathbf{M}}(z, t) - \hat{\mathbf{M}}_0$. This is given by

$$\delta \hat{\mathbf{M}} = \epsilon \left( \frac{\partial \hat{\mathbf{M}}}{\partial \theta} \theta_1(t) + \frac{\partial \hat{\mathbf{M}}}{\partial \phi} \phi_1(t) \right) + \mathcal{O}(\epsilon^2) \tag{2.7}$$

to first order in $\epsilon$. By taking the norm of Eq. (2.7), averaging it in space over one wavelength of the helix and in time over one period of oscillation, one obtains

$$\delta M = \sqrt{\langle |\delta \hat{\mathbf{M}}|^2 \rangle_{t,z}} = \sqrt{|\theta_1^{(1)}|^2 + s^2 |\phi_1^{(1)}|} + \mathcal{O}(b_\parallel^2). \tag{2.8}$$

In Fig. 2.2a we have plotted this quantity as a function of the driving frequency $\omega$. $\delta M$ has a single resonance frequency at $\omega = 0$, and the width $\delta\omega$ of the resonance peak is proportional to $\alpha(1 - c^2)(1 + \delta N_z)/(1 + \alpha^2)$.

At $\mathcal{O}(\epsilon^2)$ there are many more terms, because in addition to $\theta_2$ and $\phi_2$ and their spatial and temporal derivatives we can also get combinations of $\theta_1$ and $\phi_1$ with each other as well as with terms proportional to the driving field,

$$\text{sgn}(\gamma)\dot{\theta}_2 - \alpha\left(c\theta_1\dot{\phi}_1 + s\dot{\phi}_2\right) = -2c\phi_1'\theta_1' - c\phi_1''\theta_1 - s\phi_2''$$

$$c\theta_1\left(2\text{sgn}(\gamma)s\dot{\phi}_1 + \alpha\dot{\theta}_1\right) + s\left(\text{sgn}(\gamma)s\dot{\phi}_2 + \alpha\dot{\theta}_2\right) = c\theta_1\left(\theta_1'' - 2b_\parallel s\cos(\omega t)\right) \tag{2.9}$$

$$-\frac{5}{2}cs^2(1 + \delta N_z)\theta_1^2 - s\left(cs\phi_1'^2 + s^2(1 + \delta N_z)\theta_2 - \theta_2''\right).$$

Luckily, we can greatly simplify this mess by choosing a clever ansatz for $\theta_2, \phi_2$. By inspecting the terms containing $\theta_1(t), \phi_1(t) \sim e^{\pm i\omega t}$ in eq. (2.9), we conclude that at
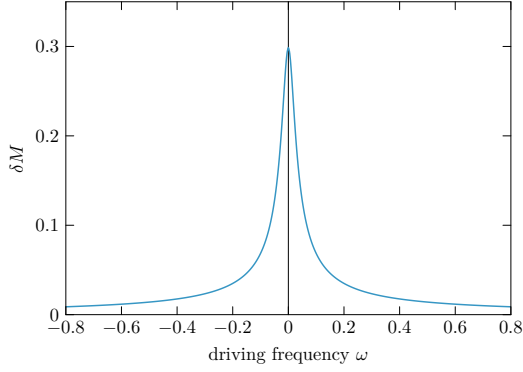
(a) $\delta M$, defined in Eq. (2.8), as a function of driving frequency $\omega$ for parameters $b_\parallel = 0.02, b_\perp = 0, c = 0.71, \alpha = 0.03, \delta = 1.76, N_x = N_y = 1/3$.

(b) Conical phase driven with $\mathbf{b}_\parallel(t)$. All spins oscillate in phase around their equilibrium value, preserving the screw symmetry.

Figure 2.2 Conical Phase Driven in the Parallel Direction

second order the response will contain terms which oscillate at frequencies $\pm 2\omega$ or $0$ — these are the only three possible ways of combining $e^{i\omega t}$ and $e^{-i\omega t}$. In addition, we see that we don't expect any spatial dependence of $\theta_2, \phi_2$ on $z$. Thus in general we would expect the following response at second order

$$
\begin{aligned}
\theta_2(t) &= \theta_2^{(2)} e^{2i\omega t} + \theta_2^{(-2)} e^{-2i\omega t} + \theta_2^{(0)} \\
\phi_2(t) &= \phi_2^{(2)} e^{2i\omega t} + \phi_2^{(-2)} e^{-2i\omega t} + \phi_2^{(0)} + \Phi_2(t).
\end{aligned}
\tag{2.10}
$$

Actually I cheated and added a mysterious function $\Phi_2(t)$ to the ansatz for $\phi_2(t)$ without giving you any warning. What is this $\Phi_2(t)$? From a physical perspective, it is exactly the mode we need to activate in order to realise an Archimedean screw-type motion. But what of its functional form? One could try to make an argument for it on the basis of symmetries. If we drive in the parallel direction we have already seen that the screw symmetry is conserved by the magnetisation at first order in $b_\parallel$, and the ansatz Eq. (2.10) suggests it is conserved at second order too. As screw symmetry remains intact, translational symmetry would therefore also be conserved by *any* choice of $\Phi_2(t)$. Considering just the symmetries of the system is insufficient, and as it turns out damping plays a vitally important role in restricting the form of $\Phi_2(t)$. Taking our equations of motion at second order, Eq. (2.9) and substituting in the first order solution Eq. (2.6) and second order ansatz Eq. (2.10), we see that the only possible non-trivial functional form for $\Phi_2(t)$ is

$$
\Phi_2(t) = \omega_{\text{screw}} t.
\tag{2.11}
$$

In contrast to all the other allowed terms at second order, which are either constant or oscillate in time, $\Phi_2(t)$ is divergent. However, it does not describe an instability in the system but rather the activation of the Archimedean screw-type rotation of the entire helix about its axis, with angular velocity $\omega_{\text{screw}}$. To determine $\omega_{\text{screw}}$ let's insert Eq. (2.11) into the first equation in Eq. (2.9). As none of the terms have any spatial dependence on $z$, the RHS of the equation vanishes, leaving

$$\alpha \left( s\omega_{\text{screw}} + ic\omega \left( \theta_1^{(-1)}\phi_1^{(1)} - \theta_1^{(1)}\phi_1^{(-1)} \right) \right) = 0. \tag{2.12}$$

Substituting values for $\theta_1^{(\pm 1)}, \phi_1^{(\pm 1)}$ from Eq. (2.6) into the above and solving for $\omega_{\text{screw}}$ we get the trivial result

$$\omega_{\text{screw}} = 0.$$

How disappointing — no Archimedean screw for a conical state driven in the parallel direction. But I guess you were expecting it, as I did warn you the result would be a bit boring at the end of the previous section :). Now we will shift our focus to perpendicular driving, which, it turns out, does activate the elusive $\omega_{\text{screw}}$ we are after.

## 2.2.2 Perpendicular Driving

We would now like to investigate the dynamic response of the conical phase to a perpendicular driving field,

$$\mathbf{b}_\perp(t) = \epsilon \left( b_x \cos(\omega t)\mathbf{e}_x + b_y \sin(\omega t)\mathbf{e}_y \right). \tag{2.13}$$

Just like for the parallel driving case, we proceed order by order in $\epsilon$. Skipping the trivial zeroth order, at first order the equations of motion read

$$\begin{aligned}
\text{sgn}(\gamma)\dot{\theta}_1 - \alpha s\dot{\phi}_1 &= -s\phi_1'' + b_x(t)\sin(z) - b_y(t)\cos(z) + \text{RHS}_{1,\theta}^{\text{dip}}, \\
s\,\text{sgn}(\gamma)\dot{\phi}_1 + \alpha\dot{\theta}_1 &= \theta_1'' - (s^2 + 2c^2\delta N_z)\theta_1 + cb_x(t)\cos(z) + cb_y(t)\sin(z) + \text{RHS}_{1,\phi}^{\text{dip}},
\end{aligned} \tag{2.14}$$

The RHS's of these equations are no longer spatially independent, in contrast to the parallel driving case — instead they oscillate with spatial momentum $\pm 1$ (remember we are working in dimensionless units, in physical units this corresponds to $\pm q$, the pitch vector of the helix). This motivates us to modify our first order steady state ansatz for

$\theta_1, \phi_1$ to

$$\theta_1(z,t) = \theta_1^{(1,1)} e^{i(\omega t+z)} + \theta_1^{(-1,-1)} e^{-i(\omega t+z)} + \theta_1^{(1,-1)} e^{i(\omega t-z)} + \theta_1^{(-1,1)} e^{-i(\omega t-z)},$$
$$\phi_1(z,t) = \phi_1^{(1,1)} e^{i(\omega t+z)} + \phi_1^{(-1,-1)} e^{-i(\omega t+z)} + \phi_1^{(1,-1)} e^{i(\omega t-z)} + \phi_1^{(-1,1)} e^{-i(\omega t-z)}. \tag{2.15}$$

In contrast to the parallel driving case, now the first order solution oscillates in both *space* and *time*, at spatial and temporal frequencies $\pm 1, \pm \omega$ (in dimensionless units), respectively. Consequently, the screw symmetry, which was conserved at all orders in $b_\parallel$ under parallel driving, is already lost at first order in $b_\perp$ under perpendicular driving. Physically, Eq. (2.15) describes two compression waves running up and down the helix, with the direction determined by the relative sign in $\omega t \pm z$, see also Fig. 2.5c. It should also be noted that the condition on both $\theta_1(z,t)$ and $\phi_1(z,t)$ being real imposes that $\theta_1^{(-1,\pm 1)} = \theta_1^{(1,\mp 1)*}, \phi_1^{(-1,\pm 1)} = \phi_1^{(1,\mp 1)*}$. As a consequence of the added $e^{\pm iz}$ spatial dependence in the first order magnetisation ansatz, Eq. (2.15), the effective dipolar field, which is itself a function of the magnetisation field, ends up being more complicated for the perpendicular driving case. See App. B.2 for details on how to incorporate these dipolar interactions terms into Eq. (2.15) and Eq. (B.10) for the precise forms of $\mathrm{RHS}_{1,\theta/\phi}^{\mathrm{dip}}$. Substituting the first order ansatz Eq. (2.15) into the first order equations of motion, Eq. (2.14), and comparing terms oscillating at the same spatial and temporal frequencies, one obtains analytical expressions for the coefficients $\theta_1^{(1,\pm 1)}, \phi_1^{(1,\pm 1)}$. These are listed in full (gory) detail in App.E. Eq. (E.3) gives the coefficients for the most general case $N_x \neq N_y$, while Eq. (E.7) gives them for the simplified symmetric case $N_x = N_y$, which we will focus on in our discussion. It should be mentioned that during the derivation of these coefficients, we defined the quantities $N_\pm = N_x \pm N_y$ as well as $b_{R/L} = b_x \pm b_y$, which lead to neater formulas. If we choose our perpendicular driving field such that either $b_L = 0$ or $b_R = 0$ we obtain right- and left- circularly polarised driving fields, respectively. Right or left circular polarisation can also be understood intuitively in the same way as the handedness of a helix. One aligns the thumb on the relevant (right or left) hand with the $+\mathbf{e}_z$ direction; the other fingers then curl in the direction in which the magnetic field rotates in time. Looking at the $\theta_1^{(1,\pm 1)}$, $\phi_1^{(1,\pm 1)}$ coefficients for the symmetric case $N_x = N_y$, Eq. (E.6), we can see that for circularly polarised driving, only one direction of traveling wave gets excited — up-traveling ($\omega t - z$) if $b_L = 0$ and down-traveling ($\omega t + z$) if $b_R = 0$.

The resonance frequencies activated by perpendicular driving constitute our next topic of discussion. In the presence of dipolar interactions there are generally two resonant frequencies, which we denote by $E_+$ and $E_-$. We give their analytical formulas, which can be obtained by setting the denominator of the $\theta_1^{(1,\pm 1)}$ or $\phi_1^{(1,\pm 1)}$ coefficients, Eq. (E.4), to
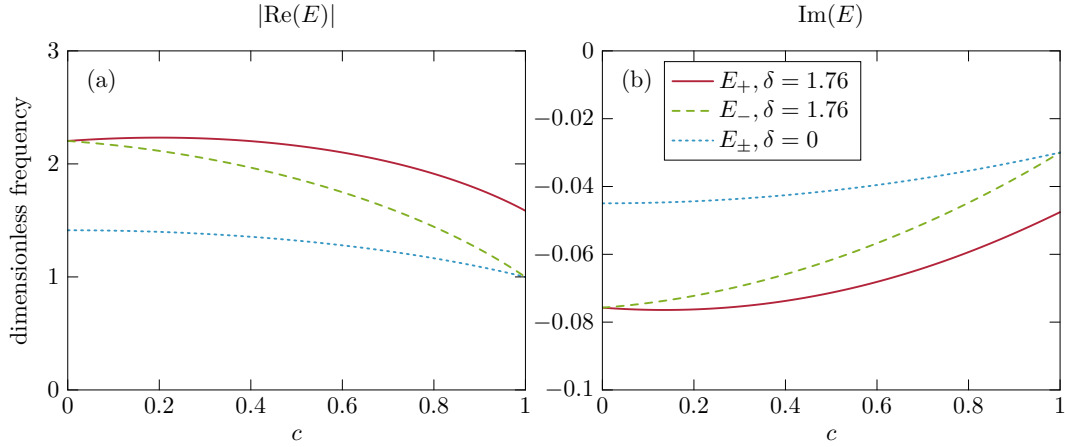
Figure 2.3 Real and imaginary parts of dimensionless resonance frequencies $E_\pm$ of the conical phase driven in the perpendicular direction, plotted as a function of $c = \cos(\theta_0)$, with $\gamma < 0, \alpha = 0.03, N_x = N_y = 1/3$ and dipolar interactions switched on ($\delta = 1.76$, which describes $Cu_2OSeO_3$) and off ($\delta = 0$). In the absence of an external static magnetic field, $b_0, c = 0$, or dipolar interactions, $\delta = 0$, the two resonances do not get split. See Eq. (E.7) for the exact analytical expressions of $E_\pm$. $Im(E)$ is not quite simply $-\alpha|Re(E)|$, see Eq. (E.8) for an expansion of $E_\pm$ in powers of $\alpha$ up to $\mathcal{O}(\alpha^1)$ for the correction factors.

zero and solving the resulting quartic equation, in Eq. (E.7). $E_\pm$ are in general complex due to the presence of damping in the system: the real part, $Re(E_\pm)$, gives the actual resonance frequency, while the imaginary part, $Im(E_\pm)$, quantifies the broadening due to damping. In Fig. 2.3 we plot the real and imaginary parts of $E_\pm$ as a function of $c = \cos(\theta_0)$, the cosine of the opening angle of the helix. With dipolar interactions switched off, $\delta = 0$, $E_- = E_+$ are the same. For finite $\delta$ they split apart, $E_+ \neq E_-$, as long as $c \neq 0$, i.e. there is a finite static magnetic field, $b_0 > 0$. It should be noted that we have chosen $\gamma$ to be negative, as that is the case for most experimental systems of interest. Switching to positive $\gamma$ would inverse the sign of $Re(E_\pm)$, which we expect from our discussion of the damped spin motion in Sec. 1.5, where we learned that the sign of the gyromagnetic ratio determines the sense of rotation of the spin. Importantly, making $\gamma > 0$ leaves $Im(E_\pm)$ unchanged, see Eq. (E.8), where we have expanded $E_\pm$ up to order $\mathcal{O}(\alpha)$ — the imaginary part is *independent* of $sgn(\gamma)$. When we do Floquet spin wave theory later we will see that the sign of $Im(E_\pm)$ determines whether the system is stable or not, with negative $Im(E_\pm)$ indicating stability in our convention. Switching the sign of $\gamma$ is an innocent act which cannot influence the stability of the system. To see what *does* cause instabilities in the driven system you'll have to keep patient until Sec. 2.3.
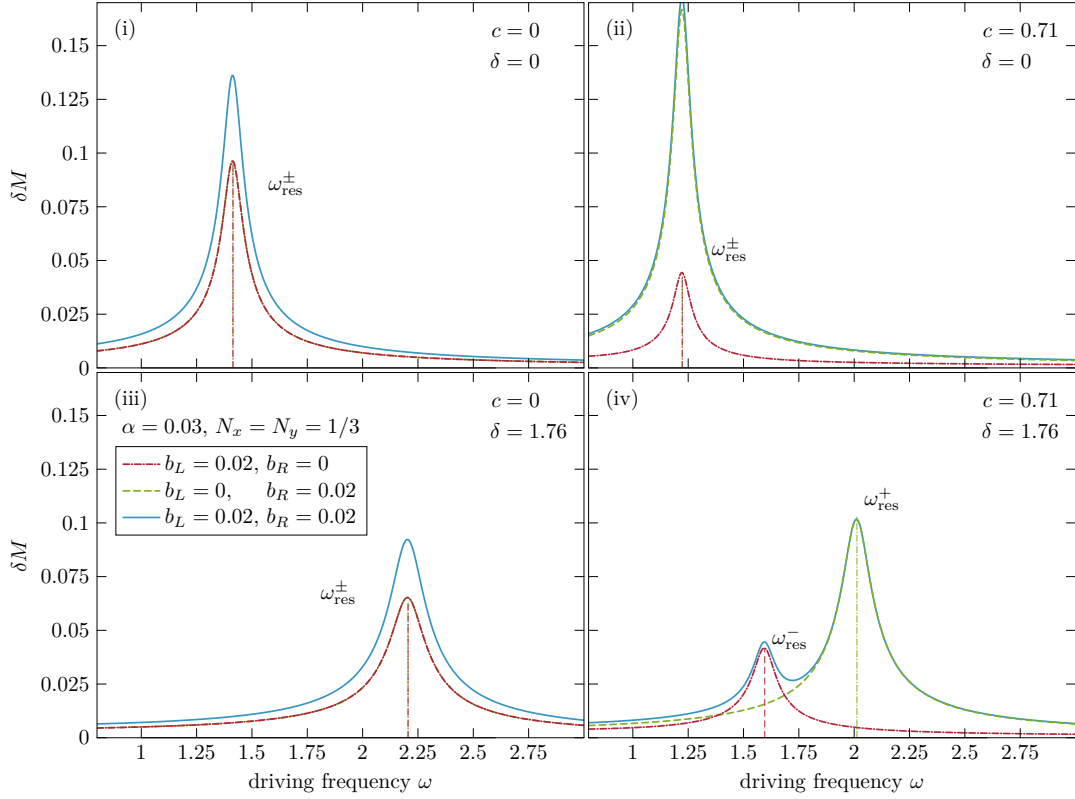
(a) $\delta M$, defined in Eq. (2.16), as a function of driving frequency $\omega$ for the conical phase driven with $\mathbf{b}_\perp(t)$ for left-, right- and linearly polarised driving, with parameters $\alpha = 0.03$, $N_x = N_y = 1/3$ and different $c, \delta$. Note how the resonant frequencies $\omega_+$, $\omega_-$ only get split when *both* $\delta$ and $c$ are finite, panel (iv).
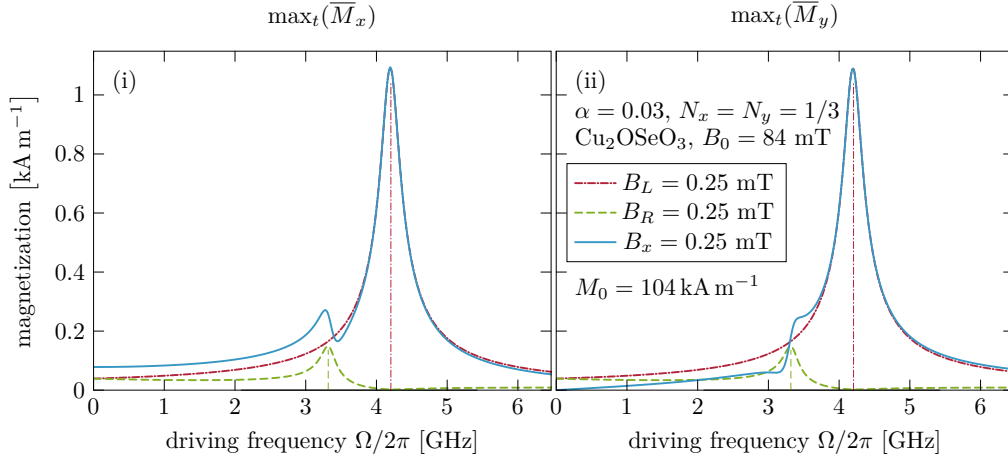


(b) Maximal values in time, over the course of one period of oscillation $T = 2\pi/\Omega$, of the space-averaged $\overline{M}_x, \overline{M}_y$ components of magnetisation for the conical phase driven with $\mathbf{b}_\perp(t)$.

Figure 2.4 Conical Phase Driven in the Perpendicular Direction, First Order Response

Using the knowledge we gained about the two resonance frequencies $E_\pm$, together with the formulas for the coefficients $\theta_1^{(1,\pm1)}, \phi_1^{(1,\pm1)}$ in Eq. (E.6), we can make some further statements about the first order driven steady state. If we choose circularly polarised driving, set $\mathrm{sgn}(\gamma) < 0$ and restrict ourselves to driving frequencies $\omega > 0$ (which contains all the physical information anyway, as negative $\omega$ just switches the polarisation from left to right and vice versa, $b_L \leftrightarrow b_R$ for $\omega < 0$), then purely left-polarised driving $b_R = 0$ excites only $\theta_1^{(1,1)}$ and $\phi_1^{(1,1)}$, with resonance frequency $-\mathrm{Re}(E_-)$, while purely right-polarised driving $b_L = 0$ excites only $\theta_1^{(1,-1)}$ and $\phi_1^{(1,-1)}$, with resonance frequency $-\mathrm{Re}(E_+)$. If we switch to positive $\gamma$, $\mathrm{Re}(E_\pm)$ become positive and the resonance frequencies excited by $b_{R/L}$ get swapped.

In the perpendicular driving case, the space and time averaged magnitude of the deviation is

$$\delta M = \sqrt{\left|\theta_1^{(1,1)}\right|^2 + \left|\theta_1^{(1,-1)}\right|^2 + s^2 \left(\left|\phi_1^{(1,1)}\right|^2 + \left|\phi_1^{(1,-1)}\right|^2\right)} + \mathcal{O}(b_\perp^2). \qquad (2.16)$$

Eq. (2.16) was obtained using the same procedure as for the parallel driving case (read the text under Eq. (2.7) for details), we just used the perpendicular ansatz Eq. (2.15) instead of the parallel version Eq. (2.5). In Fig. 2.4a we have plotted this quantity for left- ($b_R = 0$), right- ($b_L = 0$) and linearly ($b_y = 0$) polarised driving and different settings of $\delta$ and $c$. In the absence of an external magnetic field ($c = 0$) (first and third rows in Fig. 2.4a), $\delta M$ is identical for left- and right- polarised driving. For linearly polarised driving the space and time average deviation is simply $\sqrt{2}$ times either of these. At finite static magnetic field $c = 0.71$ but with dipolar interactions turned off, $\delta = 0$, the resonance frequencies are still the same for left- and right- polarised driving but the heights of the peaks are now different. For a system with both an external static field and dipolar interactions $c \neq 0, \delta \neq 0$, both the resonance frequencies and the heights of the peaks are different for left- and right- circularly polarised driving. Fig. 2.4b is perhaps a more useful way of presenting the same information for experimentalists. Here we plot the maximum value over the course of one period of oscillation of the space-averaged $x, y$ components of the magnetisation, $\max_t(\overline{\mathbf{M}}_{x,y})$, in experimental units describing $Cu_2OSeO_3$. For left and right circular polarised driving $\max_t(\overline{\mathbf{M}}_x) = \max_t(\overline{\mathbf{M}}_y)$ are the same, but for linear driving in the $x$ direction $\max_t(\overline{\mathbf{M}}_x) \neq \max_t(\overline{\mathbf{M}}_y)$. If we instead choose $y$-polarised driving $\overline{M}_x$ and $\overline{M}_y$ get swapped.
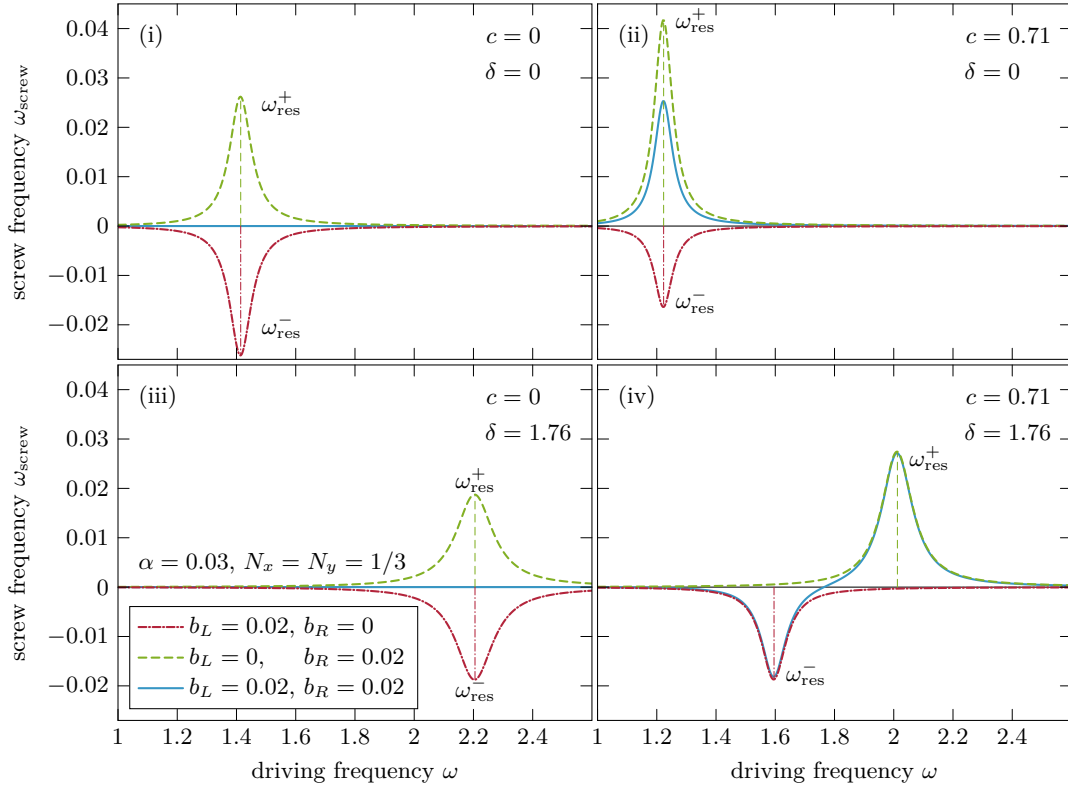
(a) Dimensionless rotational frequency $\omega_{\text{screw}}$ as a function of the driving frequency $\omega$ for left-right- and linearly polarised perpendicular driving fields with parameters $\alpha = 0.03$, $N_x = N_y = 1/3$ and different $c, \delta$. Some features we saw at first order (see Fig. 2.4a) are inherited by $\omega_{\text{screw}}$: the two resonance frequencies $\omega_{\text{res.}}^{\pm}$ only get split at finite $\delta$ and $c$. When $c = 0$ (left column) $\omega_{\text{screw}}$ is equal and opposite for left- and right- polarised driving; consequently linearly polarised driving $b_y = 0$ gives zero net $\omega_{\text{screw}}$. At finite $c$ (right column) this is no longer true, and a finite $\omega_{\text{screw}}$ exists for linearly polarised driving too. If both $\delta$ and $c$ are finite (lower right panel), the resonance peaks get split and the sign of the resulting $\omega_{\text{screw}}$ can be controlled by using linearly polarised driving field and varying the driving frequency $\omega$. The analytical formula for $\omega_{\text{screw}}$ is given in Eq. (E.12).
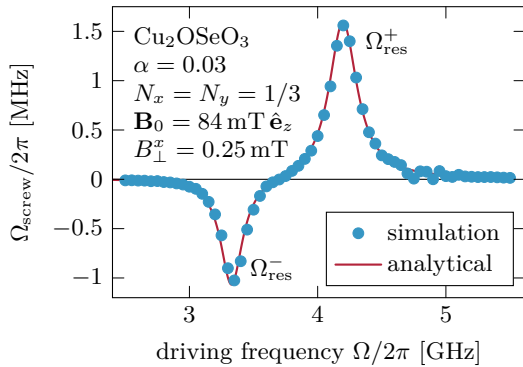


(b) Comparison between analytical $\Omega_{\text{screw}}$ and mumax3 simulations (simulations performed by Lukas Heinen). The parameters $\gamma = -1.76 \times 10^{11} \text{T}^{-1} \text{s}^{-1}$, $\tilde{J} = 7.09 \times 10^{-13} \text{ J m}^{-1}$, $\tilde{D} = 7.42 \times 10^{-5} \text{ J m}^{-2}$, $M_0 = 1.04 \times 10^5 \text{ A m}^{-1}$ and $\alpha = 0.03$ have been chosen to describe $Cu_2OSeO_3$.
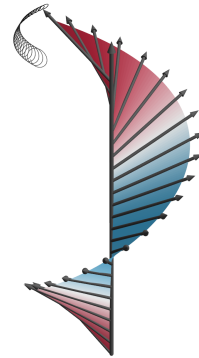


(c) Conical phase driven with $\mathbf{b}_\perp(t)$. The first order response manifests in the red and blue collective compressional wave and the small circles traced out by each spin. The second order $\omega_{\text{screw}}$ manifests in a slow rotation of the entire helix on its axis.

Figure 2.5 Conical Phase Driven in the Perpendicular Direction, Second Order Response

Now we move on to the second order response of the conical phase to perpendicular driving. The equations of motion at order $\mathcal{O}(\epsilon^2)$ (warning: very gory!) read

$$
\begin{aligned}
\operatorname{sgn}(\gamma)\dot{\theta}_2 - \alpha\left(c\theta_1\dot{\phi}_1 + s\dot{\phi}_2\right) &= \left(b_x(t)\cos(z) + b_y(t)\sin(z)\right)\phi_1 \\
&\quad - 2c\phi_1'\theta_1' - c\phi_1''\theta_1 - s\phi_2'' + \mathrm{RHS}_{2,\theta}^{\mathrm{dip}}, \\
c\theta_1\left(2\operatorname{sgn}(\gamma)s\dot{\phi}_1 + \alpha\dot{\theta}_1\right) + s\left(\operatorname{sgn}(\gamma)s\dot{\phi}_2 + \alpha\dot{\theta}_2\right) &= s\theta_2'' + c\theta_1\theta_1'' - cs^2\phi_1'^2 \\
&\quad + -s(s^2 + 2c^2\delta N_z)\theta_2 + \mathrm{RHS}_{2,\phi}^{\mathrm{dip}} \\
&\quad - \frac{1}{2}\theta_1^2 c\left(5s^2 + 2(c^2 - s^2)\delta N_z\right) \\
&\quad + (c^2 - s^2)\theta_1\left(b_x(t)\cos(z) + b_y\sin(z)\right) \\
&\quad + sc\phi_1\left(b_y\cos(z) - b_x\sin(z)\right).
\end{aligned}
\tag{2.17}
$$

The general response we expect at order $\mathcal{O}(\epsilon^2)$ includes temporal oscillations at $\pm 2\omega, 0$, just like in the parallel driving case, but now we additionally expect spatial oscillations at $k = \pm 2, 0$. We also include the Archimedean screw mode $\omega_{\mathrm{screw}}t$ in the $\phi_2(z, t)$ component. Putting this together we obtain the following ansatz for the second order response to perpendicular driving

$$
\begin{aligned}
\theta_2(z, t) &= \theta_2^{\mathrm{osc.}}(z, t) + \theta_2^{(0,0)}, \\
\phi_2(z, t) &= \phi_2^{\mathrm{osc.}}(z, t) + \phi_2^{(0,0)} + \omega_{\mathrm{screw}}t.
\end{aligned}
\tag{2.18}
$$

Again, we use Eq. (2.18) to self-consistently identify the dipolar interaction contributions $\mathrm{RHS}_{2,\theta/\phi}^{\mathrm{dip}}$ to Eq. (2.17); these are given in full detail in Eq. (B.11). We could in principle solve Eq. (2.17) completely — we have all the information we need to do it, as we have already have full knowledge of the first order coefficients. However we will *not* do this, for the good reason that the only thing we are *really* interested in is whether a non-zero $\omega_{\mathrm{screw}}$ gets activated by perpendicular driving. Also, the oscillatory terms $\theta_2^{\mathrm{osc.}}, \phi_2^{\mathrm{osc.}}$ are suppressed by a factor $\epsilon$ compared to the first order oscillatory terms, so we can safely neglect them anyway. The constant term $\theta_2^{(0,0)}$ is not so important for the present analysis but turns out to be crucial for the correctness of the Floquet spin wave analysis we will perform in Sec. 2.3, so we solve for it exactly as well. As for $\phi_2^{(0,0)}$ — a quick inspection of Eq. (2.17) shows that $\phi_2^{(0,0)}$ doesn't appear anywhere explicitly. As such we can give constant value we wish — for the sake of simplicity we choose to set $\phi_2^{(0,0)} = 0$.

We now just solve for $\omega_{\mathrm{screw}}$ and $\theta_2^{(0,0)}$ simultaneously by comparing the coefficients of the terms in Eq. (2.17) which are constant in both space and time. In the most general case of finite $\delta$ and asymmetrical demagnetisation factors $N_x \neq N_y$ the resulting formulas

for $\omega_{\text{screw}}, \theta^{(0,0)}$ are very long and complicated, eg see Eq. (E.11) for the full general form of $\omega_{\text{screw}}$. For the symmetric case $N_x = N_y$, one can write $\omega_{\text{screw}}$ and $\theta_2^{(0,0)}$ in a form which is much easier to interpret, see Eq. (E.12) and (E.13). Note that the combined transformations $\omega \to -\omega$ and $b_R \leftrightarrow b_L$ leave the formulas for $\omega_{\text{screw}}, \theta_2^{(0,0)}$ unchanged — this is expected, as inverting the sign of the driving frequency when the driving is circularly polarised is equivalent to inversing the polarisation. The formulas Eq. (E.12) and (E.13) suggest that $\omega_{\text{screw}}$ and $\theta_2^{(0,0)}$ in general have two pairs of resonant frequencies, $\omega^{\text{res.}} = \pm \text{Re}(E_-)$ and $\pm \text{Re}(E_+)$. However if we just consider positive driving frequency, $\omega > 0$, only two of these can be excited. For $\gamma < 0$ and $\omega > 0$, right-polarised driving, $b_L = 0$, excites the upper resonance $-\text{Re}(E_+)$, while left-polarised driving, $b_R = 0$, excites the lower resonance $-\text{Re}(E_+)$. This should come as no surprise, as we had seen the same behaviour in the resonances of the first order time- and space-averaged deviation $\delta M$. Neglecting dipolar interactions, $\omega_{\text{screw}}$ has the compact form

$$
\begin{aligned}
\omega_{\text{screw}} &= \frac{\omega \left[ (b_R^2 - b_L^2) \left( (\alpha^2 + 1)\,\omega^2 + 4 \right) \right]}{8 \left[ (1 + \alpha^2)^2 \omega^4 + (5\alpha^2 - 4)\,\omega^2 + 4 \right]} \\
&\approx \frac{3\sqrt{2}}{32} \frac{b_R^2 - b_L^2}{(\omega - \sqrt{2})^2 + 9\alpha^2/4},
\end{aligned}
\tag{2.19}
$$

where in the second row we expanded around the resonance frequency $\omega_{\text{res}} = \sqrt{2}$. In Fig. 2.5a we have plotted $\omega_{\text{screw}}$ as a function of the driving frequency $\omega$ for left-, right- and linearly polarised perpendicular driving and various $\delta, c$. By choosing different polarisations of the driving field, varying the static background field $b_0$ or the driving frequency $\omega$ one can control the magnitude and sign of $\omega_{\text{screw}}$.

There is actually a nicer way of obtaining $\omega_{\text{screw}}$, which allows us to write it purely as a function of the first order coefficients $\theta_{\pm 1, \pm 1}, \phi_{\pm 1, \pm 1}$. The method is inspired by the Thiele approach, where one $\hat{\mathbf{M}} \times$ LLG onto the Goldstone mode of the system, which in this case is $\frac{\partial \hat{\mathbf{M}}}{\partial z}$, and then integrates over space,

$$
\int dz\, \frac{\partial \hat{\mathbf{M}}}{\partial z} \cdot \left( \text{sgn}(\gamma) \hat{\mathbf{M}} \times \dot{\mathbf{M}} - \alpha \dot{\mathbf{M}} \right) = |\gamma| \int dz\, \frac{\partial \hat{\mathbf{M}}}{\partial z} \cdot \left( (\hat{\mathbf{M}} \cdot \mathbf{B}_{\text{eff}}) \hat{\mathbf{M}} - \mathbf{B}_{\text{eff}} \right) M_0.
$$

The RHS of the above equation disappears, as $\hat{\mathbf{M}} \perp \frac{\partial \hat{\mathbf{M}}}{\partial z}$ and $-\int dz\, \frac{\partial \mathbf{M}}{\partial z} \cdot \mathbf{B}_{\text{eff}} = \frac{\delta F}{\delta z} = 0$ due to the translational symmetry of $F$. Using the chain rule, $\frac{\partial \hat{\mathbf{M}}}{\partial z} = \theta' \partial_\theta \hat{\mathbf{M}} + \phi' \partial_\phi \hat{\mathbf{M}}$, one obtains after integration that the first term on the LHS also disappears, leaving only

$$
\int dz\, \alpha \frac{\partial \hat{\mathbf{M}}}{\partial z} \cdot \dot{\mathbf{M}} = 0.
\tag{2.20}
$$

This is a useful equation because it directly asserts that the Archimedean screw motion in the driven conical state is a mechanism driven by damping, i.e. it requires a finite $\alpha$ to exist. Note also the resemblance of Eq. (2.20) to Eq. (2.12) — this is not coincidental. It can be explained by the fact that for the system driven in the parallel direction $\frac{\partial \hat{\mathbf{M}}}{\partial z} \parallel \partial_\phi \hat{\mathbf{M}}$, as the screw symmetry is conserved. Substituting the first and second order ansatzes Eq. (2.15) and (2.18) into Eq. (2.20) and time-averaging over one period of oscillation one can solve for $\omega_{\text{screw}}$,

$$
\begin{aligned}
\omega_{\text{screw}} = \frac{2\omega}{s^2} &\left[ \left( \theta_1^{(-1,1)}\theta_1^{(1,-1)} - \theta_1^{(-1,-1)}\theta_1^{(1,1)} + s^2\phi_1^{(-1,1)}\phi_1^{(1,-1)} - s^2\phi_1^{(-1,-1)}\phi_1^{(1,1)} \right) \right. \\
&\left. + ics \left( \theta_1^{(1,1)}\phi_1^{(-1,-1)} + \theta_1^{(1,-1)}\phi_1^{(-1,1)} - \theta_1^{(-1,1)}\phi_1^{(1,-1)} - \theta_1^{(-1,-1)}\phi_1^{(1,1)} \right) \right].
\end{aligned}
\tag{2.21}
$$

This way of writing $\omega_{\text{screw}}$ is more compact and makes clear why its resonances directly coincide with those of the first order response.

The rotational frequency $\omega_{\text{screw}}$ can also be obtained numerically from mumax3 [48, 49] simulations. To extract $\omega_{\text{screw}}$ from the numerics, one plots the azimuthal angle $\phi(z,t) = \phi^{\text{osc.}} + \omega_{\text{screw}}t$ of a given single spin in the helix over time. Averaging out the $\omega$ oscillations one obtains a straight line, whose slope is $\omega_{\text{screw}}$. It is also possible to skip the averaging step by plotting $\phi(z,t)$ stroboscopically, in other words at time intervals equal to integer multiples of the time period $T = \frac{2\pi}{\omega}$ — in this case the first order oscillations are automatically suppressed. In Fig. 2.5b we show a comparison of this numerically calculated $\Omega_{\text{screw}}$ (data collection and analysis done by Lukas Heinen) with our analytical result. We observe an excellent fit between the two methods.

Let us now get an idea of the magnitude of the quantities involved. Driving the system perpendicularly in the GHz range results in a rotational screw frequency $\Omega_{\text{screw}}$ in the MHz range. Due to the helical symmetry, the rotation of the conical phase at frequency $\Omega_{\text{screw}}$ can equivalently be interpreted as a translation of the entire helical texture at constant velocity $\mathbf{V}_{\text{screw}}$ parallel to $\hat{\mathbf{q}}$, with

$$
\mathbf{V}_{\text{screw}} = \hat{\mathbf{q}}\frac{\Omega_{\text{screw}}}{q}.
\tag{2.22}
$$

For a helical pitch wavelength of roughly $\lambda = 200\,\text{Å}$, this results in $V_{\text{screw}} \sim 200\,\text{mm s}^{-1}$. We can compare this to a familiar example of the Archimedean screw from everyday life: hydro-turbines usually rotate at around 25 Hz and have a pitch wavelength on the order of 1 m [50], resulting in a $V_{\text{screw}} \sim 25\,\text{m s}^{-1}$, or roughly two orders of magnitude larger than

for our nano-Archimedean screw — so we are not doing too badly! The biggest enemy to the operation of the magnetic Archimedean screw is pinning by disorder, which is inevitable in real experiments. To overcome this pinning we need to apply a driving field larger than a minimum critical amplitude $B_1^{\mathrm{crit}}(t)$. Useful knowledge can be extracted from previous studies performed on skyrmions, which are expected to have similar friction and pinning to conical magnets because the magnetisation varies on the same length scale. In experiments were skyrmions were subjected to an electric current, it was found, using Hall effect measurements, that the skyrmions only started to move if the applied current was larger than a critical minimum current $j_c$ [51]. At current $2j_c$ the skyrmion velocity was estimated to be $0.2\,\mathrm{mm/s}$, three orders of magnitude *smaller* than $v_{\mathrm{screw}}$. Thus we can be optimistic that, at least for resonant driving, the Archimedean screw will not be hampered by pinning from the lattice and should therefore be observable in a real experimental setting.

We have reached our first goal: to realise an Achimedean screw in a driven chiral magnet. We saw that this could be achieved by driving the conical phase of a chiral magnet with an oscillating magnetic field $\mathbf{b}_1(t)$ perpendicular to the pitch vector $\mathbf{q}$, resulting in a frequency of rotation $\omega_{\mathrm{screw}} \propto b_1^2$. But how stable is this dynamics? In the next section, we will see that increasing the amplitude $b_1$ of the driving magnetic field actually causes the system to become unstable and investigate the nature of these instabilities.

## 2.3   Dynamics beyond the Archimedean Screw

The analysis presented in this section was initial motivated by unusual patterns in numerical simulations. Fig. 2.6a shows the azimuthal angle $\phi(t)$ of a single spin extracted from simulations where the conical phase was driven with an increasingly strong linearly polarised driving field $\mathbf{B}_\perp^x(t)$, oscillating at driving frequency $f = 4.15\,\mathrm{GHz}$. For weak driving, $B_\perp^x = 0.5\,\mathrm{mT}$, we recognise the regular Archimedean screw solution, obtained by perturbative treatment of the LLG in Sec. 2.2.2. As a reminder, the Archimedean screw solution is characterised by a $\phi(t)$ which oscillates at driving frequency $f$ and simultaneously increases linearly in time with slope $\Omega_{\mathrm{screw}}$. We can also check this in the frequency domain: in Fig. 2.6b we show the Fourier transform in time of $\phi_{\mathrm{osc.}}(t) = \phi(t) - \Omega_{\mathrm{screw}}t$ ($\Omega_{\mathrm{screw}}t$ was removed to obtain a cleaner spectrum). At amplitude $B_\perp^x = 0.5\,\mathrm{mT}$, frequency peaks occur at integer multiples of the driving frequency $f$, in accordance with what we expected from our perturbative analysis in Sec. 2.2.2, which only admits higher order solutions oscillating at frequency $nf, n \in \mathbb{Z}$. If we increase $B_\perp^x$ to $0.69\,\mathrm{mT}$ the Fourier

(a) $\phi(t)$ as a function of time.

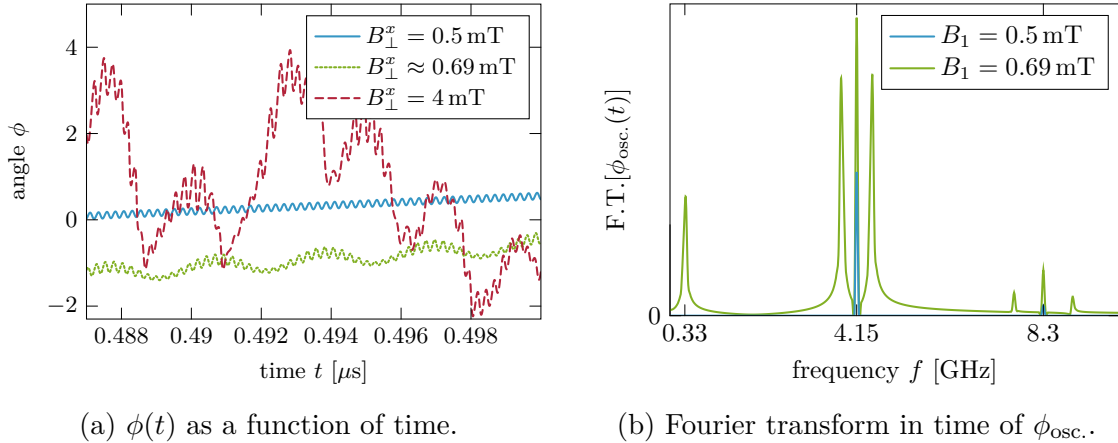(b) Fourier transform in time of $\phi_{\text{osc.}}$.

Figure 2.6 (a) Azimuthal angle $\phi(t)$ of a single spin in the conical phase driven in the perpendicular direction (data generated on mumax3 by Lukas Heinen). The parameters $\alpha, B_0, \delta, N_x, N_y$ are the same as in Fig. 2.5b, with driving frequency $f =$4.15 GHz. For weak driving field $B^x_\perp =$0.5 mT we observe the Archimedean screw solution: $\phi(t)$ oscillates at driving frequency $f$ and increases linearly in time with slope $\Omega_{\text{screw}}$. For intermediate amplitude of driving $B^x_\perp =$0.69 mT the system forms a "time quasicrystal" with one single additional frequency $f_{\text{new}} =$0.33 GHz, which we can explain using Floquet spin wave theory. At larger amplitude many additional frequencies of oscillation appear, resulting in a kind of chaotic behaviour, and an analytical explanation becomes difficult. (b) Fourier transform of $\phi(t)_{\text{screw}} = \phi(t) - \omega_{\text{screw}}t$, extracted from the time-dependent data in panel (a), for driving amplitudes $B^x_\perp = 0.5, 0.69$ mT. For 0.5 mT only peaks at integer multiples of the driving frequency $f, 2f$ are observed. At higher amplitude 0.69 mT additional peaks at the incommensurate frequency $f_{\text{new}} =$0.33 GHz, as well as Fourier copies $f \pm f_{\text{new}}, 2f \pm f_{\text{new}}$ form. At still higher amplitude 4 mT many more peaks appear (not included here to preserve the clarity of the figure).

analysis shows additional frequency peaks at $f_{\text{new}}$ and $f \pm f_{\text{new}}$, with $f_{\text{new}} =$0.33 GHz. $f_{\text{new}}$ is *incommensurate* with $f$ (not an integer multiple of $f$) — therefore it *cannot* be explained using the same perturbative techniques developed for the Archimedean screw dynamics in Sec. 2.2.2. Thus we need to develop different analytical tools to adequately describe this new response. The other main motivation for seeking an analytical explanation is that the numerics shown here is strongly influenced by factors such as system size, which reduces their reliability. The analytical approach, as we shall see, explains this strong sensitivity on system size and gives us full confidence in the results.

## 2.3.1 Floquet Spin Wave Theory

We will investigate the stability of the driven spin system using an approach related to linear spin wave theory. Linear spin wave theory helps us determine the energy spectra

of small spin excitations $\delta\mathbf{S}$ around static spin textures $\mathbf{S}_0$. We base ourselves on the Holstein-Primakoff (HP) expansion, a technique pioneered in 1940 by Theodore Holstein, then a graduate student, and Henry Primakoff [52]. To get us started, let's review how the HP expansion can be applied to obtain the spin wave spectra in ferromagnets and antiferromagnets. For a ferromagnet with spins pointing parallel to $\mathbf{e}_z$ the HP expansion reads

$$\mathbf{S} = \hat{S}_z\mathbf{e}_z + \hat{S}_+\mathbf{e}_- + \hat{S}_-\mathbf{e}_+, \tag{2.23}$$

$$\hat{S}_z = \hbar\left(s - a^\dagger a\right), \quad \hat{S}_+ = \hbar\sqrt{s}\sqrt{1 - \frac{a^\dagger a}{2s}}a, \quad \hat{S}_- = \hbar\sqrt{s}a^\dagger\sqrt{1 - \frac{a^\dagger a}{2s}},$$

where $s$ is the spin quantum number, $\mathbf{e}_\pm = \frac{1}{\sqrt{2}}(\mathbf{e}_x \pm i\mathbf{e}_y)$, $\hat{S}_\pm = \frac{1}{\sqrt{2}}(\hat{S}_x \pm i\hat{S}_y)$ and $a, a^\dagger$ are bosonic operators obeying the usual bosonic commutation relation $\left[a, a^\dagger\right] = 1$. In Eq. (2.23) the static spin $\mathbf{S}_0$ is given by the $\mathcal{O}(a^0)$ terms, i.e. $\mathbf{S}_0 = \hbar s\mathbf{e}_z$, while the higher order terms $\mathcal{O}(a^n), n > 0$ describe the perturbation $\delta\mathbf{S}$. There are two things to note about the Holstein-Primakoff expansion. The first is that it is only valid in the so-called "large $S$" limit, $s \gg 1$. The "large $S$" limit is also sometimes called the "classical limit", because the quantum expectation and classical length of the spin tend to the same value, $\sqrt{\langle\hat{\mathbf{S}^2}\rangle} = \hbar\sqrt{s(s + 1)} \approx \hbar s$. Secondly and crucially, Eq. (2.23) preserves the spin commutation relation $[\hat{S}_i, \hat{S}_j] = i\hbar\epsilon_{ijk}\hat{S}_k$ to *any* order in $a, a^\dagger$. One just needs to truncate Eq. (2.23) one order in $a, a^\dagger$ *higher* than the desired accuracy. As an example, if we consider the easiest case of accuracy to order $\mathcal{O}(a^0)$, we must truncate $\hat{\mathbf{S}}$ at order $\mathcal{O}(a)$, giving $\hat{S}_+ = \hbar\sqrt{s}a, \hat{S}_- = \hbar\sqrt{s}a^\dagger$ and $\hat{S}_z = \hbar s$. It is easy to check that the commutation relation, which can equivalently be written as $[\hat{S}_+, \hat{S}_-] = \hat{S}_z$, is in this case valid to order $\mathcal{O}(a^0)$. Satisfied that Eq. (2.23) fulfils the necessary spin algebra requirements, we substitute it into the Heisenberg Hamiltonian $H = J\sum_{\langle i,j\rangle} \mathbf{S}_i \cdot \mathbf{S}_j$, and collect all terms which are quadratic in $\delta\mathbf{S}$, or equivalently all order $\mathcal{O}(a^2)$ terms. In the final step, the quadratic Hamiltonian gets diagonalised in momentum space into the form $H = \sum_k \epsilon_k\tilde{a}_k^\dagger\tilde{a}_k$ to obtain the band energy spectra $\epsilon_k$ of the system. For a ferromagnet, one can directly read off the band energy, resulting in $\epsilon_{\mathrm{F}}(k) = \pm 4JS\hbar\sin^2(\frac{ka}{2})$ for a 1D Heisenberg chain. For an antiferromagnet, an additional Bogoliubov transformation is needed due to the presence of $a^2, a^{\dagger 2}$ terms, which results in a different band energy, $\epsilon_{\mathrm{AF}}(k) = \pm 2JS\hbar|\sin(ka)|$, see e.g. [53] for concrete details on how to do this. It is a property of Bogoliubov quasiparticles that their eigenenergies always come in positive-negative pairs $\pm\epsilon(k)$, although the negative copy is an unphysical artefact of the Bogoliubov transformation. In Fig. 2.7 we show the physical
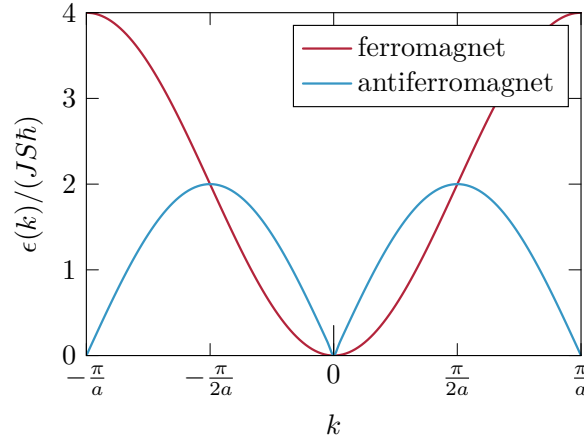
Figure 2.7 Band energy spectra for a 1D Heisenberg ferromagnet and antiferromagnet.

positive energy band spectrum $\epsilon(k)$ for a 1D ferromagnetic and antiferromagnetic chain. Notice the quadratic dependence $\lim_{k \to 0} \epsilon(k) \sim k^2$ in the ferromagnet — this is typical for systems where a rotational Goldstone mode is present with spontaneous symmetry breaking, which is the case for the Heisenberg model. Also note that the spectrum for the antiferromagnet has periodicity $\frac{\pi}{a}$ in momentum space, vs. a periodicity of $\frac{2\pi}{a}$ for the ferromagnet — this is because the unit cell for for the antiferromagnet contains two spins, one up and one down, and thus has size $2a$, twice as big as the ferromagnet.

For our Archimedean screw system, the spin wave calculation is a lot more complicated than the simple static (anti)ferromagnet case, for several reasons. Firstly, we need to expand around a non-collinear magnetic texture — the conical state, rather than the simple (anti)ferromagnetic arrangement. On top of that the magnetic texture around which we expand is not static, but moving in time according to the dynamics described in Sec. 2.2.2. Secondly, we want to include the effects of the Gilbert damping in our calculation, an aspect which is usually ignored in spin wave calculations presented in textbooks. As Gilbert damping is a classical phenomenon, we need to derive a classical equivalent to the quantum spin wave formalism discussed in the previous paragraph. We already touched on this in Sec. 1.5, where we showed that the classical equivalent of the commutation relation for spin quantum mechanical operators $\hat{S}_i$ is a Poisson bracket for the classical magnetisation field $M_i$, see Eq. (1.22). Now we want to extend this Poisson bracket property to the perturbed magnetisation $\mathbf{M} = \mathbf{M}_0 + \delta \mathbf{M}$. To this end, and taking inspiration from Eq. (2.23), we write the perturbed magnetisation as follows

$$\mathbf{M} = M_0 \left( \mathbf{e}_3 (1 - a^* a) + \mathbf{e}_- a \sqrt{1 - \frac{a^* a}{2}} + \mathbf{e}_+ a^* \sqrt{1 - \frac{a^* a}{2}} \right), \qquad (2.24)$$

where $a(\mathbf{r}, t)$ and $a^*(\mathbf{r}, t)$ are now complex time- and space-dependent fields, rather than operators. $a(\mathbf{r}, t)$ and $a^*(\mathbf{r}, t)$ obey the Poisson bracket $\{a(\mathbf{r}, a^*(\mathbf{r}')\} = \delta(\mathbf{r} - \mathbf{r}')$, which guarantees that the Poisson bracket condition on the magnetisation, $\{\hat{M}_i, \hat{M}_j\} = i\epsilon_{ijk}\hat{M}_k$, is fulfilled to any order in $a, a^*$. Writing the excitations as complex fields $a, a^*$ rather than operators $a, a^\dagger$ has a bonus from the technical point of view: the ordering no longer matters, which makes calculations easier[4]. In contrast to the global static coordinate system used in Eq. (2.23), here we must use a local, time dependent coordinate system, because the magnetisation around which we expand is space- and time-dependent. We achieve this by choosing $\mathbf{e}_3 \parallel \mathbf{M}_{\text{screw}}$, the Archimedean screw solution obtained in Sec. 2.2.2, with $\mathbf{e}_\pm$ spanning the plane perpendicular to $\mathbf{e}_3$

$$\mathbf{e}_3 = \begin{pmatrix} \sin\left(\theta(z,t)\right)\cos\left(\phi(z,t)\right) \\ \sin\left(\theta(z,t)\right)\sin\left(\phi(z,t)\right) \\ \cos\left(\theta(z,t)\right) \end{pmatrix}, \mathbf{e}_\mp = \frac{1}{\sqrt{2}} \begin{pmatrix} \cos\left(\theta(z,t)\right)\cos\left(\phi(z,t)\right) \pm i\sin\left(\phi(z,t)\right) \\ \cos\left(\theta(z,t)\right)\sin\left(\phi(z,t)\right) \mp i\cos\left(\phi(z,t)\right) \\ -\sin\left(\theta(z,t)\right) \end{pmatrix},$$
$$(2.25)$$

where $\theta(z,t), \phi(z,t)$ describe the perturbative Archimedean screw solution up to quadratic order $\mathcal{O}(b_\perp^2)$, Eq. (2.15) and (2.18). More precisely, at order $b_\perp^2$ we will only include the DC response — i.e. $\omega_{\text{screw}}$ and $\theta_2^{(0,0)}$ — neglecting any temporally or spatially oscillating terms. This makes the implementation considerably less painful, and is also sufficient to obtain the leading order instability, as we shall see. The next step is to substitute the expansion Eq. (2.24) into the LLG written in the notation of classical Hamiltonian dynamics, Eq. (1.22). A useful check that we calculated the Archimedean screw solution correctly is that all $\mathcal{O}(a^0)$ terms drop out of this equation. Thus, to leading order the LLG is linear in $a, a^*$. By projecting the LLG onto $\mathbf{e}_\mp$, see App. F.1 for details, we obtain

$$\dot{a} = \frac{i(\text{sgn}(\gamma) - i\alpha)}{1 + \alpha^2}\{F^{(2)}, a\} - i\dot{\phi}\cos(\theta)a,$$
$$\dot{a}^* = \frac{i(\text{sgn}(\gamma) + i\alpha)}{1 + \alpha^2}\{F^{(2)}, a^*\} + i\dot{\phi}\cos(\theta)a^*,$$
$$(2.26)$$

where $F^{(2)}$ is the contribution of the free energy $F$ which is quadratic in $a, a^*$, with an additional factor $|\gamma|$ absorbed into it. One immediately notices the resemblance of Eq. (2.26) to the well-known Heisenberg equations of motion for the quantum operators $a$ and $a^\dagger$, $\dot{a} = i[H, a]$ and $\dot{a}^* = -i[H, a^*]$. The differences are the additional presence of damping (terms proportional to $\alpha$) as well an extra term $\propto \dot{\phi}$ (a consequence of the time

---

[4]if you are extra observant, you might have noticed that the $\sqrt{1 - a^*a}$ term is in last position in both terms on the RHS of Eq. (2.24), which would not be allowed in Eq. (2.23) because ordering matters there.
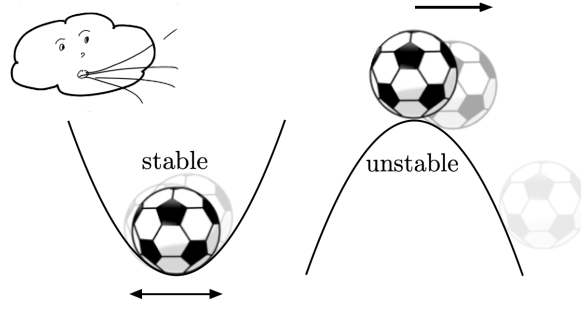
Figure 2.8 Two identical footballs, one sitting at the bottom of a valley, one at the top of the hill. A sudden gust of wind leads to two very different outcomes. The football at the bottom of the hill oscillates a little and eventually comes to rest in its equilibrium position due to damping. The football at the top of the hill rolls off the cliff, never returning to its initial position.

dependent coordinate system). The goal now is to solve Eq. (2.26) for the perturbations $a(t), a^*(t)$, as their behaviour in time determines the stability of the driven system.

Why is this the case? To understand this, let us take a step back and perform a little *gedankenexperiment* on a much more familiar physical system. Picture two identical footballs, the first sitting at the bottom of a valley and the second at the top of a hill, as shown in Fig. 2.8. The Hamiltonian for these two systems is

$$H = \frac{p^2}{2m} + V_0 x^2, \tag{2.27}$$

where $p, m, x$ are the momentum, mass and displacement of the footballs from their equilibrium position, respectively (for simplicity, we neglect the rotational energy). The sign of $V_0$ determines the system: positive for the valley and negative for the hill. We can also define a natural frequency of oscillation $\omega = \sqrt{2V_0/m}$. By using the canonical transformations

$$a = \sqrt{\frac{m\omega}{2}}x + i\sqrt{\frac{1}{2m\omega}}p, \quad a^* = \sqrt{\frac{m\omega}{2}}x - i\sqrt{\frac{1}{2m\omega}}p,$$

we can rewrite the Hamiltonians in the form $H_{\text{valley}} = \omega a^* a$, $H_{\text{hill}} = -\frac{\omega}{2}(a^2 + a^{*2})$. If we define the Poisson bracket $\{f, g\} = i\left(\frac{\partial f}{\partial x}\frac{\partial g}{\partial p} - \frac{\partial f}{\partial p}\frac{\partial g}{\partial x}\right)$[5], then Hamilton's equation of motion takes the form $\dot{f} = i\{H, f\}$ for any function $f$. Note the resemblance to Eq. (2.26) if we set $\text{sgn}(\gamma) = 1$, which motivates us to just add in the damping "by hand" here too,

---

[5]Note the extra factor $i$ compared to the usual definition! This is necessary to establish the link with our spin system formalism.

leading to $\dot{a} = \frac{i}{1+i\alpha}\{H, a\}$, $\dot{a}^* = \frac{i}{1-i\alpha}\{H, a^*\}$[6]. Using the Poisson bracket $\{x, p\} = i$ we obtain $\{a, a^*\} = 1$, and the equations of motion in matrix form are

$$\begin{pmatrix} \dot{a}_{\text{valley}} \\ \dot{a}^*_{\text{valley}} \end{pmatrix} = \begin{pmatrix} \frac{-i\omega}{1+i\alpha} & 0 \\ 0 & \frac{i\omega}{1-i\alpha} \end{pmatrix} \begin{pmatrix} a_{\text{valley}} \\ a^*_{\text{valley}} \end{pmatrix}, \quad \begin{pmatrix} \dot{a}_{\text{hill}} \\ \dot{a}^*_{\text{hill}} \end{pmatrix} = \begin{pmatrix} 0 & \frac{i\omega}{1-i\alpha} \\ \frac{-i\omega}{1+i\alpha} & 0 \end{pmatrix} \begin{pmatrix} a_{\text{hill}} \\ a^*_{\text{hill}} \end{pmatrix}. \tag{2.28}$$

These two matrix equations can be solved by the ansatz

$$\begin{pmatrix} a(t) \\ a^*(t) \end{pmatrix} = \begin{pmatrix} a(0) \\ a^*(0) \end{pmatrix} e^{-i\lambda t}, \tag{2.29}$$

which removes the time dependence from Eq. (2.28), giving the matrix eigenvalue equation

$$M \begin{pmatrix} a(0) \\ a^*(0) \end{pmatrix} = \lambda \begin{pmatrix} a(0) \\ a^*(0) \end{pmatrix}, \tag{2.30}$$

where the matrices for the two systems are defined as

$$M_{\text{valley}} = \begin{pmatrix} \frac{\omega}{1+i\alpha} & 0 \\ 0 & -\frac{\omega}{1-i\alpha} \end{pmatrix}, \quad M_{\text{hill}} = \begin{pmatrix} 0 & \frac{-1}{1-i\alpha} \\ \frac{1}{1+i\alpha} & 0 \end{pmatrix}. \tag{2.31}$$

Diagonalising the matrices $M_{\text{valley}}$, $M_{\text{hill}}$ gives the following two sets of eigenvalues,

$$\begin{aligned} \lambda_{\text{valley},1} &= \frac{\omega}{1+i\alpha}, & \lambda_{\text{hill},1} &= \frac{-i\omega}{\sqrt{1+\alpha^2}}, \\ \lambda_{\text{valley},2} &= \frac{-\omega}{1-i\alpha}, & \lambda_{\text{hill},2} &= \frac{i\omega}{\sqrt{1+\alpha^2}}. \end{aligned} \tag{2.32}$$

For both matrices, the pair of eigenvalues comes in the form $\lambda, -\lambda^*$. This is in fact a general property of damped Bogoliubov systems which we will see over and over again. It is a consequence of the property $M = -\sigma^x M^* \sigma^x$, which one can easily check for the two matrices in Eq. (2.31). Taking the trace and determinant of $M = -\sigma^x M^* \sigma^x$ gives

$$\begin{aligned} \text{tr}(M) &= -\text{tr}(M^*) & \det(M) &= \det(M^*) \\ \implies \lambda_1 + \lambda_2 &= -(\lambda_1^* + \lambda_2^*), & \implies \lambda_1 \lambda_2 &= \lambda_1^* \lambda_2^*, \end{aligned}$$

which implies that $\lambda_2 = -\lambda_1^*$.

If one substitutes the eigenvalues in Eq. (2.32) back into Eq. (2.29), it becomes clear that for $\lambda_{\text{valley},1}$, $\lambda_{\text{valley},2}$ $a(t), a^*(t)$ experience damped oscillations and for $\lambda_{\text{valley},1}$ they

---

[6]I pulled a bit of a rabbit out of the hat here, but bear with me... you'll see that it works :)

decay exponentially in time. However, $\lambda_{\text{valley},2}$ leads to exponential growth in $a(t), a^*(t)$! This is the signature of an instability. More precisely, any eigenvalue whose *imaginary* part is *positive*, $\text{Im}[\lambda] > 0$, leads to an instability. Coming back to our footballs, the initial amplitudes of the perturbations $a(0), a^*(0)$ could be provided, for instance, by a sudden gust of wind blowing on our system. If this happens we know that the football at the bottom of the hill will oscillate a little and then eventually return to equilibrium due to damping, whereas the football at the top is unstable and will fall off the hill, never to return to its initial position. The instability predicted by the maths is thus in complete accordance with our physical intuition.

Having gained some useful physical insight from this little aside, let us come back to our spin system. The goal here is the same: we want to solve the equations of motion Eq. (2.26) to determine whether the system is stable or unstable. Compared to the football system the driven spins system has two notable complications. The first is that $F$ contains energy contributions from many interacting spins rather than just the single particle contribution in Eq. (2.27) from the football. Luckily this complication can be overcome by Fourier transforming to momentum space, where we make use of the underlying periodicity of the helical texture. The second complication of the driven spin system is the presence of explicitly time-dependent terms arising from the driving and expansion around the time-dependent Archimedean screw solution. Due to the periodic nature of the drive $\mathbf{b}_\perp(t)$, all these explicitly time-dependent terms are periodic in $\omega$. This again screams for Fourier transformation, this time in the time domain. In fact, "Floquet theory" is a fancy term for doing just that. By the way, this means that the fancy-sounding title "Floquet spin wave theory" should not scare you as on the technical level it simply translates to an additional Fourier transformation in time.

As stipulated in the previous paragraph we solve the additional complications by simultaneously Fourier transformating in space and time. We begin by defining the space and time Fourier transformed fields $\tilde{a}^m_{\mathbf{k}+n\mathbf{q}}, \tilde{a}^{m*}_{\mathbf{k}+n\mathbf{q}}$ as

$$\tilde{a}^m_{\mathbf{k}} = \int dt \int d^3r\, e^{im\omega t + i\mathbf{k}\cdot(\mathbf{r}+\mathbf{v}_{\text{screw}}t)} a(\mathbf{r}),$$
$$\tilde{a}^{-m*}_{-\mathbf{k}} = \int dt \int d^3r\, e^{im\omega t + i\mathbf{k}\cdot(\mathbf{r}+\mathbf{v}_{\text{screw}}t)} a^*(\mathbf{r}). \tag{2.33}$$

Note the factor $\mathbf{r} + \mathbf{v}_{\text{screw}}t$, which puts us in a frame co-moving with the Archimedean screw. Within the perturbative scheme we are using, only the fields $\tilde{a}^m_{n\mathbf{q}+\mathbf{k}}, \tilde{a}^{m*}_{n\mathbf{q}+\mathbf{k}}$ with $m = -1, 0, 1$, $n = -1, 0, 1$ couple to each other. We can collect these fields in an 18-component Floquet vector $\Psi^F_{\mathbf{k}}$, see Eq. (F.3) for its exact definition. This restriction in both the number of Floquet zones and the number of momentum copies is justified
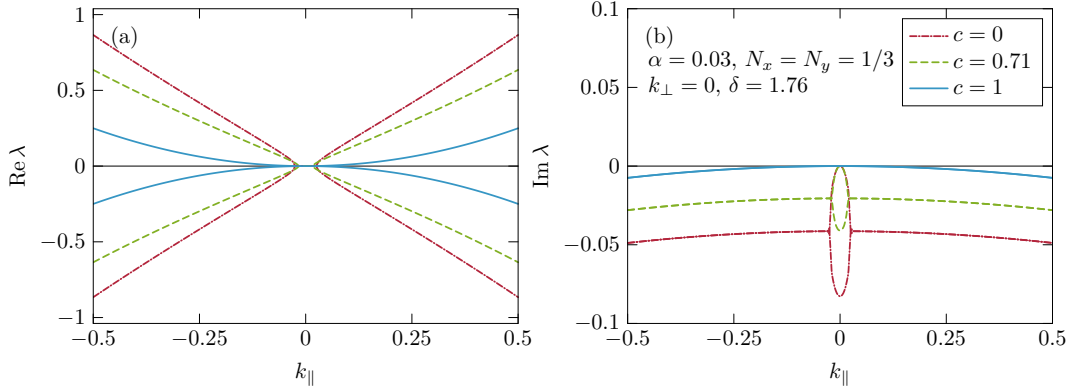
Figure 2.9 Real and imaginary parts of the eigenenergies of spin waves in the undriven conical phase, $\mathbf{b}_1 = 0$, as a function of $k_\parallel$. For small momenta $k_\parallel$ and $c < 1$ the spin waves are purely diffusive, $\lambda \sim i\alpha k_\parallel^2$. Analytical formula given in Eq. (2.36).

in the limit of small driving amplitudes $b_\perp$, and the resulting eigenvalues are formally correct to quadratic order in $b_\perp$. After a somewhat lengthy analysis involving Bogoliubov transformations and other fun stuff, see Sec. F.2 for technical details, it is possible to recast the EoM Eq. (2.26) into the following matrix eigenvalue equation

$$M_{\mathbf{k}}^F \Psi_{\mathbf{k}}^F = \lambda_{\mathbf{k}} \Psi_{\mathbf{k}}^F, \tag{2.34}$$

with $\Psi_{\mathbf{k}}^F(t) = e^{-i\lambda_{\mathbf{k}} t}\Psi_{\mathbf{k}}^F(0)$. Here $M^F(\mathbf{k})$ is the $18 \times 18$ so-called "Floquet-Bogoliubov" matrix. Just like the matrices $M_{\text{valley}}, M_{\text{hill}}$ we saw earlier $M_{\mathbf{k}}^F$ is *not* Hermitian. Thus its eigenvalues are in general complex,

$$\lambda_{\mathbf{k}} = \text{Re}[\lambda_{\mathbf{k}}] + i\text{Im}[\lambda_{\mathbf{k}}]. \tag{2.35}$$

The physical interpretation for the real and imaginary parts is very different: the real part gives the frequency of oscillation, while the imaginary part determines whether the spin wave grows or decays exponentially in time. As before, the *sign* of the imaginary part determines whether the system is stable — $\text{Im}[\lambda_{\mathbf{k}}] < 0$ — or unstable — $\text{Im}[\lambda_{\mathbf{k}}] > 0$). We will use this criterion to show that the Archimedean screw solution is stable against spin wave perturbations $a, a^*$ up until a critical strength of driving $b_\perp^{\text{crit.}}$. But first let us simplify the problem a little in order to gain some intuition on the characteristics of spin waves in the conical and helical phases. In the next short subsection we turn off the driving magnetic field and just consider the spin wave spectra around a static conical state.

**Spin Waves in the Undriven Conical State**

In the absence of driving there is no coupling between different Floquet zones and $M^F$ collapses into the block diagonal form $\ldots M^{-1,-1} \bigotimes M^{0,0} \bigotimes M^{1,1} \ldots$. The matrices $M^{n,n}$ are all equal to each other up to a term $n\omega I$ proportional to the identity — thus it is sufficient to diagonalise just $M^{0,0}$ to obtain the full spin wave spectrum of the system. Formally, $M^{0,0}$ is infinitely large, but in practice we need to truncate it in order to be able to diagonalise it numerically. After truncation, the matrix $M^{0,0}$ carrying $m$ momentum copies has size $2m \times 2m$[7]. In general, this truncated $M^{0,0}$ needs to be diagonalised on a computer, but in the special case $k_\perp = 0$ it collapses into the block diagonal form $M^{0,0} = \ldots M(k_\parallel - q) \bigotimes M(k_\parallel) \bigotimes M(k_\parallel + q)$, where $M(k_\parallel)$ is a $2 \times 2$ matrix, defined in Eq. (F.14). Diagonalising $M(k_\parallel)$ gives the lowest two energy bands of the system

$$\lambda_\pm = \frac{1}{2\left(1 + \alpha^2\right)} \left[ \pm\sqrt{4k_\parallel^4 + 4k_\parallel^2(1+\delta)s^2 - \alpha^2 s^4(1+\delta)^2} - i\alpha\left((1+\delta)s^2 + 2k_\parallel^2\right) \right]. \tag{2.36}$$

The real and imaginary parts of $\lambda_\pm$ are plotted in Fig. 2.9 as a function of the parallel momentum $k_\parallel$ in the first Brillouin zone $-\frac{1}{2} < k_\parallel < \frac{1}{2}$, for three different values of $c$, $c = 0, 0.71, 1$. For $k_\parallel \geq k_{\text{crit.}}$, where

$$k_{\text{crit.}}^2 = \frac{1}{2}(1 - c^2)(1 + \delta)\left(\sqrt{1 + \alpha^2} - 1\right),$$

$\lambda_\pm$ obey the same property $\lambda_- = -\lambda_+^*$ we derived earlier for the football system. However this is not the case for $k_\parallel < k_{\text{crit.}}$, where both $\lambda_\pm$ becomes purely diffusive, $\text{Re}\,\lambda_\pm = 0$. In this range the Goldstone mode of the system is described by $\lambda_G \sim -i\alpha k_\parallel^2$. This remains true as long as $c < 1$ and $\alpha$ is finite. Such purely diffusive behaviour has also been observed in the Goldstone modes of other systems where the translational symmetry is broken but the model simultaneously lacks momentum conservation [54–56]. Both of these conditions are fulfilled in our system as long as $c < 1$ — i.e. we remain in the conical or helical phase, where the continuous translational symmetry is broken. The momentum non-conservation comes from having finite damping in the system, $\alpha > 0$. Another important feature to note about the dispersion in Eq. (2.36) is the shift of $\lambda_\pm$ from linear to quadratic dependence on $k_\parallel$. This shift can easily be explained by considering again the energy spectra for the antiferromagnet and ferromagnet Heisenberg chains shown in Fig. 2.7. At small momenta, or large wavelengths, $k_{\text{crit.}} < k_\parallel \lesssim \sqrt{1 + \delta}s$, the magnon

---

[7]The factor 2 comes from the contribution of one $a_{k_\parallel + mq}$ and one $a_{k_\parallel + mq}^*$ field for each momentum copy.
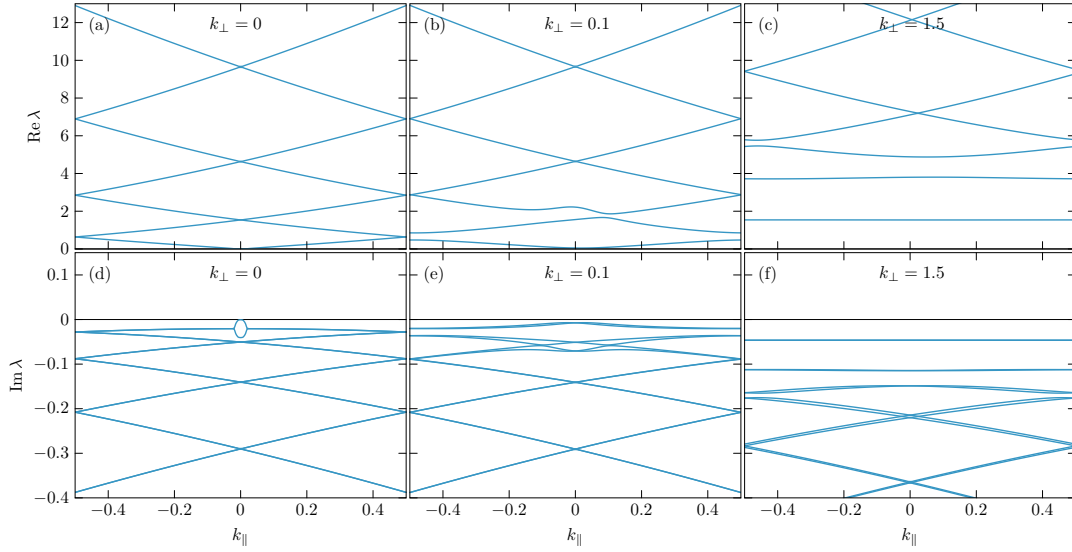
Figure 2.10 Real and imaginary parts of the eigenenergies of spin waves in the undriven conical phase, $\mathbf{b}_1 = 0$, for increasing values of $k_\perp$. The other system parameters are $\delta = 1.76$, $N_x = N_y = 1/3$, $c = 0.71$, $\alpha = 0.03$. As $k_\perp$ increases the energy bands become flat, like for a simple harmonic oscillator, and also more damped. Note the asymmetry around $k_\parallel = 0$ in the real parts, $\text{Re }\lambda$, due to the presence of a symmetry breaking finite static $b_0$-field, $c \neq 0$. If $b_0 = 0$ or $k_\perp = 0$, this symmetry is recovered.

"sees" the twisting in the helical/conical texture, similar to an antiferromagnet, which also "twists" by $\pi$ at every consecutive spin. Thus, at low $k_\parallel$ the helix and antiferromagnet share the same linear in $k_\parallel$ band energy dependence. At larger momenta, or smaller wavelengths, $k_\parallel \gtrsim \sqrt{1 + \delta}s$, the magnon only sees the nearest neighbour spins, which are practically parallel to the each other, like in a ferromagnet. Thus, at larger $k_\parallel$ the helix and ferromagnet share the same quadratic in $k_\parallel$ band energy dependence.

What happens if we now consider spin waves with finite perpendicular momentum $k_\perp \neq 0$? The matrix $M^F$ loses its block diagonal form and acquires some off-diagonal perturbations proportional to $sk_\perp$, see Eq. (F.16) for details (note that for simplicity we are neglecting dipolar interactions, $\delta = 0$). For $k_\perp \ll q, k_\parallel$, we can treat the problem perturbatively in $k_\perp$. Using degenerate perturbation theory[8], this results in band gaps opening up at the degenerate points at the edges of the Brillouin zone with gap energy $\delta\lambda_{\text{gap}} \sim sk_\perp/m^2$, where $m$ indicates the index of the band. This is pretty generic behaviour, which we know also occurs for example at the band edges in the energy spectrum of an electron placed in a periodic potential [58]. At larger $k_\perp \gg k_\parallel$,

---

[8]I haven't provided the details of the calculation but it's fairly generic, eg see [57]. One just needs to watch out a bit because $M^{0,0}$ is *not* a Hermitian matrix so the left and right eigenvectors in the first diagonalisation step are not the same.

perturbation theory is no longer valid for the lower energy bands. In this case, it is easiest to go back to the original equation of motion Eq. (2.26), Fourier transforming in the $x, y$ directions but not in the $z$ direction. For $k_\perp \gg 1$ this gives

$$\lambda a \simeq \frac{1}{\text{sgn}(\gamma) + i\alpha} \left( k_\perp^2 - \partial_z^2 + 2sk_\perp \cos(z) \right) a, \qquad (2.37)$$

where we dropped all $\mathcal{O}(k_\perp^0)$ terms. If we expand $\cos(z) = 1 - \frac{z^2}{2} + \mathcal{O}(z^4)$, we recognise this immediately as the Schrödinger equation for a simple harmonic oscillator, with energy levels given by

$$\lambda_m \simeq \frac{1}{\text{sgn}(\gamma) + i\alpha} \left( k_\perp^2 + 2sk_\perp + 2\sqrt{sk_\perp} \left( m + \frac{1}{2} \right) \right).$$

This means that at larger $k_\perp$ we expect to see the lower energy bands becoming flat bands, with spacing $\delta\lambda_m = \sqrt{sk_\perp}$, see also [46, 45] for experimental confirmation of this effect.

In Fig. 2.10 we have plot the band spectrum, evaluated numerically for three different values $k_\perp = 0, 0.1, 1.5$, as a function of $k_\parallel$. At $k_\perp = 0$, we just have Eq. (2.36) folded back into the first Brillouin zone. At $k_\perp = 0.1$, band gaps open up at the edges; they are most notable at the intersection of the $m = 0$ and $m = 1$ bands and get suppressed for higher energy bands by the factor $\frac{1}{m^2}$. At $k_\perp = 1.5$ both the real and imaginary parts of the lowest two bands are already flat, as suggested by the SHO approximation. Note the lack of symmetry about the $k_\parallel = 0$ axis for the finite $k_\perp$ plots — the finite static magnetic field $b_0$ is responsible for breaking this symmetry.

**Spin Waves in the Driven Conical State**

Now that we have gained some intuition about the spin waves in the undriven conical state, we turn on the perpendicular driving field $\mathbf{b}_{1,\perp}$, which activates the Archimedean screw. At the level of our spin wave calculation, a finite $b_{1,\perp}$ has the effect of making the off-diagonal elements $M^{0,\pm 1}, M^{1,-1}, M^{-1,1}$ in the Floquet-Bogoliubov matrix $M^F$ non-zero. This means that crossings between bands from different Floquet copies can start to couple to each other. To understand the effect of a driving perpendicular field on the spin wave spectrum, compare the two columns in Fig. 2.11. The left column, panels (a) and (c), contains the real and imaginary parts of the spectrum for the *undriven* conical state — this is the same as the leftmost panel in Fig. 2.10 with two extra $\pm\omega$ Floquet copies. These Floquet copies are visible in the real part of the eigenspectrum, where we see copies of the original spectrum translated up and down by $\omega$. When we
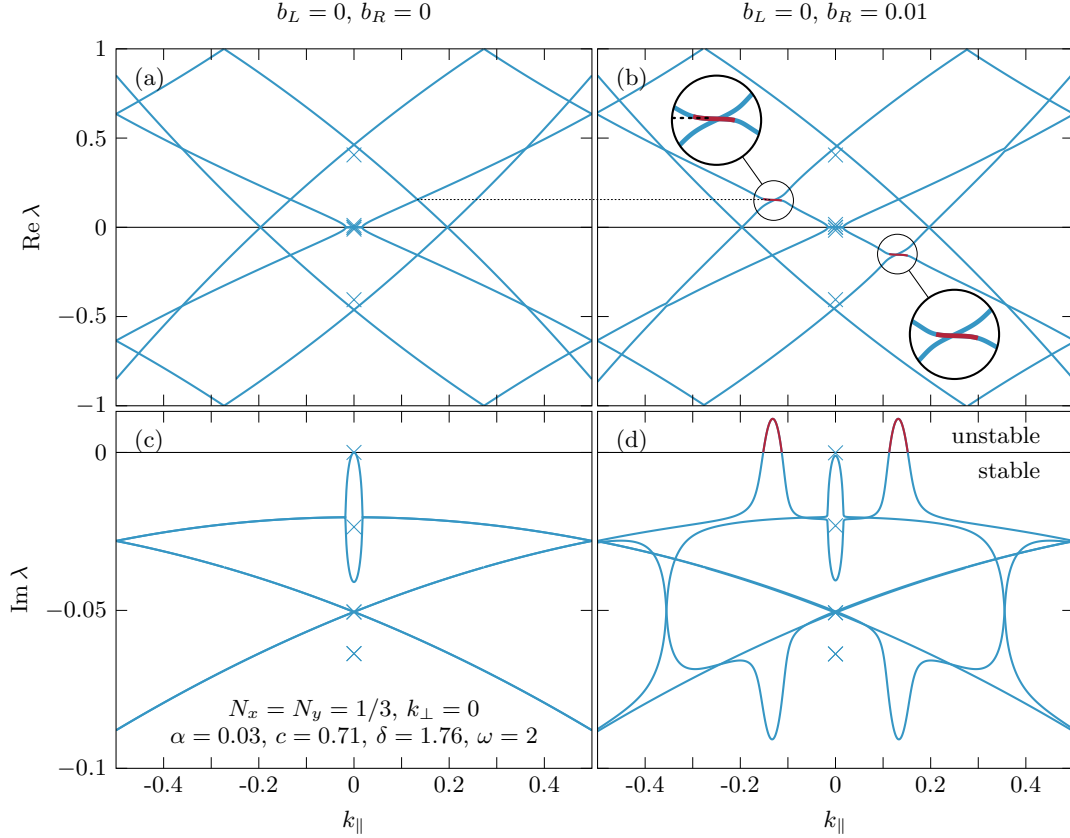
Figure 2.11 Eigenvalues $\lambda_{\mathbf{k}}$ of the matrix $M^F$ as a function of $k_\parallel$ in the first Brillouin zone $-\frac{1}{2} < k_\parallel < \frac{1}{2}$, for an undriven (left column) and driven (right column) conical state with parameters $\alpha = 0.03, c = 0.71, \delta = 1.76, N_x = N_y = N_z = 1/3, k_\perp = 0$. The real parts are plotted in the first Floquet zone $-\frac{\omega}{2} < \operatorname{Re}\lambda < \frac{\omega}{2}$ with $\omega = 2$. All eigenvalues are plotted in the first Brillouin zone $-\frac{1}{2} < k < \frac{1}{2}$. Turning on a right-polarised driving field $b_L = 0, b_R = 0.01$ causes some parts of the imaginary spectrum (highlighted in red in panel (d)) to become positive and therefore *unstable*. The instability occurs near the crossing $k_\parallel \sim \pm 0.13, \operatorname{Re}\lambda = \mp 0.16$ between the 0 and $\pm\omega$ Floquet zones (the two magnified areas in panel (b)). The crosses on the $y$ axis give the eigenvalues at exactly $k = 0$, which is not the same as for $\lim k \to 0$ in the presence of dipolar interactions.

turn on a right-polarised driving field, $b_L = 0, b_R = 0.01$, we obtain the eigenspectra in the right column, panels (b) and (d). The most notable change is in the imaginary parts in panel (d), where in the region $k_\parallel \sim \pm 0.13$, a sign change occurs in the least negative band. This changing sign of Im $\lambda$, highlighted in red, is the signature of an *instability* in the system. The origin of this instability can be explained using degenerate perturbation theory, which reduces the problem to the following simple $2 \times 2$ matrix,

$$M^{\text{res}} \approx \begin{pmatrix} \epsilon^0_{i,\mathbf{k}} - i\alpha\Gamma_i & \mu^{(1)}_\omega \\ -\mu^{(2)}_\omega & -\epsilon^0_{j,-\mathbf{k}} + \omega - i\alpha\Gamma_j \end{pmatrix}. \tag{2.38}$$

Here, $\epsilon^0_{i\mathbf{k}} = \text{Re}[\lambda^0_i]$ denotes the energies of spin waves with band index $i$ of the *unperturbed* system and $\alpha\Gamma_i = \text{Im}\,\lambda^0_i$ are the corresponding lifetimes. The indices $i$ and $j$ label the two bands whose degenerate crossing is magnified in Fig. 2.11, panel (b). The presence of the $+\omega$ term in $M^{\text{res}}_{22}$ indicates that this band belongs to the first Floquet copy of the original spectrum. The frequency-dependent prefactors $\mu^{(i)}_\omega$ describe how the oscillating fields couple the energy levels on the diagonal of the matrix to each other. The coupling is most efficient when the driving frequency hits one of the two $\mathbf{k} = 0$ resonances of the helix (these were defined analytically in Eq. (E.7) and plotted in Fig. 2.3, panel (a)). Schematically, we find

$$\mu^{(1)}_\omega \mu^{(2)}_\omega \sim \frac{b^2_\perp}{(\omega - \omega_{\text{res}})^2 + (\alpha\Gamma)^2}. \tag{2.39}$$

The instability is most pronounced when the two unperturbed energy levels are degenerate,

$$\epsilon^0_{i,\mathbf{k}} + \epsilon^0_{j,-\mathbf{k}} = \omega. \tag{2.40}$$

When this resonance condition is met, the eigenvalues of $M_{\text{res}}$ are given by

$$\lambda^\pm_{\text{res}} = \epsilon^0_{i,\mathbf{k}} - i\alpha\frac{\Gamma_1 + \Gamma_2}{2} \pm i\sqrt{\mu^{(1)}_\omega \mu^{(2)}_\omega + \alpha^2\left(\frac{\Gamma_1 - \Gamma_2}{2}\right)^2}. \tag{2.41}$$

Importantly, the sign of Im $\lambda^+_{\text{res}}$ changes when $b_\perp$ grows and the square root term becomes larger than $\alpha\frac{\Gamma_1 + \Gamma_2}{2}$. Assuming that $\Gamma_1 \sim \Gamma_2 \sim \Gamma$ the system is only stable if

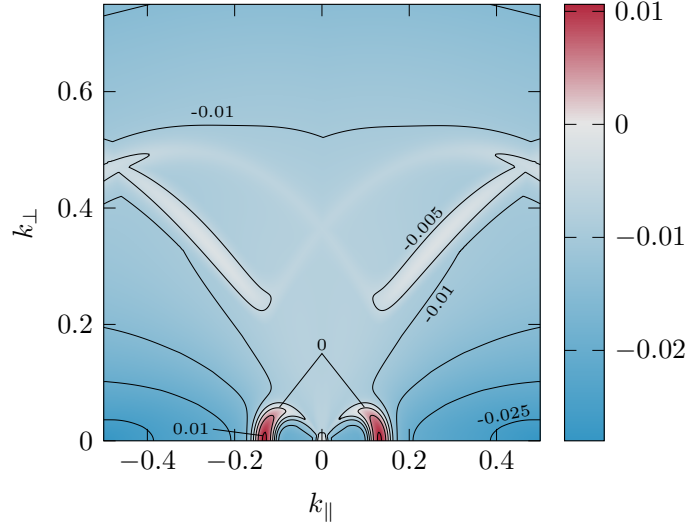$$b^2_\perp \lesssim \left((\omega - \omega_{\text{res}})^2 + (\alpha\Gamma)^2\right)\alpha^2\Gamma^2. \tag{2.42}$$

Figure 2.12 Largest Im $\lambda_\mathbf{k}$ plotted as a function of $\mathbf{k} = (k_\parallel, k_\perp)$ in the first Brillouin zone $-\frac{1}{2} < k_\parallel < \frac{1}{2}$, for $\omega = 2, b_x = 0.02, b_y = 0, \alpha = 0.03, c = 0.71, \delta = 1.76, N_x = N_y = N_z = 1/3$. The colour code works as follows: red when Im $\lambda_\mathbf{k} > 0$, white when Im $\lambda_\mathbf{k} = 0$ and blue when Im $\lambda_\mathbf{k} < 0$, indicating regions where the system is unstable, on the verge of becoming unstable and stable, respectively. The largest instability occurs for spin waves with $k_\perp = 0, k_\parallel = 0.13$, i.e. travelling parallel to the helical pitch $\mathbf{q}$.

More precisely, this formula is only valid for $\omega \approx \omega_{\text{res}}$. If one stays away from this point, then $\mu_\omega^{(i)} \sim b_\perp$ is independent of $\alpha$ and the system is only stable for

$$b_\perp \lesssim \alpha \text{ const.} \tag{2.43}$$

In the limit $\alpha \to 0$, our calculation predicts that an arbitrarily weak oscillating field induces an instability. This is, however, an artefact of our approximation, which ignores that the modes with finite energy and momentum can also decay via scattering processes. The lifetimes resulting from such processes would require an additional calculation, involving higher order magnon interactions.

The resonance condition Eq. (2.40) is met along curves in the 2D space, parametrised by $k_\parallel, k_\perp$. Therefore, we also need to investigate what happens to the spin waves with finite $k_\perp$ in the driven system. This is done in Fig. 2.12, where we plot max(Im $\lambda_\mathbf{k}$) as a function of $k_\parallel$ and $k_\perp$ with all other system parameters kept constant. We see that the dominant instability occurs at $k_\perp = 0$, with $k_\parallel = 0.13$. Thus, $k_\perp$ can safely beset to zero to determine the onset of the leading instability. We show the onset of this leading instability, as a function of the frequency and amplitude of the driving field, in Fig. 2.13. We see that as we increase the amplitude $b_x$ of the driving field, the first instabilities
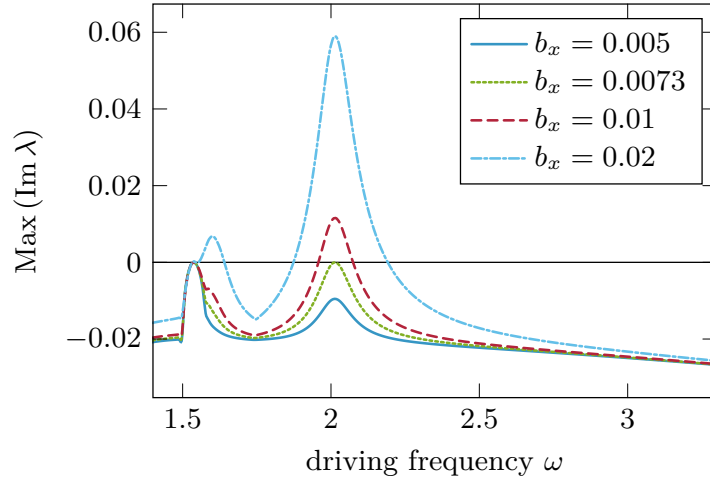
Figure 2.13 Largest $\text{Im}(\lambda_{\mathbf{k}})$ plotted as a function of driving frequency $\omega$, obtained by diagonalising $M^F$ at the momentum $\mathbf{k} = (k_{\parallel}, 0)$ of the leading instability, see Eq. (2.40) and Fig. 2.12. The parameters are $b_x = 0.02, b_y = 0, \alpha = 0.03, c = 0.71, \delta = 1.76, N_x = N_y = N_z = 1/3$ with a linearly $x$-polarised driving field ($b_y = 0$). At small driving field amplitude $b_x = 0.005$ the system is stable at all driving frequencies, $\max(\text{Im}(\lambda_{\mathbf{k}})) < 0$. At the critical field amplitude $b_{\text{crit}} = 0.0073$, $\max(\text{Im}(\lambda_{\mathbf{k}})) = 0$ at $\omega \approx 2$. For $b_x > b_{\text{crit}}$ $\max(\text{Im}(\lambda_{\mathbf{k}})) > 0$ and the system becomes unstable. The instabilities first occur around the resonance frequencies of the system, $\omega_-^{\text{res}} \approx 1.59, \omega_+^{\text{res}} \approx 2$ for these parameters.

appear at the two resonance frequencies of the system. This confirms the analysis in Eq. (2.42) and (2.43), which predicted that on-resonance the instability onset occurs at $b_{\perp} \sim \alpha^2$, whereas off-resonance it occurs at $b_{\perp} \sim \alpha \gg \alpha^2$, for $\alpha \ll 1$. A natural question to ask next is, at what frequency should we drive our system if we want to extract the maximum $\omega_{\text{screw}}$ while avoiding crossing over into the unstable regime? Surprisingly, our stability analysis suggests that ultimately, it doesn't really matter. Using Eq. (2.19), on-resonance $\max(\omega_{\text{screw}}) \sim \frac{b_{\text{crit}}^2}{\alpha^2} \sim \alpha^2$. Off-resonance, we have $\max(\omega_{\text{screw}}) \sim b_{\text{crit}}^2 \sim \alpha^2$. So, up to numerical factors, the maximum attainable, but still stable, $\omega_{\text{screw}}$ is *independent* of the driving frequency. However, the critical $b_{\text{crit}}$ to obtain this $\omega_{\text{screw}}$ is smaller by a factor $\alpha$ if we drive on-resonance, so that's perhaps the wiser choice if we want to save some energy :).

## 2.3.2 What is the Fate of the Unstable System?

While Floquet spin wave theory can predict the onset of the leading order instability in the driven system with great precision, it cannot tell us what fate awaits the unstable system. For that we need to run some numerics. Using our analytical results, we know that the leading instability occurs for $k_{\perp} = 0$, which means it is sufficient to simulate
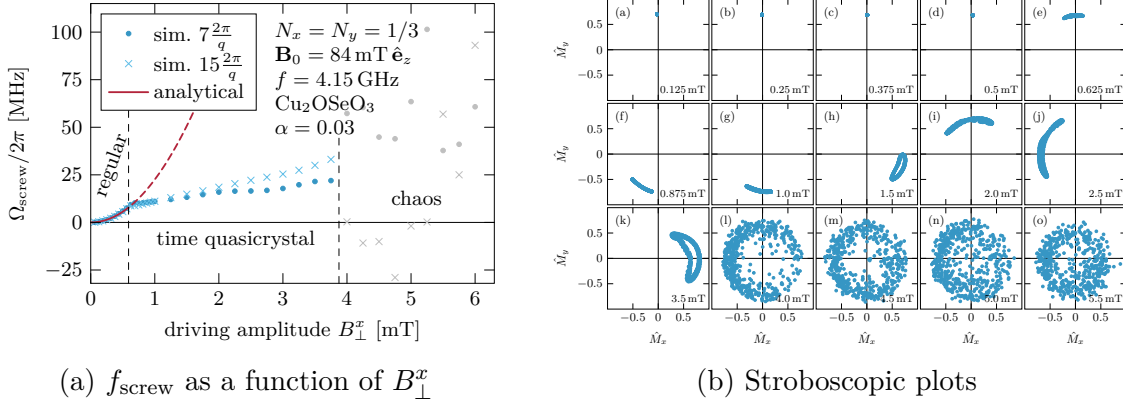
(a) $f_{\text{screw}}$ as a function of $B_\perp^x$

(b) Stroboscopic plots

Figure 2.14 (a) Rotational frequency $f_{\text{screw}}$ as a function of driving amplitude $B_\perp^x$ (in experimental units), for a system driven at $f = 4.15\,\text{GHz}$, with the other system parameters as in Fig. 2.5b. The simulation was run for two different system sizes: 7 and 15 times the pitch of the helix. For small amplitudes, $B_\perp^x < 0.56\text{mT}$, both systems host the Archimedean screw solution, where $f_{\text{screw}} \sim B_\perp^2$. At about $B_x^{\text{crit}} = 0.56 - 0.62\text{mT}$, a departure from this quadratic behaviour is observed as the system enters the quasicrystal phase and $f_{\text{screw}}$ becomes system size-dependent. The onset of the time quasicrystal regime happens later for the smaller system because the predicted wavelength of the instability, $\lambda \approx 7.7\lambda_{\text{helix}}$, doesn't fit into $7\lambda_{\text{helix}}$ as well as into $15\lambda_{\text{helix}}$. For still larger driving amplitude, $B_\perp^x = 3.8\,\text{mT}$, the system enters a chaotic regime. (b) $\hat{M}_x$ and $\hat{M}_y$ components of a single spin, recorded stroboscopically at times $t_n = 2\pi n/(\omega - \Omega_{\text{screw}})$, $n \in \mathbb{N}$, and rotated by $-\Omega_{\text{screw}} t_n$ to eliminate the screw rotation. Again we keep all parameters constant and vary only the external $B_\perp^x$ field, indicated in mT on each panel. Parameters are as in Fig. 2.14a, for the system of size $15\frac{2\pi}{q}$. (a)–(d) Archimedean screw regime, where within numerical precision we obtain a single point. (e)–(k) A closed orbit signals that we are in the time quasicrystal regime. (l)–(o) The onset of chaos manifests itself in aperiodic trajectories, covering a significant area of the configuration space. Close to the onset of chaos, panel (k), we also see signatures of higher order time quasicrystals, with extra oscillation frequencies. (Both figures were made by Lukas Heinen.)

a 1D[9] conical state propagating in the $z$ direction. We set up a numerical experiment where we drive two systems of 7 and 15 helix windings, respectively, with an increasingly strong driving field $B_\perp^x(t)$, while keeping the frequency $f =$4.15 GHz and all other system parameters constant. Fig. 2.14a and 2.14b are two different ways of visualising the results of this experiment. In Fig. 2.14a, we plot $f_{\text{screw}}$, the average slope in time of $\phi(t)$. In Fig. 2.14b, we extract a single spin from the system containing 15 windings and plot its projection onto the $xy$-plane at stroboscopic time intervals, $\Delta t = 2\pi/(\omega - \Omega_{\text{screw}})$, removing the rotational frequency $\omega_{\text{screw}}t$ to obtain neater plots. We see the emergence of three distinct regimes as the strength of the driving field, $B_\perp^x$, is increased, and will now proceed to describe each of these in detail.

### Archimedean Screw Regime

At small amplitudes of driving, $B_\perp^x \leq 0.56$mT, both the $7\lambda_{\text{helix}}$ and the $15\lambda_{\text{helix}}$ systems show exactly the same $f_{\text{screw}} \sim B_\perp^2$ behaviour, as expected for the Archimedean screw solution. In the stroboscopic plots, the signature of the Archimedean Screw is a single point, pannels (a)–(d).

### Time Quasicrystal Regime

For slightly larger driving amplitudes, $B_x^{\text{crit}} = 0.56 - 0.62$mT we see that $f_{\text{screw}}$ starts to shift away from quadratic dependence on $B_\perp^x$ and instead grows roughly linearly, $f_{\text{screw}} \sim B_\perp^x$, at a rate which is now system size *dependent*. For this set of parameters, Floquet spin wave theory predicts that $b_x^{\text{crit}} = 0.008$ or $B_x^{\text{crit}} =$0.59 mT in physical units, which fits right inside the range where we observe the change in behaviour of $f_{\text{screw}}$ in the numerics. Thus, there can be no doubt that the change in behaviour we are seeing in the numerics is connected to the Floquet instability predicted by the analytics. Looking back at Fig. 2.6a and 2.6b, the other indicator that we have entered a new regime is the emergence of a new mode with a new frequency of oscillation $f_{\text{new}} =$0.33 GHz and spatial momentum $\lambda_{\text{new}} = 7.7\lambda_{\text{helix}}$, or about $k_{\text{new}} = 0.13q$. In the stroboscopic plots, the single additional mode manifests itself as a closed orbit. There, the system takes an excursion in phase space, caused by the new incommensurate frequency of oscillation, $f_{\text{new}}$, before eventually returning to its initial position after a time $t = \frac{m}{f} = \frac{n}{f_{\text{new}}}$, $m, n \in \mathbb{Z}$. $\omega_{\text{new}}$ and $k_{\text{new}}$ correspond exactly to those of the unstable crossing $k = 0.13, \text{Re}\,\lambda = 0.16\omega$ in Fig. 2.11. The physical explanation for this new mode is that the magnetisation starts producing a cascade of magnons, all carrying the same unstable spatial momentum

---

[9]the reduction from 3D to 1D also has the very appreciable advantage of significantly reducing the computational costs associated with running the numerics!

and corresponding temporal frequency — a mechanism similar to lasers and Bose-Einstein condensates. The spatial and temporal frequencies of this magnon laser are incommensurate with the helical pitch $q$[10] and driving frequency $4.15\,\mathrm{GHz}$ of the system. In our driven system up until now time translational invariance was discrete, as we had a periodic driving term, but the introduction of an additional incommensurate frequency breaks this discrete symmetry. This broken symmetry motivates us to describe this intermediate phase as a time *quasi*crystal.

**Chaotic Regime**

At still stronger driving fields, beyond about $B_\perp^x = 3.95\,\mathrm{mT}$, $f_{\mathrm{screw}}$ loses its roughly linear dependence on $B_\perp^x$ and has no discernible pattern. In the stroboscopic plots this new phase manifests itself in the form of non-closing orbits, which cover most of the phase space when the simulations are run long enough. It should be mentioned that in this regime, the translational invariance in the $xy$-plane is lost, in contrast to the Archimedean screw and time quasicrystal phases. As a result, the dynamics also becomes dependent on $L_x, L_y$, the sample size in the $x$ and $y$ directions. Thus, the results for these larger amplitudes, beyond about $B_\perp^x \sim 3.95\,\mathrm{mT}$, are not as reliable and should be treated with a dose of scepticism.

## 2.4   Transport

In the last part of this chapter, we explore a practical application of the magnetic Archimedean screw as a tool for transport. In principle we could use our nano-screw to transport a range of nano-objects, including spin, charge and electrons. Here, we focus only on the transport of electrons, which leads to the generation of a DC electric current — for the simple reason that this quantity is easy to measure experimentally. We use the following Hamiltonian to model the electronic system,

$$
\begin{aligned}
H_{\mathrm{el}} &= H_{\mathrm{sys}} + H_{\mathrm{dis}}, \\
H_{\mathrm{sys}} &= \int d^3 r\, \mathbf{C}^\dagger(\mathbf{r}) \left( \frac{\hat{\mathbf{p}}^2}{2m} + \lambda_{\mathrm{SO}} \hat{\mathbf{p}} \cdot \sigma - J_H \mathbf{n}_{\mathrm{screw}}(\mathbf{r}, t) \cdot \sigma \right) \mathbf{C}(\mathbf{r}), \\
H_{\mathrm{dis}} &= \int d^3 r\, V(\mathbf{r}) \mathbf{C}^\dagger(\mathbf{r}) \mathbf{C}(\mathbf{r}),
\end{aligned}
\tag{2.44}
$$

---

[10]This, by the way is why one needs to pick the system size suitably in the numerical simulation in order to observe the time quasicrystal phase adequately. The total system size should simultaneously be as close as possible to an integer number of $\lambda_{\mathrm{helix}}$ and $\lambda_{\mathrm{new}}$ to see the biggest effect.
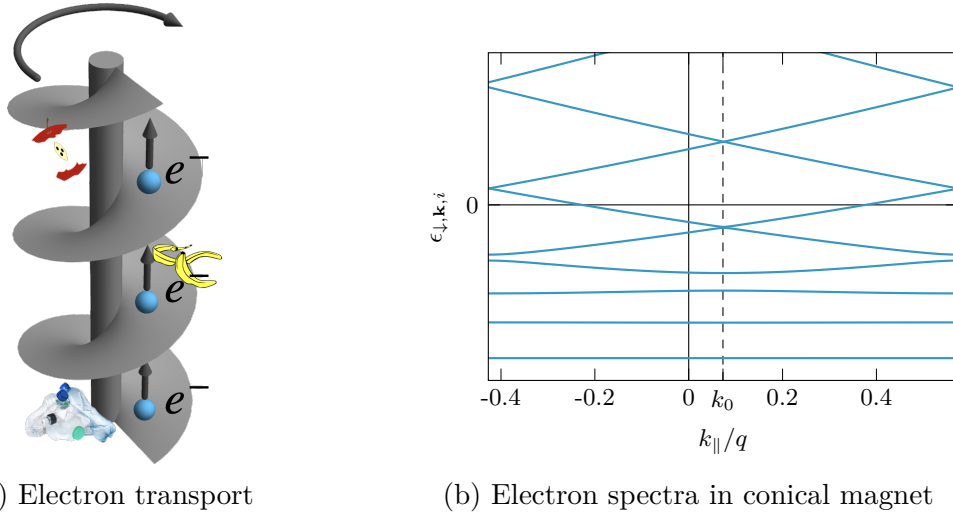
(a) Electron transport



(b) Electron spectra in conical magnet

Figure 2.15 (a) Transport of electrons by the magnetic Archimedean screw in the presence of disorder (artist's impression). (b) Band spectra of electrons in the co-moving frame (schematic). Only the majority electron bands are shown (the minority bands can be obtained by translating these spectra a distance $+2J_H$ vertically and reflecting them in the $k_\parallel = 0$ axis). The band spectra are symmetric about $k_0$, resulting in a shift of the first Brillouin zone to $-1/2 + k_0 < k_\parallel/q < 1/2 + k_0$. Finite $\lambda_{\mathrm{SO}}$ and $k_\perp$ are required to generate band gaps and mini-bands.

where $\mathbf{C}(\mathbf{r}) = (c_\uparrow(\mathbf{r}), c_\downarrow(\mathbf{r}))^T$ is a spinor containing the up and down components of the spin-$\frac{1}{2}$ electron annihilation operators. In addition to the kinetic energy $\frac{\hat{\mathbf{p}}^2}{2m}$, the electrons also experience a spin orbit interaction $\lambda_{\mathrm{SO}}\hat{\mathbf{p}} \cdot \sigma$, which tries to align the spin of the electron with its momentum. The electrons couple to the space and time dependent magnetisation through the exchange coupling $J_H \mathbf{n}_{\mathrm{screw}} \cdot \sigma$. Here $\mathbf{n}_{\mathrm{screw}}$ is the simplified Archimedean screw solution from Sec. 2.2.2,

$$\mathbf{n}_{\mathrm{screw}} = \begin{pmatrix} \sin(\theta_0)\cos(qz - \omega_{\mathrm{screw}}t) \\ \sin(\theta_0)\sin(qz - \omega_{\mathrm{screw}}t) \\ \cos(\theta_0) \end{pmatrix} \tag{2.45}$$

where we have suppressed the first order driving frequency oscillations because we want to concentrate solely on the effects of the rotational screw motion $\omega_{\mathrm{screw}}$. Finally, the disorder term $H_{\mathrm{dis}}$ captures the effects of dirt and other impurities in the system which slow the electrons down, resulting in a reduction of the net electronic current. We model $H_{\mathrm{dis}}$ as a spin-independent random potential $V(\mathbf{r})$, with a scattering rate $\frac{1}{\tau}$. We assume the hierarchy of energy scales $\epsilon_F > J_H \gg \frac{\hbar}{\tau}, \lambda_{\mathrm{SO}}\hbar k_F$, where $\epsilon_F, k_F$ are the Fermi

energy and velocity, respectively. This is typical for chiral magnets with weak spin orbit interactions.

**Electronic Current Density Operator**

Following [59] a generic spin-$\frac{1}{2}$ electron Hamiltonian takes the form

$$H = \int d^3 r \, \frac{1}{2m} \mathbf{C}^\dagger(\mathbf{r}) \left(-i\hbar \boldsymbol{\nabla} - e\mathbf{A}(\mathbf{r})\right)^2 \mathbf{C}(\mathbf{r}) + V_{\text{other}}, \qquad (2.46)$$

where $\mathbf{A}(\mathbf{r}) = A^i_{\sigma\sigma'}$ is a $2 \times 2$ matrix gauge-field and $V_{\text{other}}$ carries all the energy terms, which are independent of $\mathbf{A}$. The electronic current density operator, $\mathbf{j}$, is then given by

$$\mathbf{j}(\mathbf{r}) = -\frac{\delta H}{\delta \mathbf{A}} = \sum_{\sigma,\sigma'} -\frac{ie\hbar}{2m} \left(c_\sigma^\dagger(\mathbf{r})\boldsymbol{\nabla} c_\sigma(\mathbf{r}) - \boldsymbol{\nabla} c_\sigma^\dagger(\mathbf{r})c_\sigma(\mathbf{r})\right) - \frac{e^2}{m}c_\sigma^\dagger(\mathbf{r})\mathbf{A}_{\sigma\sigma'}c_{\sigma'}(\mathbf{r}). \quad (2.47)$$

For our specific $H_{\text{el}}$, defined in Eq. (2.44), $A^i = -\frac{\lambda_{\text{SO}}m}{e}\sigma^i$, where $\sigma^i$ with $i = x, y, z$ are the usual Pauli spin matrices. We are interested only in the $j_z$ component, which is parallel to the Archimedean screw,

$$j_z = -\frac{ie\hbar}{2m} \left(c_\uparrow^\dagger \partial_z c_\uparrow + c_\downarrow^\dagger \partial_z c_\downarrow - \partial_z c_\uparrow^\dagger c_\uparrow - \partial_z c_\downarrow^\dagger c_\downarrow\right) + e\lambda_{\text{SO}} \left(c_\uparrow^\dagger c_\uparrow - c_\downarrow^\dagger c_\downarrow\right). \qquad (2.48)$$

Using the Fourier convention $c_\sigma(\mathbf{r}) = \sum_{\sigma,\mathbf{k}} e^{-i\mathbf{k}\cdot\mathbf{r}} c_{\sigma,\mathbf{k}}, c_\sigma^\dagger(\mathbf{r}) = \sum_{\sigma,\mathbf{k}} e^{i\mathbf{k}\cdot\mathbf{r}} c_{\sigma,\mathbf{k}}^\dagger$, the total electronic current in the $z$ direction is

$$J_z = \int d^3 r \, j_z = \sum_{\mathbf{k}} -\frac{e\hbar k_z}{m} \left(c_{\uparrow,\mathbf{k}}^\dagger c_{\uparrow,\mathbf{k}} + c_{\downarrow,\mathbf{k}}^\dagger c_{\downarrow,\mathbf{k}}\right) + e\lambda_{\text{SO}} \left(c_{\uparrow,\mathbf{k}}^\dagger c_{\uparrow,\mathbf{k}} - c_{\downarrow,\mathbf{k}}^\dagger c_{\downarrow,\mathbf{k}}\right). \qquad (2.49)$$

The goal is to calculate the expectation value $\langle J_z \rangle$, where we average over quantum states and time, to obtain the DC current generated by our magnetic Archimedean screw.

**Electron Transport in the Clean System**

In a clean system, where $V(\mathbf{r}) = 0$, $\langle J_z \rangle$ is easiest to calculate in a frame which is co-moving with the Archimedean screw. In this co-moving frame, defined via $\mathbf{r}' = \mathbf{r} - v_{\text{screw}}t$, $H_{\text{el}}$ is time-independent. The band spectra for electrons in a static conical chiral magnet have been studied in the past in [60], where it was found that spin orbit coupling induces the formation of exponentially flat mini-bands with periodicity $q$. An alternative to the

method used in [60] is to define the rotated operators $\tilde{\mathbf{C}}^T = U^\dagger \mathbf{C}^T$

$$\begin{pmatrix} \tilde{c}_\uparrow(\mathbf{r}') \\ \tilde{c}_\downarrow(\mathbf{r}') \end{pmatrix} = \begin{pmatrix} \cos(\theta_0/2) & \sin(\theta_0/2)e^{-iqz'} \\ \sin(\theta_0/2)e^{iqz'} & -\cos(\theta_0/2) \end{pmatrix} \begin{pmatrix} c_\uparrow(\mathbf{r}') \\ c_\downarrow(\mathbf{r}') \end{pmatrix}, \tag{2.50}$$

$\tilde{c}_\uparrow^\dagger, \tilde{c}_\downarrow^\dagger$ create electrons whose spins align and anti-align with the local magnetisation — this can be checked by calculating $U^\dagger \mathbf{n}_{\text{screw}} \cdot \sigma U = \sigma^z$. As $J_H$ is the dominant energy scale, one can ignore spin non-conserving terms such as $\tilde{c}_{\uparrow,\mathbf{k}}^\dagger \tilde{c}_{\downarrow,\mathbf{k}}$. This leaves two types of terms: momentum-conserving diagonal terms, $\tilde{c}_{\sigma,\mathbf{k}}^\dagger \tilde{c}_{\sigma,\mathbf{k}}$, and momentum non-conserving terms, $\tilde{c}_{\sigma,\mathbf{k}}^\dagger \tilde{c}_{\sigma,\mathbf{k}\pm\mathbf{q}}$, which act as an off-diagonal perturbation,

$$H^{\text{cm}} \approx \sum_{\sigma,\mathbf{k}} \left[ \frac{\hbar^2}{2m} \left( \left(k_\parallel - \sigma k_0\right)^2 + k_\perp^2 \right) - \sigma J_H \right] \tilde{c}_{\sigma,\mathbf{k}}^\dagger \tilde{c}_{\sigma,\mathbf{k}} - \frac{1}{2}\lambda_{\text{SO}}\hbar k_\perp s(\tilde{c}_{\sigma,\mathbf{k}}^\dagger \tilde{c}_{\sigma,\mathbf{k}+\mathbf{q}} + \tilde{c}_{\sigma,\mathbf{k}}^\dagger \tilde{c}_{\sigma,\mathbf{k}-\mathbf{q}}),$$
$$k_0 = \frac{(1-c)q}{2} + \frac{cm\lambda_{\text{SO}}}{\hbar}, \tag{2.51}$$

where "cm" is shorthand for "co-moving frame". $H^{\text{cm}}$ can be diagonalised numerically to give

$$H^{\text{cm}} = \sum_{\sigma,\mathbf{k},i} \epsilon_{\sigma,\mathbf{k},i}\tilde{c}_{\sigma,\mathbf{k},i}^\dagger \tilde{c}_{\sigma,\mathbf{k},i}, \tag{2.52}$$

where $i$ denotes the index of the mini-band. In Fig. 2.15b, we plot $\epsilon_{\sigma,\mathbf{k},i}$ as a function of $k_\parallel$. The band energies $\epsilon_{\uparrow,\downarrow}$ are symmetric about the point $k_\parallel = \pm k_0, k_\perp = 0$ in momentum space. The expansion coefficients relating $\tilde{c}_{\sigma,\mathbf{k}}$ to $\tilde{c}_{\sigma,\mathbf{k},i}$ are encoded in the components of the eigenvectors of $H^{\text{cm}}$, which are also symmetric about $k_\parallel = \pm k_0, k_\perp = 0$. Notice how Eq. (2.51) has the same form as the static spin wave matrix discussed in Sec. 2.3.1. Reusing those previous results, we conclude that lowest bands becomes flat with a band gap $\Delta \sim \hbar q\sqrt{\lambda_{\text{SO}}\hbar k_\perp/m}$.

Rewriting Eq. (2.49) in terms of $\tilde{c}_\sigma, \tilde{c}_\sigma^\dagger$ gives

$$J_z^{\text{cm}} = -\frac{e\hbar}{m}\sum_{\mathbf{k}}(k_\parallel - k_0)\tilde{c}_{\uparrow,\mathbf{k}}^\dagger \tilde{c}_{\uparrow,\mathbf{k}} + (k_\parallel + k_0)\tilde{c}_{\downarrow,\mathbf{k}}^\dagger \tilde{c}_{\downarrow,\mathbf{k}}, \tag{2.53}$$

where we neglected terms such as $\tilde{c}_{\uparrow,\mathbf{k}}^\dagger \tilde{c}_{\downarrow,\mathbf{k}'}$, $\tilde{c}_{\downarrow,\mathbf{k}}^\dagger \tilde{c}_{\uparrow,\mathbf{k}'}$, $\mathbf{k} \neq \mathbf{k}'$, as they vanish once we average over the quantum eigenstates. Note that in contrast to the energy $\epsilon_{\sigma,\mathbf{k},i}$, the group velocity $v_k = (k_\parallel \mp k_0)$ is *anti*symmetric about $\pm k_0, 0$. The electronic quantum states get filled up starting from the lowest energy level, i.e. — symmetrically about $(\pm k_0, 0)$, until the Fermi energy $\epsilon_F$ is reached. This means that overall, the total current vanishes, $\langle J_z^{\text{cm}} \rangle = 0$, as there are equal amounts of electrons going in the negative and
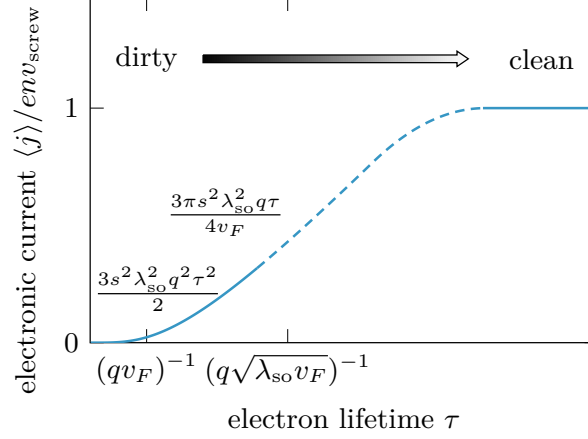
Figure 2.16 Electronic current density $\langle j_z \rangle$ as a function of electron lifetime $\tau$ (schematic). We have suppressed the spin indices, which is justified for a strongly spin polarised system $N_\uparrow \gg N_\downarrow$. For a strongly disordered system, $\tau \ll (qv_F)^{-1}$, $\langle j_\parallel \rangle = \frac{3s^2\lambda_{\mathrm{so}}^2 q^2\tau^2}{2}$ is quadratic in $\tau$. In the range $(qv_F)^{-1} \ll \tau \ll (q\sqrt{v_F})^{-1}$, $\langle j_\parallel \rangle$ grows linearly with $\tau$. Our perturbative assumptions $\lambda_{\mathrm{SO}}$ break down in the dashed region, but we know that for a very clean system with no disorder, $\tau \gg 1$, the current must plateau at $\langle j_z \rangle = env_{\mathrm{screw}}$.

positive $z$ directions. A zero net current in the co-moving frame means that we must have a finite net current back in the laboratory frame. By simple Galileo transformation, the current density in the lab frame must be

$$\langle j_z^{\mathrm{clean}} \rangle = ev_{\mathrm{screw}}(n_\uparrow + n_\downarrow). \tag{2.54}$$

**Electron Transport in the Dirty System**

In reality, disorder is always present to some extent and is actually expected to dominate electronic transport properties. If $V(r) \neq 0$, we can no longer use the same Galileo transformation trick, as the impurities move in the co-moving system. Any transformation we perform must therefore have two properties: i) the impurities remain stationary and ii) the dominant energy scale $J_H$ ends up on the diagonal of the Hamiltonian. The way to achieve this is by a local time-dependent rotation of the electron creation and annihilation operators,

$$\begin{pmatrix} d_\uparrow(\mathbf{r}) \\ d_\downarrow(\mathbf{r}) \end{pmatrix} = \begin{pmatrix} \cos(\theta_0/2) & \sin(\theta_0/2)e^{-i(qz-\omega_{\mathrm{screw}}t)} \\ \sin(\theta_0/2)e^{i(qz-\omega_{\mathrm{screw}}t)} & -\cos(\theta_0/2) \end{pmatrix} \begin{pmatrix} c_\uparrow(\mathbf{r}) \\ c_\downarrow(\mathbf{r}) \end{pmatrix}, \tag{2.55}$$

which (anti)aligns the spin axis of the electrons with the local time-dependent magnetisation $\mathbf{n}_{\mathrm{screw}}$. Importantly, under this transformation we *remain* in the laboratory frame.

In terms of the new $d_\sigma^\dagger, d_\sigma$ operators, $H_{\text{el}}$ reads

$$H_{\text{el}} \approx \sum_{\sigma,\mathbf{k}} \epsilon_{\sigma,\mathbf{k}} d_{\sigma,\mathbf{k}}^\dagger d_{\sigma,\mathbf{k}} + H_1(t) + H_{\text{dis}} \tag{2.56}$$

$$H_1(t) = \sum_{\sigma,\mathbf{k}} \frac{\hbar s k_\perp \lambda_{\text{so}}}{2} (d_{\sigma,\mathbf{k}}^\dagger d_{\sigma,\mathbf{k+q}} e^{-i\omega_{\text{screw}}t} + h.c.) \tag{2.57}$$

$$\epsilon_{\uparrow/\downarrow,\mathbf{k}} \approx \frac{\hbar^2}{2m} \left( (k_\parallel \mp k_0)^2 + k_\perp^2 \right) \mp J_H$$

$$k_0 = \frac{(1-c)q}{2} + \frac{cm\lambda_{\text{so}}}{\hbar}, s = \sin(\theta_0), c = \cos(\theta_0). \tag{2.58}$$

Here we ignored some small static correction terms to $\epsilon_{\sigma,\mathbf{k}}$, as well as spin-mixing terms of type $d_\uparrow^\dagger d_\downarrow$, due to the large separation between the energy levels of majority and minority electrons. Importantly, the unitary transformation does not affect the disorder term $H_{\text{dis}}$.

While the transformations we did for the clean case resulted in a purely static Hamiltonian, the transformation Eq. (2.55) does not remove the explicit time dependence, instead transferring it from the exchange coupling term to the spin-orbit terms in $H_1(t)$. This is the price we pay for keeping the impurities static.

The terms in the current operator relevant to our calculation are identical in form to Eq. (2.53),

$$J_z = -\frac{e\hbar}{m} \sum_{\mathbf{k}} (k_\parallel - k_0) d_{\uparrow,\mathbf{k}}^\dagger d_{\uparrow,\mathbf{k}} + (k_\parallel + k_0) d_{\downarrow,\mathbf{k}}^\dagger d_{\downarrow,\mathbf{k}}. \tag{2.59}$$

We want to calculate the expectation value of this current operator, treating $H_1(t)$ as a small perturbation. This can be formulated as a Keldysh problem [61],

$$\langle J_z(t) \rangle = \left\langle U(-\infty,+\infty)T\left(U(-\infty,+\infty)\tilde{J}_z(t)\right)\right\rangle, \tag{2.60}$$

where the time evolution operator $U(t_2,t_1) = e^{-i\int_{t_1}^{t_2}\tilde{H}_1(t')dt'}$ evolves a quantum state from time $t_1$ to time $t_2$. Note also that we are working in the interaction picture, where operators also carry some time-dependence via $\tilde{O} = e^{iH_0 t}Oe^{-iH_0 t}$. After a fairly long calculation, the details of which are given in App. G, one arrives at

$$\langle J_z \rangle = \frac{2\lambda_{\text{so}}^2 s^2 e\hbar^4 q v_{\text{screw}}}{m} \sum_{\sigma,\mathbf{k}} \frac{k_\perp^2 (k_\parallel - \sigma k_0)(n_{\sigma,\mathbf{k}} - n_{\sigma,\mathbf{k+q}})(\epsilon_{\sigma,\mathbf{k}} - \epsilon_{\sigma,\mathbf{k+q}})}{\left((\epsilon_{\sigma,\mathbf{k+q}} - \epsilon_{\sigma,\mathbf{k}})^2 + (\hbar\tau^{-1})^2\right)^2}, \tag{2.61}$$

where we have used that $\omega_{\text{screw}} = qv_{\text{screw}}$. Here, $n_{\sigma,\mathbf{k}}$ is the Fermi distribution function, $(1 + e^{\beta(\epsilon_{\sigma,\mathbf{k}} - \epsilon_{\sigma,k_F})})^{-1}$. Performing the integral in $k$ space at $T = 0$ amounts to integrating

over the previously described two Fermi spheres located at $\pm k_0$. We obtain

$$\langle j_z \rangle \approx \sum_{\sigma=\uparrow,\downarrow} e n_\sigma v_{\text{screw}} \begin{cases} \frac{3s^2\lambda_{\text{so}}^2 q^2 \tau^2}{2} \ , \ v_{F,\sigma}\tau \ll \frac{2\pi}{q} \\ \frac{3\pi s^2 \lambda_{\text{so}}^2 q\tau}{4v_{F,\sigma}} \ , \ \frac{2\pi}{q} \ll \ v_{F,\sigma}\tau \ll \frac{\sqrt{v_{F,\sigma}}}{q\sqrt{\lambda_{\text{so}}}}. \end{cases} \tag{2.62}$$

In the limit when the mean free path of the electrons is smaller than the wavelength of the helix, $v_F\tau \ll \frac{2\pi}{q}$, the current is quadratically dependent on the electron's lifetime $\tau$. In the opposite limit, $v_F\tau \gg 2\pi/q$, in contrast, the current is linear in $\tau$ and thus proportional to the conductivity of the system. Eq. (2.62) has been derived in perturbation theory in $\lambda_{\text{so}}$ — therefore it cannot describe the formation of band-gaps and mini-bands triggered by $\lambda_{\text{so}}$. These mini-bands have a band splitting of the order of $\Delta \sim \hbar q \sqrt{v_F \lambda_{\text{so}}}$, thus perturbation theory is only reliable for $\tau\Delta/\hbar \ll 1$, which sets an upper limit for the regime of validity of the second line in Eq. (2.62). We summarize these results pictorially in Fig. 2.16.

**Current Estimate for a Real Material**

We can use the calculation we did in the previous section to estimate the electronic current density induced by a rotating Archimedean screw in MnSi, arguably the best investigated metallic chiral magnet. At the end of Sec. 2.2.2 we estimated $v_{\text{screw}} \sim 200\,\text{mm}\,\text{s}^{-1}$ for a resonantly driven conical system. An estimate of $\lambda_{\text{SO}}$ can be obtained by looking at the band-splitting in the electronic spectra: in CoGe this band-splitting is on the order of 10% of the bandwidth [62], with similar values expected for MnSi. Thus we can assume $\lambda_{\text{so}}/v_F \sim 10^{-2} - 10^{-1}$. MnSi can be grown with exceptional crystal quality, with residual resistivities well below $1\,\mu\Omega\,\text{cm}$, resulting in mean free paths up to $1000\,\text{Å}$ at low $T$ [63]. Assuming a mean free path of the order of the pitch of the helix, $\lambda_{\text{helix}} = 200\,\text{Å}$, and using $n \sim 4 \cdot 10^{22}\,\text{cm}^{-3}$ [64], our calculation predicts current densities of order $10^4 - 10^7\,\text{A}\,\text{m}^{-2}$. The voltage build-up caused by values even on the smaller end of this range should be very easy to detect in an experiment.

# 3

# Driven Skyrmions

Skyrmions are undoubtedly the cool kids of the chiral magnet phase diagram. They boast a range of qualities such as robustness, mobility and easy manipulability by external forces, which make them particularly attractive for potential technological applications. In this chapter, we study how a single skyrmion responds to a homogeneous external magnetic field $\mathbf{B}_1(t) = (\mathbf{B}_\perp(t), \mathbf{B}_z(t))^T$, oscillating in the GHz range. With the help of the shooting method, we solve semi-analytically for the first order damped oscillatory response. Compared to the Archimedean screw, this is technically much trickier to implement because, due to its non-trivial Fourier decomposition, a skyrmion has infinitely many scattering modes, where the conical state has only two: $+q$ and $-q$. The skyrmion bound states and the ferromagnetic resonance coming from the background require additional careful treatment. At second order, a constant force $\propto B_z B_\perp$ appears on the RHS of the Thiele equation for the skyrmion, activating the two translational Goldstone modes so that the skyrmion starts to "sliding" at constant velocity $\mathbf{v}_{\text{slide}} = (v_x, v_y)^T$. $\mathbf{v}_{\text{slide}}$ can be computed exactly from the semi-analytical first order response, and we observe an excellent fit with results obtained from numerical simulations.

## 3.1 Background and Setup

Many mechanisms have already been proposed and, in some cases, even investigated experimentally, to manipulate skyrmions. These include, but are not limited to: placing skyrmions in magnetic field [65] or temperature [66, 67] gradients, subjecting them to external electric fields [68], electric currents or spin currents [69, 70], and even firing magnons onto skyrmions to excite their internal modes [71, 72]. However, as you might have noticed, in this thesis we are primarily interested in driving stuff with oscillating magnetic fields, and driving skyrmions in this way is the natural extension of the work we already did for the Archimedean screw. Of course, owing to their popularity, we are not the first to consider driving skyrmions with oscillating magnetic fields, and a number of publications on the topic deserve to be mentioned here. In [73], the authors studied the dynamics of single skyrmion subjected to a small constant in-plane field, $B_x$, and a weak out-of-plane field $B_z(t)$, oscillating in the GHz regime. They observed a linear in time motion of the centre of the skyrmion, $\mathbf{r}_{\text{skyr.}} = \mathbf{v}t$. In [74], my colleague Bernd Grosse Jütterman investigated two further similar setups, placing a single skyrmion placed near a wall in the first setup and near another skyrmion in the second one, before driving the system with a purely out-of-plane oscillating field $B_z(t)$. In the first setup, this again resulted in the skyrmion moving at net constant velocity, $\mathbf{v}$, while in second the two skyrmions started "dancing" around each other, but did not experience any net linear motion. It turns out that the linear motion is only achievable if one breaks certain specific symmetries in the system. In the first case of the tilted static magnetic field it is actually a combination of two separate symmetries — time translation by half a driving period followed by a rotation around the $\mathbf{e}_z$ axis by $\pi$ — that gets broken. For the systems where the skyrmion is placed near a wall or near another skyrmion the translational symmetry is broken. However the combined symmetry of time translation and rotation around the $\mathbf{e}_z$ is still there in the system with two skyrmions, which explains why there is no net linear motion. Another interesting idea is to break the time translation symmetry sufficiently strongly by using biharmonic in-plane driving fields, $B_x = \sin(m\omega t) + \sin(n\omega t), n + m \in \text{odd}\,\mathbb{Z}$, as done in [75]. There, they applied this type of asymmetrical driving to a skyrmion placed both in the bulk and at the edge of a sample. The only problem with this approach is that the resulting speeds are very small in the bulk if one uses weak driving fields — at least three powers of $b_1$ for the smallest allowed values ($n = 1, m = 2$) would be required to obtain a DC response from the magnetisation. Nevertheless, the authors report that the skyrmion accelerates dramatically near the edge, with the speed increasing about tenfold as a consequence of the strong repulsive force coming from the edge. Other creative setups could probably

be found, but our aim will be instead to get a detailed analytical understanding of the phenomenon, instead of trying to play the "break enough symmetries and it starts to move" numerical game. To this end, we want to use the simplest possible setup such that enough symmetries are broken but the problem is still analytically tractable. It turns out that placing a skyrmion in the bulk and subjecting it to an external magnetic field

$$\mathbf{B}^{\text{ext}} = \mathbf{B}_0 + \epsilon \mathbf{B}_1(t), \quad \mathbf{B}_0 = \begin{pmatrix} 0 \\ 0 \\ B_0 \end{pmatrix}, \mathbf{B}_1(t) = \begin{pmatrix} B_x \cos(\omega t) \\ B_y \sin(\omega t) \\ B_z \cos(\omega t + \delta) \end{pmatrix}, \quad (3.1)$$

fulfils both of these conditions. In the above equation, $\epsilon$ is the same book-keeping parameter we introduced for the Archimedean screw calculation in Chapter 2. $\delta$ is a parameter which changes the relative phase between the out-of-plane and in-plane driving field components, which allows us to control the angle at which the skyrmion moves, as we shall later see. Actually, this setup has already been investigated purely numerically in [76], but their results are confusing and seem to differ from ours. Also, the fully analytical treatment we provide is novel. With all that said, let us roll up our sleeves and get our hands dirty with some concrete calculations.

## 3.2   Static Skyrmion

The first thing we need to do is to get more familiar with the static skyrmion solution (oscillating field $\mathbf{B}_1(t)$ turned off). This is already well known in the literature, but for completeness we show how to do it here too, as all the analysis that follows also depends on it. Substituting the skyrmion parametrisation, Eq. (1.15) with $h = \frac{\pi}{2}$[1], into the chiral magnet free energy, Eq. (1.3), one obtains the energy of the skyrmion

$$\epsilon_{\text{skyrmion}} = \iint dr\, d\chi\, r \left( \frac{\sin^2(\theta_0) + r^2 \theta_0'^2}{2r^2} + \frac{1}{2r} \sin(2\theta_0) + \theta_0' - b_0 \left( \cos(\theta_0) - 1 \right) \right), \quad (3.2)$$

where for simplicity we ignored dipolar interactions and switched to the reduced quantities $r, b_i$, following the convention introduced in Chapter 2. In eq. (3.2), we also subtracted off the energy $\iint r\, dr\, d\chi\, b_0$, corresponding to a ferromagnetic system with no skyrmion. Thus, $\epsilon_{\text{skyrmion}}$ actually represents the energy that the skyrmion adds or subtracts from the ferromagnetic background. If $\epsilon_{\text{skyrmion}}$ is positive, the skyrmion is considered to

---

[1]For the free energy in Eq. (1.3) with the bulk DMI, $D\hat{\mathbf{M}} \cdot \boldsymbol{\nabla} \times \hat{\mathbf{M}}$, one must use the Bloch skyrmion, $h = \frac{\pi}{2}$. The Néel skyrmion, $h = 0$, requires a slightly different DMI energy term, $D(\hat{M}_z \boldsymbol{\nabla} \cdot \hat{\mathbf{M}} - \hat{\mathbf{M}} \cdot \boldsymbol{\nabla} \hat{M}_z)$, known as interfacial DMI. The resulting energy Eq. (3.2) is however identical in both cases.

be a stable excitation, as it is energetically unfavourable for more skyrmions to form. However if it is negative, the system is unstable towards the creation of more skyrmions, which leads to the formation of a skyrmion lattice. This is something we do *not* want in the present setup, as we are interested in driving a single skyrmion rather than a skyrmion lattice[2]. By using the Euler-Lagrange equations $\frac{\partial L}{\partial \theta_0} = \frac{1}{r} \frac{d}{dr} \left( r \frac{\partial L}{\partial \theta_0'} \right)$, where $L$ is the integrand of Eq. (3.2), one obtains a differential equation for the skyrmion profile angle $\theta_0$,

$$r^2 \theta_0'' + r \theta_0' - \sin(\theta_0) \left( b_0 r^2 - 2r \sin(\theta_0) + \cos(\theta_0) \right) = 0, \tag{3.3}$$

with boundary conditions $\theta(0) = \pi$ and $\theta(\infty) = 0$. Eq. (3.3) is a non-linear second order differential equation with no known analytical solution, but it can be solved numerically using the shooting method. The idea of the shooting method is very simple: one numerically solves the differential equation, varying the boundary condition $\theta'(0)$ (the other boundary condition $\theta(0) = \pi$ is already fixed) until the other boundary condition, $\lim_{r \gg r_0} \theta_0 = 0$, is reached with sufficient accuracy[3]. Fig. 3.1a shows the resulting skyrmion profiles $\theta_0(r)$ for a few different values of $b_0$. In Fig. 3.1b we show the energy of the skyrmion as a function of $b_0$, obtained by substituting the numerical solution $\theta_0$ back into Eq. (3.2) and numerically integrating. As the external field $b_0$ increases, it becomes more and more energetically unfavourable for the skyrmion to form, so its size decreases. The most important thing to note is that at $b_0 \approx 0.8$, $\epsilon_{\text{skyrmion}}$ switches sign. As we are interested in the regime where the single skyrmion is stable, $\epsilon_{\text{skyrmion}} > 0$, we conclude that we need a minimum static background field, $b_0 \geq 0.8$. For simplicity, we pick $b_0 = 1$ for all the calculations that follow.

## 3.3   Damped Eigenbasis

In Chapter 2, we saw that a spatially homogeneous, time-oscillating magnetic field excites the two internal $k = 0$ modes (also known as $\pm q$ in the literature [44]) of the conical state. Naturally, we can expect that driving a single skyrmion with the same spatially homogeneous driving field will excite its internal modes in similar fashion. The trouble is that the skyrmion is a very non-trivial object compared to the conical state. Unlike the

---

[2]driving a skyrmion lattice with an oscillating field is also an interesting problem. As we speak, calculations aiming to calculate the rotational torque exerted on the SkX lattice as a consequence of such driving are being done in the Rosch group.

[3]In technical terms, the shooting method reduces an insoluble problem with boundary conditions at two different points, $\theta_0(r = 0)$ and $\theta_0(r = \infty)$, into an easier problem where the two boundary conditions are at the same point, $\theta_0(r = 0)$ and $\theta_0'(r = 0)$. In a nutshell, we "shoot" for a solution from the origin $r = 0$ by varying $\theta'(0)$ until the other boundary condition, $\theta(r \gg 0) = 0$, is satisfied.
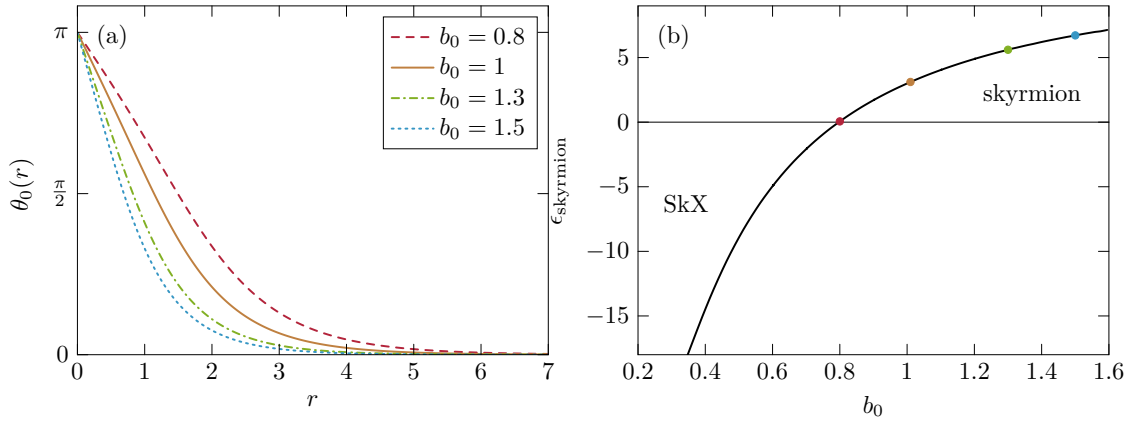
Figure 3.1 (a) Skyrmion angle $\theta_0(r)$ as a function of radius $r$, for static fields $b_0 = 0.8, 1, 1.3, 1.5$, obtained using the shooting method. As $b_0$ increases the radius of the skyrmion decreases. (b) Energy of a single skyrmion as a function of the exernal static field $b_0$. The skyrmion is only stable for $b_0 \gtrsim 0.8$, as below this value of $b_0$ its energy is negative and it becomes energetically favourable for the system to form a skyrmion lattice.

conical state, which has a neat Fourier spatial decomposition carrying only two momenta $\pm q$, see Eq. (1.14), in the case of the skyrmion we do not even know the analytical form of its profile $\theta_0(r)$! This forces us to stick to real space for our analysis, which on the technical level will translate into a lot of overlap integrals in the 2D plane.

Fortunately for us, some of the path has already been paved, in the sense that work has already been done to identify the eigenmodes of a skyrmion. In [71], the eigenspectrum were evaluated numerically, while [72] presents a very useful semi-analytical approach for calculating the eigenspectrum and eigenmodes of the undamped system. As damping is present in our problem, we need to extend these analyses to allow for a finite $\alpha$ damping contribution to the eigenefrequencies and eigenmodes. In [71], they touched upon the correction due to damping to the scattering mode eigenfrequencies, but this is insufficient for our purposes, as we also need to correct the scattering eigenmodes, as well as the bound state eigenenergies and eigenmodes, for finite damping. To incorporate damping, we will resort to perturbation theory, correct in the small damping limit, $\alpha \ll 1$. Luckily, the low damping limit also happens to be the experimentally relevant limit in many systems.

So how do we actually go about obtaining the eigenmodes and corresponding eigen-frequencies of the skyrmion? One way is to reuse the spin wave formalism we developed in Sec. 2.3.1, where we expanded around the dynamic Archimedean screw solution, $\hat{\mathbf{M}}_{\text{screw}}(\mathbf{r}, t)$, in small excitations $a, a^*$ and then solved for the energy spectra of these

excitations. To adapt it to the present problem, we expand instead around the static skyrmion, $\hat{\mathbf{M}}_{\text{skyrmion}}(r, \chi)$, in $a, a^*$, and use polar coordinates, as they are more suited to the symmetry of the problem. To obtain the eigenmodes of the system, we switch off the driving field, $\mathbf{b}_1(t) = 0$. In this case the free energy $F$ is to lowest order quadratic in $a, a^*$, and the equation of motion reads

$$(\text{sgn}(\gamma) + i\alpha\sigma^z)\begin{pmatrix} \dot{a} \\ \dot{a}^* \end{pmatrix} = i\begin{pmatrix} \{F_{\text{skyr.}}^{(2)}, a\} \\ \{F_{\text{skyr.}}^{(2)}, a^*\} \end{pmatrix} + \mathcal{O}(a^2), \tag{3.4}$$

where $F_{\text{skyr.}}^{(2)}$ depends on both $r$ and $\chi$, see Eq. (H.2) for its detailed form. The $\chi$ dependence can be removed by switching to angular momentum eigenstates $a_m(r) = \frac{1}{2\pi}\int d\chi\, e^{-im\chi}a(r, \chi)$, $a_m^*(r) = \frac{1}{2\pi}\int d\chi\, e^{im\chi}a^*(r, \chi)$, see App H.2 for technical details. The resulting $r$- and $t$-dependent equation can be reduced to a time-independent eigenvalue equation by choosing the ansatz $(a_m(t), a_{-m}(t))^T = e^{-iEt}(a_m(0), a_{-m}(0))^T$, giving

$$(\text{sgn}(\gamma) + i\alpha\sigma^z)E_{m,n,\alpha}\,|m, n, \alpha\rangle = \sigma^z H_m\,|m, n, \alpha\rangle, \tag{3.5}$$

where we defined the vector $|m, n, \alpha\rangle = (a_m(0), a_{-m}(0))^T$. Here, $m$ is the angular momentum number, and shall see in Sec. 3.4.1 that only the $m = 0, \pm1$ eigenmodes can be activated by a spatially homogeneous driving field. $n$ is a further label to parametrise the energy $E_{m,n,\alpha}$ — this is necessary to distinguish between the different bound and scattering states within each $m$-sector. The label $\alpha$ has been included to remind us that the eigenmode is damped. Beneath all the fancy QM-inspired notation, Eq. (3.5) is "just" a non-linear second order differential equation in $r$, which we need to solve for different $m$ and $n$, while treating $\alpha$ as a perturbative parameter. Before proceeding with this, it's worth pointing out an important property of the eigensystem of Eq. (3.5). As can easily be checked from its definition, Eq. (H.8), $H_m = \sigma^x H_{-m}\sigma^x$ and $H_m = H_m^*$. Supposing we know an eigenstate $|m, n, \alpha\rangle$ with eigenenergy $E_{n,\alpha}$, we can apply this property to give

$$(\text{sgn}(\gamma) + i\alpha\sigma_z)(-E_{n,\alpha}^*)\sigma^x\,|m, n, \alpha\rangle^* = \sigma^z H_{-m}\sigma^x\,|m, n, \alpha\rangle^*, \tag{3.6}$$

which means that $\sigma^x\,|m, n, \alpha\rangle^*$ is also an eigenstate of $H_{-m}$, with eigenenergy $-E_{n,\alpha}^*$. This is a useful property which saves us doing half the work in the long run. The idea now is to solve eq. (3.5) perturbatively in $\alpha$, using the perturbative expansions

$$\begin{aligned} |m, n, \alpha\rangle &= \left|m, n^{(0)}\right\rangle + i\alpha\,\text{sgn}(\gamma)\left|m, n^{(1)}\right\rangle + \mathcal{O}(\alpha^2), \\ E_{n,\alpha} &= \text{sgn}(\gamma)\epsilon_n^{(0)} - i\alpha\epsilon_n^{(1)} + \mathcal{O}(\alpha^2). \end{aligned} \tag{3.7}$$

### 3.3.1 Zeroth Order in $\alpha$

At order $\mathcal{O}(\alpha^0)$, Eq. (3.5) reads

$$\epsilon_n^{(0)} \left| m, n^{(0)} \right\rangle = \sigma^z H_m \left| m, n^{(0)} \right\rangle. \tag{3.8}$$

This eigenvalue equation is not Hermitian, but its eigenvalues and eigenvectors still obey some useful mathematical properties. For example, the eigenvectors still form an orthogonal eigenbasis, provided we modify the definition of the inner product between eigenvectors. We can find out these properties by taking the conjugate transpose of Eq. (3.8) and projecting it onto $|m, n, 1\rangle^{(0)}$ and integrating this over all 2D space[4], giving

$$\epsilon_{n,1}^{(0)*} \left\langle m, n, 1^{(0)} \right| = \left\langle m, n, 1^{(0)} \right| H_m \sigma^z$$
$$\implies \epsilon_{n,1}^{(0)*} \left\langle m, n, 1^{(0)} \right| \sigma^z \left| m, n, 1^{(0)} \right\rangle = \epsilon_{n,1}^{(0)} \left\langle m, n, 1^{(0)} \right| \sigma^z \left| m, n, 1^{(0)} \right\rangle,$$

where we used the hermiticity of $H_m$, $H_m^\dagger = H_m$. The second line implies that $\epsilon_{n,1}^{(0)}$ is real. The same argument can be used to show that eigenstates with different eigenvalues are orthogonal, if we redefine the inner product to be $\langle m, n | \sigma^z | m', n' \rangle$. The zeroth order eigenstates therefore form an orthogonal eigenbasis,

$$\left\langle m, n, s \right| \sigma^z \left| m', n', s' \right\rangle = N \delta_{m,m'} \delta_{n,n'} \delta_{s,s'}, \tag{3.9}$$

where $N$ is a normalisation factor we can freely choose.

Let us now inspect in more detail the kind of eigenmodes and eigenenergies admitted by Eq. (3.8). Two types of modes exist — bound and scattering — which we now discuss in short succession. We base ourselves strongly on the formalism developed in [72].

**Bound Modes**

Bound modes are characterised by eigenenergies $\epsilon_{\text{bound}}^{(0)}$ which are *smaller* than the gap energy of the bulk ferromagnet surrounding the skyrmion, $\epsilon_{\text{bound}}^{(0)} < \epsilon_{\text{gap}} = b_0$. As these energies are forbidden in the bulk, the bound states are "bound" to the region of the skyrmion. Just like for the famous particle-in-a-box quantum mechanics problem, bound states are quantised. In the $m = 0$ sector, there is a single bound state, known as the breathing mode, $\left| m = 0, \text{br}, +^{(0)} \right\rangle$, with energy $+\epsilon_{\text{br.}}^{(0)}$. As we have already explained, this physical eigenstate will also have an unphysical copy, given by $\left| m = 0, \text{br.}, -^{(0)} \right\rangle = \sigma^x \left| m = 0, \text{br}, +^{(0)} \right\rangle$, with negative energy $-\epsilon_{\text{br.}}^{(0)}$. $\left| m = 0, \text{br.}, -^{(0)} \right\rangle$, as well as all the

---

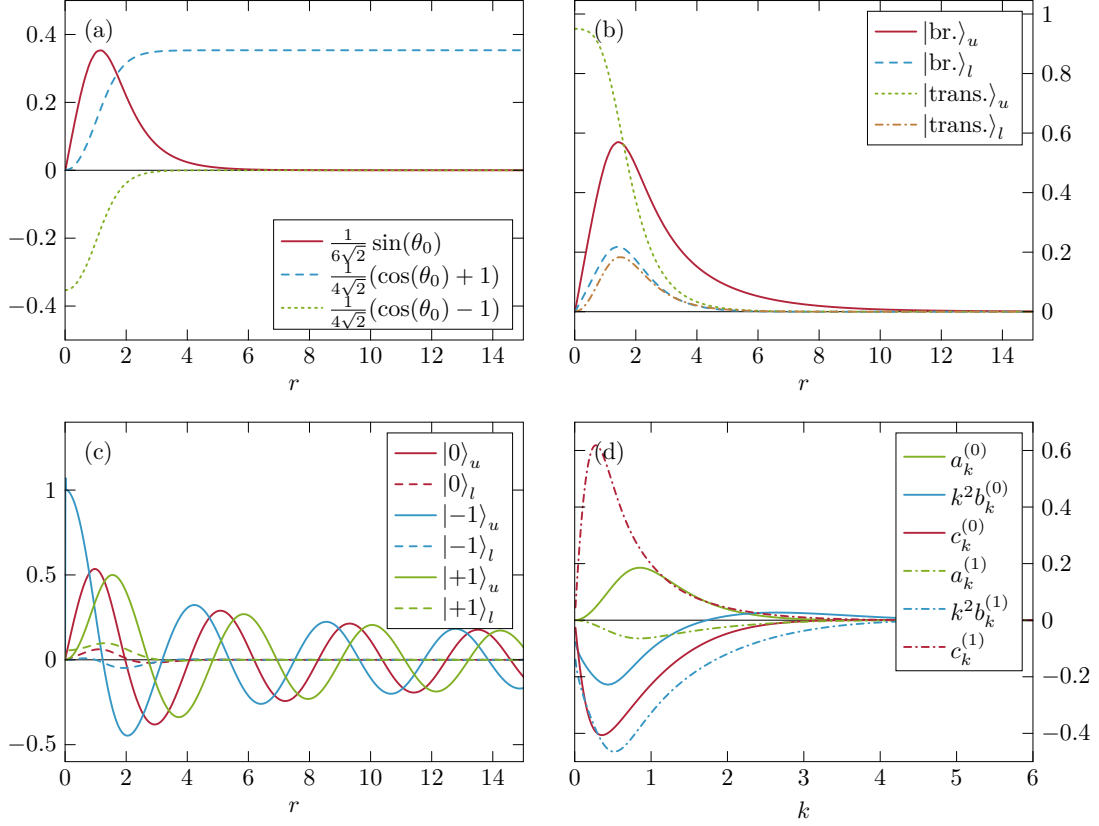[4]defined here in polar coordinates, i.e. $\langle ... \rangle = \iint ... r \, dr \, d\chi$.

Figure 3.2 (a) Spatial profile of magnetic drive. Out-of-plane driving profile is $\frac{b_z}{2\sqrt{2}}\sin(\theta_0)$. In-plane driving has two different contributions, $\frac{b_{L/R}}{4\sqrt{2}}(\cos(\theta_0) \pm 1)$. $\frac{b_z}{2\sqrt{2}}\sin(\theta_0)$ and $\frac{b_{L/R}}{4\sqrt{2}}(\cos(\theta_0) - 1)$ are bounded, but importantly the $\frac{b_{L/R}}{4\sqrt{2}}(\cos(\theta_0) + 1)$ profile is *unbounded* at $r = \infty$, as there we excite the ferromagnetic resonance of the background. (b) Skyrmion bound states in the $m = 0, \pm 1$ angular momentum sectors. For $m = 0$ there is a single positive energy bound state, the breathing mode, denoted $\left|m = 0, \text{br.}, +^{(0)}\right\rangle$ (shortened to $|\text{br.}\rangle$ in the plot). The $m = \pm 1$ sectors each have a bound state which is also the translational Goldstone mode of the system, $\left|m = \pm 1, \text{trans.}^{(0)}\right\rangle$. They are related via $\left|m = -1, \text{trans.}^{(0)}\right\rangle = \sigma^x \left|m = +1, \text{trans.}^{(0)}\right\rangle^*$, so we show only the $m = +1$ components in the plot (shortened to $|\text{trans.}\rangle$). Only the $m = 0$ breathing modes are excited at first order by a homogeneous driving field. (c) Skyrmion positive energy scattering states $|m, k, +\rangle^{(0)}$ (shortened to $|m\rangle$ in the plot) obtained via the shooting method, here with $k = 1.5$, $m = 0, +1, -1$. The upper "u" components are well-described in the asymptotic limit by Bessel functions of the first and second kind, $\cos(\delta_m)J_{m-1}(kr) - \sin(\delta_m)Y_{m-1}(kr)$, while the lower "l" components decay exponentially. (d) Fourier weights of the scattering states $|m, k, +, \alpha\rangle$ which are required to construct the first order steady state solutions in Eq. (3.20) and (3.30).

other negative energy copies, don't require any additional work to calculate, but we can't forget about them either as they constitute half the orthogonal basis, eq. (3.9), in our mathematical formalism. We can obtain $\left|m=0,\text{br.},+^{(0)}\right\rangle$ numerically using the shooting method in similar fashion to how we solved for the profile $\theta_0(r)$. One uses the energy $\epsilon_{\text{br.}}^{(0)}$ and the ratio of the initial slopes at $r=0$ of the upper and lower vector components in $\left|m=0,\text{br.},+^{(0)}\right\rangle$, $\left|m=0,\text{br.},+^{(0)}\right\rangle_u'(0)$ and $\left|m=0,\text{br.},+^{(0)}\right\rangle_l'(0)$, as the two shooting parameters, varying both until the boundary condition that both $\left|m=0,\text{br.},+^{(0)}\right\rangle_u$ and $\left|m=0,\text{br.},+^{(0)}\right\rangle_l$ vanish at $r=\infty$ is satisfied. In a last step, we pick a normalisation factor $N$ such that $\left\langle m=0,\text{br.},+\right|^{(0)}\sigma^z\left|m=0,\text{br.},+^{(0)}\right\rangle=1$ is normalised to unity. For $b_0=1$, we obtain $\epsilon_{\text{br.}}^{(0)}=0.839$ and the eigenstate components shown in Fig. 3.2b, which both vanish beyond the radius of the skyrmion $r_0\approx 5$, as required for a bound mode. In each of the $m=\pm 1$ sectors, there is also a single bound state, each of which also happens to be a translational mode of the system (as we are in 2D, there are two translational modes). We denote these as $\left|m=\pm 1,\text{trans.}^{(0)}\right\rangle$, and both have energy $\epsilon_{\text{trans}}^{(0)}=0$, as it costs no energy to translate the skyrmion in the $xy$-plane. We do not need to solve numerically for these, as there is a neat analytical formula, given in Eq. (3.33). A useful exercise to make sure these are indeed the translational modes is to apply $H_{\pm 1}$ to each of them, and check that the result vanishes. It turns out that these translational modes do not get activated at all by homogeneous driving at first order, but they do get activated at second order. In Fig. 3.2b we plot the spatial profiles of the upper and lower components of $\left|m=1,\text{trans.}^{(0)}\right\rangle$ (those of $\left|m=-1,\text{trans.}^{(0)}\right\rangle=\sigma^x\left|m=1,\text{trans.}\right\rangle^{*(0)}$ are the same but inverted).

**Scattering Modes**

Scattering modes are modes whose energy $\epsilon_{\text{scatt}}^{(0)}$ is greater than or equal to the gap energy, $\epsilon_{\text{scatt}}^{(0)}\geq\epsilon_{\text{gap}}$. As they are able to propagate in the ferromagnetic bulk, we expect them to extend spatially to infinity, albeit with decreasing amplitude in order to conserve energy (e.g. in 2D, amplitude is expected to decay as $\frac{1}{\sqrt{r}}$[5]). Unlike the bound states, which are quantised, they exist on an energy continuum, which we can parametrise through $\epsilon_k^{(0)}=b_0+k^2$. To solve for the scattering eigenfunctions, it is useful to get some intuition by first considering the large $r$-limit, where $r\gg r_0$. There, the spin waves do not see the skyrmion, as $V_z^m, V_x$ and $V_0^m$ all vanish. In this limit, $H_m$ is therefore reduced to a

---

[5]remember that we have not yet included the effects of the damping term $\alpha$ in this Subsection. Once $\alpha$ is included, the scattering modes actually decay with amplitude $\frac{e^{-\alpha\omega r/v_g}}{\sqrt{r}}$, where $v_g=2k_0$ is the group velocity of a scattering mode with momentum $k_0$.

diagonal form, giving rise to the following two decoupled equations

$$
\left(-\frac{d}{dr^2} - \frac{1}{r}\frac{d}{dr} + \frac{(m-1)^2}{r} + b_0\right)|m,k\rangle_u^{(0)} = (b_0 + k^2)|m,k\rangle_u^{(0)},
$$
$$
-\left(-\frac{d}{dr^2} - \frac{1}{r}\frac{d}{dr} + \frac{(m+1)^2}{r} + b_0\right)|m,k\rangle_l^{(0)} = -(b_0 + k^2)|m,k\rangle_l^{(0)},
$$
(3.10)

which admit the solutions

$$
\lim_{r\gg r_0}|m,k,+\rangle^{(0)} = \begin{pmatrix}\cos(\delta_m)J_{m-1}(kr) - \sin(\delta_m)Y_{m-1}(kr)\\ 0\end{pmatrix}, \quad \epsilon_{k,+}^{(0)} = b_0 + k^2,
$$
$$
\lim_{r\gg r_0}|m,k,-\rangle^{(0)} = \begin{pmatrix}0\\ \cos(\tilde{\delta}_m)J_{m+1}(kr) - \sin(\tilde{\delta}_m)Y_{m+1}(kr)\end{pmatrix}, \quad \epsilon_{k,-}^{(0)} = -(b_0 + k^2).
$$
(3.11)

Here, $J_m, Y_m$ are Bessel functions of the first and second kind. The eigenvectors in eq. (3.11) are normalised according to $\langle m,k,s|\,\sigma^z\,|m',k',s'\rangle = \frac{1}{k}\delta_{m,m'}\delta_{k,k'}\delta_{s,s'}\mathrm{sgn}(s)$, thanks to the property $\int r\,dr\,J_m(kr)J_m(k'r) = \frac{1}{k}\delta_{k,k'}$ of Bessel Functions (also true for $Y_m(kr)$). $\delta_m, \tilde{\delta}_m$ are phase shifts, analogous to the phase degree of freedom $\phi_0$ we know from the solution of an non-damped, non-driven 1D simple harmonic oscillator, $x(t) = x_0\cos(\omega t + \phi_0)$. If this really were a free problem, we could choose $\delta_m, \tilde{\delta}_m$ freely. However, as we shall see, the presence of the skyrmion at $r = 0$ restricts $\delta_m, \tilde{\delta}_m$ for us.

As we can't ignore the influence of the skyrmion on the scattering modes for too long, we now switch to the near-field limit, at $r \lesssim r_0$. Amazingly, $H_m$ is again diagonal to leading order, $\mathcal{O}\left(\frac{1}{r^2}\right)$, and takes the same form as Eq. (3.10), but with the sign change $m \to -m$. Thus, the Bessel solutions $J_{m\pm1}(kr)$ are again valid, although we discard $Y_{m\pm1}(kr)$ because it has a singularity at $r = 0$. For small arguments $kr \ll 1$, $\lim_{kr\to0} J_{m\pm1} = (kr)^{m\pm1}$, suggesting the following near-field form,

$$
\lim_{kr\to0}|m,k,+\rangle^{(0)} = N_+\begin{pmatrix}(kr)^{m+1}\\ c_+(kr)^{m-1}\end{pmatrix},
$$
$$
\lim_{kr\to0}|m,k,-\rangle^{(0)} = N_-\begin{pmatrix}(kr)^{m+1}\\ c_-(kr)^{m-1}\end{pmatrix}.
$$
(3.12)

$c_\pm$ are shooting parameters, which we determine by enforcing that $|m,k,+\rangle_l^{(0)}$ and $|m,k,-\rangle_u^{(0)}$ vanish as $r \gg r_0$ to match the far field solutions, Eq. (3.11). $N_\pm$ and $\delta_m, \tilde{\delta}_m$ can then be determined by matching the near- and far-field non-vanishing components, $|m,k,+\rangle_u^{(0)}$ and $|m,k,-\rangle_l^{(0)}$, as well as their derivatives, at $r \sim \frac{2\pi}{k}$. Such a scheme needs

to be implemented numerically for each value of $m, k$[6]. An example of the scattering modes obtained using this method are shown in Fig. 3.2c, where we show the upper and lower components of the positive energy eigenstates for $k = 1.5$ of the three angular momentum sectors $m = 0, \pm 1$ relevant to our problem. One can easily check that the asymptotic limit, $|\psi\rangle_u \sim r^{m+1}, |\psi\rangle_l \sim r^{m-1}$ for $r \approx 0$, is satisfied for each of these components. In the far field, the non-vanishing components oscillate with wavelength $\lambda = \frac{2\pi}{k} \sim 4$ and decay at a rate $\frac{1}{\sqrt{r}}$.

### 3.3.2 First Order in $\alpha$

At order $\mathcal{O}(\alpha)$, Eq. (3.5) reads

$$\epsilon_n^{(0)} \left| m, n, s^{(1)} \right\rangle - \epsilon_n^{(1)} \left| m, n, s^{(0)} \right\rangle + \sigma^z \epsilon_n^{(0)} \left| m, n, s^{(0)} \right\rangle = \sigma^z H_m \left| m, n, s^{(1)} \right\rangle, \qquad (3.13)$$

where we have added $s$, which denotes the sign of the energy of eigenstate, as we proved in Sec. 3.3.1 that they occur in positive-negative pairs $\pm\epsilon^{(0)}$. The analysis done in Sec. 3.3.1 also gifted us a complete orthogonal eigenbasis, which we can use to expand the first order in $\alpha$ eigenstate corrections $|m, n, s\rangle^{(1)}$,

$$\begin{aligned}
\left| m, n, s^{(1)} \right\rangle &= \sum_{\text{scatt.}, k, s'=\pm} \Delta k \, k \left\langle m, k, s'^{(0)} \right| \sigma^z \left| m, n, s^{(1)} \right\rangle \left| m, k, s'^{(0)} \right\rangle \\
&\quad + \sum_{\text{bound}, s=\pm} \left\langle m, s'^{(0)} \right| \sigma^z \left| m, n, s \right\rangle^{(1)} \left| m, s'^{(0)} \right\rangle,
\end{aligned} \qquad (3.14)$$

where we sum over all the $\mathcal{O}(\alpha^0)$ positive and negative energy scattering and bound states of the same angular momentum sector $m$. Note the extra $k\Delta k \, k$ factor in the first sum, which is required because the scattering states carry a $1/k$ in their normalisation factor. The $\sigma^z$ sandwiching the projections is required because of the definition of the inner product between zeroth order eigenstates, Eq. (3.9). We can check that Eq. (3.14) is a valid expansion by projecting it onto any of the zeroth order bound or scattering modes, $\left\langle m, k', s'^{(0)} \right|, \left\langle m, \text{bound}, s'^{(0)} \right|$. Using the orthogonality property, we recover the expected overlaps $\left\langle m, k', s'^{(0)} \middle| m, n, s^{(1)} \right\rangle, \left\langle m, \text{bound}, \pm^{(0)} \middle| m, n^{(1)} \right\rangle$. By going through the usual motions of perturbation theory, see App. H.3 for technical details, one obtains the

---

[6]Here I must thank my colleague Vivek Lohani, who wrote an efficient Julia [77, 78] code to generate these scattering eigenmodes. I promptly "borrowed" this code, as my own version written on Mathematica was not as numerically precise and also periodically caused my laptop to crash.

following damped complex energies

$$E_{\text{br.},+,\alpha} = 0.839\text{sgn}(\gamma) - 1.02i\alpha \quad E_{\text{br.},-,\alpha} = -0.839\text{sgn}(\gamma) - 1.02i\alpha,$$
$$E_{k,+,\alpha} = (1 + k^2)(\text{sgn}(\gamma) - i\alpha) \quad E_{k,-,\alpha} = (1 + k^2)(-\text{sgn}(\gamma) - i\alpha), \quad (3.15)$$
$$E_{m=\pm 1,\text{trans.},\alpha} = 0,$$

correct to order $\mathcal{O}(\alpha)$. The numerical values for the breathing mode energy are given for the case $b_0 = 1$. The first order in $\alpha$ corrections to the eigenmodes have also been calculated and are listed in App. H.3, as they are quite long.

## 3.4 Dynamic Response to Drive

Now we turn on the external driving field $\mathbf{b}_1(t)$, defined in Eq. (3.1). We want to solve for $a(t), a^*(t)$, to describe the dynamic response of the magnetisation to the drive. To this end we expand both fields in powers of $b_1$, using the same book-keeping parameter $\epsilon$ as before

$$a(t) = \epsilon a^{(1)} + \epsilon^2 a^{(2)} + \mathcal{O}(\epsilon^3),$$
$$a^*(t) = \epsilon a^{*(1)} + \epsilon^2 a^{*(2)} + \mathcal{O}(\epsilon^3). \quad (3.16)$$

We will see that solving up to quadratic order in $\epsilon$ is sufficient to get the salient physics.

### 3.4.1 First Order Oscillatory Response

At order $\mathcal{O}(\epsilon)$, the EoM for $a^{(1)}, a^{*(1)}$ looks the same as Eq. (3.4), provided we replace $a \to a^{(1)}$, $a^* \to a^{*(1)}$ and add the term

$$i\begin{pmatrix} \{F_{\text{drive}}^{(1)}, a^{(1)}\} \\ \{F_{\text{drive}}^{(1)}, a^{*(1)}\} \end{pmatrix} \quad (3.17)$$

to the RHS of the equation. $F_{\text{drive}}^{(1)}$, given in Eq. (H.1), is the only *linear* in $a, a^*$ contribution to the free energy $F$. Remember that the undriven system is by definition to lowest order *quadratic* in $a, a^*$ (otherwise the static texture around which we are expanding would not be at an energy minimum) — hence finite $b_z$, $b_R$ or $b_L$ are required to obtain a finite $F_{\text{drive}}^{(1)}$. Let us look at purely out-of-plane ($b_R = b_L = 0$) and purely in-plane ($b_z = 0$) driving separately.

**Out-of-Plane Drive**

For out-of-plane driving, $b_L = b_R = 0$, the driving term Eq. (3.17) takes the form

$$-\frac{ib_z s\sigma^z}{2\sqrt{2}}\begin{pmatrix} e^{i(\omega t+\delta)} + e^{-i(\omega t+\delta)} \\ e^{i(\omega t+\delta)} + e^{-i(\omega t+\delta)} \end{pmatrix}, \tag{3.18}$$

where $s = \sin(\theta_0(r))$. We plot the spatial profile of this driving term in Fig. 3.2a, and see that it vanishes for $r \gtrsim r_0$. This is what we expect from a physical perspective, as for $r \gg r_0$ the spins are parallel to the driving field, $\hat{\mathbf{M}} \parallel \mathbf{b}_z$, so that the torque $\hat{\mathbf{M}} \times \mathbf{b}_z = 0$ to order $\mathcal{O}(\epsilon)$. As there is no angular dependence on $\chi$ in Eq. (3.20), we conclude that out-of-plane driving can only excite the $m = 0$ angular momentum eigenstates. The equation of motion then reads

$$(\mathrm{sgn}(\gamma) + i\alpha\sigma_z)\begin{pmatrix} \dot{a}_0^{(1)} \\ \dot{a}_0^{*(1)} \end{pmatrix} = -i\sigma^z \left[ H_0 \begin{pmatrix} a_0^{(1)} \\ a_0^{*(1)} \end{pmatrix} + \frac{b_z s}{2\sqrt{2}} \begin{pmatrix} e^{i(\omega t+\delta)} + e^{-i(\omega t+\delta)} \\ e^{i(\omega t+\delta)} + e^{-i(\omega t+\delta)} \end{pmatrix} \right], \tag{3.19}$$

We can solve eq. (3.19) using the eigenbasis we developed in Sec. 3.3,

$$\begin{pmatrix} a_0^{(1)}(t) \\ a_0^{*(1)}(t) \end{pmatrix} = \begin{pmatrix} a_{0,1}^{(1)} e^{i\omega t} + a_{0,-1}^{(1)} e^{-i\omega t} \\ a_{0,1}^{*(1)} e^{-i\omega t} + a_{0,-1}^{*(1)} e^{i\omega t} \end{pmatrix} =$$

$$b_z \left[ \sum_k \Delta k k \left[ c_{k,\alpha} \left| m = 0, k, +, \alpha \right\rangle \left( \frac{e^{i(\omega t+\delta)}}{\omega + E_k} + \frac{e^{-i(\omega t+\delta)}}{-\omega + E_k} \right) \right. \right.$$

$$\left. - c_{k,\alpha}^* \left| m = 0, k, -, \alpha \right\rangle \left( \frac{e^{i(\omega t+\delta)}}{\omega - E_k^*} + \frac{e^{-i(\omega t+\delta)}}{-\omega - E_k^*} \right) \right] \tag{3.20}$$

$$+ c_{\mathrm{br.},\alpha} \left| \mathrm{br.}, +, \alpha \right\rangle \left( \frac{e^{i(\omega t+\delta)}}{\omega + E_{\mathrm{br.}}} + \frac{e^{-i(\omega t+\delta)}}{-\omega + E_{\mathrm{br.}}} \right)$$

$$\left. - c_{\mathrm{br.},\alpha}^* \left| \mathrm{br.}, -, \alpha \right\rangle \left( \frac{e^{i(\omega t+\delta)}}{\omega - E_{\mathrm{br.}}^*} + \frac{e^{-i(\omega t+\delta)}}{-\omega - E_{\mathrm{br.}}^*} \right) \right].$$

The Fourier coefficients $c_{k,\alpha}, c_{\mathrm{br.},\alpha}$ can also be expanded perturbatively in $\alpha$,

$$c_{k,\alpha} = c_k^{(0)} + i\alpha\,\mathrm{sgn}(\gamma)c_k^{(1)} + \mathcal{O}(\alpha^2),$$
$$c_{\mathrm{br.},\alpha} = c_{\mathrm{br.}}^{(0)} + i\alpha\,\mathrm{sgn}(\gamma)c_{\mathrm{br.}}^{(1)} + \mathcal{O}(\alpha^2). \tag{3.21}$$

$c_{k,\mathrm{br.}}^{(0)}, c_{k,\mathrm{br.}}^{(1)}$ are calculated by substituting ansatz (3.20) into Eq. (3.19), expanding up to zeroth and linear order in $\alpha$ and then projecting $\left\langle m = 0, k, +^{(0)} \right|, \left\langle m = 0, \mathrm{br.}, +^{(0)} \right|$ onto

the two resulting equations. We obtain

$$
\begin{aligned}
c_{k'}^{(0)} &= -\mathrm{sgn}(\gamma)\frac{b_z}{2\sqrt{2}} \left\langle k',+^{(0)} \middle| \sin(\theta_0) \begin{pmatrix} 1 \\ 1 \end{pmatrix} \right\rangle, \\
c_{\mathrm{br.}}^{(0)} &= -\mathrm{sgn}(\gamma)\frac{b_z}{2\sqrt{2}} \left\langle \mathrm{br.},+^{(0)} \middle| \sin(\theta_0) \begin{pmatrix} 1 \\ 1 \end{pmatrix} \right\rangle \approx -0.618\,\mathrm{sgn}(\gamma).
\end{aligned}
\tag{3.22}
$$

The expressions for $c_{k'}^{(1)}, c_{\mathrm{br.}}^{(1)}$ are longer and given in Eq. (H.14). These Fourier coefficients are evaluated by numerically integrating the integrand over $r$. In Fig. 3.2d we plot the resulting $c_{k'}^{(0)}, c_{k'}^{(1)}$ and note with relief and happiness that they are both bounded, so that we don't need to include any scattering wavefunctions with $k \gtrsim 6$ in the sum over scattering states, Eq. (3.20). We implement Eq. (3.20) numerically on Mathematica by summing over the $m = 0$ scattering wavefunctions between $k = 0$ and $k = 6$ in steps $\Delta k = 0.01$, evaluating the sum for different driving frequencies $\omega$. One way to visualise the result is to look at the time-averaged deviation from the equilibrium skyrmion configuration, $\delta M = \sqrt{\langle |\hat{\mathbf{M}}(t) - \hat{\mathbf{M}}_0|^2 \rangle_t}$. The result is plotted in Fig. 3.3a, for a few different values of $\omega$. We note that the biggest deviation occurs when we drive near the breathing mode resonance frequency, $\omega = 0.84$. The snapshots in Fig. 3.4a–e show the time-dependent first order response when we drive a Néel skyrmion at this breathing mode resonance. Note how the radial symmetry is preserved as we are only exciting the $m = 0$ eigenstates.

**In-Plane Drive**

For in plane driving, $b_z = 0$, the driving term Eq. (3.17) takes the form

$$
\frac{i\sigma^z}{4\sqrt{2}} \left[ \begin{pmatrix} (b_R e^{-i\omega t} + b_L e^{+i\omega t})(c-1) \\ (b_R e^{-i\omega t} + b_L e^{i\omega t})(c+1) \end{pmatrix} e^{i\chi} + \begin{pmatrix} (b_R e^{i\omega t} + b_L e^{-i\omega t})(c+1) \\ (b_R e^{i\omega t} + b_L e^{-i\omega t})(c-1) \end{pmatrix} e^{-i\chi} \right], \quad (3.23)
$$

where $c = \cos(\theta_0(r))$. We plot the two spatial profiles of this driving term in Fig. 3.2a, and notice that while $\frac{1}{4\sqrt{2}}(\cos(\theta_0) - 1)$ is bounded and vanishes for $r \gtrsim r_{\mathrm{skyr.}}$, this is not the case for $\frac{1}{4\sqrt{2}}(\cos(\theta_0) + 1)$, which plateaus at $\frac{1}{2\sqrt{2}}$. This means that we cannot blindly repeat the procedure we used in Sec. 3.4.1 to calculate the Fourier coefficients of the steady state, as we would now have to deal with unbounded integrands arising from the non-vanishing driving profile $\frac{1}{4\sqrt{2}}(\cos(\theta_0) + 1)$. To come up with a solution to this problem it is helpful to understand where this finite plateau comes from. As it happens in the bulk, far away from the skyrmion, the behaviour must be related to the presence
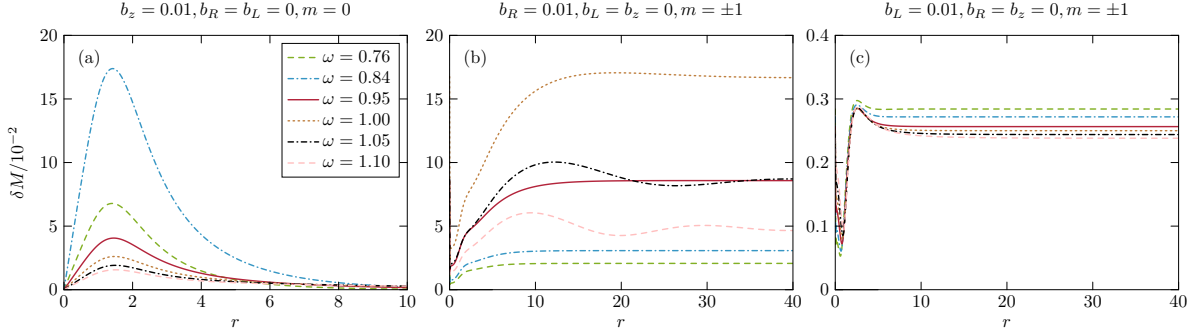
Figure 3.3 Time averaged deviation of the unit magnetisation, $\delta M = \sqrt{\langle 2a^{*(1)}a^{(1)}\rangle_{\chi,t}}$, for a range of driving frequencies $\omega$ and polarisations $b_z, b_R, b_L$, with damping $\alpha = 0.03$, a fixed static magnetic field $b_0 = 1$ and $\gamma < 0$. (a) Purely out-of-plane driving $b_z = 0.01, b_R = b_L = 0$. The resonance is at the breathing mode frequency, $\omega_{\text{br.}} = 0.839$. $\delta M$ is confined to the region of the skyrmion, $r \lesssim r_0$, because out-of-plane driving does *not* excite the ferromagnetic background. (b) In-plane right-polarised driving, $b_R = 0.01, b_z = b_L = 0$. The Kittel (background ferromagnet) mode at $\omega_{\text{Kittel}} = 1$ is resonantly excited. For $\omega > 0$ we also start to excite the scattering modes, resulting in oscillations at wavelength $2\pi/k$ in the spatial profile of $\delta M$. (c) In-plane left-polarised driving, $b_L = 0.01, b_z = b_R = 0$. The Kittel mode is *not* resonantly excited, and $\delta M$ is three orders of magnitude smaller than for right-polarised driving. Using a material with positive $\gamma$ would inverse panels (b) and (c). For both left- and right-polarised driving $\delta M$ is not confined to the radius of the skyrmion, $\delta M > 0$ for $r \gg r_0$, because in-plane driving excites the ferromagnetic background. (Made using Eq. (3.20) and (3.30).)
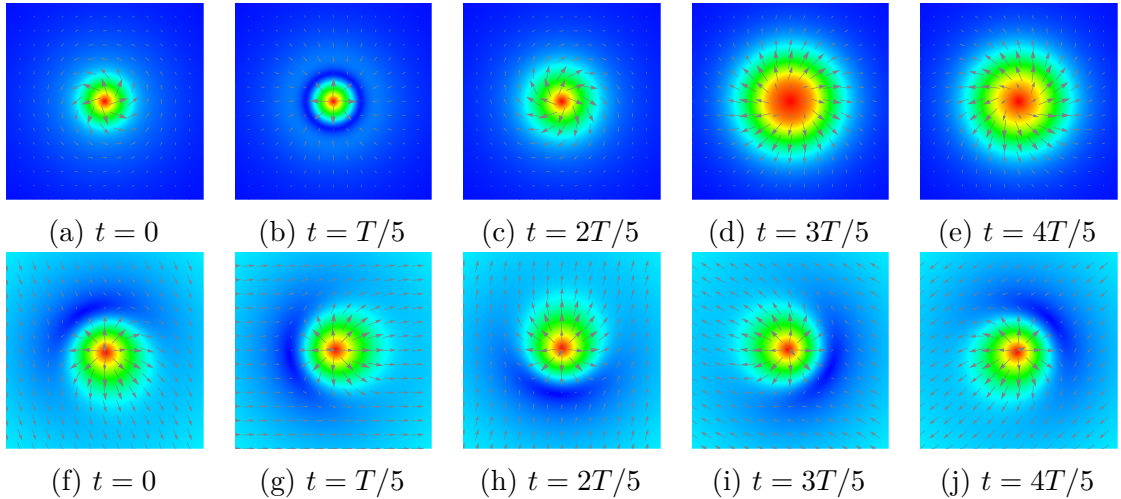


Figure 3.4 Snapshots of a skyrmion driven with (a)–(e) out-of-plane, $b_z = 0.05, b_R = b_L = 0$, $\omega = 0.84$, and (f)–(j) in-plane right-polarised magnetic field, $b_R = 0.05, b_z = b_L = 0$, $\omega = 1$. In both cases, $\alpha = 0.03$ and $b_0 = 1$.

of the ferromagnet. Imagine for a moment that there is no skyrmion at all, $\theta_0 = 0$ in Eq. (3.23). This leads to the following EoM,

$$
\begin{aligned}
(\operatorname{sgn}(\gamma) + i\alpha\sigma_z) \begin{pmatrix} \dot{a}_{\mathrm{FM}} \\ \dot{a}^*_{\mathrm{FM}} \end{pmatrix} = -i\sigma^z \Big[ & H_0 \begin{pmatrix} a^{(1)}_{\mathrm{FM}} \\ a^{*(1)}_{\mathrm{FM}} \end{pmatrix} \\
& - \begin{pmatrix} 0 \\ 1 \end{pmatrix} \frac{e^{i\chi}}{2\sqrt{2}} \left( b_R e^{-i\omega t} + b_L e^{i\omega t} \right) - \begin{pmatrix} 1 \\ 0 \end{pmatrix} \frac{e^{i\chi}}{2\sqrt{2}} \left( b_R e^{i\omega t} + b_L e^{-i\omega t} \right) \Big].
\end{aligned}
\tag{3.24}
$$

As the driving terms on the RHS are spatially independent, we would expect that only spatially independent scattering eigenfunctions get excited. The positive energy ferromagnetic eigenstates are given by $J_{m-1}(kr)$, and the only spatially independent non-trivial eigenstate is the one with $m = 1, k = 0$, as $J_0(0) = 1$. If we had instead considered the (unphysical) negative energy copies, we would have gotten that the only relevant spatially independent mode is in the $m = -1$ sector. Thus, we know that, at least in the case of a bulk ferromagnet, perpendicular driving excites only the $|m = 1, k = 0\rangle$ and $|m = -1, k = 0\rangle$ eigenfunctions, with eigenenergies $E_{0,+,\alpha} = b_0(\operatorname{sgn}(\gamma) - i\alpha)$ and $E_{0,-,\alpha} = -b_0(\operatorname{sgn}(\gamma) + i\alpha)$, respectively. Together, these constitute the Kittel mode of the ferromagnet. Now we put the skyrmion back into the system. The trouble with identifying the $k = 0$ eigenfunction in this case is that the boundary matching approach we used so far to determine the skyrmion scattering eigenfunctions fails for $k = 0$, as the boundaries between the near-field and far-field solutions need to be matched at $r \gg \frac{1}{k}$, which is effectively infinity for $k = 0$. But we *know* from the physical point of view that one such $k = 0$ eigenstate must exist for each of the angular momentum sectors $m = 1$ and $m = -1$. Assuming they do exist, the $m = \pm 1, k = 0$ modes should obey the following eigenvalue equations,

$$
\begin{aligned}
(\operatorname{sgn}(\gamma) + i\alpha\sigma_z)(-E^*_{0,\alpha}) |m = 1, k = 0, -, \alpha\rangle &= \sigma^z H_1 |m = 1, k = 0, -, \alpha\rangle, \\
(\operatorname{sgn}(\gamma) + i\alpha\sigma_z) E_{0,\alpha} |m = -1, k = 0, +\alpha\rangle &= \sigma^z H_{-1} |m = -1, k = 0, +\alpha\rangle.
\end{aligned}
\tag{3.25}
$$

It is in fact sufficient to determine just $|m = 1, k = 0, -, \alpha\rangle$, as $|m = -1, k = 0, +, \alpha\rangle$ is automatically obtained by taking the complex conjugate of $|m = 1, k = 0, -, \alpha\rangle$ and pre-multiplying with $\sigma^x$. We know that for large $r$, $|m = 1, k = 0, -, \alpha\rangle$ is the only surviving contribution to the steady state, as all the finite $k$ average each other out with their oscillations. We can use this and the form of the driving term, Eq. (3.23), to make

a guess at the form of $|m = 1, k = 0, \alpha, -\rangle$. How about trying

$$
\begin{aligned}
|m = 1, k = 0, -, \alpha\rangle &= \frac{\text{sgn}(\gamma)}{1 + i\alpha\text{sgn}(\gamma)\sigma^z} \frac{\sigma^z}{4\sqrt{2}} \begin{pmatrix} c - 1 \\ c + 1 \end{pmatrix} + d_{\text{trans.},\alpha} |m = 1, \text{trans.}\rangle \\
&+ \sum_{k>0} \Delta k \, k \left[ a_{k,\alpha} |m = 1, k, +, \alpha\rangle - b_{k,\alpha} |m = 1, k, -, \alpha\rangle \right].
\end{aligned}
\tag{3.26}
$$

What is the logic of this? Well, in the limit $r \gg r_0$ the first term on the RHS of Eq. (3.26) solves the EoM by balancing the driving term Eq. (3.23). This term guarantees that the lower component of the $m = 1, k = 0$ mode plateaus to a constant finite value as $r \gg r_0$, which we have argued is a requirement of the $k = 0$ mode. But this gives us no guarantee that $|m = 1, k = 0, -, \alpha\rangle$ will also be a solution of the $k = 0$ eigenvalue, Eq. (3.25), so there must be a missing part of the wavefunction for which we need to solve. We expand this missing part in the complete eigenbasis provided by the scattering eigenfunctions, $|m = 1, k, +, \alpha\rangle, |m = 1, k, -, \alpha\rangle$ and translational mode, $|m = 1, \text{trans.}\rangle$. The coefficients $a_{k,\alpha}, b_{k,\alpha}, d_{\text{trans.}}$ can be Taylor expanded in $\alpha$ just like $c_{k,\alpha}$,

$$
\begin{aligned}
a_{k,\alpha} &= a_k^{(0)} + i\alpha\text{sgn}(\gamma)a_k^{(1)} + \mathcal{O}(\alpha^2), \\
b_{k,\alpha} &= b_k^{(0)} + i\alpha\text{sgn}(\gamma)b_k^{(1)} + \mathcal{O}(\alpha^2), \\
d_{\text{trans},\alpha} &= d_{\text{trans.}}^{(0)} + i\alpha\text{sgn}(\gamma)d_{\text{trans.}}^{(1)}.
\end{aligned}
\tag{3.27}
$$

To determine these coefficients we substitute ansatz (3.26) into Eq. (3.25), expand the resulting equation order by order in $\alpha$ and project $\langle m = 1, k, +|^{(0)} \sigma^z, \langle m = 1, k, \alpha, -^{(0)}| \sigma^z$ or $\langle m = 1, \text{trans.}, \alpha^{(0)}| \sigma^z$ onto it. At order $)(\alpha^0)$ we obtain

$$
\begin{aligned}
a_k^{(0)} &= -\frac{\text{sgn}(\gamma)}{\epsilon_k^{(0)} + \epsilon_0^{(0)}} \int_0^\infty dr \, r \langle m = +1, k, +|^{(0)} (\epsilon_0^{(0)} + H_1\sigma^z) \left| \frac{1}{4\sqrt{2}} \begin{pmatrix} c - 1 \\ c + 1 \end{pmatrix} \right\rangle, \\
b_k^{(0)} &= \frac{\text{sgn}(\gamma)}{\epsilon_k^{(0)} - \epsilon_0^{(0)}} \int_0^\infty dr \, r \langle m = +1, k, -|^{(0)} (\epsilon_0^{(0)} + H_1\sigma^z) \left| \frac{1}{4\sqrt{2}} \begin{pmatrix} c - 1 \\ c + 1 \end{pmatrix} \right\rangle, \\
d_{\text{tr.}}^{(0)} &= -\frac{\text{sgn}(\gamma)}{\epsilon_0^{(0)}} \int_0^\infty dr \, r \langle m = +1, \text{tr.}|^{(0)} (\epsilon_0^{(0)} + H_1\sigma^z) \left| \frac{1}{4\sqrt{2}} \begin{pmatrix} c - 1 \\ c + 1 \end{pmatrix} \right\rangle = 0.
\end{aligned}
\tag{3.28}
$$

In eq. (3.28), $\epsilon_k = b_0 + k^2$. $a_k^{(0)}$ is well behaved at all values of $k$, but $b_k \sim \frac{1}{k^2}$ diverges at low $k$[7]. The $\mathcal{O}(\alpha)$ corrections are too long to be listed here and given instead in

---

[7]Note, however, that this divergence is counteracted by a factor $E_k - E_0 \sim k^2$ in the steady state, see Eq. (3.30). Thus, there are no convergence problems if we consider the steady state, instead of the $k = 0$ mode in isolation

Eq. (H.15). We plot $a_k^{(0)}, a_k^{(1)}, k^2 b_k^{(0)}, k^2 b_k^{(1)}$ (adding a factor $k^2$ to remove the singularity) as a function of $k$ in Fig. 3.2d and note with relief and satisfaction that they too are bounded to within about $k \lesssim 6$, which is great news for numerical implementation.

Given that in-plane driving activates the $m = \pm 1$ angular momentum sectors, we can write down the following general ansatz for the first order response,

$$\begin{pmatrix} a^{(1)}(t) \\ a^{*(1)}(t) \end{pmatrix} = \begin{pmatrix} a_1(t) \\ a_{-1}^*(t) \end{pmatrix} e^{i\chi} + \begin{pmatrix} a_{-1}(t) \\ a_1^*(t) \end{pmatrix} e^{-i\chi}, \tag{3.29}$$

with

$$\begin{aligned} \begin{pmatrix} a_1^{(1)}(t) \\ a_{-1}^{*(1)}(t) \end{pmatrix} = &\; |m = 1, k = 0, -, \alpha\rangle \left( \frac{b_L e^{i\omega t}}{\omega - E_{0,\alpha}^*} + \frac{b_R e^{-i\omega t}}{-\omega - E_{0,\alpha}^*} \right) \\ &- \sum_k \Delta k k \left[ a_{k,\alpha} |m = 1, k, +, \alpha\rangle \left( \frac{b_L e^{i\omega t}}{\omega + E_{k,\alpha}} + \frac{b_R e^{-i\omega t}}{-\omega + E_{k,\alpha}} \right) \right. \\ &\left. - b_{k,\alpha} |m = 1, k, -, \alpha\rangle \left( \frac{b_L e^{i\omega t}}{\omega - E_{k,\alpha}^*} + \frac{b_R e^{-i\omega t}}{-\omega - E_{k,\alpha}^*} \right) \right]. \end{aligned} \tag{3.30}$$

Just as for the out-of-plane driving case we implement Eq. (3.30) numerically on Mathematica, summing over the scattering eigenstates for $0.01 < k < 6$ in steps $\Delta k = 0.01$. We plot the polar angle- and time-averaged deviation $\delta M = \langle 2(a_1^{*(1)} a_1^{(1)} + a_{-1}^{*(1)} a_{-1}^{(1)}) \rangle_{\chi,t}$ in Fig. 3.3b and c for a system with $\alpha = 0.03$ and $\gamma < 0$, for right- and left-polarised in plane driving, respectively. Negative $\gamma$ means that the real part of $E_{0,\alpha} = b_0(\text{sgn}(\gamma) - i\alpha)$, $b_0(\text{sgn}(\gamma)$, is negative. Therefore we need to use a right-polarised driving field if we wish to drive the $|m = 1, k = 0, \alpha, -\rangle$ mode resonantly. This is exactly what we observe in Fig. 3.3b and c, the deviation *deltaM* is more than one hundred times larger for right-polarised than left-polarised driving when we drive at the Kittel resonance $\omega_{\text{Kit.}} = b_0 = 1$. We also used Eq. (3.30) to generate the snapshots in Fig. 3.4f–j, which shows the time-dependent first order response of a Néel skyrmion in a background field $b_0 = 1$ driven at the Kittel resonance $\omega = 1$ with a right-polarised in plane driving field. Note how the radial symmetry we had for the out-of-plane driving case has been replaced by an angular dependence $e^{i(\chi - \omega t)}$, as we are now exciting the $m = \pm 1$ angular momentum eigenstates of the system.

### 3.4.2 Second Order Translational Motion

At $\mathcal{O}(\epsilon^2)$, our perturbative approach once again admits three kinds of response: oscillations at twice the driving frequency, $\pm 2\omega$, a DC response at $0\omega$ and a linear in $t$ growing term, which describes the translational motion of the skyrmion at velocity $\mathbf{v}_{\text{slide}} = (v_x, v_y, 0)^T$. We can write the full response in the language of the $\mathcal{O}(\epsilon^2)$ contributions to $a, a^*$,

$$\begin{pmatrix} a^{(2)} \\ a^{*(2)} \end{pmatrix} = \begin{pmatrix} a^{(2)}_{\text{osc.}} + a^{(2)}_{\text{stat.}} + a^{(2)}_{\text{trans.}} \\ a^{*(2)}_{\text{osc.}} + a^{*(2)}_{\text{stat.}} + a^{*(2)}_{\text{trans.}} \end{pmatrix}. \tag{3.31}$$

As before, we are mainly interested in calculating the $\mathbf{v}_{\text{slide}} t$ response, encoded in the $a^{(2)}_{\text{trans.}}, a^{*(2)}_{\text{trans.}}$ terms. The full $\mathcal{O}(\epsilon^2)$ equation of motion reads

$$(\text{sgn}(\gamma) + i\alpha\sigma_z) \begin{pmatrix} \dot{a}^{(2)}_{\text{trans.}} + \dot{a}^{(2)}_{\text{osc.}} \\ \dot{a}^{*(2)}_{\text{trans.}} + \dot{a}^{*(2)}_{\text{osc.}} \end{pmatrix} = i \begin{pmatrix} \{F^{(3)}_{\text{skyr.}} + F^{(2)}_{\text{skyr.}} + F^{(2)}_{\text{drive}}, a\} \\ \{F^{(3)}_{\text{skyr.}} + F^{(2)}_{\text{skyr.}} + F^{(2)}_{\text{drive}}, a^*\} \end{pmatrix}. \tag{3.32}$$

Note how the static components disappears from the LHS, as by definition $\dot{a}^{(2)}_{\text{stat}}, \dot{a}^{*(2)}_{\text{stat}} = 0$. The free energies densities for the terms $F^{(3)}_{\text{skyr.}}$, $F^{(2)}_{\text{skyr.}}$, and $F^{(2)}_{\text{drive}}$ on the RHS are defined in Eq. (H.3) and (H.4). We left the $a, a^*$-fields general on the RHS on purpose, as there will be contributions from both $a^{(1)}, a^{*(1)}$ and $a^{(2)}, a^{*(2)}$ after the Poisson bracket operations, depending on which part of the free energy we evaluate the Poisson bracket with.

When written in the $a^{(2)}, a^{*(2)}$ language, the translational mode $-t(\mathbf{v}_{\text{slide}} \cdot \nabla)\hat{\mathbf{M}}^{(0)}$ takes the form

$$\begin{pmatrix} a^{(2)}_{\text{trans.}} \\ a^{(2)}_{\text{trans.}} \end{pmatrix} = v_{\text{slide}} t \left[ |m = 1, \text{trans.}\rangle e^{-i\beta} + |m = -1, \text{trans.}\rangle e^{i\beta} \right], \tag{3.33}$$

where $v_{\text{slide}} = \sqrt{v_x^2 + v_y^2}$ and $\beta$ is the angle the velocity vector makes with the $x$-axis, $\mathbf{v}_{\text{slide}} = v_{\text{slide}}(\cos(\beta), \sin(\beta), 0)^T$. For the derivation of eq. (3.33), see App. H.4. Note that eq. (3.33) is only valid for *short* times, as over time it grows linearly, eventually breaking the perturbative assumption that the $\mathcal{O}(\epsilon^2)$ terms are small. However, its time derivative is constant in time and therefore valid for *all* times.

As there are two translational modes in the $xy$-plane, we need to solve for two parameters $v_x, v_y$, or equivalently, $v_{\text{slide}}, \beta$. We do this in two steps. First, we project $\langle m = 1, \text{trans.}^{(0)} | \sigma^z$ onto Eq. (3.33), which gets rid of the problematic (because it grows linearly in time!) $a^{(2)}_{\text{trans.}}$ and the unknown $a^{(2)}_{\text{stat.}}$ terms on the RHS. To understand how this works, notice that the $a^{(2)}_{\text{trans.}}, a^{(2)}_{\text{trans.}}$ can only result from the $\{F^{(2)}_{\text{skyr.}}, a\}, \{F^{(2)}_{\text{skyr.}}, a^*\}$ Poisson bracket, which is also the Poisson bracket we originally showed could be written

as $\sigma^z H_m (a_m^{(1)}, a_m^{*(1)})^T$. Projecting onto this with $\langle m = 1, \text{trans.} | \sigma^z$, and remembering that translational modes have zero energy, $\langle m = 1, \text{trans.} |^{(0)} H_1 = 0$, we conclude that this contribution conveniently vanishes. After the projection step, the next step is to take the time average $\langle ... \rangle_t$, which removes the oscillatory parts of the response. This gives the familiar (dimensionless) Thiele equation

$$\text{sgn}(\gamma) \tilde{\mathbf{G}} \times \mathbf{v}_{\text{slide}} - \alpha \tilde{\mathcal{D}} \mathbf{v}_{\text{slide}} = \mathbf{f}_{\text{slide}}, \tag{3.34}$$

where $\tilde{\mathbf{G}}$ and $\tilde{\mathcal{D}}$ are the dimensionless gyro-coupling and dissipative matrix of the skyrmion. While $\tilde{\mathbf{G}} = -4\pi \mathbf{e}_z$ is a topological invariant, and therefore the same for any skyrmion, $\tilde{\mathcal{D}}$ depends on the static external field $b_0$ in the system, see Eq. (C.4). For $b_0 = 1$ $\tilde{\mathcal{D}}_{xx} = \tilde{\mathcal{D}}_{yy} = 14.6$. The force $\mathbf{f}_{\text{slide}}$ causing the skyrmion to "slide" at constant velocity $\mathbf{v}_{\text{slide}}$ is given by

$$\begin{aligned}
\mathbf{f}_{\text{slide}} &= \begin{pmatrix} \text{Im}(f) \\ \text{Re}(f) \\ 0 \end{pmatrix}, \\
f &= -\frac{i}{\sqrt{2}} \iint r \, d\chi \, dr \, e^{-i\chi} \Bigg[ \\
&\quad \left( -\theta_0' + \frac{\sin(\theta_0)}{r} \right) \left\langle \{ F_{\text{skyr.}}^{(3)} + F_{\text{drive}}^{(1)}, a \} \right\rangle_t \\
&\quad + \left( \theta_0' + \frac{\sin(\theta_0)}{r} \right) \left\langle \{ F_{\text{skyr.}}^{(3)} + F_{\text{drive}}^{(1)}, a^* \} \right\rangle_t \Bigg].
\end{aligned} \tag{3.35}$$

In Eq. (H.16) we list the time- and angle- averaged Poisson bracket $\left\langle \{ F_{\text{skyr.}}^{(3)} + F_{\text{drive}}^{(1)}, a^* \} \right\rangle_{\chi, t}$. Due to the $e^{-i\chi}$ factor in the integrand of $f$, the only non-vanishing contributions come from products of $a^{(1)}, a^{*(1)}$ terms which carry a net angular momentum $m = 1$. The only way to have this at quadratic order is to have one $a^{(1)}$ or $a^{*(1)}$ field which carries no angular momentum, $m = 0$, and is therefore proportional to $b_z$, and one which carries angular momentum $m = \pm 1$, and is thus proportional to $b_R$ or $b_L$. This explains why Eq. (H.16), and consequently also $f_{\text{slide}}$, have two mixed contributions proportional to $b_z b_R$ and $b_z b_L$, but no contributions proportional to $b_z^2$ or $b_L^2, b_R^2$. Thus, we need a *tilted* magnetic field $\mathbf{b}_1(t) = (b_\perp, b_z)$, $b_\perp, b_z > 0$, in order to obtain a finite translational motion of the skyrmion at order $\mathcal{O}(\epsilon^2)$. The resulting skyrmion speed is proportional to a product of the out-of-plane and in-plane components of the driving field, $v_{\text{slide}} \sim b_z b_{R/L}$. It is interesting to contrast this with the Archimedean screw, where we saw that $\omega_{\text{screw}} \sim b_L^2, b_R^2$, meaning that a perpendicular driving field $b_{1,\perp}(t)$ was sufficient to activate the Goldstone mode.
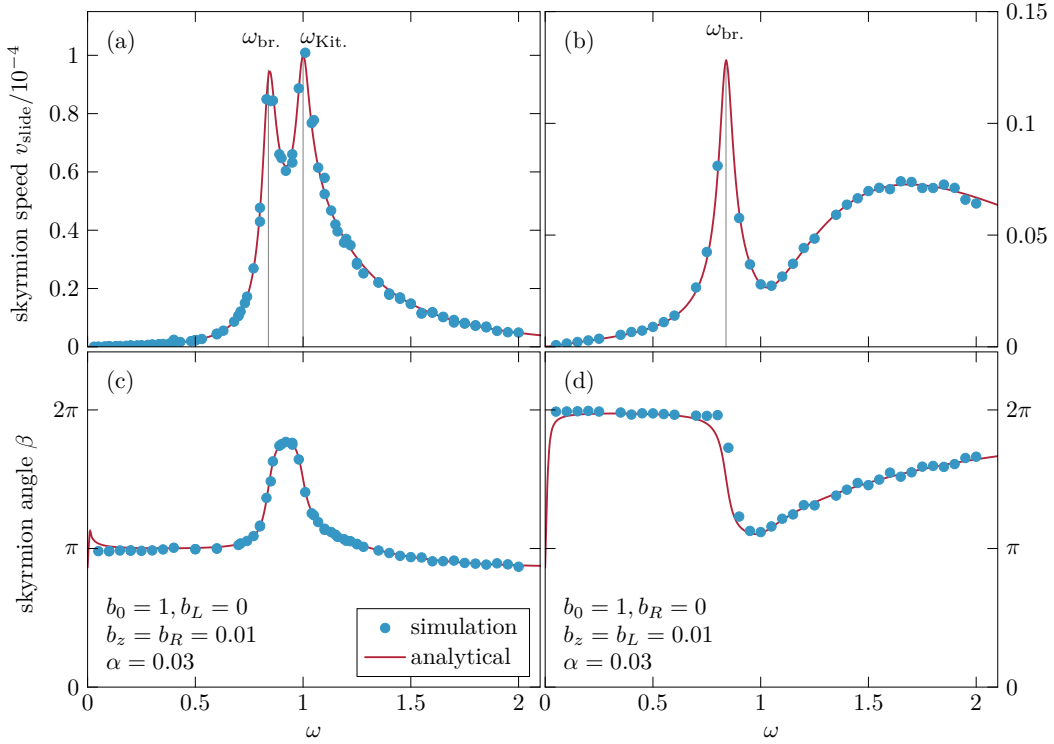
Figure 3.5 Comparison between analytically predicted (red smooth curves) and numerically extracted (blue dots, data from mumax3) second order skyrmion velocities $\mathbf{v}_{\text{slide}}$ for a system with damping $\alpha = 0.03$, fixed static magnetic field $b_0 = 1$, phase difference $\delta = 0$ and $\gamma < 0$. (a) Skyrmion speed $v_{\text{slide}}$ for out-of-plane, $b_z = 0.01$, and right-polarised in-plane, $b_R = 0.01, b_L = 0$, driving. Both the breathing mode and Kittel mode are resonantly excited. (b) Skyrmion speed $v_{\text{slide}}$ for out-of-plane, $b_z = 0.01$, and left-polarised in-plane, $b_R = 0, b_L = 0.01$, driving. Only the breathing mode is resonantly excited, and $v_{\text{slide}}$ is about an order of magnitude smaller on-resonance than in panel (a). (c) Angle $\beta$ between $\mathbf{v}_{\text{slide}}$ and the $x$-axis for out-of-plane, $b_z = 0.01$, and right-polarised in-plane, $b_R = 0.01, b_L = 0$, driving. (d) Angle $\beta$ for out-of-plane, $b_z = 0.01$, and left-polarised in-plane, $b_R = 0.01, b_L = 0$, driving.

Using the previously calculated Fourier coefficients $a_{0,\pm 1}^{(1)}, a_{1,\pm 1}^{(1)}, a_{-1,\pm 1}^{(1)}$ for the first order response, we evaluate $f_{\text{slide}}$. Solving the simple $2 \times 2$ matrix equation Eq. (3.34), we obtain values for the translational second order velocity of the skyrmion, $\mathbf{v}_{\text{slide}} = v_{\text{slide}} (\cos(\beta), \sin(\beta))$. In Fig. 3.5 we plot the resulting speed $v_{\text{slide}}$ and angle $\beta$ of the velocity vector for a range of driving frequencies, $0 < \omega < 2$. We do this for two different polarisations of the in-plane field: purely right-polarised, $b_R = 0.01, b_L = 0$, panels a and c), and a purely left-polarised, $b_L = 0.01, b_R = 0$, panels b and d), while keeping the out-of-plane driving field component, $b_z = 0.01$, constant. We also choose to set the phase difference (see Eq. (3.1) for the definition) to zero, $\delta = 0$. For these in-plane circularly polarised drives, the phase difference $\delta$ can actually be tuned to control the direction of the skyrmion (see Eq. (H.16)) — a finite $\delta$ will rotate the angle $\beta$ to $\beta \pm \delta$ for left- and right-polarised in-plane driving, respectively. Purely left- and right- polarised in plane field are in a sense the "normal modes" of the system. This means that the velocity vector resulting from any mixed in-plane driving can be obtained by adding vectorially the individual velocities resulting from the decomposed purely circularly polarised drives, $\mathbf{v}_{\text{slide}}(b_R, b_L) = \mathbf{v}_{\text{slide}}(b_R = 0) + \mathbf{v}_{\text{slide}}^R(b_L = 0)$. Thus we can obtain all the information we need to make any further predictions already from Fig. 3.5. The first thing to note is that for negative $\gamma$, right-polarised driving excites both the breathing and the Kittel modes, whereas left-polarised driving excites only the breathing mode. As a consequence, the speed $v_{\text{slide}}$ is about an order of magnitude smaller on-resonance for left-polarised driving compared to right-polarised driving. The second thing to note is that we can also tune the direction of motion of the skyrmion by varying the driving frequency $\omega$, with left-polarised driving affording more control, as for right-polarised driving the change in $\beta$ happens very fast in a small region around $\omega_{\text{br}}, \omega_{\text{Kit.}}$. To test our analytical predictions we also ran some numerical simulations on mumax3, driving a single Néel skyrmion with a tilted oscillating field and tracking its centre $\mathbf{r}_c$[8]. This data was only taken at stroboscopic time intervals $\Delta t = \frac{2\pi}{\omega}$, so that $\mathbf{v}_{\text{slide}}$ could be calculated simply as the slope in time of $\mathbf{r}_c$, $\mathbf{v}_{\text{slide}} = \frac{d\mathbf{r}_c}{dt}$. The resulting data matches our analytical prediction very well.

To get an idea of the size of the velocity in experimentally relevant units we switch back to dimensional quantities $r = \frac{\tilde{J}}{\tilde{D}}\tilde{r}$, $t = \tilde{t}\frac{\tilde{J}M_0}{\tilde{D}^2|\gamma|}$, giving $V = v\frac{\tilde{D}|\gamma|}{M_0}$. Using the MnSi values $\tilde{D} = 2.46 \times 10^{-4} \text{Jm}^{-2}$, $M_0 = 1.52 \times 10^5 \text{Am}^{-1}$, $\gamma = 1.76 \times 10^{11} \text{T}^{-1}\text{s}^{-1}$ [44, 79, 80] and $v \sim 10^{-4}$ for right-polarised driving on resonance, we obtain $V \sim 28 \, \text{mms}^{-1}$ for a tilted right-polarised driving field with amplitude $\sim 10 \, \text{mT}$. For comparison, this is

---

[8]We took $\mathbf{r}_c$ to be the coordinates of the most negative spin in the output magnetisation data. To get a more precise value of $\mathbf{r}_c$, we actually interpolated using two parabolas, one in the $x$ and one in the $y$ directions, in the neighbourhood of the most negative spin. We then took the minimum of both parabolas as the $\mathbf{r}_c = (x, y)$ coordinates of the centre of the skyrmion.

two orders of magnitude larger than the experimentally verified speed of skyrmions driven by ultra-small electric currents, recorded using Hall effect measurements to be $V_c \sim 0.2\,\mathrm{mms^{-1}}$ at twice the de-pinnning current $2j_c$ [20]. Therefore, pinning is not expected to dominate the dynamics and the "slide of the skyrmion" should be easy to observe in an experiment!

# 4

# Fractional Charges
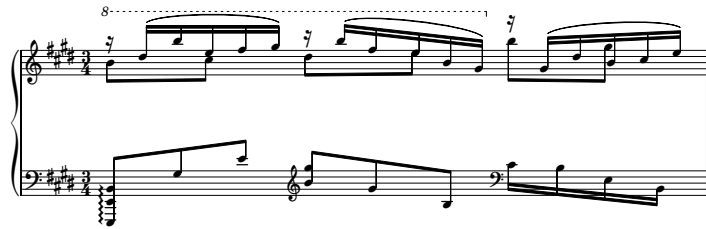


$-\frac{1}{8}, \frac{1}{12}, \frac{1}{16}, \frac{1}{24}$ in just one bar (!) of A. Scriabin's 1898 "*Sonate-Fantaisie*"

As it happens, fractions exist not just to torture small children in maths and music class — they can also turn up in magnets. So-called fractional magnetic charges are characterised by a non-integer topological charge $Q$. In this chapter, we will go on a hunt for these mysterious creatures and try to understand more about their properties. We will uncover fractional charges of both quantised $\left(\frac{1}{4}, \frac{1}{6}\right)$ and non-quantised (0.603, 0.23, whatever you like..) $Q$, hiding at intersections of cubic domain walls, inside magnetic skyrmions and vortices and at domain walls with a spontaneously broken symmetry. We will also look at some of their superpowers and what distinguishes them from well-behaved integer-valued magnetic charges, in particular their ability to scatter low energy electrons and magnons with exceptional strength.

The work presented in this chapter was done in collaboration with Imane El Achchi, Vivek Lohani and Achim Rosch [81].

## 4.1 Definition & Examples

In this final chapter, our protagonist is the topological charge $Q$, a quantity we already met briefly in Sec. 1.4 and defined in Eq. (1.16). There we saw examples of objects with integer $Q$: the ferromagnet with $Q = 0$ and the Néel and Bloch skyrmions with $Q = -1$, and how they could be represented as stereographic projections from a 2-sphere onto the 2D plane, see Fig. 1.1c and 1.2 v),vi). In both cases the magnetic textures covered the entire sphere, from north pole to south pole. What distinguishes fractional topological charges from integer charges is that they *cannot* be represented in this way, i.e. — they cover only a *fraction* of the 2-sphere. Consider Fig. 4.1, where we represent three different topological textures — an antiskyrmion, an antimeron and a fractional antivortex (we chose the anti-versions for all three as they result in a positive $Q$) — on both a 2-sphere and on the 2D plane. While the antiskyrmion magnetisation covers the entire sphere once, the antimeron covers only half of it and the fractional antivortex an even smaller fraction. The key distinguishing feature between these types of textures is the boundary condition at $x, y = \infty$. For the antiskyrmion it is single-valued, $\hat{M}_z = 1$, whereas for the antimeron and fractional vortex it is multi-valued, $\hat{M}_x^2 + \hat{M}_y^2 = \text{const.}$. This makes representing the antimeron and fractional antivortex on the full area of the sphere impossible, as it would require a multi-valued magnetisation $\hat{\mathbf{M}}$ at the pole which maps to $x, y = \infty$[1]. In terms of realisation, it has been shown that (anti)merons are one of the leading instabilities for (anti)skyrmions to decay into when the stabilising external magnetic field $B_0 \mathbf{e}_z$ is decreased [82], with each skyrmion decaying into two identical merons to keep the topological charge $Q = -1$ constant. Recently, pairs of oppositely charged (anti)merons have also been created and observed experimentally in Py films [83]. The fractional (anti)vortex could be realised for instance in a system with an out-of-plane external magnetic field and easy-plane anisotropy, with free energy density

$$\mathcal{F} = \tilde{J} \left( \frac{1}{2} \nabla_i \hat{M}_j \nabla_i \hat{M}_j - b_0 \hat{M}_z + \kappa_u \hat{M}_z^2 \right), \tag{4.1}$$

where we have defined the parameters $b_0 = \frac{M_0 B_0}{\tilde{J}}$, $\kappa_u = \frac{K_c}{\tilde{J}}$, which have dimension $1/\text{length}^2$. As the potential energy density terms in Eq. (4.1) are independent of the azimuthal angle $\phi$, the minimum energy configuration $\hat{\mathbf{M}}_{\text{min}}$ lies on a circle with constant $n_z = \cos(\theta_0)$, and it is easy to show that the minimum potential energy is obtained when $\cos(\theta_0) = \frac{b_0}{2\kappa_u}$. Assuming that at the edges of the sample, $x, y = \infty$, the magnetisation

---

[1]in this case the South Pole. We switched around the pole convention in Fig. 4.1 compared to the standard one used in Fig. 1.1c and 1.2 to get a clearer picture, as otherwise the magnetisation would have mostly been on the bottom of the sphere for the meron and fractional vortex!
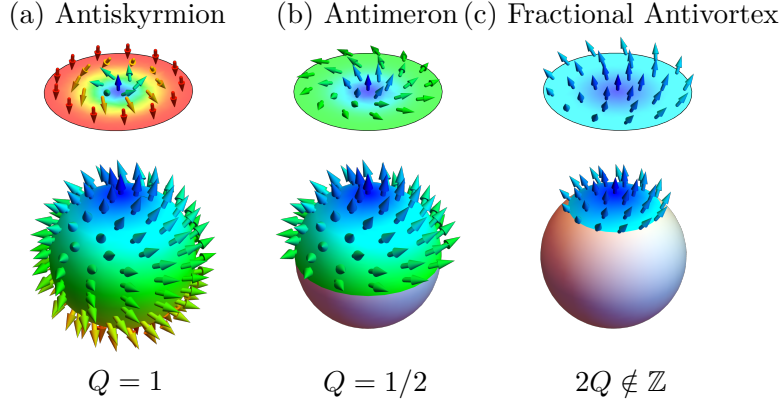
Figure 4.1 Representation of integer and fractional topological magnetic textures in 2D and on a 2-sphere. (a) Antiskyrmion. $Q = 1 \in \mathbb{Z}$ (note the sign change compared to the normal skyrmions in Fig. 1.1c v),vi)!). The magnetisation $\hat{\mathbf{M}}$ covers the entire sphere. The boundary condition is single-valued, $\hat{M}_z = 1$. (b) Antimeron. $Q = -\frac{1}{2} \notin \mathbb{Z}$, but $2Q \in \mathbb{Z}$. $\hat{\mathbf{M}}$ covers exactly half of the entire sphere. The boundary condition is multi-valued, $\hat{M}_x^2 + \hat{M}_y^2 = 1$. (c) Fractional Antivortex. $Q = \frac{1}{2}\left(1 - \frac{b_0}{2\kappa_p}\right)$, $2Q = \notin \mathbb{Z}$. $\hat{\mathbf{M}}$ covers less than half of the entire sphere, and the boundary condition is multi-valued, $\hat{M}_x^2 + \hat{M}_y^2 = 1 - \frac{b_0^2}{4\kappa_u^2}$. (Figure made by Vivek Lohani.)

adopts this minimum energy configuration and the azimuthal angle $\phi$ spans the full range $(0, 2\pi)$, $Q$ is simply given by the area of the enclosed spherical cap,

$$Q_{\text{(anti)vortex}} = \mp\frac{1}{4\pi}\int_0^{2\pi} d\phi \int_0^{\theta_0} d\theta \sin(\theta) = \mp\frac{1}{2}\left(1 - \frac{b_0}{2\kappa_u}\right), \qquad (4.2)$$

where the sign is negative for vortices and positive for antivortices. If there is no external magnetic field, $b_0 = 0$, we get back our (anti)meron with $Q = \mp\frac{1}{2}$. Here we have done the most straightforward spin interpolation for a boundary vortex configuration. For more exotic examples see [84], where the authors investigated so-called screw dislocations and the resulting non-integer topological charges.

While the fractional vortex is a nice theoretical object to demonstrate the concept of fractional topological charges, it is not the easiest thing to realise experimentally, as it involves controlling the boundaries of the sample in a very specific way to obtain the required spin interpolation. Luckily, we were able to find some more experimentally-friendly systems which also host fractional charges. We discuss these next.
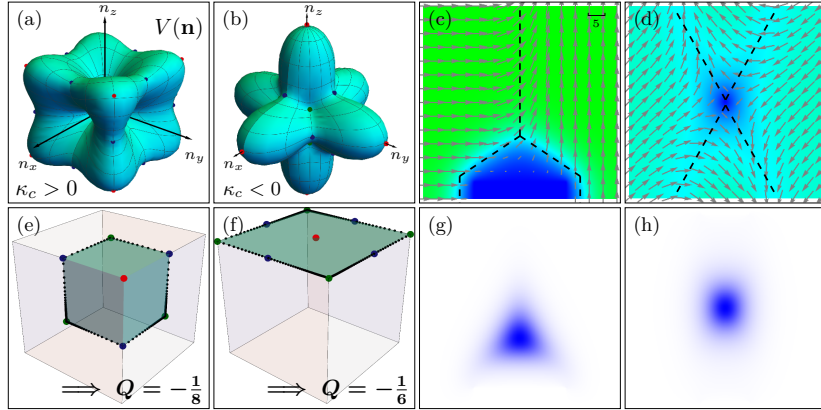
Figure 4.2 Fractional charges in magnets with cubic anistropy. (a) and (b) Potentials (in
$\hat{\mathbf{M}}$-space) for $\kappa_c > 0$, $\kappa_c < 0$, respectively, see Eq. (4.3) for the definition of $V(\hat{\mathbf{M}})$. The
easy/medium/hard axis directions are indicated by green/blue/red dots. (c) Meeting
point (in real space) between three domains $(1, 0, 0)$, $(0, 0, 1)$ and $(0, 1, 0)$ for $\kappa_c = 0.05$.
Colour code indicates the magnitude of the $n_z$ component: green for $n_z = 0$, dark blue for
$n_z = +1$. (d) Meeting point between four domains $\frac{1}{\sqrt{3}}(\pm 1, \pm 1, 1)$ for $\kappa_c = -0.05$. Colour
code as in (c). (e) and (f) Representation of magnetisation interpolation in $\hat{\mathbf{M}}$ space
of the magnetisation shown in panels (c) and (d). In the case $\kappa_c > 0$ $\hat{\mathbf{M}}$ interpolates
directly from $(1, 0, 0)$ to $(0, 0, 1)$ via $(1, 0, 1)$, etc. and therefore covers $1/8$ of the unit
cube, resulting in $Q = -1/8$. In the case $\kappa_c < 0$ $\hat{\mathbf{M}}$ interpolates directly from $(1, 1, 1)$ to
$(1, -1, 1)$ via $(1, 0, 1)$, etc. and covers $1/6$ of the. cube, yielding $Q = -1/6$. The negative
sign results from the magnetisation winding in the opposite sense (clockwise) as one
moves on an anticlockwise loop around the origin in the real space space representation
in panel (c), (d). (g) and (h) Representations of the topological charge in real space for
the cases $\kappa_c > 0$, $\kappa_c < 0$. Most of the charge is concentrated in the region where all three
or four domain walls meet.

### 4.1.1 Meeting of Domains in Cubic Magnets

To lowest order, a magnet with cubic magnetocrystalline anisotropy can be described by
the following free energy,

$$\mathcal{F} = \frac{\tilde{J}}{2}\nabla_i \hat{M}_j \nabla_i \hat{M}_j - K_c \left( \hat{M}_x^4 + \hat{M}_y^4 + \hat{M}_z^4 \right) + K_d(\hat{M}_x^2 \hat{M}_y^2 \hat{M}_z^2). \tag{4.3}$$

The constants $K_c, K_d$ determine the easy, medium and hard axes of the magnetisation,
which correspond to the directions of lowest, medium and highest energy, respectively.
Owing to the cubic symmetry, the three possible orientations for these axes are $(\pm1, 0, 0)$,
$(\pm1, \pm1, 0)$ and $(\pm1, \pm1, \pm1)$, and permutations thereof. To simplify matters, we will set
$K_d = 0$, which has the effect of fixing the direction of the medium axis to $(1, 1, 0)$ and its
permutations. Meanwhile, the directions of the easy and hard axes are determined entirely
by the sign of $K_c$[2]. We define $\kappa_c = K_c/\tilde{J}$, from which we obtain the natural length scale
$l \sim 1/\sqrt{\kappa_c}$ in the system. In Fig. 4.2, panels (a) and (b), we plot the potential defined in
Eq. (4.3) for the cases $\kappa_c > 0$, $\kappa_c < 0$, as a function of $\hat{M}_x, \hat{M}_y, \hat{M}_z$. We conclude from
these plots that the easy and hard axes for $\kappa_c > 0$ are $(1, 0, 0)$, $(1, 1, 1)$ respectively, and
vice versa for $\kappa_c < 0$. In a cubic magnet, magnetic domains, where the magnetisation
aligns with one of the easy axis directions, will form naturally. Suppose we have a 1D
system with two different domains at the boundaries, let's say $\hat{\mathbf{M}}(x = -\infty) = (1, 0, 0)$
and $\hat{\mathbf{M}}(x = +\infty) = (0, 1, 0)$ for the case $\kappa_c > 0$ — what will happen then to $\hat{\mathbf{M}}$ in
between these two domains? To find out, we need to solve the Euler Lagrange equations
resulting from Eq. (4.3). Looking at the shape of the potential, it is logical to assume
that $\theta = \frac{\pi}{2}$ stays constant throughout the interpolation, as that is the path of minimum
energy between $(1, 0, 0)$ and $(0, 1, 0)$. Thus, we obtain an equation of motion purely in
terms of the $\phi$ angle, $\frac{d^2\phi}{dx^2} = \sin(4\phi)$, also known as the Sine-Gordon equation [86]. This
equation admits the so-called kink and and anti-kink solutions $\phi(x) = \arctan\left(e^{\pm2\sqrt{\kappa_c}x}\right)$.
Er conclude that the magnetisation interpolates smoothly between the two domains
$\phi(x = -\infty) = 0$, $\phi(x = +\infty) = \pi/2$, with most of the change happening in the region
$-\frac{1}{2\sqrt{\kappa_c}} < x < \frac{1}{2\sqrt{\kappa_c}}$. This is something we could also have guessed just dimensional
analysis. One can understand this intuitively as follows: if $\kappa_c \gg 1$ then $\hat{\mathbf{M}}$ wants to stay
close to the easy axis directions as long as possible, so the domain wall is very thin. As $\kappa_c$
is reduced, there is less energy penalisation for drifting away from the easy axis directions,
and so the domain wall thickens. An analogous calculation can also be done for the $\kappa_c < 0$
case, one just has to add an extra minus sign to one of the sides in the Sine-Gordon

---

[2]for a full discussion with $K_d \neq 0$, see [85]. If both couplings are finite, the direction of the easy,
medium and hard axes depends on their ratios as well as signs.

equation and change the boundary conditions to, e.g., $\hat{\mathbf{M}}(x = -\infty) = (1, 1, 1)$ and $\hat{\mathbf{M}}(x = +\infty) = (1, -1, 1)$. The results of this analysis are qualitatively the same as in the $\kappa_c > 0$ case.

Now, what happens when we upgrade from a 1D system, where two domains at $x = \pm\infty$ meet, to a 2D system, where more than two domains can coexist? This is exactly the situation depicted in Fig. 4.2, panels (c) and (d) (data from mumax simulations). In panel (c) we have placed three domains $(1, 0, 0)$, $(0, 0, 1)$ and $(0, 1, 0)$ on the left, bottom and right of the sample, fixing about 25% of the spins along each edge, with a width corresponding to about 5% of the total width. In (d) we have done the analogous thing, but with four domains, $(1, 1, 1)$, $(1, -1, 1)$, $(-1, -1, 1)$ and $(-1, 1, 1)$. These domains are also depicted as green points on a cube in spin space in panels (e) and (f). After relaxing the system, 1D domain walls, indicated by dashed lines in panels (c) and (d), form between the different domains. The spin interpolation inside the domain walls happens along straight lines via the medium axes $(\pm 1, \pm 1, 1)$ in spin space, as shown in panels (e) and (f). Thus, the topological charge $Q$, represented by the green area enclosed by these lines, is quantised. It is given by $Q = -1/8$ for $\kappa_c > 0$ and $Q = -1/6$ for $\kappa_c < 0$ (the sign is negative because the magnetisation winds clockwise as we move anticlockwise around the edge of the system). In panels (g) and (h) we finally show the spatial distribution of the topological charge density (integrand of Eq. (1.16)) in 2D, and see that it is mostly concentrated around the region where the three or four domain walls meet.

## 4.1.2 Exploding Skyrmion

We already mentioned that a skyrmion can decay into two identical merons, but could it decay into anything smaller? In this subsection we will show that by adding some cubic anistropy to the system, it is indeed possible to get it to decay into smaller quantised charges of $Q = -\frac{1}{4}$. We use the following free energy density,

$$\mathcal{F} = \frac{\tilde{D}^2}{\tilde{J}} \left( \frac{1}{2} \nabla_i \hat{M}_j \nabla_i \hat{M}_j + \epsilon_{ijk} \hat{M}_i \nabla_j \hat{M}_k - b_0 \hat{M}_z - \tilde{\kappa}_c (\hat{M}_x^4 + \hat{M}_y^4 + \hat{M}_z^4) \right), \qquad (4.4)$$

where we rewrote everything inside the brackets in dimensionless parameters by defining $b = M_0 B_0 \tilde{J} / \tilde{D}^2$, $\tilde{\kappa}_c = K_c \tilde{J} / \tilde{D}^2$ and the length scale $1/q = \tilde{J} / \tilde{D}$. Using mumax3, we prepare a system where a skyrmion placed at the origin, with parameters $b_0 = 0.8$, $\tilde{\kappa}_c = 3.2$. After relaxing the system, the skyrmion remains in the middle with a somewhat shrunken radius (a consequence of using a relatively high value of $\tilde{\kappa}_c$), which suggests that the parameters $b_0, \tilde{\kappa}_c$ we have chosen are stable. We then suddenly switch off
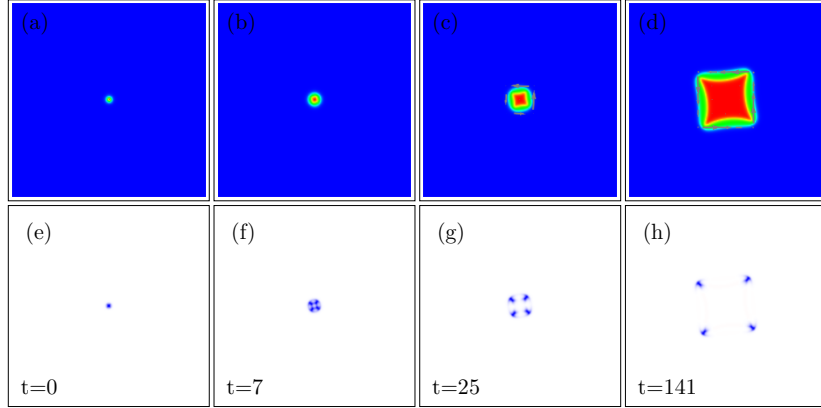
Figure 4.3 A skyrmion with $Q = -1$ is prepared in a system with cubic anistoropy, $\tilde{\kappa}_c = 3.2$, and a stabilising magnetic field, $b_0 = 0.8$. Suddenly turning off the magnetic field, $b_0 = 0$, makes the skyrmion unstable, and it decays into four topological sub particles of charge $Q = -\frac{1}{4}$. Panels (a)–(d) show the magnetisation, with the colour describing the value of the $\hat{M}_z$ component: blue for $\hat{M}_z = +1$, green for $\hat{M}_z = 0$ and red for $\hat{M}_z = -1$. Panels (e)–(f) show the spatial distribution of the topological charge density.

the stabilising magnetic field, $b_0 = 0$. In Fig. 4.3 we show how the magnetisation, panels (a)–(d), and distribution of topological charge, panels (e)–(h), are affected by this quench. Looking at panels (e)–(h), we see that over time the skyrmion decays into four sub-particles with charge $Q = -\frac{1}{4}$. Looking at the panels (a)–(d), we conclude that each of these $Q = -\frac{1}{4}$ charges is concentrated at the meeting of two domain walls. In each of these domain walls, $\phi = (0, \pi/2, \pi, 3\pi/4)$ stays constant, but $\theta$ interpolates between 0 and $\pi$, with the in-plane magnetisation in the two neighbouring domain walls differing by $\Delta\phi = \pi/2$. We also tried a similar experiment with negative $\tilde{\kappa}_c$. In this case, the domains become $(\pm 1, \pm 1, \pm 1)$, so that following a similar domain wall argument we would expect six $Q = -\frac{1}{6}$ particles to form when the skyrmion explodes. However this is not what happens — instead, positive and negative $Q = -\frac{1}{6}$ charges proliferate (although always such that there are six more negative ones than positive ones to conserve $Q_{\text{tot}} = -1$) in the system, resulting in a very messy-looking magnetisation. The reason for this is that for $\tilde{\kappa}_c < 0$, we no longer have an easy axis that aligns nicely with the background ferromagnetic magnetisation $\hat{\mathbf{M}}_{\text{FM}} = (0, 0, 1)$. Instead the system has to "choose" between the four closest identically-likely possibilities, $(\pm 1, \pm 1, 1)$, and thus gets "confused" about how to form its domain walls.
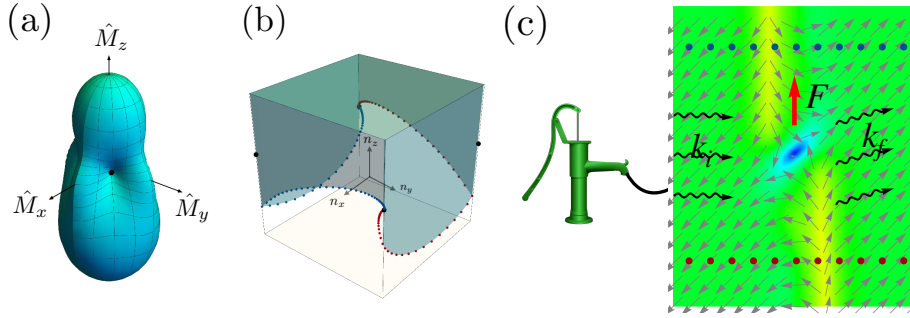
Figure 4.4 (a) Potential $V(\hat{\mathbf{M}})$ plotted for Eq. (4.5), with $b_0 = 0.35$, $\tilde{\kappa}_p = 1.25$, $\tilde{\kappa}_u = 2.5$. There are four energy minima, with coordinates $\phi = \frac{\pi}{4}, \frac{3\pi}{4}, \frac{5\pi}{4}, \frac{7\pi}{4}$, $\cos(\theta_0) = 0.137$. (b) Asymmetric domain walls (red and blue dotted lines) between the $\phi = \frac{\pi}{4}$ and $\phi = \frac{5\pi}{4}$ domains. (c) Magnetisation plot showing the fractional defect, which forms at the meeting point between the two asymmetric domain walls from (b). To plot the domain wall interpolation in (b) we used the spins located along the red/blue dashed lines in panel (c). Due to the asymmetry of the domain walls, the defect has fractional, non-quantised topological charge $Q = -0.603$. The system is translationally symmetric in the $y$ direction, but not in the $x$ direction. Magnons with $\mathbf{k}_i = (k, 0)$ are pumped into the system by wiggling the spins on the left boundary with a frequency $\omega(k)$ in a spatially uniform manner. As the magnons scatter off the defect they transfer momentum $\Delta \mathbf{k} = \mathbf{k}_i - \mathbf{k}_f$ to the defect, generating a force which makes it move.

### 4.1.3 Trapping by Domain Walls with Broken Symmetry

So far, the fractional magnetic charges we have generated share the unfortunate property that they are pretty difficult to control externally. In the case of the cubic magnet domain walls, we would have to move one of the domains to move the topological charge, which is energetically costly. In the case of the exploding skyrmion, the $Q = -\frac{1}{4}$ charges forming at the intersections of two domain walls naturally move apart by themselves over time. This comes about because the domain walls have negative energy, so that it is energetically favourable for the system to make them as long as possible. Again, this is something we have little control over. In this subsection, we show how to generate a topological defect which is fractionally charged but also, at least in theory, mobile and easy to manipulate.

The idea is to use the following free energy density,

$$\mathcal{F} = \frac{\tilde{D}^2}{\tilde{J}} \left( \frac{1}{2} \nabla_i \hat{M}_j \nabla_i \hat{M}_j + \hat{M}_z \boldsymbol{\nabla} \cdot \hat{\mathbf{M}} - \hat{\mathbf{M}} \cdot \boldsymbol{\nabla} \hat{M}_z + \tilde{\kappa}_p (\hat{M}_x^4 + \hat{M}_y^4) + \tilde{\kappa}_u \hat{M}_z^2 - b_0 \hat{M}_z \right),$$

$$(4.5)$$

where in addition to the usual Heisenberg term we included some interfacial DMI as part of the spatial gradient terms. The potential energy terms include in-plane anisotropy, $\tilde{\kappa}_p(\hat{M}_x^4 + \hat{M}_y^4)$, uniaxial anisotropy, $\tilde{\kappa}_u \hat{M}_z^2 - b_0 \hat{M}_z$, and a Zeeman term due to an external magnetic field, $-b_0 \hat{M}_z$, with the dimensionless couplings defined as $\tilde{\kappa}_c = K_c \tilde{J}/\tilde{D}^2$, $\tilde{\kappa}_p = K_p \tilde{J}/\tilde{D}^2$, and $b_0 = M_0 B_0 \tilde{J}/\tilde{D}^2$. For $\tilde{\kappa}_p, \tilde{\kappa}_u > 0$ the potential energy has four equal energy minima at $\phi_n = \frac{\pi}{4} + \frac{n\pi}{2}, n \in 0, 1, 2, 3$, with $\theta_0$ determined by the relative sizes of $b_0, \tilde{\kappa}_p, \tilde{\kappa}_u$. In Fig. 4.4a we plot the potential energy for the parameters $b_0 = 0.35$, $\tilde{\kappa}_p = 1.25$, $\tilde{\kappa}_u = 2.5$. Suppose we take a 1D system and fix the magnetisation at $x = \pm\infty$ to point in the $\phi_0$ and $\phi_2$ minimum energy directions, respectively, $\hat{\mathbf{M}}(x = \infty) = (\frac{1}{\sqrt{2}}\sin(\theta_0), \frac{1}{\sqrt{2}}\sin(\theta_0), \cos(\theta_0))$ and $\hat{\mathbf{M}}(x = -\infty) = (-\frac{1}{\sqrt{2}}\sin(\theta_0), -\frac{1}{\sqrt{2}}\sin(\theta_0), \cos(\theta_0))$. This time, the interpolation between the two boundaries can happen via two different energy degenerate paths, shown in Fig. 4.4b. The cause of this symmetry-breaking is the DMI term, which breaks the chiral symmetry of the system. To see what happens in 2D, we prepare a system of size $-x_0 < x < x_0, -y_0 < y < y_0$, where we again fix the spins on the two edges $x = \pm x_0$ to point in the same $\phi_0$ and $\phi_2$ minimum energy directions. In Fig. 4.4c we see that between $y = -y_0$ and $y = 0$, $\hat{\mathbf{M}}$ chooses to interpolate via the red path, but then at around $y = 0$ it spontaneously switches to the blue path and remains this way until $y = y_0$. The blue region in Fig. 4.4c, where the interpolation switches from the red path to the blue path, results in a "trapped" topological charge of $Q \approx -0.603$. If the system were infinite in the $y$ direction it would be translationally invariant in that direction, as the two domain walls are degenerate. Thus we have a Goldstone mode which we could potentially activate to set the fractional defect into motion, something we will try to exploit in Sec. 4.4.

## 4.2 Emergent Electromagnetic Fields

Back in Sec. 1.4.1, we claimed that electrons traversing a topologically non-trivial magnetisation experience emergent $B$ and $E$ fields, given in Eq. (1.17). This is in fact also true for magnons, but they experience emergent fields twice as large as electrons, so that we should update Eq. (1.17) to

$$
\begin{aligned}
E_i^e &= s\frac{\hbar}{|e|}\hat{\mathbf{M}} \cdot (\partial_i \hat{\mathbf{M}} \times \partial_t \hat{\mathbf{M}}), \\
B_i^e &= s\frac{\hbar}{|e|}\frac{1}{2}\epsilon_{ijk}\hat{\mathbf{M}} \cdot (\partial_j \hat{\mathbf{M}} \times \partial_k \hat{\mathbf{M}}),
\end{aligned}
\tag{4.6}
$$

where $s = \frac{1}{2}$ for the electron and $s = 1$ for the magnon. The theory for this is well-known and provided in detail for example in [87] for the magnons and [88] for the electrons. The similarity comes about because for both particles their spin vector instantaneously aligns with the local magnetisation, $\mathbf{S}_e, \mathbf{S}_m \parallel \hat{\mathbf{M}}$, as the particles move through the system. In the case of the electrons this is because the exchange coupling $-J_H \hat{\mathbf{M}} \cdot \sigma$ is the dominant energy scale of the system, while in the case of the magnons it is because magnons are by definition the small excitations around the local magnetisation, $\hat{\mathbf{M}}$. Here we will briefly derive the result for electrons, with the understanding that the calculation for magnons is analogous. Let $\psi = (c_\uparrow, c_\downarrow)$, $\psi' = (c'_\uparrow, c'_\downarrow)$ be the original and rotated wavefunction of the electron, respectively, where the spin axis of $\psi'$ is parallel to $\hat{\mathbf{M}}$. We can write $\psi' = U^{-1}\psi$, where

$$U = \begin{pmatrix} \cos(\theta/2) & -\sin(\theta/2)e^{-i\phi} \\ \sin(\theta/2)e^{i\phi} & \cos(\theta/2) \end{pmatrix}. \tag{4.7}$$

In terms of $\psi'$, the kinetic energy (for the magnon, it would be the Heisenberg energy) reads

$$\frac{1}{2m}\psi'^\dagger U^{-1} p_\mu p_\mu (U\psi') = \frac{1}{2m}\psi'^\dagger (p_\mu - i\hbar U^{-1}\partial_\mu U)^2 \psi'. \tag{4.8}$$

This reminds us of minimal coupling, $p_i \to p_i - qA_i$ for a charged particle with charge $q$. The difference is that here we are dealing with two-component spinors $\psi$, rather than one component fields, so that the effective gauge field sandwiching them, $\frac{i\hbar}{q}U^{-1}\partial_\mu U$, is a $2 \times 2$ "vector matrix", rather than a one-component vector field. Only the *diagonal* part[3] of $i\hbar U^{-1}\partial_\mu U$ is relevant for calculating the emergent electromagnetic fields. This leads us to define the vector gauge field

$$A_\mu = \pm\frac{\hbar}{|e|}\frac{1}{2}(1 - \cos(\theta))\partial_\mu\phi, \tag{4.9}$$

where the sign depends on the spin alignment of the electron's spin axis with respect to $\hat{\mathbf{M}}$: positive for $c'_\uparrow$ (aligned) and negative for $c'_\downarrow$ (anti-aligned). Most of the electrons align with $\hat{\mathbf{M}}$, as this is energetically much more favourable, so we suppress the $-$ sign. From this gauge field we can easily obtain the electric and magnetic fields Eq. (4.6) via the EM tensor defined in the usual way, $F_{\mu\nu} = \partial_\mu A_\nu - \partial_\nu A_\mu$.

---

[3]For the magnon the corresponding thing to do would be to take only the $L_z$ component of the $i\hbar U^{-1}\partial_\mu U$ object. In this case $U$ is a $3 \times 3$ rather than $2 \times 2$ matrix, $U = e^{i\theta(-\sin(\phi)L_x + \cos(\phi)L_y)}$ with $[L_j, L_k] = i\epsilon_{ijk}L_i$.
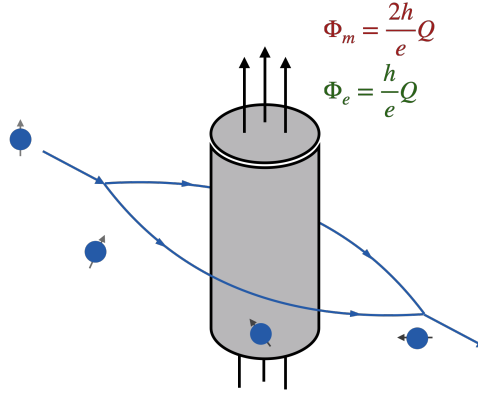
Figure 4.5 Ahoronov Bohm effect for electrons and magnons traveling in a magnetic system with a localised topological charge, $Q$. Electrons experience a flux $\Phi_e = \frac{h}{e}Q$, while magnons experience a flux $\Phi_m = \frac{2h}{e}Q$.

## 4.3   Scattering from Fractional Charges

Let us now provide an argument for why scattering of low energy electrons and magnons from fractional (as opposed to integer) charges is particularly strong. We use the setup depicted in Fig. 4.5, for simplicity sending the radius of the cylinder $r_c \to 0$, where all the topological charge is concentrated at the origin $r = 0$. This mimics the Aharonov-Bohm setup, which was already solved in 1959 [89]. We can define the gauge field as $A_\chi = \frac{\hbar s Q}{r}$, $A_r = A_z = 0$, which gives the Schrödinger equation

$$\frac{\hbar^2}{2m} \left[ -\frac{\partial^2}{\partial r^2} - \frac{1}{r}\frac{\partial}{\partial r} + \frac{1}{r^2}\left(-i\frac{\partial}{\partial\chi} - sQ\right)^2 \right] = E\psi,$$

Expanding the wavefunction into angular momentum eigenstates, $\psi = \sum_m e^{im\chi}\psi_m(kr)$, we can be reduce this to Bessel's equation

$$r^2\frac{\partial^2\psi_m(r)}{\partial r^2} + r\frac{\partial\psi_m(r)}{\partial r} + \left(k^2r^2 - (m - sQ)^2\right)\psi_m(r) = 0 \qquad (4.10)$$

with $k^2 = 2mE/\hbar^2$. The solution of this Bessel equation is the Bessel function of the first kind, $\psi_m(r) = J_{|m-sQ|}(kr)$ (we throw away $Y_{|m-sQ|}(kr)$ as it blows up at $r = 0$, which we don't want). For large arguments, $kr \gg 1$, the Bessel function has the asymptotic form $J_m(kr) = \sqrt{\frac{2}{\pi kr}}\cos\left(kr - \frac{|m|\pi}{2} - \frac{\pi}{4}\right)$. The phase shift, defined through $\lim_{kr\gg1}\psi_m(kr) = \sqrt{\frac{2}{\pi kr}}\cos\left(kr + \delta_m - \frac{|m|\pi}{2} - \frac{\pi}{4}\right)$, is given by

$$\delta_m = \frac{\pi}{2}\left(|m| - |m - sQ|\right). \qquad (4.11)$$

Phase shifts are important for calculations involving scattering. Following the convention used in [72], we send in a stream of electrons or magnons from $x = -\infty$ with momentum $\mathbf{k} = (k, 0, 0)^T$ onto the topological charge located at $r = 0$. As usual for scattering theory, we assume that in the far field the resulting scattered wavefunction consists of a free part, $e^{ik\cos(\chi)r}$, and a scattered part, $\frac{e^{ikr}}{\sqrt{r}}f(\chi)$. We can set this equal to the general solution of the differential equation Eq. (4.10), $\sum_m c_m \psi_m(kr)$,

$$\sum_m c_m \sqrt{\frac{2}{\pi k r}} \cos\left(kr + \delta_m - \frac{|m|\pi}{2} - \frac{\pi}{4}\right) \simeq e^{ikr\cos(\chi)} + \frac{e^{ikr}}{\sqrt{r}}f(\chi).$$

Using the plane wave expansion, $\sum_n i^n J_n(kr)e^{in\chi}$, and comparing the coefficients of $e^{i(\pm kr + m\chi)}$, it is possible to solve for the unknown coefficients $c_m$. Using those, we obtain the following standard result for the scattering amplitude,

$$f(\chi) = \frac{e^{-i\pi/4}}{\sqrt{2\pi k}} \sum_m e^{im\chi}\left(e^{i\delta_m} - 1\right). \tag{4.12}$$

The scattering cross-section is then given by $\frac{d\sigma(\chi)}{d\chi} = |f(\chi)|^2$. We can also define the following parallel and perpendicular transport scattering cross-sections,

$$\begin{aligned}
\sigma_\parallel &= \int d\chi(1 - \cos(\chi))\frac{d\sigma}{d\chi} = \frac{2}{k}\sum_{m\in\mathbb{Z}} \sin^2\left(\delta_{m+1} - \delta_m\right), \\
\sigma_\perp &= \int d\chi \sin(\chi)\frac{d\sigma}{d\chi} = \frac{1}{k}\sum_{m\in\mathbb{Z}} \sin\left(2(\delta_{m+1} - \delta_m)\right).
\end{aligned} \tag{4.13}$$

Using the formula in Eq. (4.11), all terms in the sum for $\sigma_{\parallel,\perp}$ vanish if $sQ \in \mathbb{Z}$. Physically speaking, all integer flux can be gauged away and won't scatter an incoming magnon or electron. However, if $sQ \notin \mathbb{Z}$, then $\delta_{\lfloor sQ\rfloor} = \frac{\pi}{2}(2\lfloor sQ\rfloor - sQ)$ and $\delta_{\lfloor sQ\rfloor+1} = \frac{\pi}{2}sQ$, so the terms $\frac{1}{k}\sin^2\left(\delta_{m+1} - \delta_m\right) = \frac{1}{k}\sin^2(\pi sQ)$ or $\frac{1}{k}\sin\left(2(\delta_{m+1} - \delta_m)\right) = \frac{1}{k}\sin(2\pi sQ)$ don't vanish, as long as $sQ, 2sQ \notin \mathbb{Z}$, respectively. If these conditions are fulfilled, $\sigma_\parallel$ and $\sigma_\perp$ can get really large for low energy particles, $k \to 0$.

## 4.4 Magnon Engine

We now want to test the knowledge we gained about the scattering cross-sections $\sigma_\parallel$ and $\sigma_\perp$ in a concrete numerical experiment involving magnons. We know from the analysis we just performed that $2Q \notin \mathbb{Z}$ in order to see any effects from scattering, so we must avoid using a $Q = \frac{1}{2}$ fractional charge. Luckily, the fractional defect we found

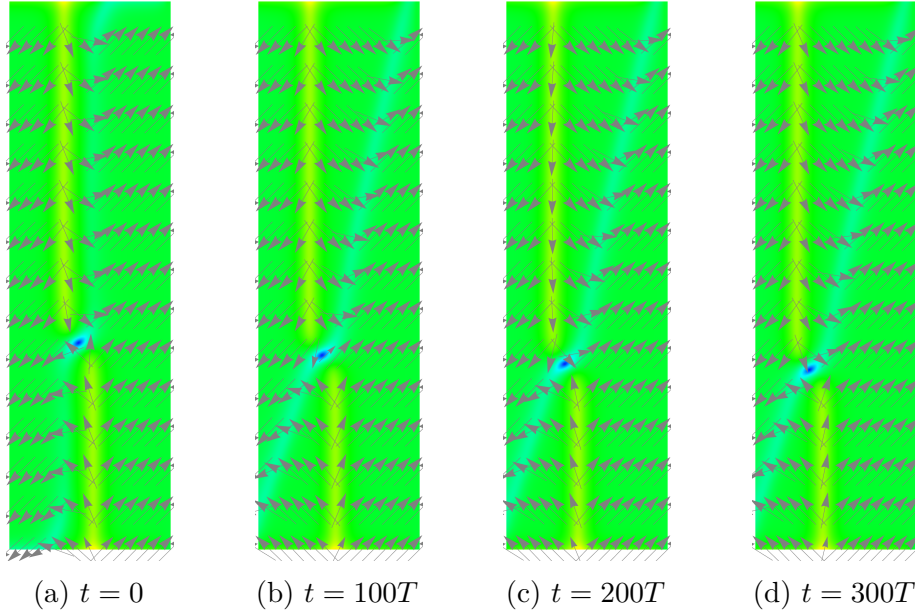(a) $t = 0$      (b) $t = 100T$      (c) $t = 200T$      (d) $t = 300T$

Figure 4.6 Fractional defect (parameters $b_0 = 0.62$, $\tilde{\kappa}_p = 2.22$, $\tilde{\kappa}_u = 4.44$, $\alpha = 0.1$) driven by magnons with $\omega = 3.65$ (dimensionless units). The defect moves both left and down over time, and loses its translational invariance in the $y$ direction. Time $t$ is counted in units of the time period $T = \frac{2\pi}{\omega}$.

in Fig. 4.4 had $Q = -0.603$, so it fits the bill nicely. By simultaneously wiggling all the spins in the region $x = -x_0$, $-y_0 < y < y_0$ at the frequency $\omega(k) = \epsilon(k)/\hbar$, where $\epsilon(k)$ is the dispersion of the magnons, we pump magnons with momentum $\mathbf{k}_i = (k, 0)$ into the system. As the magnons scatter off the topological defect, their momentum changes by $\Delta \mathbf{k} = \mathbf{k}_f - \mathbf{k}_i = k(\cos(\chi) - 1, \sin(\chi))$[4], so that by conservation of momentum $d\mathbf{P} = -\hbar \Delta \mathbf{k}$ is transferred to the defect. Assuming that the magnons are being pumped at a rate $N\mathrm{m}^{-1}\mathrm{s}^{-1}$, there will be $N d\sigma$ magnons being scattered into the differential angle $d\Omega$ per second. This generates a differential force $d\mathbf{F}^{\mathrm{scatt.}} = -N(d\sigma_\parallel, d\sigma_\perp)\hbar k$ on the defect. Integrating $d\mathbf{F}^{\mathrm{scatt.}}$ over all polar angles we obtain the total scattering force,

$$\mathbf{F}^{\mathrm{scatt.}}(k) = -\begin{pmatrix} \sigma_\parallel(k) \\ \sigma_\perp(k) \end{pmatrix} N\hbar k. \tag{4.14}$$

Assuming that the fractional defect retains its shape and only its translational Goldstone mode is activated in the ensuing dynamics, we can obtain the velocity of the defect by solving the 2D Thiele equation, Eq. (1.20). The general solution for the defect's velocity

---

[4]Here we assume that scattering is elastic, $k_f = k_i$, which is valid if we assume that the energy of the incoming magnon is much larger than the scattering potential of the defect (Born approximation)

is then

$$\begin{pmatrix} V_x \\ V_y \end{pmatrix} = \frac{1}{\alpha^2 D_{xx} D_{yy} - \alpha^2 D_{xy}^2 + (4\pi Q)^2} \begin{pmatrix} -\alpha F_x D_{yy} + F_y \left( 4\pi \text{sgn}(\gamma) Q + \alpha D_{xy} \right) \\ -\alpha F_y D_{xx} + F_x \left( -4\pi \text{sgn}(\gamma) Q + \alpha D_{xy} \right) \end{pmatrix},$$
(4.15)

where $\mathbf{F} = \mathbf{F}^{\text{scatt.}} + \mathbf{F}^{\text{wall}}$ is the *total* force acting on the defect, made up of the scattering force, $\mathbf{F}^{\text{scatt.}}$, and any other additional forces from the sample walls, $\mathbf{F}^{\text{wall}}$. For our defect, $\mathcal{D}_{xx}$ scales with the system length in the $y$-direction, while $\mathcal{D}_{xy}, \mathcal{D}_{yy}, Q$ are all constant. Thus, $\mathcal{D}_{xx} \gg \mathcal{D}_{xy}, \mathcal{D}_{yy}, Q$ for a long enough system. In addition, we will assume that the scattering force in the $x$ direction is compensated by an equal and opposite reaction force from the wall, such that $F_x = F_x^{\text{scatt.}} + F_x^{\text{wall}} = 0$. Under these two assumptions, the velocity in Eq. (4.15) reduces to $\mathbf{V} = -F_y^{\text{scatt.}}/(\alpha D_{yy})\mathbf{e}_y$. Thus, we would expect the defect to start moving in the vertical direction with constant speed proportional to $\sigma_\perp$ as we pump the system with magnons. Unfortunately, this theory is contradicted by the reality of the numerical experiment, where we actually observe something else! The defect indeed does move over time, but it does so diagonally rather than vertically, see Fig. 4.6. In addition, the defect does not retain its translational symmetry in the $y$-direction, but actually deforms, see Fig. 4.6. The intermediate domains which form in the upper right and lower left of the sample are none other than the domains corresponding to the remaining two easy axis directions, $\phi = \frac{3\pi}{4}$ and $\frac{7\pi}{4}$. The ensuing loss of translational invariance means that the approximations $\mathcal{D}_{xx} \gg \mathcal{D}_{xy}, \mathcal{D}_{yy}$ we used are no longer valid. One possible way to remedy this is to use anisotropic exchange coupling, with $\tilde{J}_y \gg \tilde{J}_x$. This makes the system stiffer in the $y$-direction, and increases the chances of translational invariance being preserved in that direction. Preliminary experiments with a system where $\tilde{J}_y = 100\tilde{J}_x$ are showing encouraging results, as the defect does not deform over the course of the driving anymore. However, the fact that the defect's mass tensor now becomes non-isotropic means that more work is needed to give an accurate analytical prediction for $\mathbf{F}^{\text{scatt.}}$.

# Conclusion and Outlook

As all good things, this thesis too must come to an end. Before we part, dear reader, a few words to summarise what we have achieved and what still remains to be done.

Our story began with the Archimedean screw, and how a nano-sized version of it could be constructed using a chiral magnet. We saw that, by driving the conical phase of the magnet with an oscillating GHz magnetic field $\mathbf{B}_1(t)$, we could activate the translational/rotational Goldstone mode of the system, resulting in rotational motion reminiscent of the Archimedean screw, with rotational speed $\omega_{\text{screw}} \sim |\mathbf{B}_1|^2$. We derived this effect analytically and confirmed it with numerical simulations, obtaining a perfect match between the two methods. We suggested how, by tuning external parameters such as the polarisation and driving frequency of $\mathbf{B}_1(t)$, or the strength of the static magnetic field $\mathbf{B}_0$, the user could adjust the size and direction of $\omega_{\text{screw}}$. Just like the Archimedean screws we know from everyday life (turbines, drills, etc), the nano Archimedean screw can be used as a tool to transport nano-materials such as spin and charge, resulting in spin and electric currents. A calculation of the Archimedean screw-generated electric current, taking into account the effects of disorder, yielded a current density estimate on the order of $10^4 - 10^7 \text{Am}^{-2}$ for the metallic chiral magnet MnSi — a huge number which gives every hope of being experimentally detectable. In fact, an experiment to test this is currently under way in the group of Prof. Pfleiderer in TUM. The plan is to drive a sample of MnSi both parallel and perpendicular to the helical axis $\mathbf{q}$ and measure the DC voltage generated by the electric current parallel to $\mathbf{q}$. As the Archimedean screw mode is only activated by perpendicular driving, $\mathbf{B}_\perp(t) \perp \mathbf{q}$, a finite voltage should only build up in the latter of the two setups. This provides an easy way, at least in theory, to confirm the origin of the Archimedean screw effect.

To test the stability of the Archimedean screw we investigated what fate awaited small magnonic excitations. Using Floquet spin wave theory, we calculated the eigenspectra (in particular, the imaginary parts) of these magnons, and concluded that the Archimedean screw solution would be stable up to a critical driving strength proportional to the Gilbert damping in the system, $B_1^{\text{crit.}} \sim \alpha$. We saw in numerical experiments that upon increasing

the driving strength, $B_1 > B_1^{\text{crit.}}$, the system developed a new mode with incommensurate frequency $\omega_{\text{new}}$ and momentum $k_{\text{new}}$ — the signature of a time quasicrystal. The $\omega_{\text{new}}$ and $k_{\text{new}}$ found numerically corresponded exactly to the values calculated analytically for the leading order magnon instability, confirming that this was indeed the correct theoretical explanation for the effect. Actually, such magnon instabilities are pretty universal and one could expect them to occur in other driven systems too. A possible extension would be to do this same calculation for driven skyrmions, although it might be technically much more challenging to implement, as we cannot use the same neat spatial Fourier transform tricks there. Experimentally speaking, the detection of a monochromatic frequency in the $100 - 1000$ MHz range would be a smoking gun for identifying the time quasicrystal instability.

After the conical state, we shifted our attention to skyrmions. We saw that, just like for the Archimedean screw, the two translational Goldstone modes of a single skyrmion could also be activated at quadratic order in $\mathbf{B}_1$, but only if the driving field was tilted, $\mathbf{B}_1(t) = (\mathbf{B}_{1,\perp}(t), \mathbf{B}_{1,\parallel}(t))$. In the Thiele equation framework, such driving generates a constant force $f_{\text{slide}} \sim B_{1,\parallel} B_{1,\perp}$ which results in a constant "sliding" velocity of the skyrmion, $v_{\text{slide}} \sim B_{1,\parallel} B_{1,\perp}$. To calculate $\mathbf{f}_{\text{slide}}$ we needed detailed knowledge of the first order oscillatory response of the skyrmion. Using a semi-analytical approach we were able to obtain this first order response in terms of the $m = 0, \pm 1$ angular momentum bound and scattering states of the skyrmion. The non-trivial treatment of damping and the Kittel resonance of the ferromagnetic background made this a much more technically challenging calculation than its analogue in the Archimedean screw project. Comparing our analytically obtained $\mathbf{v}_{\text{screw}}$ with numerical simulations we again observed a perfect fit. The success of the perturbative approach we used for both the Archimedean screw and the sliding skyrmion gives us hope that it could be replicated in other magnetic systems with Goldstone modes. For example, the skyrmion lattice has a Goldstone mode involving a combined local spin and a global orbital angular momentum rotation of the magnetisation about the $z$ axis — it would only be natural to expect $\mathbf{B}_1(t)$ to activate this too. Using the well-known approximation of the skyrmion lattice as a three-pronged node of helices propagating at $120°$ to each other, it might even be possible to develop an analytical expression for the resulting rotational speed of the skyrmion lattice.

In the final part, we looked at fractional topological charges in two-dimensional magnetic systems. We saw that such quantised charges could manifest themselves at the meeting point between three or more magnetic domains in systems with cubic anistropy ($Q = -\frac{1}{6}, -\frac{1}{8}$), or in the shrapnel of exploding skyrmions ($Q = -\frac{1}{4}$). By trapping some (non-quantised) topological charge between two symmetry-broken degenerate domain

walls, we were able to construct a system which could host a fractional charge, while remaining translationally invariant in the direction perpendicular to the domain walls. This implies the existence of a Goldstone mode in the direction parallel to the domain walls. We tried to exploit the strong scattering properties of fractional charges to activate this Goldstone by pumping the system with magnons. Unfortunately, the numerical simulations for this experiment are not yet fully working as expected, probably due to the translational symmetry which guarantees the Goldstone mode's existence being too sensitive to the driving. One idea we are currently trying out to better protect the translational symmetry is stiffening the system preferentially in the direction of translational invariance, for instance by using an anisotropic exchange constant. This is showing promising numerical results, but an anisotropic theory to understand how this modifies the forces pushing the defect still needs to be developed.

As always in science though, we can plot and plan all we like but nature dances to its own tune. And the right idea is just as likely to be borne out of some craftily constructed argument as it is to hit you in the head, like Newton's apple, when you least expect it!

# Bibliography

[1] Xichao Zhang, G.P. Zhao, Hans Fangohr, J. Ping Liu, W.X. Xia, J. Xia, and F.J. Morvan. Skyrmion-skyrmion and skyrmion-edge repulsions in skyrmion-based racetrack memory. *Scientific reports*, 5(1):1–6, 2015.

[2] N.S. Kiselev, A.N. Bogdanov, R. Schäfer, and UK Rößler. Chiral skyrmions in thin magnetic films: New objects for magnetic storage technologies? *Journal of Physics D: Applied Physics*, 44(39):392001, 2011.

[3] I.E. Dzyaloshinskii. The theory of helicoidal structures in antiferromagnets. ii. metals. *Sov. Phys. JETP*, 20(1):223–231, 1965.

[4] Per Bak and M. Høgh Jensen. Theory of helical magnetic structures and phase transitions in mnsi and fege. *Journal of Physics C: Solid State Physics*, 13(31):L881, 1980.

[5] Tôru Moriya. Anisotropic superexchange interaction and weak ferromagnetism. *Physical review*, 120(1):91, 1960.

[6] Lukas Heinen. *Chiral Magnets in and out of Equilibrium*. PhD thesis, Universität zu Köln, 2021.

[7] Andreas Bauer and Christian Pfleiderer. Generic aspects of skyrmion lattices in chiral magnets. In *Topological Structures in Ferroic Materials*, pages 1–28. Springer, 2016.

[8] Sebastian Mühlbauer, Benedikt Binz, F Jonietz, Christian Pfleiderer, Achim Rosch, Anja Neubauer, Robert Georgii, and Peter Böni. Skyrmion lattice in a chiral magnet. *Science*, 323(5916):915–919, 2009.

[9] C. Pfleiderer, S. R. Julian, and G. G. Lonzarich. Non-fermi-liquid nature of the normal state of itinerant-electron ferromagnets. *Nature*, 414(6862):427–430, nov 2001.

[10] Johannes Waizner. *Spin Wave Excitations in Magnetic Helices and Skyrmion Lattices*. PhD thesis, Universität zu Köln, 2016.

[11] Charles Kittel. On the theory of ferromagnetic resonance absorption. *Physical review*, 73(2):155, 1948.

[12] Tony Hilton Royle Skyrme. A non-linear field theory. In *Selected papers, with commentary, of Tony Hilton Royle Skyrme*, pages 195–206. World Scientific, 1994.

[13] Alexei N. Bogdanov and D.A. Yablonskii. Thermodynamically stable "vortices" in magnetically ordered crystals. the mixed state of magnets. *JETP*, 95(1):178, 1989.

[14] Bill Casselman. Stereographic projection. American Mathematical Society. Accessed December 27, 2021 https://www.ams.org/publicoutreach/feature-column/fc-2014-02, 2014.

[15] Peter McGrath. An extremely short proof of the hairy ball theorem. *The American Mathematical Monthly*, 123(5):502–503, 2016.

[16] B. Binz, A. Vishwanath, and V. Aji. Theory of the helical spin crystal: A candidate for the partially ordered state of mnsi. *Phys. Rev. Lett.*, 96:207202, May 2006.

[17] Benedikt Binz and Ashvin Vishwanath. Theoretical proposal predicting anomalous magnetoresistance and quadratic hall effect in the partially ordered state of mnsi. *Journal of magnetism and magnetic materials*, 310(2):1062–1064, 2007.

[18] Minhyea Lee, W. Kang, Y. Onose, Y. Tokura, and N. P. Ong. Unusual hall effect anomaly in mnsi under pressure. *Phys. Rev. Lett.*, 102:186601, May 2009.

[19] A. Neubauer, C. Pfleiderer, B. Binz, A. Rosch, .R Ritz, P.G. Niklowitz, and P. Böni. Topological hall effect in the a phase of mnsi. *Physical review letters*, 102(18):186602, 2009.

[20] Tomek Schulz, R. Ritz, Andreas Bauer, Madhumita Halder, Martin Wagner, Chris Franz, Christian Pfleiderer, Karin Everschor, Markus Garst, and Achim Rosch. Emergent electrodynamics of skyrmions in a chiral magnet. *Nature Physics*, 8(4):301–304, 2012.

[21] Lingyao Kong and Jiadong Zang. Dynamics of an insulating skyrmion under a temperature gradient. *Physical review letters*, 111(6):067203, 2013.

[22] Karin Everschor, Markus Garst, Benedikt Binz, Florian Jonietz, Sebastian Mühlbauer, Christian Pfleiderer, and Achim Rosch. Rotating skyrmion lattices by spin torques and field or temperature gradients. *Physical Review B*, 86(5):054432, 2012.

[23] Masahito Mochizuki, XZ Yu, Shinichiro Seki, Naoya Kanazawa, Wataru Koshibae, Jiadong Zang, Maxim Mostovoy, Yoshinori Tokura, and Naoto Nagaosa. Thermally driven ratchet motion of a skyrmion microcrystal and topological magnon hall effect. *Nature materials*, 13(3):241–246, 2014.

[24] Jan Müller and Achim Rosch. Capturing of a magnetic skyrmion with a hole. *Physical Review B*, 91(5):054410, 2015.

[25] Shi-Zeng Lin, Charles Reichhardt, Cristian D Batista, and Avadh Saxena. Particle model for skyrmions in metallic chiral magnets: Dynamics, pinning, and creep. *Physical Review B*, 87(21):214419, 2013.

[26] Lev Landau and Evgeny Lifshitz. On the theory of the dispersion of magnetic permeability in ferromagnetic bodies. In *Perspectives in Theoretical Physics*, pages 51–65. Elsevier, 1992.

[27] Thomas L. Gilbert. A lagrangian formulation of the gyromagnetic equation of the magnetization field. *Phys. Rev.*, 100:1243, 1955.

[28] A. A. Thiele. Steady-state motion of magnetic domains. *Phys. Rev. Lett.*, 30:230–233, Feb 1973.

[29] Jan Masell, Xiuzhen Yu, Naoya Kanazawa, Yoshinori Tokura, and Naoto Nagaosa. Combing the helical phase of chiral magnets with electric currents. *Physical Review B*, 102(18):180402, 2020.

[30] Roberto E. Troncoso and Alvaro S. Núñez. Thermally assisted current-driven skyrmion motion. *Physical Review B*, 89(22):224403, 2014.

[31] Karin Everschor-Sitte, Jan Masell, Robert M. Reeve, and Mathias Kläui. Perspective: Magnetic skyrmions—overview of eecent progress in an active research field. *Journal of Applied Physics*, 124(24):240901, 2018.

[32] Junichi Iwasaki, Masahito Mochizuki, and Naoto Nagaosa. Universal current-velocity relation of skyrmion motion in chiral magnets. *Nature communications*, 4(1):1–8, 2013.

[33] Daniel Manzano. A short introduction to the Lindblad master equation. *AIP Advances*, 10(2):025106, 2020.

[34] Nina del Ser, Lukas Heinen, and Achim Rosch. Archimedean screw in driven chiral magnets. *SciPost Physics*, 11(1):009, 2021.

[35] Schtroumpfette, schtroumpf à fleur, schtroumpf paysan, schtroumpf qui regarde le ciel. Accessed February 17, 2022 https://coloriage.gulli.fr/Coloriages-Dessins-animes/Les-Schtroumpfs.

[36] Schtroumpf à lunettes. Accessed February 17, 2022 https://www.momes.net/coloriages/coloriages-de-heros-et-dessins-animes/coloriage-schtroumpf-a-lunettes-836466.

[37] Schtroumpf cuisinier. Accessed February 17, 2022 https://www.coloriages-a-imprimer.com/coloriage/schtroumpf-cuisinier.

[38] Schtroumpf poète. Accessed February 17, 2022 https://les-schtroumpfs.fandom.com/fr/wiki/Schtroumpf_poète.

[39] Smurfs news. Accessed February 17, 2022 https://www.smurf.com.

[40] Chris Rorres. The turn of the screw: Optimal design of an archimedes screw. *Journal of hydraulic engineering*, 126(1):72–80, 2000.

[41] JASS. Siracusa, el gigantesco barco de lujo construido por arquímedes en el año 240 a.c. *Informe Insólito*. Accessed November 20, 2021 http://informeinsolito.com/siracusa-barco-arquimedes, 2016.

[42] Encyclopaedia Britannica Editors. Archimedes screw. *Encyclopaedia Britannica*. Accessed November 15, 2021 https://www.britannica.com/technology/Archimedes-screw, 2014.

[43] Y. Onose, Y. Okamura, S. Seki, S. Ishiwata, and Y. Tokura. Observation of magnetic excitations of skyrmion crystal in a helimagnetic insulator $Cu_2OSeO_3$. *Phys. Rev. Lett.*, 109:037603, Jul 2012.

[44] T. Schwarze, Johannes Waizner, Markus Garst, Andreas Bauer, Ioannis Stasinopoulos, Helmuth Berger, Christian Pfleiderer, and Dirk Grundler. Universal helimagnon and skyrmion excitations in metallic, semiconducting and insulating chiral magnets. *Nature materials*, 14(5):478–483, 2015.

[45] M. Kugler, G. Brandl, J. Waizner, M. Janoschek, R. Georgii, A. Bauer, K. Seemann, A. Rosch, C. Pfleiderer, P. Böni, et al. Band structure of helimagnons in MnSi resolved by inelastic neutron scattering. *Physical review letters*, 115(9):097203, 2015.

[46] Markus Garst, Johannes Waizner, and Dirk Grundler. Collective spin excitations of helices and magnetic skyrmions: Review and perspectives of magnonics in non-centrosymmetric magnets. *Journal of Physics D: Applied Physics*, 50(29):293002, 2017.

[47] I. Stasinopoulos, S. Weichselbaumer, A. Bauer, J. Waizner, H. Berger, Markus Garst, C. Pfleiderer, and D. Grundler. Linearly polarized GHz magnetization dynamics of spin helix modes in the ferrimagnetic insulator $Cu_2OSeO_3$. *Scientific reports*, 7(1):1–8, 2017.

[48] Arne Vansteenkiste, Jonathan Leliaert, Mykola Dvornik, Mathias Helsen, Felipe Garcia-Sanchez, and Bartel Van Waeyenberge. The design and verification of mumax3. *AIP advances*, 4(10):107133, 2014.

[49] Lukas Exl, Simon Bance, Franz Reichel, Thomas Schrefl, Hans Peter Stimming, and Norbert J Mauser. Labonte's method revisited: An effective steepest descent method for micromagnetic energy minimization. *Journal of Applied Physics*, 115(17):17D118, 2014.

[50] Archimedean screw hydro turbine. Accessed February 23, 2022 https://www.renewablesfirst.co.uk/hydropower/hydropower-learning-centre/archimedean-screw-hydro-turbine/.

[51] T. Schulz, R. Ritz, A. Bauer, M. Halder, M. Wagner, C. Franz, C. Pfleiderer, K. Everschor, M. Garst, and A. Rosch. Emergent electrodynamics of skyrmions in a chiral magnet. 8(4):301–304, Apr 2012.

[52] T. Holstein and H. Primakoff. Field dependence of the intrinsic domain magnetization of a ferromagnet. *Phys. Rev.*, 58:1098–1113, Dec 1940.

[53] Franz Utermohlen. Spin-wave theory using the Holstein–Primakoff transformation. Accessed February 26, 2022 https://cpb-us-w2.wpmucdn.com/u.osu.edu/dist/3/67057/files/2020/02/spin-wave_theory_using_the_Holstein-Primakoff_transformation.pdf, February 2020.

[54] W Finger and TM Rice. Theory of the crossover in the low-frequency dynamics of an incommensurate system, hg 3- $\delta$ as f 6. *Physical Review Letters*, 49(7):468, 1982.

[55] TC Lubensky, Sriram Ramaswamy, and John Toner. Hydrodynamics of icosahedral quasicrystals. *Physical Review B*, 32(11):7444, 1985.

[56] Lukas M Sieberer, Michael Buchhold, and Sebastian Diehl. Keldysh field theory for driven open quantum systems. *Reports on Progress in Physics*, 79(9):096001, 2016.

[57] JJ Sakurai and J Napolitano. Modern quantum mechanics, 2nd edition. *Person New International edition*, 2011.

[58] Alexander Altland and Ben D Simons. *Condensed matter field theory*. Cambridge University Press, 2010.

[59] Piers Coleman. *Introduction to many-body physics*. Cambridge University Press, 2015.

[60] I Fischer and A Rosch. Weak spin-orbit interactions induce exponentially flat mini-bands in magnetic metals without inversion symmetry. *EPL (Europhysics Letters)*, 68(1):93, 2004.

[61] Akira Oguri. Transport theory for interacting electrons connected to reservoirs. *arXiv preprint cond-mat/0606316*, 2006.

[62] Charles S. Spencer, Jacob Gayles, Nicholas A. Porter, Satoshi Sugimoto, Zabeada Aslam, Christian J. Kinane, Timothy R. Charlton, Frank Freimuth, Stanislav Chadov, Sean Langridge, Jairo Sinova, Claudia Felser, Stefan Blügel, Yuriy Mokrousov, and Christopher H. Marrows. Helical magnetic structure and the anomalous and topological hall effects in epitaxial b20 $fe_{1-y}co_y$Ge films. *Phys. Rev. B*, 97:214406, Jun 2018.

[63] C. Pfleiderer, S. R. Julian, and G. G. Lonzarich. Non-fermi-liquid nature of the normal state of itinerant-electron ferromagnets. *Nature*, 414(6862):427–430, nov 2001.

[64] A. Neubauer, C. Pfleiderer, B. Binz, A. Rosch, R. Ritz, P. G. Niklowitz, and P. Böni. Topological hall effect in the *a* phase of mnsi. *Phys. Rev. Lett.*, 102:186602, May 2009.

[65] Felix Büttner, C Moutafis, M Schneider, B Krüger, CM Günther, J Geilhufe, C v Korff Schmising, J Mohanty, B Pfau, S Schaffert, et al. Dynamics and inertia of skyrmionic spin structures. *Nature Physics*, 11(3):225–228, 2015.

[66] Karin Everschor, Markus Garst, RA Duine, and Achim Rosch. Current-induced rotational torques in the skyrmion lattice phase of chiral magnets. *Physical Review B*, 84(6):064401, 2011.

[67] Shi-Zeng Lin, Cristian D Batista, Charles Reichhardt, and Avadh Saxena. Ac current generation in chiral magnetic insulators and skyrmion motion induced by the spin seebeck effect. *Physical review letters*, 112(18):187203, 2014.

[68] Chuang Ma, Xichao Zhang, Jing Xia, Motohiko Ezawa, Wanjun Jiang, Teruo Ono, SN Piramanayagam, Akimitsu Morisako, Yan Zhou, and Xiaoxi Liu. Electric field-induced creation and directional motion of domain walls and skyrmion bubbles. *Nano letters*, 19(1):353–361, 2018.

[69] Tomek Schulz, R Ritz, Andreas Bauer, Madhumita Halder, Martin Wagner, Chris Franz, Christian Pfleiderer, Karin Everschor, Markus Garst, and Achim Rosch. Emergent electrodynamics of skyrmions in a chiral magnet. *Nature Physics*, 8(4):301–304, 2012.

[70] Florian Jonietz, Sebastain Mühlbauer, Christian Pfleiderer, Andreas Neubauer, Wolfgang Münzer, Andreas Bauer, T Adams, Robert Georgii, Peter Böni, Rembert A Duine, et al. Spin transfer torques in mnsi at ultralow current densities. *Science*, 330(6011):1648–1651, 2010.

[71] Shi-Zeng Lin, Cristian D Batista, and Avadh Saxena. Internal modes of a skyrmion in the ferromagnetic state of chiral magnets. *Physical Review B*, 89(2):024415, 2014.

[72] Christoph Schütte and Markus Garst. Magnon-skyrmion scattering in chiral magnets. *Physical Review B*, 90(9):094423, 2014.

[73] Weiwei Wang, Marijan Beg, Bin Zhang, Wolfgang Kuch, and Hans Fangohr. Driving magnetic skyrmions with microwave fields. *Physical Review B*, 92(2):020403, 2015.

[74] Bernd Grosse Jütterman. Driving magnetic skyrmions by oscillating magnetic fields. Master's thesis, Universität zu Köln, 2021.

[75] Weijin Chen, Linjie Liu, and Yue Zheng. Ultrafast ratchet dynamics of skyrmions by defect engineering in materials with poor conductivity under gigahertz magnetic fields. *Physical Review Applied*, 14(6):064014, 2020.

[76] Kyoung-Woong Moon, Duck-Ho Kim, Soong-Geun Je, Byong Sun Chun, Wondong Kim, ZQ Qiu, Sug-Bong Choe, and Chanyong Hwang. Skyrmion motion driven by oscillating magnetic field. *Scientific reports*, 6(1):1–8, 2016.

[77] Vivek Lohani. *SYK Dot Out of Equilibrium & Scattering from Fractional Topological Textures*. PhD thesis, Universität zu Köln, 2022.

[78] Jeff Bezanson, Alan Edelman, Stefan Karpinski, and Viral B Shah. Julia: A fresh approach to numerical computing. *SIAM review*, 59(1):65–98, 2017.

[79] Y. Ishikawa, G. Shirane, J. A. Tarvin, and M. Kohgi. Magnetic excitations in the weak itinerant ferromagnet mnsi. *Phys. Rev. B*, 16:4956–4970, Dec 1977.

[80] H. J. Williams, J. H. Wernick, R. C. Sherwood, and G. K. Wertheim. Magnetic properties of the monosilicides of some 3d transition elements. *Journal of Applied Physics*, 37(3):1256–1256, 1966.

[81] Imane el Achchi, Nina del Ser, Vivek Lohani, and Achim Rosch. Magnetic textures with fractional topological or electric charge. *In Preparation*, 2022.

[82] XZ Yu, W Koshibae, Y Tokunaga, K Shibata, Y Taguchi, N Nagaosa, and Y Tokura. Transformation between meron and skyrmion topological spin textures in a chiral magnet. *Nature*, 564(7734):95–98, 2018.

[83] Ningbo Gao, S-G Je, M-Y Im, Jun Woo Choi, Masheng Yang, Qin-ci Li, TY Wang, S Lee, H-S Han, K-S Lee, et al. Creation and annihilation of topological meron pairs in in-plane magnetized films. *Nature communications*, 10(1):1–9, 2019.

[84] Maria Azhar, Volodymyr P. Kravchuk, and Markus Garst. Screw dislocations in chiral magnets. *Phys. Rev. Lett.*, 128:157204, Apr 2022.

[85] Imane el Achchi. Fractional topological charges in magnetic textures, 2020.

[86] Universität Münster. Sine-gordon equation. https://www.uni-muenster.de/imperia/md/content/physik_tp/lectures/ws2016-2017/num_methods_i/sinegordon.pdf Accessed March 30, 2022.

[87] KY Guslienko. Gauge and emergent electromagnetic fields for moving magnetic topological solitons. *EPL (Europhysics Letters)*, 113(6):67002, 2016.

[88] Jung Hoon Han. *Skyrmions in Condensed Matter*, volume 278. Springer, 2017.

[89] Yakir Aharonov and David Bohm. Significance of electromagnetic potentials in the quantum theory. *Physical Review*, 115(3):485, 1959.

# Appendix A

# Minimizing the Hamiltonian for the Static Conical State

Substituting the conical spin parametrization Eq. (1.4), into the discrete Hamiltonian eq. (1.1), we obtain

$$
H_0 = NJS^2 \Big[ - \underbrace{(\cos^2 \theta + \sin^2(\theta_0) \cos(qa))}_{\text{Heisenberg}} - \underbrace{d \sin^2(\theta_0) \sin(qa)}_{\text{DMI}}
$$
$$
- \underbrace{b_0 d^2 \cos(\theta_0)}_{\text{Zeeman}} + \underbrace{\frac{1}{2} \delta N_z d^2 \cos^2(\theta_0)}_{\text{Demag}} \Big],
\tag{A.1}
$$

where $N$ is the total number of spins and we have switched to dimensionless units $d = D/J, b_0 = \gamma B_0 / JSd^2, \delta = \gamma^2 \mu_0 / d^2 a^3 J$ inside the square braces. Note that for the Heisenberg term we get two different contributions: one where the neighbouring spins are parallel (if the bond joining them is parallel to $\hat{\mathbf{e}}_x / \hat{\mathbf{e}}_y$) and one where they are not (if the bond is parallel to $\hat{\mathbf{e}}_z$). Now we minimize Eq. (A.1) with respect to $q, \theta_0$

$$
\frac{\partial H}{\partial q} = NJS^2 \sin^2(\theta_0) a [\sin(qa) - d \cos(qa)] = 0
$$
$$
\implies \tan(qa) = d
\tag{A.2}
$$
$$
\frac{\partial H}{\partial \theta_0} = NJS^2 \sin(\theta_0) a [2 \cos(\theta_0)(1 - \cos(qa) - d \sin(qa)) + d^2 (b_0 - \delta N_x \cos(\theta_0))] = 0
$$
$$
\implies \cos(\theta_0) = \frac{b_0}{\frac{2}{d^2}(\sqrt{1 + d^2} - 1) + \delta N_z},
\tag{A.3}
$$

where we have used $\sin(qa) = \frac{d}{\sqrt{1+d^2}}, \cos(qa) = \frac{1}{\sqrt{1+d^2}}$ to simplify the expression for $\cos(\theta_0)$.

# Appendix B

# Dipolar Interactions: Further Details

## B.1 Derivation of Eq. (1.10)

The energy contribution due to dipolar interactions is

$$F_{\text{dip}} = -\frac{\mu_0}{2} \int \mathrm{d}^3 r \mathbf{M}(\mathbf{r}) \cdot \mathbf{B}_{\text{dip}},$$

Note the extra factor of $\frac{1}{2}$ compared to, for example, energy contributions due to static external magnetic fields. This is needed because dipolar field $\mathbf{B}_{\text{dip}}$ is itself a function of $\mathbf{M}$. Without the factor of $\frac{1}{2}$ the effective dipolar field, $\frac{\partial F}{\partial \mathbf{M}}$ would be double what it should be due to this extra dependence. Inserting $\mathbf{B}_{\text{dip}}$ from Eq. (1.6) we have

$$F_{\text{dip}} = \frac{\mu_0}{2} \int \mathrm{d}^3 r \, d^3 r' \, M_i(\mathbf{r}) N_{ij}(r - r') M_j(\mathbf{r}'),$$

$$N_{ij}(\mathbf{r} - \mathbf{r}') = \left( \frac{\delta_{ij}}{|\mathbf{r} - \mathbf{r}'|^3} - \frac{3(r_i - r_i')(r_j - r_j')}{|\mathbf{r} - \mathbf{r}'|^5} \right).$$

(B.1)

We want to Fourier transform Eq. (B.1) using the Fourier conventions

$$M(\mathbf{r}) = \frac{1}{(2\pi)^3} \int d^3 k \, \mathbf{M}(\mathbf{k}) e^{-i\mathbf{k} \cdot \mathbf{r}} \qquad \mathbf{M}(\mathbf{k}) = \int \mathrm{d}^3 r \mathbf{M}(\mathbf{r}) e^{i\mathbf{k} \cdot \mathbf{r}}$$

$$N_{ij}(\mathbf{r}) = \frac{1}{(2\pi)^3} \int d^3 k \, N_{ij}(\mathbf{k}) e^{-i\mathbf{k} \cdot \mathbf{r}} \qquad N_{ij}(\mathbf{k}) = \int \mathrm{d}^3 r N_{ij}(\mathbf{r}) e^{i\mathbf{k} \cdot \mathbf{r}}$$

(B.2)

$$\delta(\mathbf{r} - \mathbf{r}') = \frac{1}{(2\pi)^3} \int d^3 k \, e^{-i\mathbf{k} \cdot (\mathbf{r} - \mathbf{r}')} \qquad \delta(\mathbf{k} - \mathbf{k}') = \int \mathrm{d}^3 r e^{-i\mathbf{r} \cdot (\mathbf{k} - \mathbf{k}')}.$$

Here is a trick which will save us a lot of effort: $N_{ij}$ can actually be rewritten as a perfect double derivative

$$N_{ij}(\mathbf{r} - \mathbf{r}') = -\frac{\partial}{\partial r_i}\frac{\partial}{\partial r'_j}\frac{1}{|\mathbf{r} - \mathbf{r}'|}$$

which means that its Fourier transform is just given by

$$\tilde{N}_{ij} = k_i k_j \, \text{F.T.} \left[\frac{1}{|\mathbf{r} - \mathbf{r}'|}\right]$$

Thus we just need to calculate the Fourier Transform of $\frac{1}{r}$. This is the same functional form as for the Coulomb potential, or the $\lim_{\lambda \to 0} \frac{Ae^{-\lambda r}}{r}$ of the Yukawa potential and is given by $\frac{4\pi}{k^2}$ using the convention Eq. (B.2). Finally we can write Eq. (B.1) in momentum space as follows

$$
\begin{aligned}
F_{\text{dip}} &= \frac{\mu_0}{2} \int d^3r \, d^3r' \int \frac{d^3k_1}{(2\pi)^3}\frac{d^3k_2}{(2\pi)^3}\frac{d^3k}{(2\pi)^3} M_i(\mathbf{k}_1)\frac{k_i k_j}{k^2}M_j(\mathbf{k}_2)e^{-i(\mathbf{k}_1+\mathbf{k})\cdot\mathbf{r}}e^{-i(\mathbf{k}_2-\mathbf{k})\cdot\mathbf{r}'} \\
&= \frac{\mu_0 V}{2} \int \frac{V d^3k}{(2\pi^3)}\frac{(\mathbf{M}_{-\mathbf{k}}\cdot\mathbf{k})(\mathbf{M}_{\mathbf{k}}\cdot\mathbf{k})}{k^2},
\end{aligned}
\tag{B.3}
$$

For textures with discretised spatial wave-vectors (eg. the conical state, which has only 3 wave-vectors $k = 0, \pm q$), we want the discrete, rather than continuous version of Eq. (B.3). This is obtained by using the quantisation properties of wave-vectors and changing $\int \frac{V d^3k}{(2\pi)^3} \to \sum_{\mathbf{k}}$. These two steps finally result in Eq. (1.10).

## B.2 Incorporating Dipolar Interactions into the LLG for the Driven Conical Phase

The two dipolar energy terms given in Eq. (1.11) contribute the following total magnetic field to the LLG

$$\mathbf{B}_{\text{eff, dip}}(\mathbf{r}) = -\frac{\partial}{\partial \mathbf{M}(\mathbf{r})}\frac{\mu_0}{2}\left((\overline{\mathbf{M}}\cdot\underline{\underline{N}}\cdot\overline{\mathbf{M}}) + \sum_{\mathbf{k}\neq 0}\frac{(\mathbf{M}_{\mathbf{k}}\cdot\mathbf{k})(\mathbf{M}_{-\mathbf{k}}\cdot\mathbf{k})}{k^2}\right)$$

Tidying this up a little bit by using $\mathbf{M} = M_0\hat{\mathbf{M}}$ together with the reduced magnetic field $b_i$ and strength of dipolar interactions $\delta$ introduced in the main text we obtain

$$\mathbf{b}_{\text{eff, dip}}(\mathbf{r}) = -\frac{\delta}{2}\frac{\partial}{\partial \hat{\mathbf{M}}(\mathbf{r})}\left((\overline{\hat{\mathbf{M}}}\cdot\underline{\underline{N}}\cdot\overline{\hat{\mathbf{M}}}) + \sum_{\mathbf{k}\neq 0}\frac{(\hat{\mathbf{M}}_{\mathbf{k}}\cdot\mathbf{k})(\hat{\mathbf{M}}_{-\mathbf{k}}\cdot\mathbf{k})}{k^2}\right) \tag{B.4}$$

In the above equation, we can use the chain rule and the definition of the Fourier transform for $\hat{\mathbf{M}}$ (same as for $\mathbf{M}(\mathbf{r})$, $\mathbf{M_k}$ in Eq. (B.2), divided by $M_0$) to replace $\frac{\partial}{\partial \hat{\mathbf{M}}} \to \sum_{\mathbf{k'}} e^{i\mathbf{k'}\cdot\mathbf{r}} \frac{\partial}{\partial \hat{\mathbf{M}}_{k'}}$. Also, $\overline{\hat{\mathbf{M}}} = \int \mathrm{d}^3 r \hat{\mathbf{M}}(\mathbf{r}) = \hat{\mathbf{M}}_{\mathbf{k}=0} = \hat{\mathbf{M}}_0$. This allows us to write Eq. (B.4) purely in terms of the Fourier components $\hat{\mathbf{M}}_{\mathbf{k}}$ of magnetisation

$$\mathbf{b}_{\text{eff, dip}}(\mathbf{r}) = -\delta \left( \underline{\underline{N}} \cdot \hat{\mathbf{M}}_0 + \sum_{\mathbf{k}\neq 0} \frac{e^{-i\mathbf{k}\cdot\mathbf{r}}(\hat{\mathbf{M}}_{\mathbf{k}} \cdot \mathbf{k})\mathbf{k}}{k^2} \right). \tag{B.5}$$

Now, for the driven conical phase Eq. (B.6) can be considerably simplified because of our assumption that the system remains translationally invariant in the $xy$ plane. This means that only $\mathbf{k} \parallel \mathbf{e}_z$ wave-vectors are allowed, which simplifies the effective magnetic field due to dipolar interactions to

$$\mathbf{b}_{\text{eff, dip, conical phase}}(\mathbf{r}) = -\delta \Big( \underline{\underline{N}} \cdot \hat{\mathbf{M}}_0 + \underbrace{\sum_{\mathbf{k}\neq 0} e^{-ikz}(\hat{\mathbf{M}}_k)_z\, \hat{\mathbf{e}}_z}_{=n_z(\mathbf{r})|_{\text{no DC}}} \Big). \tag{B.6}$$

Depending on the type of driving (parallel or perpendicular), the form of the dipolar effective field is different. This occurs because the different driving directions force us to adopt different ansatzes for $\hat{\mathbf{M}}$ at first and second order in $\epsilon$.

For parallel driving these ansatzes are given by Eq. (2.5) and (2.10) – substituting these into Eq. (B.6) suggests that the only non-zero contribution comes from the first term originating from the demagnetisation fields. This is given by

$$\begin{aligned}
\mathbf{b}_{\text{eff, dip, conical phase},\parallel}(\mathbf{r})\hat{\mathbf{e}}_z &= -\delta N_z \cos(\theta) \\
&= -\delta N_z \left( c - \epsilon s\theta_1(t) - \epsilon^2 \left( s\theta_2(t) + \frac{1}{2}c\theta_1^2(t) \right) + \mathcal{O}(\epsilon^3) \right) \hat{\mathbf{e}}_z,
\end{aligned} \tag{B.7}$$

where we have expanded up to order $\epsilon^2$.

For perpendicular driving, the effective dipolar field is more complicated. Using the ansatzes Eq. (2.15) and (2.18) we obtain

$$
\begin{aligned}
(\hat{\mathbf{M}}_0)_x &= \frac{\epsilon}{2}\Big( c\left((\theta_1^{(1,1)} + \theta_1^{(1,-1)})e^{i\omega t} + (\theta_1^{(-1,1)} + \theta_1^{(-1,-1)})e^{-i\omega t}\right) \\
&\quad - is\left((\phi_1^{(1,1)} - \phi_1^{(1,-1)})e^{i\omega t} + (\phi_1^{(-1,1)} - \phi_1^{(-1,-1)})e^{-i\omega t}\right)\Big) \\
(\hat{\mathbf{M}}_0)_y &= \frac{\epsilon}{2}\Big( ic\left((\theta_1^{(1,1)} - \theta_1^{(1,-1)})e^{i\omega t} + (\theta_1^{(-1,1)} - \theta_1^{(-1,-1)})e^{-i\omega t}\right) \\
&\quad + s\left((\phi_1^{(1,1)} + \phi_1^{(1,-1)})e^{i\omega t} + (\phi_1^{(-1,1)} + \phi_1^{(-1,-1)})e^{-i\omega t}\right)\Big) \\
(\hat{\mathbf{M}}_0)_z &= c - \epsilon^2\left(c(\theta_1^{(1,1)}e^{i\omega t} + \theta_1^{(-1,1)e^{-i\omega t}})(\theta_1^{(1,-1)}e^{i\omega t} + \theta_1^{(-1,-1)}e^{-i\omega t}) + s\theta_2^{(0,0)}\right)
\end{aligned}
\tag{B.8}
$$

and

$$
\sum_{\mathbf{k}\neq 0} e^{-ikz}(\hat{\mathbf{M}}_k)_z = -\epsilon s\theta_1(z,t) - \epsilon^2 c\theta_2^{\text{osc.}}(z,t).
\tag{B.9}
$$

So, in contrast to the parallel driving case for perpendicular driving the effective dipolar field now contains additional $x, y$ component contributions from the demagnetisation fields, as well as a non-zero contribution from the finite $k$ term.

Below we list the contributions from dipolar interactions to the RHS of the first order and second order equations of motion, Eq. (2.14) and (2.17), for a system driven in the perpendicular direction. These are obtained by taking the cross product of $\hat{\mathbf{M}}$ with Eq. (B.6) (with Eq. (B.8) and (B.9) substituted in), projecting onto $\frac{\partial \hat{\mathbf{M}}}{\partial \theta, \phi}$ and Taylor expanding in $\epsilon$. Also we define $N_+ = N_x + N_y$, $N_- = N_x - N_y$, without which the following ugly formulas would look even uglier.

First order:

$$
\begin{aligned}
\text{RHS}_{1,\theta}^{\text{dip}} &= \frac{\delta e^{i\omega t}}{4}\Big( (N_+ e^{iz} - N_- e^{-iz})(ic\theta_1^{(1,1)} + s\phi_1^{(1,1)}) \\
&\quad + (N_+ e^{-iz} - N_- e^{iz})(-ic\theta_1^{(1,-1)} + s\phi_1^{(1,-1)})\Big) + h.c. \\
\text{RHS}_{1,\phi}^{\text{dip}} &= -\frac{\delta e^{i\omega t}}{4}\Big( \left(c^2 N_- e^{-iz} + e^{iz}(4 - 12c^2 + 9N_+ c^2)\right)\theta_1^{(1,1)} \\
&\quad + \left(c^2 N_- e^{iz} + e^{-iz}(4 - 12c^2 + 9N_+ c^2)\right)\theta_1^{(1,-1)} \\
&\quad - ics\left((N_- e^{-iz} + N_+ e^{iz})\phi_1^{(1,1)} - (N_+ e^{-iz} + N_- e^{iz})\phi_1^{(1,-1)}\right)\Big) + h.c.
\end{aligned}
\tag{B.10}
$$

Second order:

$$
\text{RHS}_{2,\theta}^{\text{dip}}|_{0,0} = -\frac{\delta}{4}\Bigg( c(N_+\phi_1^{(-1,-1)} + N_-\phi_1^{(-1,1)})\theta_1^{(1,1)} + c(N_+\phi_1^{(-1,1)} + N_-\phi_1^{(-1,-1)})\theta_1^{(1,-1)}
$$

$$
+ \left( c(N_+\theta_1^{(-1,-1)} + N_-\theta_1^{(-1,1)} - 2isN_-\phi_1^{(-1,1)}) \right)\phi_1^{(1,1)}
$$

$$
+ \left( c(N_+\theta_1^{(-1,1)} + N_-\theta_1^{(-1,-1)} + 2isN_-\phi_1^{(-1,-1)}) \right)\phi_1^{(1,-1)} \Bigg) + h.c.
$$

$$
\text{RHS}_{2,\phi}^{\text{dip}}|_{0,0} = -\frac{\delta}{4}\Bigg(
$$

$$
+ \left( N_+c\theta_1^{(-1,-1)} \left(6c^2 - 6s^2 - 1\right) + 2N_-c(c^2 - s^2)\theta_1^{(-1,1)} \right.
$$

$$
\left. + i(N_+\phi_1^{(-1,-1)} - N_+\phi_1^{(-1,1)})s\left(2c^2 - s^2\right) \right)\theta_1^{(1,1)}
$$

$$
+ \left( N_+c\theta_1^{(-1,1)} \left(6c^2 - 6s^2 - 1\right) + 2N_-c(c^2 - s^2)\theta_1^{(-1,-1)} \right.
$$

$$
\left. + i(N_+\phi_1^{(-1,-1)} - N_+\phi_1^{(-1,1)})s\left(2c^2 - s^2\right) \right)\theta_1^{(1,-1)}
$$

$$
+ \left( cs(N_+\phi_1^{(-1,-1)} - 2N_-\phi_1^{(-1,1)}) - i(2c^2 - s^2)(N_+\theta_1^{(-1,-1)} + N_-\theta_1^{(-1,1)}) \right)s\phi_1^{(1,1)}
$$

$$
+ \left( cs(N_+\phi_1^{(-1,1)} - 2N_-\phi_1^{(-1,-1)}) + i(2c^2 - s^2)(N_+\theta_1^{(-1,1)} + N_-\theta_1^{(-1,-1)}) \right)s\phi_1^{(1,-1)}
$$

$$
\Bigg) + h.c. - \delta s^2(c + s(1 - N_+))\theta_2^{(0,0)}
$$

$$
\tag{B.11}
$$

Note that for the second order contribution, we have given only the DC frequency and momentum component – $|_{0,0}$ stands for $\omega = 0, k = 0$. This is because this is the only component relevant to the calculation of $\omega_{\text{screw}}$.

# Appendix C

# Derivation of the Thiele Equation

The derivation of the Thiele equation from the LLG involves two steps: i) crossing Eq. (1.18) with $\hat{\mathbf{M}}$ and ii) dotting the resulting expression with $\nabla_i \hat{\mathbf{M}}$ and integrating over space. We also make use of the translational ansatz $\dot{\hat{\mathbf{M}}}(\mathbf{r} - \mathbf{R}) = -(\dot{\mathbf{R}} \cdot \nabla)\hat{\mathbf{M}}$.

Step i):

$$\hat{\mathbf{M}} \times \dot{\hat{\mathbf{M}}} = -\gamma \mathbf{B}_{\text{eff}} + \frac{\gamma}{|\gamma|}\alpha\dot{\hat{\mathbf{M}}}$$

$$\implies -\text{sgn}(\gamma)\epsilon_{jkl}\hat{M}_k\partial_m\hat{M}_l\dot{R}_m + \alpha\partial_m\hat{M}_j\dot{R}_m = \frac{|\gamma|}{M_0}\frac{\delta F[\hat{\mathbf{M}}]}{\delta\hat{M}_j} \tag{C.1}$$

where we used $\mathbf{M} = M_0\hat{\mathbf{M}}$ and got rid of the $(\mathbf{B}_{\text{eff}} \cdot \hat{\mathbf{M}})\hat{\mathbf{M}}$ term because it is orthogonal to $\hat{\mathbf{M}} \times \dot{\hat{\mathbf{M}}}$.

Step ii):

$$\int \mathrm{d}^3r \left[ -\text{sgn}(\gamma)\partial_i\hat{M}_j\epsilon_{jkl}\hat{M}_k\partial_m\hat{M}_l\dot{R}_m + \alpha\partial_i\hat{M}_j\partial_m\hat{M}_j\dot{R}_m \right] = \int \mathrm{d}^3r \frac{|\gamma|}{M_0}\frac{\delta F[\hat{\mathbf{M}}]}{\delta\hat{M}_j}\partial_i\hat{M}_j$$

$$\implies -\text{sgn}(\gamma)\epsilon_{inm}G_n\dot{R}_m + \mathcal{D}_{ij}\dot{R}_j = -\frac{\partial F}{\partial R_i} \tag{C.2}$$

with

$$G_k = \frac{1}{2}\frac{M_0}{|\gamma|}\epsilon_{ijk}\int \mathrm{d}^3r\hat{\mathbf{M}} \cdot (\partial_i\hat{\mathbf{M}} \times \partial_j\hat{\mathbf{M}})$$

$$\mathcal{D}_{ij} = \frac{M_0}{|\gamma|}\int \mathrm{d}^3r\partial_i\hat{\mathbf{M}} \cdot \partial_j\hat{\mathbf{M}}. \tag{C.3}$$

$G_k$ is a three component vector with $k = \{x, y, z\}$, while $\mathcal{D}_{ij}$ is a $3 \times 3$ symmetric matrix, also with $i, j = \{x, y, z\}$.

For a static skyrmion, $\mathbf{G} = -4\pi \frac{M_0}{|\gamma|} \mathbf{e}_z$ and $\mathcal{D}$ is a diagonal matrix,

$$
\mathcal{D} = \begin{pmatrix} \mathcal{D}_{xx} & 0 & 0 \\ 0 & \mathcal{D}_{yy} & 0 \\ 0 & 0 & 0 \end{pmatrix},
$$

$$
\text{with} \quad \mathcal{D}_{xx} = \mathcal{D}_{yy} = \frac{M_0}{|\gamma|} \pi \int_0^\infty r \, dr \left( \theta_0'^2 + \frac{\sin^2(\theta_0)}{r^2} \right).
$$

(C.4)

# Appendix D

# Motion of a Damped, Non-Driven Spin

It turns out that the motion in time of a damped non-driven spin can be easily obtained by generalising the spin position vector ansatz which we always use for Larmor precession, $\hat{\mathbf{M}} = (\sin(\theta_0)\cos(\omega_L t), \sin(\theta_0)\cos(\omega_L t), \cos(\theta_0))^T$ to allow $\theta, \phi$ to be time dependent

$$\hat{\mathbf{M}} = \begin{pmatrix} \sin(\theta(t))\cos(\phi(t)) \\ \sin(\theta(t))\sin(\phi(t)) \\ \cos(\theta(t)) \end{pmatrix}. \tag{D.1}$$

We now introduce two useful vectors $\frac{\partial \hat{\mathbf{M}}}{\partial \theta}, \frac{\partial \hat{\mathbf{M}}}{\partial \phi}$, which span the plane perpendicular to $\mathbf{S}$

$$\frac{\partial \hat{\mathbf{M}}}{\partial \theta} = \begin{pmatrix} \cos(\theta)\cos(\phi) \\ \cos(\theta)\sin(\phi) \\ -\sin(\theta) \end{pmatrix}, \quad \frac{\partial \hat{\mathbf{M}}}{\partial \phi} = \begin{pmatrix} -\sin(\theta)\sin(\phi) \\ \sin(\theta)\cos(\phi) \\ 0 \end{pmatrix}$$

Substituting Eq. (D.1) into the LLG Eq. (1.18) and projecting it onto $\frac{\partial \hat{\mathbf{M}}}{\partial \theta, \phi}$ respectively gives us two differential equations for $\phi(t), \theta(t)$

$$\mathrm{sgn}(\gamma)\dot{\theta} = \alpha \sin(\theta)\dot{\phi}$$
$$\alpha\dot{\theta} + \mathrm{sgn}(\gamma)\sin(\theta)\dot{\phi} = -\omega_L \sin(\theta), \tag{D.2}$$

where we have already substituted in the Larmor frequency $\omega_L = \gamma B$. We can easily solve for $\phi(t)$ by substituting the first equation into the second, giving $\phi(t) = -\frac{1}{1+\alpha^2}\mathrm{sgn}(\gamma)|\omega_L|t$. Substituting this back into either of the two equations gives us a differential equation in

$\theta$ only, which can be integrated by parts

$$\int \frac{d\theta}{\sin(\theta)} = -\frac{\alpha|\omega_L|}{1+\alpha^2} \int dt.$$

Here we can use the standard integral $\int d\theta\, \csc(\theta) = -\ln\left(\cot(\theta) - \csc(\theta)\right)$. Then, setting the initial condition $\theta(t_0) = \theta_0$, and with the help of the trigonometric identities $\cot(\theta) - \csc(\theta) = \cot(\theta/2)$, we obtain

$$\tan\left(\frac{\theta(t)}{2}\right) = \tan\left(\frac{\theta_0}{2}\right) e^{-\frac{\alpha}{1+\alpha^2}|\omega_L|t}.$$

Thus we can describe the damped motion of a spin around a static field $\mathbf{B} = B\mathbf{e}_z$ via

$$\theta(t) = 2\arctan\left(\tan\left(\frac{\theta_0}{2}\right) e^{-\frac{\alpha}{1+\alpha^2}|\omega_L|t}\right)$$

$$\phi(t) = -\frac{1}{1+\alpha^2}\mathrm{sgn}(\gamma)|\omega_L|t. \tag{D.3}$$

# Appendix E

# Steady State Formulas for the Archimedean Screw

In this appendix we list the main analytical expressions for the steady state response of the system to perpendicular driving. As a reminder $c = \cos(\theta_0)$, $\omega$ is the driving frequency, $\alpha$ is the damping, $\delta$ is the strength of dipolar interactions and $N_x, N_y$ are demagnetisation factors ($N_z$ is already constrained to be $N_z = 1 - N_x - N_y$, so needn't be included as an argument). All the parameters are dimensionless as we are working with reduced units.

In Sec. E.0.1 we list the $\theta_1^{(1,\pm 1)}, \phi_1^{(1,\pm 1)}$ coefficients of the time and space dependent first order steady state response

$$
\begin{aligned}
\theta_1(z,t) &= \theta_1^{(1,1)} e^{i(\omega t + qz)} + \theta_1^{(1,-1)} e^{i(\omega t - qz)} + h.c. \\
\phi_1(z,t) &= \phi_1^{(1,1)} e^{i(\omega t + qz)} + \phi_1^{(1,-1)} e^{i(\omega t - qz)} + h.c.
\end{aligned}
\tag{E.1}
$$

At second order the steady state response also contains oscillating terms with Fourier space and time components $\pm q, \pm 2q$ and $\pm \omega, \pm 2\omega$. More importantly there is an emergent linearly increasing term $\omega_{\text{screw}} t$ in $\phi_2$, so that we can write the general steady state response as

$$
\begin{aligned}
\theta_2(z,t) &= \theta_2^{\text{osc.}}(z,t) + \theta_2^{(0,0)} \\
\phi_2(z,t) &= \phi_2^{\text{osc.}}(z,t) + \omega_{\text{screw}} t.
\end{aligned}
\tag{E.2}
$$

In Sec. E.0.2 we give the analytical forms of $\omega_{\text{screw}}$ and $\theta_2^{(0,0)}$, both of which are necessary for the Floquet stability analysis.

### E.0.1 First Order Response to Perpendicular Driving

The most general first order steady state coefficients with dipolar interactions, $\delta > 0$, and not necessarily symmetrical demagnetisation factors, $N_x \neq N_y$, are given by

$$\theta_1^{(1,1)} = \frac{(-\omega\,\mathrm{sgn}(\gamma) - c(1 + i\alpha\omega))}{f(\omega, \alpha, c, \delta, N_+, N_-)} \Bigg[$$

$$b_R\delta N_- \Big(i\alpha\omega(1 + c^2) + (1 - c^2)\delta - 2c\omega\,\mathrm{sgn}(\gamma) + 2\Big)$$

$$+ b_L\Big(4\left(\alpha^2\omega^2 - 3i\alpha\omega + \omega^2 - 2\right) + c^2\left(4i\alpha\omega + \delta(4 - i\alpha\omega(N_+ - 4)) + \delta^2 N_+ + 4\right)$$

$$+ 2c\delta N_+\omega\,\mathrm{sgn}(\gamma) + \delta(-4i\alpha\omega - i\alpha\omega N_+ - 2N_+ - 4) - \delta^2 N_+\Big)\Bigg]$$

$$\phi_1^{(1,1)} = \frac{i\left(-i\alpha\omega + c^2(\delta + 1) - c\omega\,\mathrm{sgn}(\gamma) - \delta - 2\right)}{\sqrt{1 - c^2}\,f(\omega, \alpha, c, \delta, N_+, N_-)} \Bigg[$$

$$b_R\delta N_- \Big(i\alpha\omega(1 + c^2) + (1 - c^2)\delta - 2c\omega\,\mathrm{sgn}(\gamma) + 2\Big)$$

$$+ b_L\Big(4\left(\alpha^2\omega^2 - 3i\alpha\omega + \omega^2 - 2\right) + c^2\left(4i\alpha\omega + \delta(4 - i\alpha\omega(N_+ - 4)) + \delta^2 N_+ + 4\right)$$

$$+ 2c\delta N_+\omega\,\mathrm{sgn}(\gamma) + \delta(-4i\alpha\omega - i\alpha\omega N_+ - 2N_+ - 4) - \delta^2 N_+\Big)\Bigg]$$

$$\theta_1^{(1,-1)} = \frac{(\omega\,\mathrm{sgn}(\gamma) - c(1 + i\alpha\omega))}{f(-\omega, \alpha, c, \delta, N_+, N_-)} \Bigg[$$

$$b_L\delta N_- \Big(i\alpha\omega(1 + c^2) + (1 - c^2)\delta + 2c\omega\,\mathrm{sgn}(\gamma) + 2\Big)$$

$$+ b_R\Big(4\left(\alpha^2\omega^2 - 3i\alpha\omega + \omega^2 - 2\right) + c^2\left(4i\alpha\omega + \delta(4 - i\alpha\omega(N_+ - 4)) + \delta^2 N_+ + 4\right)$$

$$- 2c\delta N_+\omega\,\mathrm{sgn}(\gamma) + \delta(-4i\alpha\omega - i\alpha\omega N_+ - 2N_+ - 4) - \delta^2 N_+\Big)\Bigg]$$

$$\phi_1^{(1,-1)} = \frac{-i\left(-i\alpha\omega + c^2(\delta + 1) + c\omega\,\mathrm{sgn}(\gamma) - \delta - 2\right)}{\sqrt{1 - c^2}\,f(-\omega, \alpha, c, \delta, N_+, N_-)} \Bigg[$$

$$b_L\delta N_- \Big(i\alpha\omega(1 + c^2) + (1 - c^2)\delta + 2c\omega\,\mathrm{sgn}(\gamma) + 2\Big)$$

$$+ b_R\Big(4\left(\alpha^2\omega^2 - 3i\alpha\omega + \omega^2 - 2\right) + c^2\left(4i\alpha\omega + \delta(4 - i\alpha\omega(N_+ - 4)) + \delta^2 N_+ + 4\right)$$

$$- 2c\delta N_+\omega\,\mathrm{sgn}(\gamma) + \delta(-4i\alpha\omega - i\alpha\omega N_+ - 2N_+ - 4) - \delta^2 N_+\Big)\Bigg]$$

$$(\mathrm{E.3})$$

where we have used the shortened notation $N_+ = N_x + N_y$ and $N_- = N_x - N_y$. The denominator $f(\omega, \alpha, c, \delta, N_x, N_y)$ is given by

$$
\begin{aligned}
f(\omega,&\alpha, c, \delta, N_+, N_-) = 4\Bigg[ \\
&-\frac{1}{4}c^4 \left( 4i\alpha\omega - 4\delta + i\alpha\delta\omega(N_- - N_+ + 4) + \delta^2(N_- - N_+) - 4 \right) \cdot \\
&\left( -4i\alpha\omega + \delta(4 + i\alpha\omega(N_- + N_+ - 4)) + \delta^2(N_- + N_+) + 4 \right) \\
&+ \frac{1}{2}c^2 \Big( 16 \left( -i\alpha^3\omega^3 + 4\alpha^2\omega^2 - i\alpha \left( \omega^2 - 5 \right)\omega + \omega^2 - 2 \right) \\
&+ \delta^2 \big( \alpha^2 \left( N_-^2 + 16 \right)\omega^2 + 2i\alpha \left( N_-^2 + 16 \right)\omega + 2 \left( N_-^2\omega^2 - 8 \right) \\
&+ N_+^2(-\omega) \left( \alpha^2\omega + 2i\alpha + 2\omega \right) + 4N_+ \left( \alpha^2\omega^2 + 6i\alpha\omega + \omega^2 - 5 \right) \big) \\
&+ \delta^4 \left( N_-^2 - N_+^2 \right) + 2\delta^3 \left( N_-^2 - N_+(-4i\alpha\omega + N_+ + 4) \right) \\
&+ 4i\delta \Big( N_+ \left( \alpha^3\omega^3 + 2i\alpha^2\omega^2 + \alpha \left( \omega^3 + \omega \right) + 2i \right) \\
&- 4 \left( \alpha^3\omega^3 + 5i\alpha^2\omega^2 + \alpha \left( \omega^2 - 7 \right)\omega + i \left( \omega^2 - 3 \right) \right) \Big) \Big) \\
&+ \Big( -2 \left( \alpha^2\omega^2 + 3i\alpha\omega + \omega^2 - 2 \right) + \delta \left( -2i\alpha\omega + \frac{1}{2}i(\alpha\omega + 2i)(N_- - N_+) + 2 \right) \\
&+ \frac{1}{2}\delta^2(N_+ - N_-) \Big) \cdot \\
&\Big( -2 \left( \alpha^2\omega^2 + 3i\alpha\omega + \omega^2 - 2 \right) + \delta \left( -2i\alpha\omega + \frac{1}{2}(2 - i\alpha\omega)(N_- + N_+) + 2 \right) \\
&+ \frac{1}{2}\delta^2(N_- + N_+) \Big) \Bigg]
\end{aligned}
$$

(E.4)

$f(\omega, \alpha, c, \delta, N_x, N_y)$ is quartic in $\omega$ and has four complex roots which are related to the complex resonance frequencies of the system. Due to time translation symmetry these four roots can be grouped into two pairs $-E, E_-^*$ and $-E_+, E_+^*$, letting us write $f(\dots)$ as

$$
f(\omega, \alpha, c, \delta, N_x, N_y) = 16(1 + \alpha^2)^2(\omega + E_-)(\omega - E_-^*)(\omega + E_+)(\omega - E_+^*).
\tag{E.5}
$$

In the main text we simplify the geometry by setting the demagnetisation factors in the plane perpendicular to the conical state equal to each other, i.e. $N_x = N_y$. This sets

$N_- = 0$ and the expressions in Eq. (E.3) and (E.4) simplify to

$$
\begin{aligned}
\theta_1^{(1,1)} &= \frac{b_L(-\operatorname{sgn}(\gamma)\omega + c(-1 - i\alpha\omega))}{4(1 + \alpha^2)(\omega + E_-)(\omega - E_+^*)} \\
\theta_1^{(1,-1)} &= \frac{b_R(\operatorname{sgn}(\gamma)\omega + c(-1 - i\alpha\omega))}{4(1 + \alpha^2)(\omega + E_+)(\omega - E_-^*)} \\
\phi_1^{(1,1)} &= \frac{ib_L\left(-i\alpha\omega + c^2(\delta + 1) - c\operatorname{sgn}(\gamma)\omega - \delta - 2\right)}{\sqrt{1 - c^2}4(1 + \alpha^2)(\omega + E_-)(\omega - E_+^*)} \\
\phi_1^{(1,-1)} &= \frac{-ib_R\left(-i\alpha\omega + c^2(\delta + 1) + c\operatorname{sgn}(\gamma)\omega - \delta - 2\right)}{\sqrt{1 - c^2}4(1 + \alpha^2)(\omega + E_+)(\omega - E_-^*)}
\end{aligned}
\tag{E.6}
$$

Where the complex energies $E_-, E_+$ are given by

$$
\begin{aligned}
E_- = -\frac{1}{8\left(\alpha^2 + 1\right)}\Bigg[ &4i\alpha\delta + 12i\alpha - 4i\alpha c^2\delta - 4i\alpha c^2 + i\alpha c^2\delta N_+ + 2c\delta N_+\operatorname{sgn}(\gamma) + i\alpha\delta N_+ \\
&- \operatorname{sgn}(\gamma)\sqrt{\Bigg(-16\left(\alpha^2 + 1\right)\left(c^2\left(4\delta + \delta^2 N_+ + 4\right) - (\delta + 2)(\delta N_+ + 4)\right)} \\
&- \left(\alpha\left(c^2(\delta(N_+ - 4) - 4) + \delta(N_+ + 4) + 12\right) - 2ic\delta N_+\operatorname{sgn}(\gamma)\right)^2\Bigg)\Bigg] \\
E_+ = -\frac{1}{8\left(\alpha^2 + 1\right)}\Bigg[ &4i\alpha\delta + 12i\alpha - 4i\alpha c^2\delta - 4i\alpha c^2 + i\alpha c^2\delta N_+ - 2c\delta N_+\operatorname{sgn}(\gamma) + i\alpha\delta N_+ \\
&- \operatorname{sgn}(\gamma)\sqrt{\Bigg(-16\left(\alpha^2 + 1\right)\left(c^2\left(4\delta + \delta^2 N_+ + 4\right) - (\delta + 2)(\delta N_+ + 4)\right)} \\
&- \left(\alpha\left(c^2(\delta(N_+ - 4) - 4) + \delta(N_+ + 4) + 12\right) + 2ic\delta N_+\operatorname{sgn}(\gamma)\right)^2\Bigg)\Bigg]
\end{aligned}
\tag{E.7}
$$

We can expand the above energies up to first order in $\alpha$, giving

$$
\begin{aligned}
E_- &= \epsilon_-\left(\operatorname{sgn}(\gamma) - \frac{i\alpha\left(c^2(\delta(N_+ - 4) - 4) + \delta(N_+ + 4) + 12\right)}{2(4\epsilon_- + c\delta N_+)}\right) + \mathcal{O}(\alpha^2) \\
E_+ &= \epsilon_+\left(\operatorname{sgn}(\gamma) - \frac{i\alpha\left(c^2(\delta(N_+ - 4) - 4) + \delta(N_+ + 4) + 12\right)}{2(4\epsilon_+ - c\delta N_+)}\right) + \mathcal{O}(\alpha^2)
\end{aligned}
\tag{E.8}
$$

where

$$
\epsilon_\pm = \frac{1}{4}\left(\sqrt{(\delta N_+ + 4)\left(c^2(\delta(N_+ - 4) - 4) + 4(\delta + 2)\right)} \pm c\delta N_+\right)
\tag{E.9}
$$

This expansion makes clear the fact that changing the sign of $\gamma$ inverses the sign of the real part of the complex eigenergies of the system, leaving the imaginary part unaffected.

We expect this physically because the sign of $\gamma$ controls the direction of precession while having no effect on the rate at which the spins get damped.

## E.0.2 Second Order Response to Perpendicular Driving

At second order the general expression ($\delta \neq 0$ and $N_x \neq N_y$) for $\omega_{\text{screw}}$ reads

$$
\omega_{\text{screw}} = \omega \Bigg[
$$

$$
2 b_R b_L c \omega \text{sgn}(\gamma) \delta N_- \Big( -4 \left( \alpha^4 \omega^4 + \alpha^2 \left( 2\omega^2 + 3 \right) \omega^2 + \omega^4 - 4 \right)
$$

$$
+ c^4 \Big( 4 \left( \alpha^2 \omega^2 + 3 \right) + \delta \left( 24 - \alpha^2 (N_+ - 4)\omega^2 \right)
$$

$$
+ 2\delta^4 N_+ + \delta^3 (7 N_+ + 4) + 2\delta^2 (3 N_+ + 8) \Big)
$$

$$
- 2c^2 \Big( \delta^2 \left( -2 \left( \alpha^2 + 1 \right) \omega^2 + N_+ \left( \left( \alpha^2 + 1 \right) \omega^2 + 13 \right) + 18 \right)
$$

$$
+ \delta \left( -4 \left( \alpha^2 + 1 \right) \omega^2 + N_+ \left( \left( \alpha^2 + 2 \right) \omega^2 + 6 \right) + 28 \right)
$$

$$
+ 2\delta^4 N_+ + \delta^3 (9 N_+ + 4) - 4 \left( \omega^2 - 4 \right) \Big)
$$

$$
+ 2\delta^2 \left( -2 \left( \alpha^2 + 1 \right) \omega^2 + N_+ \left( \left( \alpha^2 + 1 \right) \omega^2 + 10 \right) + 10 \right)
$$

$$
+ \delta \left( -4 \left( 3\alpha^2 + 2 \right) \omega^2 + N_+ \left( \left( 3\alpha^2 + 4 \right) \omega^2 + 12 \right) + 32 \right)
$$

$$
+ 2\delta^4 N_+ + \delta^3 (11 N_+ + 4) \Big)
$$

$$
+ (b_R^2 + b_L^2) \frac{1}{2} c\omega \text{sgn}(\gamma) \Big( 16 \left( \left( \alpha^2 + 1 \right)^2 \omega^4 + \left( 5\alpha^2 - 4 \right) \omega^2 + 4 \right)
$$

$$
- c^4 \Big( -16 \left( \alpha^2 \omega^2 + 1 \right) - \delta^2 \left( \alpha^2 \left( N_-^2 + 16 \right) \omega^2 + \alpha^2 N_+^2 \omega^2 - 8 N_+ \left( \alpha^2 \omega^2 + 6 \right) + 16 \right)
$$

$$
+ 2\delta^5 \left( N_-^2 + N_+^2 \right) + \delta^4 \left( 7 N_-^2 + N_+ (7 N_+ + 8) \right)
$$

$$
+ \delta^3 \left( 6 N_-^2 + 2 N_+ (3 N_+ + 16) \right) + 8\delta \left( -4\alpha^2 \omega^2 + \alpha^2 N_+ \omega^2 + 3 N_+ - 4 \right) \Big)
$$

$$
+ 2c^2 \Big( 16 \left( \left( 1 - 2\alpha^2 \right) \omega^2 - 2 \right) + \delta^2 \Big( -16 \left( \alpha^2 \omega^2 + 1 \right) + N_-^2 \left( \left( \alpha^2 + 2 \right) \omega^2 + 6 \right)
$$

$$
+ N_+^2 \left( \left( \alpha^2 + 2 \right) \omega^2 + 6 \right) - 8 N_+ \left( \left( \alpha^2 + 1 \right) \omega^2 - 7 \right) \Big) + 2\delta^5 \left( N_-^2 + N_+^2 \right)
$$

$$
+ \delta^3 \Big( N_-^2 \left( \left( \alpha^2 + 1 \right) \omega^2 + 13 \right)
$$

$$
+ N_+ \left( -4 \left( \alpha^2 + 1 \right) \omega^2 + N_+ \left( \left( \alpha^2 + 1 \right) \omega^2 + 13 \right) + 36 \right) \Big)
$$

$$
+ \delta^4 \left( 9 N_-^2 + N_+ (9 N_+ + 8) \right) - 8\delta \left( \left( 6\alpha^2 - 2 \right) \omega^2 + N_+ \left( \omega^2 - 4 \right) + 6 \right) \Big)
$$

$$
- \delta^2 \Big( -16 \left( \alpha^2 \omega^2 + 1 \right) + N_-^2 \left( \left( 3\alpha^2 + 4 \right) \omega^2 + 12 \right)
$$

$$
+ N_+^2 \left( \left( 3\alpha^2 + 4 \right) \omega^2 + 12 \right) - 8 N_+ \left( \left( 3\alpha^2 + 2 \right) \omega^2 - 8 \right) \Big) - 2\delta^5 \left( N_-^2 + N_+^2 \right)
$$

$$
- 2\delta^3 \Big( N_-^2 \left( \left( \alpha^2 + 1 \right) \omega^2 + 10 \right)
$$

$$
+ N_+ \left( -4 \left( \alpha^2 + 1 \right) \omega^2 + N_+ \left( \left( \alpha^2 + 1 \right) \omega^2 + 10 \right) + 20 \right) \Big)
$$

$$
- \delta^4 \left( 11 N_-^2 + N_+ (11 N_+ + 8) \right)
$$

$$
+ 8\delta \left( \left( 8\alpha^2 - 4 \right) \omega^2 + N_+ \left( \alpha^4 \omega^4 + \alpha^2 \left( 2\omega^2 + 3 \right) \omega^2 + \omega^4 - 4 \right) + 8 \right) \Big)
$$

$$+ \frac{1}{4}(b_L^2 - b_R^2)\Bigg[$$

$$\Bigg(-3\left(N_-^2 - N_+^2\right)\delta^6 - 8\left(2N_-^2 - N_+(2N_+ + 3)\right)\delta^5$$

$$+\left(\left(3\omega^2 - 26\right)N_-^2 + 48\left(\alpha^2\omega^2 + 1\right) - 8N_+\left(2\alpha^2\omega^2 + \omega^2 - 18\right) + N_+^2\left(26 - 3\omega^2\right)\right)\delta^4$$

$$+4\Big(\left(\left(\alpha^2 + 2\right)\omega^2 - 3\right)N_-^2 + 80\alpha^2\omega^2 - 8\omega^2 - N_+^2\left(\left(\alpha^2 + 2\right)\omega^2 - 3\right)$$

$$+ N_+\left(72 - 2\left(10\alpha^2 + 3\right)\omega^2\right) + 80\Big)\delta^3$$

$$+\Big(-\left(N_-^2 - 16\right)\alpha^2\left(\alpha^2 + 1\right)\omega^4$$

$$+2\left(\left(\alpha^2 + 6\right)N_-^2 + 384\alpha^2 - 72\right)\omega^2 + N_+^2\left(\omega^2\alpha^4 + \left(\omega^2 - 2\right)\alpha^2 - 12\right)\omega^2$$

$$- 8N_+\left(\left(\alpha^4 + \alpha^2\right)\omega^4 + 2\left(9\alpha^2 - 1\right)\omega^2 - 27\right) + 752\Big)\delta^2$$

$$-8\left(N_+\left(\left(\alpha^4 + \alpha^2\right)\omega^4 + 2\left(5\alpha^2 - 2\right)\omega^2 - 6\right) - 4\left(\left(\alpha^4 + \alpha^2\right)\omega^4 + 6\left(4\alpha^2 - 1\right)\omega^2 + 23\right)\right)\delta$$

$$+ 16\left(\left(\alpha^4 + \alpha^2\right)\omega^4 + \left(17\alpha^2 - 5\right)\omega^2 + 16\right)\Bigg)c^4$$

$$-\Bigg(-3\left(N_-^2 - N_+^2\right)\delta^6 - 4\left(5N_-^2 - N_+(5N_+ + 6)\right)\delta^5 + \Big(-\left(\left(\alpha^2 - 2\right)\omega^2 + 47\right)N_-^2$$

$$+48\left(\alpha^2\omega^2 + 1\right) + N_+^2\left(\left(\alpha^2 - 2\right)\omega^2 + 47\right) - 8N_+\left(\left(\alpha^2 + 2\right)\omega^2 - 21\right)\Big)\delta^4$$

$$+4\left(\left(\omega^2 - 11\right)N_-^2 + 88\alpha^2\omega^2 - 16\omega^2 - N_+^2\left(\omega^2 - 11\right) - 2N_+\left(\left(3\alpha^2 + 8\right)\omega^2 - 53\right) + 88\right)\delta^3$$

$$+\Bigg(\left(2\alpha^4\omega^4 + \alpha^2\left(6\omega^2 + 5\right)\omega^2 + 4\left(\omega^4 - 3\right)\right)N_-^2$$

$$-8N_+\left(\left(\alpha^2 + 1\right)^2\omega^4 + 3\left(\alpha^2 + 2\right)\omega^2 - 56\right)$$

$$+16\left(\left(3\alpha^4 + 4\alpha^2 + 1\right)\omega^4 + \left(62\alpha^2 - 20\right)\omega^2 + 59\right)$$

$$-N_+^2\left(2\alpha^4\omega^4 + \alpha^2\left(6\omega^2 + 5\right)\omega^2 + 4\left(\omega^4 - 3\right)\right)\Bigg)\delta^2$$

$$-8\Big(N_+\left(2\left(\alpha^4 + 3\alpha^2 + 2\right)\omega^4 + \left(3\alpha^2 - 4\right)\omega^2 - 20\right)$$

$$-4\left(\left(5\alpha^4 + 6\alpha^2 + 1\right)\omega^4 + \left(39\alpha^2 - 16\right)\omega^2 + 34\right)\Big)\delta$$

$$+16\left(\left(7\alpha^4 + 8\alpha^2 + 1\right)\omega^4 + \left(35\alpha^2 - 16\right)\omega^2 + 28\right)\Bigg)c^2$$

$$+\left(\delta^2 + 4\delta + \left(\alpha^2 + 1\right)\omega^2 + 4\right)\Bigg(\left(N_+^2 - N_-^2\right)\delta^4$$

$$+\left(4N_+(N_+ + 2) - 4N_-^2\right)\delta^3$$

$$+\left(-\left(\alpha^2\omega^2 + 4\right)N_-^2 - 8N_+\left(\omega^2 - 4\right) + 16\left(\alpha^2\omega^2 + 1\right) + N_+^2\left(\alpha^2\omega^2 + 4\right)\right)\delta^2$$

$$+8\left(\left(8\alpha^2 - 4\right)\omega^2 + N_+\left(\left(\alpha^2 - 2\right)\omega^2 + 4\right) + 8\right)\delta$$

$$+16\left(\left(\alpha^2 + 1\right)^2\omega^4 + \left(5\alpha^2 - 4\right)\omega^2 + 4\right)\Bigg)$$

$$-c^6\left(\delta^2 + 4\delta + 3\right)\Bigg(\left(N_+^2 - N_-^2\right)\delta^4$$

$$+8N_+\delta^3 + \left(N_+^2\alpha^2\omega^2 - \left(N_-^2 - 16\right)\alpha^2\omega^2 + N_+\left(8 - 8\alpha^2\omega^2\right) + 16\right)\delta^2$$

The general expression for $\theta_2^{(0,0)}$ is even more complicated, and not given here out of laziness (contact me if you need it...). In the case $N_x = N_y$ things simplify somewhat and we obtain the following expression for $\omega_{\text{screw}}$ and $\theta_2^{(0,0)}$, where the energies $E_\pm$ are the same as the ones we defined in Eq. (E.7)

$$\omega_{\text{screw}} = 2\omega \left[ \frac{b_R^2 \left((1+\alpha^2)\omega^2 - c^2\left(\delta^2 + 4\delta + 3\right) + \delta^2 + 4\delta + 4 - 2\text{sgn}(\gamma)c\omega\right)}{(\omega - E_-)(\omega - E_-^*)(\omega + E_+)(\omega + E_+^*)} \right.$$
$$\left. - \frac{b_L^2 \left((1+\alpha^2)\omega^2 - c^2\left(\delta^2 + 4\delta + 3\right) + \delta^2 + 4\delta + 4 + 2\text{sgn}(\gamma)c\omega\right)}{(\omega + E_-)(\omega + E_-^*)(\omega - E_+)(\omega - E_+^*)} \right] \tag{E.12}$$

$$\theta_2^{(0,0)} = \frac{-b_R^2}{\sqrt{1 - c^2}(\delta N_z + 1)(\omega - E_-)(\omega - E_1^*)(\omega + E_2)(\omega + E_2^*)} \Bigg($$
$$+ 2\text{sgn}(\gamma)\omega \left(2\left(\alpha^2 + 1\right)\omega^2 + \delta^2 + 3\delta + 2\right) - 2\text{sgn}(\gamma)c^2\omega \left(\delta^2 - \delta(N_+ - 6) + 5\right)$$
$$+ c^3 \left(\alpha^2\omega^2 + 1\right)(1 + \delta N_z) + c\left(\left(4\alpha^2 - 3\right)\omega^2 + \delta \left(\omega^2 \left(2\alpha^2 - N_+ + 3\right) + 2\right) + 4\right)\Bigg)$$

$$+ \frac{-b_L^2}{\sqrt{1 - c^2}(\delta N_z + 1)(\omega + E_-)(\omega + E_1^*)(\omega - E_2)(\omega - E_2^*)} \Bigg($$
$$- 2\text{sgn}(\gamma)\omega \left(2\left(\alpha^2 + 1\right)\omega^2 + \delta^2 + 3\delta + 2\right) + 2\text{sgn}(\gamma)c^2\omega \left(\delta^2 - \delta(N_+ - 6) + 5\right)$$
$$+ c^3 \left(\alpha^2\omega^2 + 1\right)(1 + \delta N_z) + c\left(\left(4\alpha^2 - 3\right)\omega^2 + \delta \left(\omega^2 \left(2\alpha^2 - N_+ + 3\right) + 2\right) + 4\right)\Bigg) \tag{E.13}$$

# Appendix F

# Floquet Spin Wave Theory: Auxiliary Calculations

## F.1 Derivation of Eq. (2.26)

Let us first state a few identities between the basis vectors $\mathbf{e}_3, \mathbf{e}_\pm$ which will be useful for our calculation:

$$
\begin{aligned}
\mathbf{e}_3 \cdot \mathbf{e}_3 &= 1 & \mathbf{e}_\pm \cdot \mathbf{e}_\pm &= 0 \\
\mathbf{e}_\pm \cdot \mathbf{e}_\mp &= 1 & \mathbf{e}_\pm \cdot \dot{\mathbf{e}}_\mp &= \pm i \cos(\theta) \dot{\phi} \\
\mathbf{e}_\pm \cdot \dot{\mathbf{e}}_\pm &= 0 & \mathbf{e}_\pm \cdot (\dot{\mathbf{e}}_3 \times \mathbf{e}_\mp) &= 0 \\
\mathbf{e}_\pm \cdot (\dot{\mathbf{e}}_\pm \times \mathbf{e}_3) &= 0 & \mathbf{e}_\pm \cdot (\dot{\mathbf{e}}_\mp \times \mathbf{e}_3) &= \cos(\theta) \dot{\phi}.
\end{aligned}
$$

As suggested in the main text, the idea is to substitute the expansion Eq. (2.24) into Eq. (1.22), retaining only terms linear in $a, a^*$, and then project this equation onto $\mathbf{e}_\mp$. Here we list the results of this operation for each term in Eq. (2.24)

$$
\begin{aligned}
\mathbf{e}_+ \cdot \hat{\mathbf{M}} &= \mathbf{e}_\mp \left( \dot{a} \mathbf{e}_- + a \dot{\mathbf{e}}_+ \dot{a}^* \mathbf{e}_+ + a^* \dot{\mathbf{e}}_+ \right) = i \cos(\theta) \dot{\phi} a + \dot{a} \\
\mathbf{e}_+ \cdot \left( \hat{\mathbf{M}} \times \dot{\hat{\mathbf{M}}} \right) &= \mathbf{e}_+ \cdot \left( (a \mathbf{e}_- + a^* \mathbf{e}_+) \times \dot{\mathbf{e}}_3 + \mathbf{e}_3 \times (\dot{\mathbf{e}}_- a + \mathbf{e}_- \dot{a} + \dot{\mathbf{e}}_+ a^* + \mathbf{e}_+ \dot{a}^*) \right) \\
&= i \dot{a} - \cos(\theta) \dot{\phi} a \\
\mathbf{e}_+ \cdot i \{ F^{(2)}, \mathbf{e}_- a + \mathbf{e}_+ a^* \} &= i \{ F^{(2)}, a \}
\end{aligned}
$$

Collecting these terms back together in the EoM and bringing the damping term over to the LHS gives

$$\text{sgn}(\gamma)(\dot{a} + i\cos(\theta)\dot{\phi}a) = i\{F^{(2)}, a\} - i\alpha(\dot{a} + i\cos(\theta)\dot{\phi}a).$$

Finally, multiplying both sides of the equation by $\frac{\text{sgn}(\gamma)-i\alpha}{1+\alpha^2}$ gives us the equation of motion shown in Eq. (2.26). Note that we have only shown the projection onto $\mathbf{e}_+$ here, the analogous result for projection with $\mathbf{e}_-$ can be obtained by simply taking the complex conjugate of the result.

## F.2  Derivation of $M^F$

In this sub-appendix we derive the Floquet equation Eq. (2.34) as well as the Floquet matrix $M^F$. Using the definition in Eq. (2.33) for the Fourier transformed fields $\tilde{a}_{\mathbf{k}}^m, \tilde{a}_{\mathbf{k}}^{*m}$ we can write the back Fourier transform for $a, a^*$ as

$$
\begin{aligned}
a(\mathbf{r}, t) &= \sum_{\substack{k_\|, k_\perp \\ m,j \in \mathbb{Z}}} \tilde{a}_{j\mathbf{q}+\mathbf{k}}^m e^{-i\left(m\omega t + (jq+k_\|)(z+v_{\text{screw}}t)+\rho k_\perp\right)} \\
a^*(\mathbf{r}, t) &= \sum_{\substack{k_\|, k_\perp \\ m,j \in \mathbb{Z}}} \tilde{a}_{-j\mathbf{q}-\mathbf{k}}^{-m*} e^{-i\left(m\omega t + (jq+k_\|)(z+v_{\text{screw}}t)+\rho k_\perp\right)},
\end{aligned}
\tag{F.1}
$$

where $\mathbf{k} = \mathbf{k}_\| + \mathbf{k}_\perp$ and we switched to cylindrical coordinates $\mathbf{r} = (z, \boldsymbol{\rho})^T$, with $\boldsymbol{\rho} = (x, y)^T$. Due to the cylindrical symmetry of the problem, the azimuthal angle between $k_x, k_y$ has no physical importance and can be set to zero. Also note that $k_\|$ is only defined in the first Brillouin zone, $-q/2 < k_\| < q/2$ due to the periodic nature of the underlying helical texture.

Now we define the column vector $\Psi^m(\mathbf{k})$ from which we then build the Floquet vector $\Psi^F(\mathbf{k})$, Eq. (F.3).

$$\Psi^m(\mathbf{k}) = \left(\ldots \quad \tilde{a}_{\mathbf{k}-\mathbf{q}}^m, \quad \tilde{a}_{-\mathbf{k}-\mathbf{q}}^{-m*}, \quad \tilde{a}_{\mathbf{k}}^m, \quad \tilde{a}_{-\mathbf{k}}^{-m*}, \quad \tilde{a}_{\mathbf{k}+\mathbf{q}}^m, \quad \tilde{a}_{-\mathbf{k}+\mathbf{q}}^{-m*} \quad \ldots\right)^T \tag{F.2}$$

$$\Psi^F(\mathbf{k}) = \left(\ldots \quad \Psi^{-1}(\mathbf{k})e^{i\omega t}, \quad \Psi^0(\mathbf{k}), \quad \Psi^1(\mathbf{k})e^{-i\omega t}, \quad \ldots\right)^T \tag{F.3}$$

Let us now substitute Eq. (F.1) into the EoM Eq. (2.26). The LHS of this equation requires calculating the time derivative of $\dot{a}, \dot{a}^*$,

$$\dot{a} = \sum_{m,j \in \mathbb{Z}} (\dot{\tilde{a}}_{j\mathbf{q}+\mathbf{k}}^m - (im\omega + (jq + k_{\parallel})v_{\text{screw}})\tilde{a}_{j\mathbf{q}+\mathbf{k}}^m)e^{-i(m\omega t + (jq+k_{\parallel})(z+v_{\text{screw}}t) + \rho k_{\perp})} \quad (\text{F.4})$$
$$= \sum_{m,\text{odd } l} \left(\dot{\Psi}_l^m(\mathbf{k}) - i(m\omega + (f(l)q + k_{\parallel})v_{\text{screw}}t)\Psi_l^m(\mathbf{k})\right) e^{-i(m\omega t + (f(l)q + k_{\parallel})\tilde{z} + \rho k_{\perp})}$$

$$\dot{a}^* = \sum_{m,j \in \mathbb{Z}} (\dot{\tilde{a}}_{-j\mathbf{q}-\mathbf{k}}^{-m*} - (im\omega + (jq + k_{\parallel})v_{\text{screw}})\tilde{a}_{-j\mathbf{q}-\mathbf{k}}^{-m*})e^{-i(m\omega t + (jq+k_{\parallel})(z+v_{\text{screw}}t) + \rho k_{\perp})} \quad (\text{F.5})$$
$$= \sum_{m,\text{even } l} \left(\dot{\Psi}_l^m(\mathbf{k}) - i(m\omega + (f(l)q + k_{\parallel})v_{\text{screw}}t)\Psi_l^m(\mathbf{k})\right) e^{-i(m\omega t + (f(l)q + k_{\parallel})\tilde{z} + \rho k_{\perp})},$$

where we defined $\tilde{z} = z + v_{\text{screw}}t$ and $f(l) = \left\lfloor \frac{1}{2}(l - \frac{l_{\text{max}}}{2}) \right\rfloor$. Here the index $l$ designates the $l^{\text{th}}$ component of the Floquet subvector vector $\Psi_l^m(\mathbf{k})$. Due to two fields $\tilde{a}_k^m$ and $\tilde{a}_k^{m*}$ for each value of $l$ $l_{\text{max}}$ is always even. Formally $l$ runs from $l_{\text{min}} = 1$ to $l_{\text{max}} = \infty$ but in our perturbative scheme it needs to be cut off at $l_{\text{max}} = 6$ because we only include three momentum copies $q = -1, 0, 1$. For the $\dot{a}$ expression we sum over only odd $l = 1, 3, 5$, whereas for the $\dot{a}^*$ expression we sum over even $l = 2, 4, 6$.

Let's now look at the RHS of Eq. (2.26). The first term involves computing the Poisson bracket $\{F^{(2)}, a/a^*\}$. As mentioned in the main text, $F^{(2)}$ is obtained by inserting Eq. (2.24) into Eq. (1.3) and keeping only the terms quadratic in $a, a^*$. By using the Fourier convention Eq. (2.33) we obtain $F^{(2)}$ in terms of the $\tilde{a}_{j\mathbf{q}+\mathbf{k}}^m, \tilde{a}_{j\mathbf{q}+\mathbf{k}}^{m*}$ operators. Here are the ways in which these fields could be combined

$$\tilde{a}_{j'\mathbf{q}+\mathbf{k}}^{m*}\tilde{a}_{j\mathbf{q}+\mathbf{k}}^l, \quad \tilde{a}_{j'\mathbf{q}-\mathbf{k}}^m\tilde{a}_{j\mathbf{q}+\mathbf{k}}^l, \quad \tilde{a}_{j'\mathbf{q}-\mathbf{k}}^{m*}\tilde{a}_{j\mathbf{q}+\mathbf{k}}^{l*}$$

Note how the perpendicular component $k_{\perp}$ must be the same (up to a negative sign) in both fields but the parallel component $k_{\parallel}$ is allowed to differ by an integer multiple of $q$, a consequence of the underlying helical texture which allows for Umklapp scattering. Due to the presence of the $a^2, a^{*2}$ terms a Bogoliubov transformation is required, and the method we use implicitly accomplishes the same thing. By choosing appropriate values for $j, j'$ in the expression $\Psi^{m*}(\mathbf{k})_{j'}\Psi^l(\mathbf{k}_j)$ (definition given in Eq. (F.2)) one can obtain all the combinations given in Sec. F.2. This makes it possible to write $F^{(2)}$ as

$$F^{(2)} = \sum_{\mathbf{k},n,m,l,j,j'} e^{-i\omega t(n-m+l)} \Psi_j^{m*}(\mathbf{k})\tilde{F}_{jj'}^n(\mathbf{k})\Psi_{j'}^l(\mathbf{k}). \quad (\text{F.6})$$

$\tilde{F}_{jj'}^n$ can be quite tricky to calculate – if you need help contact me for the Mathematica code. Now, the Poisson bracket of $F^{(2)}$ with $a, a^*$ can also be written purely in terms of the vector $\Psi_i^m$ as

$$
\begin{aligned}
\{F^{(2)}, a/a^*\} &= \\
&\sum_{\substack{\mathbf{k}, \mathbf{k}', j, j', j'' \\ n, m, l, m'}} e^{-i\omega t(n-m+l)} e^{-i(m'\omega t + (jq + k_\parallel)\tilde{z} + \rho k_\perp)} \tilde{F}_{j'j''}^n(\mathbf{k}') \left\{ \Psi_{j'}^{m*}(\mathbf{k}') \Psi_{j''}^l(\mathbf{k}'), \Psi_j^{m'}(\mathbf{k}) \right\} \\
&= \sum_{\mathbf{k}, n, l, j, j''} e^{-i\omega t(n+l)} e^{-i((f(j)q + k_\parallel)\tilde{z} + \rho k_\perp)} \\
&\qquad \left( (-1)^j \tilde{F}_{jj''}^n(\mathbf{k}) \Psi_{j''}^l(\mathbf{k}) + \left( \underbrace{\tilde{F}_{j',j+1}^n(-\mathbf{k})}_{j \text{ odd}} - \underbrace{\tilde{F}_{j',j-1}^n(-\mathbf{k})}_{j \text{ even}} \right) \Psi_{j'}^{-l*}(-\mathbf{k}) \right) \\
&= 2 \sum_{\mathbf{k}, n, l, j, j'} (-1)^j e^{-i\omega t(n+l)} e^{-i((f(j)q + k_\parallel)\tilde{z} + \rho k_\perp)} \tilde{F}_{jj'}^n(\mathbf{k}) \Psi_{j'}^l(\mathbf{k}),
\end{aligned}
\tag{F.7}
$$

where $j$ is odd if we are evaluating the Poisson bracket with $a$ and even for the Poisson bracket with $a^*$. Above we used

$$
\begin{aligned}
\left\{ \Psi_i^m(\mathbf{k}), \Psi_j^{n*}(\mathbf{k}') \right\} &= (-1)^{i-1} \delta_{i,j} \delta_{m,n} \delta_{\mathbf{k}, \mathbf{k}'} \\
\left\{ \Psi_i^m(\mathbf{k}), \Psi_j^n(\mathbf{k}') \right\} &= (\delta_{i\in\text{odd}:i,j-1} - \delta_{i\in\text{even}:i,j+1}) \delta_{m,-n} \delta_{\mathbf{k},-\mathbf{k}'} \\
\left\{ \Psi_i^{m*}(\mathbf{k}), \Psi_j^{n*}(\mathbf{k}') \right\} &= (\delta_{i\in\text{even}:i,j+1} - \delta_{i\in\text{odd}:i,j-1}) \delta_{m,-n} \delta_{\mathbf{k},-\mathbf{k}'}.
\end{aligned}
\tag{F.8}
$$

and

$$
\tilde{F}_{i,j}^n(\mathbf{k}) = \begin{cases} \tilde{F}_{j+1,i+1}^n(-\mathbf{k}) & i \text{ odd}, j \text{ odd} \\ \tilde{F}_{j-1,i+1}^n(-\mathbf{k}) & i \text{ odd}, j \text{ even} \\ \tilde{F}_{j+1,i-1}^n(-\mathbf{k}) & i \text{ even}, j \text{ odd} \\ \tilde{F}_{j-1,i-1}^n(-\mathbf{k}) & i \text{ even}, j \text{ even} \end{cases}, \quad \Psi_j^{-l*}(-\mathbf{k}) = \begin{cases} \Psi_{j+1}^l(\mathbf{k}) & j \text{ odd} \\ \Psi_{j-1}^l(\mathbf{k}) & j \text{ even} \end{cases}.
\tag{F.9}
$$

The second term on the RHS of Eq. (2.26) is the $\dot{\phi} \cos(\theta)$ term. This term, built from the steady state solutions $\theta(z,t), \phi(z,t)$, oscillates in both space and time with components $e^{im\omega t}, e^{inq\tilde{z}}, m, n \in \mathbb{Z}$, and can be written as

$$
\dot{\phi} \cos(\theta) = \sum_{m,n\in\mathbb{Z}} e^{-i(m\omega t + nq\tilde{z})} g_n^m.
\tag{F.10}
$$

Finally, putting together Eq. (F.4), (F.7) and (F.10) and setting the coefficients of the terms which oscillate at the same spatial and temporal frequencies equal to each

other, we obtain an equation of motion for $\Psi_j^m$

$$\dot{\Psi}_j^m = i\left(\left(m\omega + (f(l)q + k_\parallel)v_{\text{screw}}\right)\delta_{m,l}\delta_{j,j'} + \frac{2\left(\text{sgn}(\gamma)(-1)^j + i\alpha\right)}{1 + \alpha^2}\tilde{F}_{jj'}^{m-l} + (-1)^j g_{j-j'}^{m-l}\right)\Psi_{j'}^l.$$

(F.11)

From this, we can define the matrix $M^{ml}$ used to build the Floquet matrix $M^F$ with

$$M_{jj'}^{ml} = -\left(\left(m\omega + (f(l)q + k_\parallel)v_{\text{screw}}\right)\delta_{m,l}\delta_{j,j'} + \frac{2\left(\text{sgn}(\gamma)(-1)^j + i\alpha\right)}{1 + \alpha^2}\tilde{F}_{jj'}^{m-l} + (-1)^j g_{j-j'}^{m-l}\right)$$

(F.12)

$$M^F = \begin{pmatrix} \ddots & & & & \\ & M^{1,1} & M^{1,0} & M^{1,-1} & \\ & M^{0,1} & M^{0,0} & M^{0,-1}. & \\ & M^{-1,1} & M^{-1,0} & M^{-1,-1} & \\ & & & & \ddots \end{pmatrix}.$$

(F.13)

The Floquet matrix $M^F$ is non-Hermitian, meaning its eigenvalues are complex. These complex eigenvalues describe the energy and decay rate of the the spin wave excitations on top of the Archimedean screw solution.

## F.2.1  $M^F$ for the Non-Driven Conical State

When $\mathbf{b}_1 = 0$, only the $\omega = 0$ Floquet zone needs to be included in $M^F$, i.e. the matrix $M^{0,0}$. For spin waves which propagate purely parallel to the pitch of the helix, $\mathbf{k} \parallel \mathbf{q}$, the matrix $M^{0,0}$ can be decomposed into $2 \times 2$ block diagonal form,

$$M^{0,0} = \begin{pmatrix} \ddots & 0 & 0 & 0 & 0 \\ 0 & M(k_\parallel - q) & 0 & 0 & 0 \\ 0 & 0 & M(k_\parallel) & 0 & 0 \\ 0 & 0 & 0 & M(k_\parallel + q) & 0 \\ 0 & 0 & 0 & 0 & \ddots \end{pmatrix}$$

with

$$M(k_\parallel) = \frac{1}{2}\begin{pmatrix} \frac{s^2(\delta+1)+2k_\parallel^2}{\text{sgn}(\gamma)+i\alpha} & \frac{s^2(\delta+1)}{\text{sgn}(\gamma)+i\alpha} \\ -\frac{s^2(\delta+1)}{\text{sgn}(\gamma)-i\alpha} & -\frac{s^2(\delta+1)+2k_\parallel^2}{\text{sgn}(\gamma)-i\alpha} \end{pmatrix}.$$

(F.14)

The two eigenvalues of $M(k_\parallel)$ are given in Eq. (2.36).

For spin waves with finite perpendicular momentum $k_\perp$ $M^{0,0}$ acquires some off-diagonal perturbations proportional to $k_\perp$. For $\delta = 0$, these are quite simple,

$$
\begin{pmatrix}
\ddots & P & 0 & 0 & 0 \\
P & M(k_\parallel - q) + L & P & 0 & 0 \\
0 & P & M(k_\parallel) + L & P & 0 \\
0 & 0 & P & M(k_\parallel + q) + L & P \\
0 & 0 & 0 & P & \ddots
\end{pmatrix}
\tag{F.15}
$$

with

$$
L = k_\perp^2 \begin{pmatrix} \frac{1}{\mathrm{sgn}(\gamma) + i\alpha} & 0 \\ 0 & \frac{1}{\mathrm{sgn}(\gamma) - i\alpha} \end{pmatrix}, \ P = sk_\perp \begin{pmatrix} \frac{1}{\mathrm{sgn}(\gamma) + i\alpha} & 0 \\ 0 & \frac{1}{\mathrm{sgn}(\gamma) - i\alpha} \end{pmatrix}.
\tag{F.16}
$$

If $k_\perp \ll 1$ perturbation theory can be used to solve Eq. (F.15).

# Appendix G

# Electron Transport Calculation

In order to evaluate the expectation value of Eq. (2.59) up to second order in $H_1(t)$, we must also expand the time-evolution operator $U(+\infty, -\infty)$ up to second order

$$U(+\infty, -\infty) \approx 1 - i \int_{-\infty}^{\infty} H_1(t)dt - \frac{1}{2} \iint_{-\infty}^{\infty} T[H_1(t)H_1(t')]dtdt'. \qquad (G.1)$$

The expression for $U(-\infty, +\infty)$ is the same as Eq. (G.1) with the changes $-i \to i, T \to \tilde{T}$, where $\tilde{T}$ is the anti-time ordering operator.

We define the electron Green's function as usual through

$$G_\sigma(k, t'-t) = -i\langle Td_{\sigma,k}(t')d_{\sigma,k}^\dagger(t)\rangle_{H_0} = [-i\theta(t'-t)(1 - \langle n_{\sigma,k}\rangle) + i\theta(t-t')\langle n_k\rangle] e^{-i\epsilon_k(t'-t)}$$

$$= \lim_{\delta \to 0} \int_{-\infty}^{\infty} \frac{d\omega}{2\pi} e^{-i\omega(t'-t)} \underbrace{\left[ \frac{1 - \langle n_{\sigma,k}\rangle}{\omega - \epsilon_k + i\delta} + \frac{\langle n_{\sigma,k}\rangle}{\omega - \epsilon_k - i\delta} \right]}_{G(k,\omega)},$$

$$(G.2)$$

where we use the Fourier convention $G_\sigma(\mathbf{k}, \omega) = \int dt e^{i\omega(t-t')} G_\sigma(\mathbf{k}, t-t')$ to switch between frequency and time domain. Here $n_{\sigma,\mathbf{k}} = (1 + e^{\beta(\epsilon_{\sigma,\mathbf{k}} - \epsilon_{\sigma,k_F})})^{-1}$ is the Fermi distribution function and $\epsilon_{\sigma\mathbf{k}}$ are the eigen-energies given in Eq. (2.58).
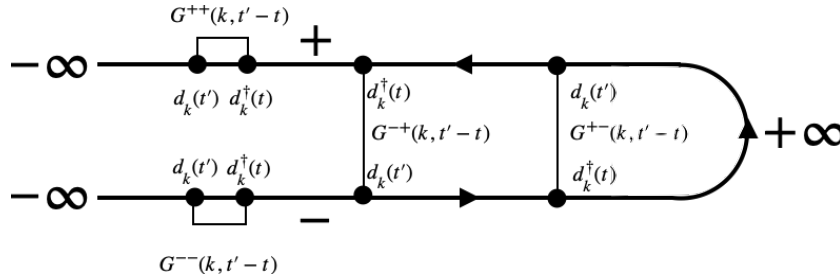


Figure G.1 Keldysh Contour

On the Keldysh contour, one needs to define four such Green's functions, which can be split into two pairs: $G^{++}$ and $G^{--}$ which are same-branch Green's functions and $G^{+-}$ and $G^{-+}$ which are opposite-branch Green's functions, see fig. G.1 for a pictoral representation. Below we list the four Keldysh Green's function in the frequency domain

$$
\begin{aligned}
G_\sigma^{++}(\mathbf{k},\omega) &= \frac{-(1-n_{\sigma,\mathbf{k}})}{\omega-\epsilon_{\sigma,\mathbf{k}}-\frac{i}{2\tau}} - \frac{n_{\sigma,\mathbf{k}}}{\omega-\epsilon_{\sigma,\mathbf{k}}+\frac{i}{2\tau}} \\
G_\sigma^{--}(\mathbf{k},\omega) &= \frac{1-n_{\sigma,\mathbf{k}}}{\omega-\epsilon_{\sigma,\mathbf{k}}+\frac{i}{2\tau}} + \frac{n_{\sigma,\mathbf{k}}}{\omega-\epsilon_{\sigma,\mathbf{k}}-\frac{i}{2\tau}} \\
G_\sigma^{+-}(\mathbf{k},\omega) &= \frac{1-n_{\sigma,\mathbf{k}}}{\omega-\epsilon_{\sigma,\mathbf{k}}+\frac{i}{2\tau}} - \frac{1-n_{\sigma,\mathbf{k}}}{\omega-\epsilon_{\sigma,\mathbf{k}}-\frac{i}{2\tau}} \\
G_\sigma^{-+}(\mathbf{k},\omega) &= \frac{n_{\sigma,\mathbf{k}}}{\omega-\epsilon_{\sigma,\mathbf{k}}-\frac{i}{2\tau}} - \frac{n_{\sigma,\mathbf{k}}}{\omega-\epsilon_{\sigma,\mathbf{k}}+\frac{i}{2\tau}},
\end{aligned}
\tag{G.3}
$$

We model the effects of disorder by a finite scattering rate $1/(2\tau)$. To simplify the calculation, we ignore the vertex corrections arising from disorder as for short-ranged impurities they are expected to be minor.

We now have all the tools we need to evaluate $\langle J_z(t)\rangle$. Using Wick's theorem, we obtain

$$
\langle J_z(t)\rangle \propto \iint_{-\infty}^{+\infty} dt_1 dt_2 \sum_{\sigma,\mathbf{k}_1,\mathbf{k}_2,\mathbf{k}} k_\perp^2 (k_\parallel - \sigma k_0) e^{-i\omega_{\text{screw}}(t_1-t_2)}.
$$
$$
\langle T_C d_{\sigma,\mathbf{k}_1}^\dagger(t_1) d_{\sigma,\mathbf{k}_1+\mathbf{q}}(t_1) d_{\sigma,\mathbf{k}_2+\mathbf{q}}^\dagger(t_2) d_{\sigma,\mathbf{k}_2}(t_2) d_{\sigma,\mathbf{k}}^\dagger(t) d_{\sigma,\mathbf{k}}(t)\rangle + h.c.
\tag{G.4}
$$

$$
= \frac{1}{i} \sum_{\sigma,\mathbf{k}} k_\perp^2(k_\parallel - \sigma k_0) \iint_{-\infty}^{+\infty} dt_1 dt_2 e^{-i\omega_{\text{screw}}(t_1-t_2)}
$$
$$
\Big[ G_\sigma^{--}(\mathbf{k},t-t_1) G_\sigma^{--}(\mathbf{k},t_2-t) G_\sigma^{--}(\mathbf{k}+\mathbf{q},t_1-t_2)
$$
$$
+ G_\sigma^{--}(\mathbf{k},t_1-t) G_\sigma^{--}(\mathbf{k},t-t_2) G_\sigma^{--}(\mathbf{k}-\mathbf{q},t_2-t_1)
$$
$$
+ G_\sigma^{-+}(\mathbf{k},t-t_1) G_\sigma^{+-}(\mathbf{k},t_2-t) G_\sigma^{++}(\mathbf{k}+\mathbf{q},t_1-t_2)
$$
$$
+ G_\sigma^{+-}(\mathbf{k},t_1-t) G_\sigma^{-+}(\mathbf{k},t-t_2) G_\sigma^{++}(\mathbf{k}-\mathbf{q},t_2-t_1)
$$
$$
- G_\sigma^{-+}(\mathbf{k},t-t_1) G_\sigma^{--}(\mathbf{k},t_2-t) G_\sigma^{+-}(\mathbf{k}+\mathbf{q},t_1-t_2)
$$
$$
- G_\sigma^{+-}(\mathbf{k},t_1-t) G_\sigma^{--}(\mathbf{k},t-t_2) G_\sigma^{-+}(\mathbf{k}-\mathbf{q},t_2-t_1) + h.c. \Big]
\tag{G.5}
$$

The next step consists in Fourier transforming the Green's functions in time, as well as time-averaging $\langle J_z(t)\rangle$ to obtain the DC component $\langle J_z^{\text{DC}}\rangle$. In addition, we can Taylor expand to first order in $\omega_{\text{screw}} = q v_{\text{screw}}$ (as $\omega_{\text{screw}}$ will be smaller than all electronic energy

scales) to obtain

$$\langle J_z \rangle \propto \frac{2qv_{\text{screw}}}{i} \int_{-\infty}^{\infty} \frac{d\omega}{2\pi} \sum_{\sigma,\mathbf{k}} k_\perp^2 (k_\parallel - k_{0,\sigma})$$

$$\Big[ G_\sigma^{--}(\mathbf{k},\omega)^2 \partial_\omega G_\sigma^{--}(\mathbf{k}+\mathbf{q},\omega) + G_\sigma^{+-}(\mathbf{k},\omega) G_\sigma^{-+}(\mathbf{k},\omega) \partial_\omega G_\sigma^{++}(\mathbf{k}+\mathbf{q},\omega)$$

$$- G^{--}(\mathbf{k},\omega) \Big( G^{-+}(\mathbf{k},\omega) \partial_\omega G_\sigma^{+-}(\mathbf{k}+\mathbf{q},\omega) + G_\sigma^{+-}(\mathbf{k},\omega) \partial_\omega G_\sigma^{-+}(\mathbf{k}+\mathbf{q},\omega) \Big) \Big]. \tag{G.6}$$

Restoring pre-factors and using cylindrical momentum coordinates, we obtain at $T=0$

$$\langle J_z \rangle = \sum_{\sigma=\uparrow,\downarrow} \tilde{J}_\sigma \int_{-k_{F,\sigma}}^{k_{F,\sigma}} \int_{k_\perp=0}^{\sqrt{k_{F,\sigma}^2 - k_\parallel^2}} \frac{dk_\parallel dk_\perp k_\perp^3 (q/2 - k_\parallel)}{\left( (k_\parallel - q/2)^2 + (q\tilde{\tau}^{-1})^2 \right)^2}$$

$$\tilde{J}_\sigma = e N_\sigma v_{\text{screw}} \frac{3s^2 \lambda_{\text{so}}^2}{v_{F,\sigma}^3} \frac{\hbar}{qm} \tag{G.7}$$

$$\tilde{\tau} = \frac{\hbar q^2 \tau}{m}, \quad v_{F,\sigma} = \frac{\hbar k_{F,\sigma}}{m}.$$

Integrating first over $k_\perp$ and then by parts over $k_\parallel$ yields

$$\langle J_z \rangle \simeq \sum_{\sigma=\uparrow,\downarrow} e N_\sigma v_{\text{screw}} \frac{3s^2 \lambda_{\text{so}}^2}{v_{F,\sigma}^3} \frac{\left( q^2 v_{F,\sigma}^2 \tau^2 + 3 \right) \arctan(qv_{F,\sigma}\tau) - 3qv_{F,\sigma}\tau}{2q\tau}, \tag{G.8}$$

where we have neglected small contributions of order $q/k_{F,\sigma}$. Taking the limits $v_F \tau \ll q^{-1}$, $v_F \tau \gg q^{-1}$ gives Eq. (2.62).

# Appendix H

# Driven Skyrmion Auxiliary Calculations

## H.1 Free Energy Terms

### H.1.1 Linear in $a, a^*$ contribution, $\mathcal{F}^{(1)}$

When we turn on a driving field

$$
\mathbf{b}_1(t) = \begin{pmatrix} \frac{1}{2}(b_R + b_L)\cos(\omega t) \\ \frac{1}{2}(b_R - b_L)\sin(\omega t) \\ b_z \cos(\omega t + \delta) \end{pmatrix}
$$

there is a linear in $a, a^*$ contribution to the free energy density,

$$
\begin{aligned}
\mathcal{F}^{(1)}_{\text{drive}} = -\frac{1}{2\sqrt{2}} \Bigg[ \\
+ b_R \left( \cos(\theta_0)\cos(\chi - \omega t)(a + a^*) - \frac{1}{i}(a - a^*)\sin(\chi - \omega t) \right) \\
+ b_L \left( \cos(\theta_0)\cos(\chi + \omega t)(a + a^*) - \frac{1}{i}(a - a^*)\sin(\chi + \omega t) \right) \\
- 2b_z \cos(\omega t + \delta)\sin(\theta_0)(a + a^*) \Bigg].
\end{aligned}
\tag{H.1}
$$

## H.1.2   Quadratic in $a, a^*$ contribution, $\mathcal{F}^{(2)}$

The quadratic in $a, a^*$ contribution to the free energy density independent of the driving field $b_1(t)$ contribution, is

$$
\begin{aligned}
\mathcal{F}^{(2)}_{\text{skyr.}} = -\frac{1}{4r^2} \Bigg[ \\
+ aa^* \left( -4b_0 r^2 \cos(\theta_0) + 2r^2 \theta_0'^2 + 4r^2 \theta_0' + 6r \sin(2\theta_0) - 3\cos(2\theta_0) - 1 \right) \\
+ 4ia^* \partial_\chi a(\cos(\theta_0) - r\sin(\theta_0)) - 4ia\partial_\chi a^*(\cos(\theta_0) - r\sin(\theta_0)) \\
- 4 \left( \partial_\chi a \partial_\chi a^* + r^2 a' a^{*\prime} \right) \\
+ a^2 \left( -r^2 \theta_0'^2 - 2r^2 \theta_0' + \sin^2(\theta_0) + r\sin(2\theta_0) \right) \\
+ a^{*2} \left( -r^2 \theta_0'^2 - 2r^2 \theta_0' + \sin^2(\theta_0) + r\sin(2\theta_0) \right) \Bigg].
\end{aligned}
\tag{H.2}
$$

$\mathcal{F}^{(2)}_{\text{skyr.}}$ is the free energy density we use in order to calculate the eigenbasis of the system. There is also a quadratic contribution which is proportional to $b_L, b_R, b_z$

$$
\begin{aligned}
\mathcal{F}^{(2)}_{\text{drive}} = \frac{1}{2} a^* a \Big[ b_R \sin(\theta_0) \cos(\omega t - \chi) + b_L \sin(\theta_0) \cos(\omega t + \chi) \\
+ 2 b_z \cos(\theta_0) \cos(\omega t + \delta) \Big]
\end{aligned}
\tag{H.3}
$$

which does not contribute to the EoM for $a, a^*$ at order $\mathcal{O}(\epsilon)$, but does contribute at order $\mathcal{O}(\epsilon^2)$.

## H.1.3   Cubic in $a, a^*$ contribution, $\mathcal{F}^{(3)}$

The cubic in $a, a^*$ contribution to the free energy density is

$$
\begin{aligned}
\mathcal{F}^{(3)}_{\text{skyr.}} = \frac{1}{4\sqrt{2}r} \Bigg[ \\
- \frac{1}{2} aa^* \Big[ 4r\left(\theta_0' + 1\right)\left(\partial_r a + \partial_r a^*\right) - 4i(\partial_\chi a - \partial_\chi a^*)(r\sin(\theta_0) + \cos(\theta_0)) \\
+ (a + a^*)\left(2r\sin(\theta_0)(b_0 + 5\cos(\theta_0)) + 10\cos(2\theta_0)\right) \Big] \\
+ 3a^{*2} \Big[ r\left(\theta_0' + 1\right)\partial_r a + i\partial_\chi a(r\sin(\theta_0) + \cos(\theta_0)) \Big] \\
+ 3a^2 \Big[ r\left(\theta_0' + 1\right)\partial_r a^* - i\partial_\chi a^*(r\sin(\theta_0) + \cos(\theta_0)) \Big] \Bigg]
\end{aligned}
\tag{H.4}
$$

There will also be a cubic in $a, a^*$ contribution from the driving terms, but we don't care about it as it will produce $\mathcal{O}(\epsilon)$ terms, which are one order too high for our calculation, after the Poisson bracket operation.

## H.2   Angular Momentum Eigenstates

We use the approach presented in [72], where the problem is simplified by switching to angular momentum eigenstates $a_m, a^*m$ with the following Fourier definition

$$
\begin{aligned}
a(r, \chi) &= \sum_m e^{im\chi} a_m(r) & a_m(r) &= \frac{1}{2\pi} \int_0^{2\pi} d\chi \, e^{-im\chi} a(r, \chi) \\
a^*(r, \chi) &= \sum_m e^{-im\chi} a_m^*(r) & a_m^*(r) &= \frac{1}{2\pi} \int_0^{2\pi} d\chi \, e^{im\chi} a^*(r, \chi).
\end{aligned}
\tag{H.5}
$$

The Poisson bracket in polar coordinates carries an extra factor $\frac{1}{r}$ compared to the Cartesian version

$$
\{a(r, \chi), a^*(r', \chi')\} = \frac{1}{r'}\delta(\chi - \chi')\delta(r - r'), \quad \{a_m(\mathbf{r}), a_{m'}^*(\mathbf{r}')\} = \frac{1}{2\pi r'}\delta_{m,m'}\delta(r - r'). \tag{H.6}
$$

Using these definitions one obtains

$$
\begin{pmatrix} \{F_{\text{skyr.}}^{(2)}, a\} \\ \{F_{\text{skyr.}}^{(2)}, a^*\} \end{pmatrix} = -\sum_m e^{im\chi} \sigma^z H_m \begin{pmatrix} a_m \\ a_{-m}^* \end{pmatrix}
\tag{H.7}
$$

with

$$
\begin{aligned}
H_m &= \mathbb{1}\left(-\frac{d}{dr^2} - \frac{1}{r}\frac{d}{dr} + \frac{m^2 + 1}{r^2} + b_0 + V_0^m\right) - \sigma^z \frac{2m}{r^2} + \sigma^z V_z^m + \sigma^x V_x \\
V_0^m &= \frac{3\left(\cos(2\theta_0) - 1\right)}{4r^2} - \frac{3\sin(2\theta_0)}{2r} + b_0\left(\cos(\theta_0) - 1\right) - \theta_0' - \frac{\theta_0'^2}{2} \\
V_z^m &= \frac{2m}{r^2}\left(\cos(\theta_0) - 1 - r\sin(\theta_0)\right) \\
V_x &= -\frac{1}{2r^2}\left(\sin^2(\theta_0) + r\sin(2\theta_0) - r^2\theta_0'^2 - 2r^2\theta_0'\right)
\end{aligned}
\tag{H.8}
$$

## H.3   Perturbation Theory in $\alpha$

To obtain the first order in $\alpha$ correction to the eigenenergies, we project $\langle m, n, s | \sigma^z$ onto Eq. (3.13). Using the property $\langle m, n, s | H_m = \epsilon_{n,s} \sigma^z \langle m, n, s |$ we obtain

$$\epsilon_{n,s}^{(1)} = \frac{\langle m, n, s | m, n, s \rangle}{\langle m, n, + | \sigma^z | m, n, + \rangle} \epsilon_{n,+}^{(0)}. \tag{H.9}$$

where we additionally used the fact that we normalised $\langle m, n, s | \sigma^z | m, n, s \rangle = \text{sgn}(s)$. We immediately see that the first order energy correction for the translational mode also vanishes, as $\epsilon_{\text{trans.}}^{(0)} = 0$. For the scattering modes, the prefactor in front of $\epsilon_{n,+}$ is unity, as in the far limit only one component is non-vanishing so that the top and the bottom of the fraction are the same. For the breathing mode this is not the case and $\langle \text{br.} | \text{br.} \rangle$ needs to be calculated explicitly; in the case $b_0 = 1$ its value is approximately 1.22.

To obtain the first order in $\alpha$ correction to the eigenmodes, we instead project $\langle m', n', s' | \sigma^z \neq \langle m, n, s | \sigma^z$ onto Eq. (3.13). After some algebra, we obtain the following corrections to the $m = 0, \pm 1$ scattering states, $m = 0$ breathing mode and $m = \pm 1$ translational modes

$$
\begin{aligned}
\left| m = 0, k, +^{(1)} \right\rangle = -\Bigg[ &\sum_{k'} -\Delta k' k' \frac{\epsilon_k^{(0)}}{\epsilon_k^{(0)} + \epsilon_{k'}^{(0)}} \left\langle 0, k', -^{(0)} \middle| 0, k, +^{(0)} \right\rangle \left| 0, k', -^{(0)} \right\rangle \\
&+ \frac{\epsilon_k^{(0)}}{\epsilon_k^{(0)} - \epsilon_{\text{br.}}^{(0)}} \left\langle 0, \text{br.}, +^{(0)} \middle| 0, k, +^{(0)} \right\rangle \left| 0, \text{br.}, +^{(0)} \right\rangle \\
&- \frac{\epsilon_k^{(0)}}{\epsilon_k^{(0)} + \epsilon_{\text{br.}}^{(0)}} \left\langle 0, \text{br.}, -^{(0)} \middle| 0, k, +^{(0)} \right\rangle \left| 0, \text{br.}, -^{(0)} \right\rangle \Bigg]
\end{aligned} \tag{H.10}
$$

$$
\begin{aligned}
\left| m = 0, k, -^{(1)} \right\rangle = -\Bigg[ &\sum_{k'} \Delta k' k' \frac{\epsilon_k^{(0)}}{\epsilon_k^{(0)} + \epsilon_{k'}^{(0)}} \left\langle 0, k', +^{(0)} \middle| 0, k, -^{(0)} \right\rangle \left| 0, k', +^{(0)} \right\rangle \\
&+ \frac{\epsilon_k^{(0)}}{\epsilon_k^{(0)} + \epsilon_{\text{br.}}^{(0)}} \left\langle 0, \text{br.}, +^{(0)} \middle| 0, k, -^{(0)} \right\rangle \left| 0, \text{br.}, +^{(0)} \right\rangle \\
&- \frac{\epsilon_k^{(0)}}{\epsilon_k^{(0)} - \epsilon_{\text{br.}}^{(0)}} \left\langle 0, \text{br.}, -^{(0)} \middle| 0, k, -^{(0)} \right\rangle \left| 0, \text{br.}, -^{(0)} \right\rangle \Bigg]
\end{aligned}
$$

$$\left|m=0,\text{br.},+^{(1)}\right\rangle = -\left[-\frac{1}{2}\left\langle 0,\text{br.}-^{(0)}\middle|0,\text{br.}+^{(0)}\right\rangle\left|0,\text{br.}-^{(0)}\right\rangle +\right.$$

$$\sum_{k'}\Delta k'k'\left[\frac{\epsilon_{\text{br.}}^{(0)}}{\epsilon_{\text{br.}}^{(0)}-\epsilon_{k'}^{(0)}}\left\langle 0,k',+^{(0)}\middle|0,\text{br.},+^{(0)}\right\rangle\left|0,k',+^{(0)}\right\rangle\right.$$

$$\left.\left.-\frac{\epsilon_{\text{br.}}^{(0)}}{\epsilon_{\text{br.}}^{(0)}+\epsilon_{k'}^{(0)}}\left\langle 0,k',-^{(0)}\middle|0,\text{br.},+^{(0)}\right\rangle\left|0,k',-^{(0)}\right\rangle\right]\right]$$

$$\left|m=0,\text{br.},-^{(1)}\right\rangle = -\left[\frac{1}{2}\left\langle 0,\text{br.}+^{(0)}\middle|0,\text{br.}-^{(0)}\right\rangle\left|0,\text{br.}+^{(0)}\right\rangle +\right.$$

$$\sum_{k'}\Delta k'k'\left[-\frac{\epsilon_{\text{br.}}^{(0)}}{\epsilon_{\text{br.}}^{(0)}-\epsilon_{k'}^{(0)}}\left\langle 0,k',-^{(0)}\middle|0,\text{br.},-^{(0)}\right\rangle\left|0,k',-^{(0)}\right\rangle\right.$$

$$\left.\left.+\frac{\epsilon_{0,\text{br.}}^{(0)}}{\epsilon_{\text{br.}}^{(0)}+\epsilon_{k'}^{(0)}}\left\langle 0,k',+^{(0)}\middle|0,\text{br.},-^{(0)}\right\rangle\left|0,k',+^{(0)}\right\rangle\right]\right]$$

$$\left|m=+1,k,+^{(1)}\right\rangle = -\left[\sum_{k'}-\Delta k'k'\frac{\epsilon_k^{(0)}}{\epsilon_k^{(0)}+\epsilon_{k'}^{(0)}}\left\langle 1,k',-^{(0)}\middle|1,k,+^{(0)}\right\rangle\left|1,k',-^{(0)}\right\rangle\right.$$

$$\left.+\left\langle 1,\text{tr.},+^{(0)}\middle|1,k,+^{(0)}\right\rangle\left|1,\text{tr.}^{(0)}\right\rangle\right]$$

$$\left|m=+1,k,-^{(1)}\right\rangle = -\left[\sum_{k'}\Delta k'k'\frac{\epsilon_k^{(0)}}{\epsilon_k^{(0)}+\epsilon_{k'}^{(0)}}\left\langle 1,k',+^{(0)}\middle|1,k,-^{(0)}\right\rangle\left|1,k',+^{(0)}\right\rangle\right.$$

$$\left.+\left\langle 1,\text{tr.},+^{(0)}\middle|1,k,-^{(0)}\right\rangle\left|1,\text{tr.}^{(0)}\right\rangle\right]$$

$$\left|m=+1,\text{tr.}\right\rangle^{(1)} = 0$$

where $\epsilon_{\text{br.}}^{(0)} \approx 0.839$ and $\epsilon_k^{(0)} = 1+k^2$ for $b_0 = 1$. The corrections from the $m=-1$ sector can be calculated from the corrections in the $m=1$ sector via $|m=-1,\mp\rangle = \sigma^x\,|m=1,\pm\rangle^*$ and are therefore not listed here explicitly.

## H.4  Translational Mode in Terms of $a, a^*$

The ansatz which describes pure translation of an otherwise static magnetic texture $\hat{\mathbf{M}}^{(0)}$ by velocity $\mathbf{v}_{\text{slide}}$ is $\hat{\mathbf{M}}(\mathbf{r},t) = \hat{\mathbf{M}}^{(0)}(\mathbf{r}-\mathbf{v}_{\text{slide}}t)$[1]. Taylor expanding to first order in $\mathbf{v}_{\text{slide}}t$,

---

[1]note that this is *not* the same situation as our driven texture. There, there would be extra contributions coming from the first and second order oscillating terms $\mathbf{M}_{\text{osc.}}^{(1)}$, $\mathbf{M}_{\text{osc.}}^{(2)}$, as well as the static second order component, $\mathbf{M}_{\text{stat.}}^{(2)}$.

we obtain the translational mode $\mathbf{M}^{(2)}_{\text{trans.}} = -t(\mathbf{v}_{\text{slide}} \cdot \boldsymbol{\nabla})\hat{\mathbf{M}}^{(0)}$. We want to express this in the $a, a^*$ basis. We use the definition Eq. (2.24),

$$\mathbf{M}^{(2)} = (1 - a^*a)\mathbf{e}_3 + \mathbf{e}_- a + \mathbf{e}_+ a^*. \tag{H.11}$$

Projecting $\mathbf{e}_{\pm}$ onto $\mathbf{M}^{(2)}_{\text{trans.}}$, and using $\hat{\mathbf{M}}^{(0)} = \mathbf{e}_3$ and $\nabla \hat{\mathbf{M}}^{(0)} \perp \hat{\mathbf{M}}^{(0)}$, we obtain

$$\begin{pmatrix} a_{\text{trans.}} \\ a_{\text{trans.}} \end{pmatrix} = -t \begin{pmatrix} \mathbf{e}_+ \cdot ((\mathbf{v}_{\text{slide}} \cdot \boldsymbol{\nabla})\mathbf{e}_3) \\ \mathbf{e}_- \cdot ((\mathbf{v}_{\text{slide}} \cdot \boldsymbol{\nabla})\mathbf{e}_3) \end{pmatrix}. \tag{H.12}$$

Using the following coordinate identities

$$\begin{aligned} \partial_x &= \cos(\chi)\partial_r - \frac{1}{r}\sin(\chi)\partial_\chi \\ \partial_y &= \sin(\chi)\partial_r + \frac{1}{r}\cos(\chi)\partial_\chi \end{aligned} \tag{H.13}$$

as well as the identities $\partial_r \mathbf{e}_3 = \theta'_0 \partial_\theta \mathbf{e}_3$, $\partial_\chi \mathbf{e}_3 = \partial_\phi \mathbf{e}_3$ $\partial_r \mathbf{e}_3 = \theta'_0 \partial_\theta \mathbf{e}_3$, which are valid in the case that $\mathbf{e}_3$ describes a static skyrmion Eq. (1.15), we obtain Eq. (3.33).

It is easy to check that each of the translational mode vectors in Eq. (3.33) is normalised under

$$\langle m = \pm 1, \text{trans.} | \sigma^z | m = \pm 1, \text{trans.} \rangle = \pm 1.$$

## H.5  Fourier Coefficients for First Order Steady State

The first order in $\alpha$ Fourier coefficients for the out of plane driving case are

$$
\begin{aligned}
c_{k'}^{(1)} = -\Bigg( & c_{k'}^{(0)} + \sum_k \Delta k \, k c_k^{(0)} \left[ -\left\langle k', +^{(0)} \middle| \sigma_z \middle| k, -^{(1)} \right\rangle - \left\langle k', +^{(0)} \middle| k, -^{(0)} \right\rangle \right] \\
& + c_{\mathrm{br.}}^{(0)} \Big[ \left\langle k', +^{(0)} \middle| \sigma_z \middle| \mathrm{br.}+^{(1)} \right\rangle - \left\langle k', +^{(0)} \middle| \sigma_z \middle| \mathrm{br.}-^{(1)} \right\rangle \\
& + \left\langle k', +^{(0)} \middle| \mathrm{br.}+^{(0)} \right\rangle - \left\langle k', +^{(0)} \middle| \mathrm{br.}-^{(0)} \right\rangle \Big] \Bigg) \\
c_{\mathrm{br.}}^{(1)} = -\Bigg( & c_{\mathrm{br.}}^{(0)} \left[ -\left\langle \mathrm{br.}, +^{(0)} \middle| \sigma_z \middle| \mathrm{br.}-^{(1)} \right\rangle + \left\langle \mathrm{br.}, +^{(0)} \middle| \mathrm{br.}+^{(0)} \right\rangle - \left\langle \mathrm{br.}, +^{(0)} \middle| \mathrm{br.}-^{(0)} \right\rangle \right] \\
& + \sum_k \Delta k \, k c_k^{(0)} \Big[ \left\langle \mathrm{br.}, +^{(0)} \middle| \sigma_z \middle| k, +^{(1)} \right\rangle - \left\langle \mathrm{br.}, +^{(0)} \middle| \sigma_z \middle| k, -^{(1)} \right\rangle \\
& + \left\langle \mathrm{br.}, +^{(0)} \middle| k, +^{(0)} \right\rangle - \left\langle \mathrm{br.}, +^{(0)} \middle| k, -^{(0)} \right\rangle \Big] \Bigg)
\end{aligned}
$$

$$ \text{(H.14)} $$

For $b_0 = 1$, $c_{\mathrm{br.}}^{(1)} \approx 0.491$.

The first order in $\alpha$ Fourier coefficients for the $|m = 1, k = 0, \alpha, -\rangle$ mode are

$$
\begin{aligned}
a_{k'}^{(1)} = -\frac{1}{\epsilon_0^{(0)} + \epsilon_{k'}^{(0)}} \Bigg[ & 2\epsilon_0^{(0)} a_{k'}^{(0)} + \sum_k \Delta k \, k \frac{\epsilon_k^{(0)} - \epsilon_0^{(0)}}{\epsilon_k^{(0)} + \epsilon_{k'}^{(0)}} \epsilon_{k'}^{(0)} b_k^{(0)} \langle m = 1, k', +|^{(0)} |m = 1, k, -\rangle^{(0)} \\
& + \mathrm{sgn}(\gamma) \langle m = 1, k', +|^{(0)} (\epsilon_0^{(1)} - H_1) \left| \frac{1}{4\sqrt{2}} \begin{pmatrix} c - 1 \\ c + 1 \end{pmatrix} \right\rangle \Bigg] \\
b_{k'}^{(1)} = \frac{1}{\epsilon_{k'}^{(0)} - \epsilon_0^{(0)}} \Bigg[ & \sum_k \Delta k \, k \frac{\epsilon_0^{(0)} + \epsilon_k^{(0)}}{\epsilon_k^{(0)} + \epsilon_{k'}^{(0)}} \epsilon_{k'}^{(0)} a_k^{(0)} \langle m = 1, k', -|^{(0)} |m = 1, k, +\rangle^{(0)} \\
& + \mathrm{sgn}(\gamma) \langle m = 1, k', -|^{(0)} (\epsilon_0^{(1)} - H_1) \left| \frac{1}{4\sqrt{2}} \begin{pmatrix} c - 1 \\ c + 1 \end{pmatrix} \right\rangle \Bigg] \\
d_{\mathrm{tr.}}^{(1)} = 0 &
\end{aligned}
$$

$$ \text{(H.15)} $$

# H.6   Poisson Bracket $\mathcal{O}(\epsilon^2)$ Contribution

For reference, we list the time- and angular– averaged Poisson bracket at order $\epsilon^2$,

$$
\left\langle \frac{1}{2\pi} \int d\chi\, e^{-i\chi} \{F^{(3)}_{\text{skyr.}} + F^{(1)}_{\text{drive}}, a^*\} \right\rangle_t =
$$

$$
\frac{b_z b_L e^{-i\delta}}{8r^2} \Bigg( 8\sqrt{2} r^2 \left(\theta_0' + 1\right) \left( a^{(1)}_{1,1} a^{*(1)'}_{0,1} + a^{(1)}_{0,-1} a^{*(1)'}_{-1,-1} \right)
$$

$$
+ a^{*(1)}_{0,1} \Big( 2r^2 \left( \sin(\theta_0) - 4\sqrt{2}\left(\theta_0' + 1\right) a^{*(1)'}_{-1,-1} \right)
$$

$$
- \sqrt{2} a^{(1)}_{1,1} \left( 2b_0 r^2 \sin(\theta_0) - 2r^2 \theta_0'' - 2r\theta_0' + 5\sin(2\theta_0) + 10r\cos(2\theta_0) - 2r \right) \Big)
$$

$$
- a^{*(1)}_{-1,-1} \Big( \sqrt{2} a^{*(1)}_{0,1} \big( 2b_0 r^2 \sin(\theta_0) + 6r^2 \theta_0'' + 6r\theta_0' - 8\sin(\theta_0)
$$

$$
+ 5\sin(2\theta_0) - 8r\cos(\theta_0) + 10r\cos(2\theta_0) + 6r \big)
$$

$$
- 4r^2 \left( \cos(\theta_0) - 2\sqrt{2}\left(\theta_0' + 1\right) a^{*(1)'}_{0,1} \right)
$$

$$
+ \sqrt{2} a^{(1)}_{0,-1} \big( 2b_0 r^2 \sin(\theta_0) - 2r^2 \theta_0'' - 2r\theta_0' - 8\sin(\theta_0)
$$

$$
+ 5\sin(2\theta_0) - 8r\cos(\theta_0) + 10r\cos(2\theta_0) - 2r \big) \Big) \Bigg)
$$

$$
+ \frac{b_z b_R e^{i\delta}}{8r^2} \Bigg( 8\sqrt{2} r^2 \left(\theta_0' + 1\right) \left( a^{(1)}_{1,-1} a^{*(1)'}_{0,-1} + a^{*(1)}_{0,1} a^{*(1)'}_{-1,1} \right)
$$

$$
+ a^{*(1)}_{0,-1} \Big( 2r^2 \left( \sin(\theta_0) - 4\sqrt{2}\left(\theta_0' + 1\right) a^{*(1)'}_{-1,1} \right)
$$

$$
- \sqrt{2} a^{(1)}_{1,-1} \left( 2b_0 r^2 \sin(\theta_0) - 2r^2 \theta_0'' - 2r\theta_0' + 5\sin(2\theta_0) + 10r\cos(2\theta_0) - 2r \right) \Big)
$$

$$
- a^{*(1)}_{-1,1} \Big( \sqrt{2} a^{*(1)}_{0,-1} \big( 2b_0 r^2 \sin(\theta_0) + 6r^2 \theta_0'' + 6r\theta_0' - 8\sin(\theta_0)
$$

$$
+ 5\sin(2\theta_0) - 8r\cos(\theta_0) + 10r\cos(2\theta_0) + 6r \big)
$$

$$
- 4r^2 \left( \cos(\theta_0) - 2\sqrt{2}\left(\theta_0' + 1\right) a^{*(1)'}_{0,-1} \right)
$$

$$
+ \sqrt{2} a^{*(1)}_{0,1} \big( 2b_0 r^2 \sin(\theta_0) - 2r^2 \theta_0'' - 2r\theta_0' - 8\sin(\theta_0)
$$

$$
+ 5\sin(2\theta_0) - 8r\cos(\theta_0) + 10r\cos(2\theta_0) - 2r \big) \Big) \Bigg),
$$

$$\tag{H.16}$$

where the subscripts $\chi, \omega$ on the $a^{(1)}_{\chi,\omega}, a^{*(1)}_{-\chi,-\omega}$ field components give us the angular momentum $m$ and frequency $\omega$, eg. $a_{11}$ would be the coefficient of the $e^{i(\chi+\omega t)}$ in the

dynamic response. $\left\langle \frac{1}{2\pi} \int d\chi \, e^{-i\chi} \{ F_{\text{skyr.}}^{(3)} + F_{\text{drive}}^{(1)}, a \} \right\rangle_t$ can be obtained by taking the complex conjugate of all the Fourier components in Eq. (H.16) and inverting the signs of the subscripts, eg $a_{1,1}^{(1)} \to a_{-1,-1}^{*(1)}$, $a_{1,-1}^{(1)} \to a_{-1,1}^{*(1)}$, as well as inverting the sign in front of the blue-coloured terms.

# Acknowledgements

I also cannot forget my office neighbours: Jan, Bernd, Zihao, Anne and Alla, who all shared office 112b with me at some point over the past three and a half years. I only hope that you enjoyed my company as much as I enjoyed yours and that my incessant humming or listening to classical music did not disturb you too much from doing your work. A special mention to Dennis, although you were in the next door office, for being a reliable source of banter and fun when I did not feel motivated to work. Many thanks too to Asuka who, while not officially part of thp, effectively became an honorary member, testament to her frequent visits. I will hold our many visits to the Philharmonie and bubble tea store, as well as our hilarious attempts to learn German from Pixar movies at the local cinema, in fond memory.

Several people have enabled me to continue to develop as a person as well as a physicist. Lucie, Christoph and Dimitris were all great Sprachtandem partners who also quickly became my friends — I cherished our weekly conversations in German, French and Greek. For a period, Daniel, Marek and Mike faced the cold and dark every Wednesday evening to go swimming with me in Stadionbad, with Aprem and Asuka joining in on Sundays in Agrippabad. On the music front, we had tremendous fun sight-reading anything we could get our hands on with Marcel. I can only hope to meet another duet partner who is as eager to take on the complete symphonic works of Beethoven and Schumann wherever I end up next :). Prof. Millet, Prof. Natochenny and Prof. Lebedeva also provided a welcome musical and cultural push.

Last but not least, I would like to mention the people who played a defining role in getting me to even study physics in the first place. I am forever indebted to my two sixth form teachers Mr. Vaccaro and Dr. Cheung — they were the first to really challenge me on maths and physics at school. From them I inherited a fiery passion for the subject as well an arsenal of "street-fighting" mathematical tricks that still serve me to this day. Over the course of my undergraduate studies in Cambridge, Prof. Khmelnitskii was also a constant source of support, and were it not for him directing me towards Cologne, I would probably not even be here, writing these words.

Finally, I must thank my family, especially my wonderful parents Leonor and Javier, for identifying and nurturing my interest in science from a young age. All the meccano, domino and chemistry sets, paint-making experiments on the verge of turning into disaster, Pipo learns maths/physics/biology computer games, endless visits to the Villette, Palais de la Découverte and Science and Natural History Museum ended up bearing their fruit. A special *clin d'œil* too to my four younger brothers Octavio, Adrian, Diego and Hector for providing a healthy dose of competition and always keeping me on my toes as we were growing up.

# Historical Context

The first words of this thesis were written just as the new covid vaccines were beginning to be rolled out around the world. We were all filled with optimism, having endured two years of maddening cyclical lockdowns during which so many people died. Then, on the 24th of February 2022 the Russian government unleashed an unprovoked and vicious war on its peaceful neighbour Ukraine. I must admit it felt at times pointless and decadent to have the luxury of writing a PhD thesis in warmth and safety while others less fortunate were hiding in cold bomb shelters without food, water or electricity. Nevertheless, in the long term I believe that only knowledge, beauty and science can prevail over hate, violence and destruction. I would like to dedicate this thesis to all the victims of this senseless war, and hope for better days ahead.

# Erklärung zur Dissertation

Hiermit versichere ich an Eides statt, dass ich die vorliegende Dissertation selbstständig und ohne die Benutzung anderer als der angegebenen Hilfsmittel und Literatur angefertigt habe. Alle Stellen, die wörtlich oder sinngemäß aus veröffentlichten und nicht veröffentlichten Werken dem Wortlaut oder dem Sinn nach entnommen wurden, sind als solche kenntlich gemacht. Ich versichere an Eides statt, dass diese Dissertation noch keiner anderen Fakultät oder Universität zur Prüfung vorgelegen hat; dass sie - abgesehen von unten angegebenen Teilpublikationen und eingebundenen Artikeln und Manuskripten - noch nicht veröffentlicht worden ist sowie, dass ich eine Veröffentlichung der Dissertation vor Abschluss der Promotion nicht ohne Genehmigung des Promotionsausschusses vornehmen werde. Die Bestimmungen dieser Ordnung sind mir bekannt. Darüber hinaus erkläre ich hiermit, dass ich die Ordnung zur Sicherung guter wissenschaftlicher Praxis und zum Umgang mit wissenschaftlichem Fehlverhalten der Universität zu Köln gelesen und sie bei der Durchführung der Dissertation zugrundeliegenden Arbeiten und der schriftlich verfassten Dissertation beachtet habe und verpflichte mich hiermit, die dort genannten Vorgaben bei allen wissenschaftlichen Tätigkeiten zu beachten und umzusetzen. Ich versichere, dass die eingereichte elektronische Fassung der eingereichten Druckfassung vollsändig entspricht.

## Teilpublikationen

"Archimedean Screw in Driven Chiral Magnets." **del Ser N.**, Heinen L., Rosch A., 2021. *SciPost Physics, 11(1):009.*

<div align="right">

Nina del Ser

Köln 2022

</div>